Depletion of CMOS pixel sensors : studies, characterization, and applications

Julian Heymes

Université de Strasbourg

UNIVERSITÉ DE STRASBOURG

pcp

ÉCOLE DOCTORALE PHYSIQUE ET CHIMIE PHYSIQUE

Institut Pluridisciplinaire Hubert Curien

THÈSE

présentée par :

Julian HEYMES

soutenue le : **17 juillet 2018**

pour obtenir le grade de : **Docteur de l'université de Strasbourg**

Discipline/ Spécialité : PHYSIQUE

Désertion de Capteurs à Pixel CMOS : Etude, Caractérisations et Applications

Depletion of CMOS Pixel Sensors: Studies, Characterization, and Applications

THÈSE dirigée par :

Mr Jérôme BAUDOT	Professeur, Université de Strasbourg

RAPPORTEURS :

Mr Marlon BARBERO	Professeur, Université d'Aix-Marseille
Mr Konstantin STEFANOV	Docteur, Open University, Milton Keynes (UK)

EXAMINATEURS :

Mr Luc HEBRARD	Professeur, Université de Strasbourg
Mme Petra RIEDLER	Docteur, CERN (CH)
Mme Cornelia WUNDERER	Docteur, DESY, Hambourg (DE)

À ma mère

Remerciements

Pour commencer, je tiens à remercier Jérôme, pour m'avoir fait confiance et guidé au cours des trois années, de m'avoir permis d'avoir toutes ces opportunités. Ensuite, il est plus que normal de remercier mon co-directeur de thèse officieux, Maciej, qui a toujours été d'une grande aide. Je ne peux continuer sans remercier Christine et Claude avec qui toute cette aventure a commencé.

Je veux remercier ceux qui ont été en mesure de m'aider sur des points très précis mais également avec qui j'ai pu avoir des discussions agréables. J'espère donc n'oublier personne (si c'est le cas, il ne faut pas m'en vouloir) et je remercie donc Fred, Hung, Isabelle, Andrei, Greg, Kader, Christian, Mathieu, Gilles, Matthieu, Kimmo, Marc, Isabelle, Auguste, Alejandro, Rachid, Xiaochao, Sylviane. À nouveau, j'espère n'avoir oublié personne et si c'est le cas il ne faut pas m'en vouloir. Je tiens aussi à remercier la microtechnique pour le bonding rapide qui a évité de grandes pertes de temps dans certains travaux. Merci aussi à l'équipe de Cyrcé pour avoir fourni rapidement une place pour effectuer des mesures et pour cette expérience supplémentaire. Je remercie également tous ceux de la collaboration MAPSSIC avec qui il a été très agréable d'échanger et surtout merci de laisser sa chance aux étudiants et doctorants.

Ensuite, un grand merci au jury de thèse dont les remarques, avis et questions qui ont grandement permis d'améliorer la qualité de cette thèse. Je tiens tout particulièrement à remercier Luc Hébrard d'avoir accepté de présider ce jury et surtout pour avoir été celui qui m'a donné envie de me lancer dans la microélectronique un peu par hasard il y a quelques années (évitons de compter).

Je tiens à remercier toute ma famille au sens très large du terme qui a toujours été présente et d'un grand support surtout dans les moments difficiles. Je remercie donc mes parents, avec toujours une pensée particulière pour ma mère, pour m'avoir toujours soutenu et encouragé à aller de l'avant. Merci à Agnès d'avoir été présente même si tu m'as bien pris la tête aux mauvais moments. Merci aussi à Maki pour les ronrons et Leia pour les conneries.

Résumé

Introduction

Les résultats de nombreuses expériences scientifiques, notamment en physique, dépendent de capteurs dédiés. Les capteurs pixélisés fabriqués en technologie CMOS (*Complementary Metal Oxide Semiconductor*) dont le développement technologique est mené par les applications grand public, avec l'intégration d'un nombre croissant de capteurs photographiques dans les *smartphones*, sont de plus en plus considérés pour des applications scientifiques.

Ces capteurs sont des détecteurs semi-conducteurs dont le procédé de fabrication se trouve sur le même substrat servant à la détection. Des puits n et p sont réalisés afin d'obtenir des transistors NMOS et PMOS permettant donc les architectures CMOS. Afin d'utiliser les PMOS, la technologie utilisée dispose de puits p profonds permettant d'isoler le puits n pour qu'il n'entre pas en concurrence dans la phase de collection.

Afin de garantir les performances de détection dans des expériences de physique utilisant des rayonnements ionisants, ces capteurs nécessitent un grand volume déserté. Les premières versions de capteurs ne pouvaient qu'être partiellement désertés, les rendant incompatibles pour la plupart des applications à cause d'une collection de charge incomplète minimisant le rapport signal à bruit d'autant plus marqué par des dégâts dues aux irradiations. Avec l'accès, depuis quelques années, à des substrats de haute résistivité et la possibilité d'utiliser des procédés de fabrication modifiés, adaptés aux besoins dictés par ces expériences, il devient possible de déserter intégralement les volumes sensibles. Ainsi, les capteurs à pixel CMOS (CPS, *CMOS Pixel Sensor*) sont considérés pour des applications allant de la physique des hautes énergies aux applications utilisant des rayons X mous en passant par la microscopie électronique ultra rapide ou à de la testabilité non destructrice.

Les études de cette thèse sont principalement dirigées vers les applications utilisant les rayons X mous (de quelques dizaine d'eV à environ une dizaine de keV), telles que la spectroscopie ou de l'imagerie par comptage de photons, ainsi que pour des applications

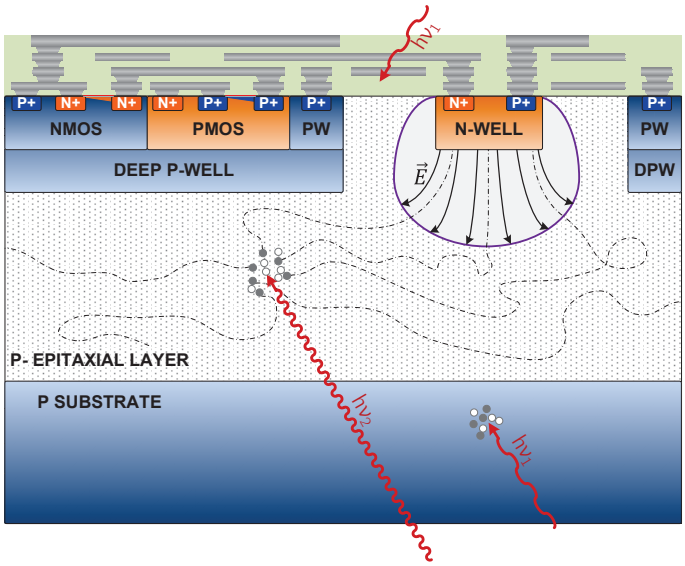

Figure 1: CPS dont la couche épitaxiée est partiellement désertée. Les rayons X de faible énergie sont absorbés dans des parties insensibles (métallisation et substrat insensible). Un photon interagissant dans la couche sensible (epi) génère une charge proportionnelle à son énergie. Les électrons diffusent jusqu'à être collectés par le champ électrique de la faible zone désertée soit dans le pixel où le photon à intéragi soit dans un pixel voisin. Si l'électron n'est pas collecté suffisament rapidement, il se recombine avec un trou et est perdu.

d'imagerie moléculaire utilisant des positrons jusqu'à quelques MeV.

Signal Attendu

Les électrons dans la gamme d'énergie de cette dernière application interagissent dans le silicium par des collisions successives provoquant l'ionisation de la matière le long de son passage. Au minimum d'ionisation, une charge totale proportionnelle à l'épaisseur sensible est déposée à hauteur de 74 paires électron/trou par micromètre. Ainsi pour des épaisseurs de volume sensibles pour les applications étudiées, une charge de plusieurs milliers d'électrons est attendue.

Dans la gamme des rayons X mous, les photons interagissent par effet photoélectrique. Lorsque ces photons sont absorbés, une charge proportionnelle à l'énergie du photon est déposée localement. La variation de charge déposée est dépendante du facteur de Fano

et joue un rôle important dans la résolution en énergie. Le nombre de photons d'un faisceau absorbés dans un volume augmente avec l'épaisseur de ce dernier suivant la loi de Beer-Lambert et est dépendant de l'énergie. Ainsi une épaisseur sensible minimale en illumination par l'arrière est nécessaire pour garantir l'efficacité quantique. Les épaisseurs les plus fines ne peuvent être atteintes sans utilisation de méthodes coûteuses pour garantir la rigidité du capteur et limite donc l'épaisseur minimale. Cette épaisseur doit être intégralement désertée pour garantir l'efficacité de collection. Pour les photons de plus faible énergie, l'illumination par l'avant est exclue car ceux-ci ont une très grande probabilité d'être absorbés par les couches de métallisation formées par les interconnections de la technologie CMOS.

Lorsque les électrons formant la charge sont générés dans un substrat partiellement ou non-déserté, ceux-ci diffusent dans le volume sensible et peuvent être soit collectés par un champ électrique limité à un faible volume autour de la diode de collection (jonction pn). Cette collection peut se répartir sur plusieurs pixels adjacents, formant du partage de charge. Egalement, une partie des électrons peuvent ne jamais être collectés et, après un certain temps (temps de recombinaison), se recombinent avec un trou dans le silicium du volume sensible. Cette proportion de la charge est donc perdue et ne contribue pas au signal.

Application de la Désertion par la Face Avant du Capteur

Dans un volume intégralement déserté, le champ électrique est présent en tout point et permet donc la collection de la charge en un temps très faible et sur un seul pixel, garantissant ainsi un signal élevé correspondant à la charge déposée. La désertion complète peut être obtenue avec l'utilisation de substrats de haute résistivité et/ou avec l'application d'une forte tension de polarisation inverse sur la jonction pn, la diode de collection.

Dans le cadre de cette étude, l'architecture proposée consiste à appliquer une tension de polarisation par l'avant du capteur (du coté de la métallisation) fabriqué sur un substrat de haute résistivité. L'application de la polarisation par la face avant du capteur permet

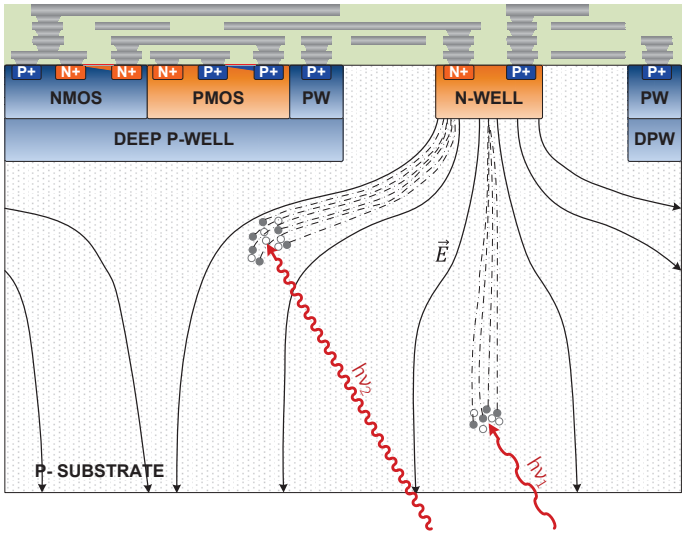

Figure 2: CPS fabriqué dans un substrat massif (type Czochralski) intégralement déserté. Les charges générées dans le volume sont intégralement collectées par dérive dans un unique pixel.

de s'affranchir d'un contact sur la face arrière pour minimiser la fenêtre d'entrée et ainsi permettre la détection de rayons X de faible énergie.

L'application de la forte polarisation est effectuée au travers de la diode de collection (en inverse) via une diode en direct. L'application de cette forte tension sur le nœud d'entrée est incompatible avec les architectures couplées DC. En effet, les tensions tolérées par la technologie sont largement dépassées. Ainsi, une capacité de couplage est insérée entre la diode de collection et l'amplificateur et permet l'application de la haute tension sans risquer l'intégrité de l'architecture de lecture. L'utilisation de cette méthode permet l'utilisation des technologies proposées sans modifications pouvant se révéler coûteuses.

Un prototype nommé PIPPER-2 utilisant l'architecture de la polarisation par la face avant a été conçu en 2015 à l'IPHC par Maciej Kachel et Andreï Dorokhov en technologie TowerJazz 180nm CIS (*CMOS Image Sensor*).

Ce capteur de 5 mm^2 est composé de 4 sous-matrices de pixels (*pitch :* 22µm) ordonnés dans chaque en 16 colonnes et 128 lignes. Trois de ces sous-matrices sont destinées à l'étude de la désertion dans les capteurs à pixels CMOS et la quatrième est une architecture d'amplificateur qui n'est pas détaillée dans ce travail. Chaque colonne de la sous-matrice sélectionnée est connectée à un plot de connexion dédié. Le signal analogique en sortie

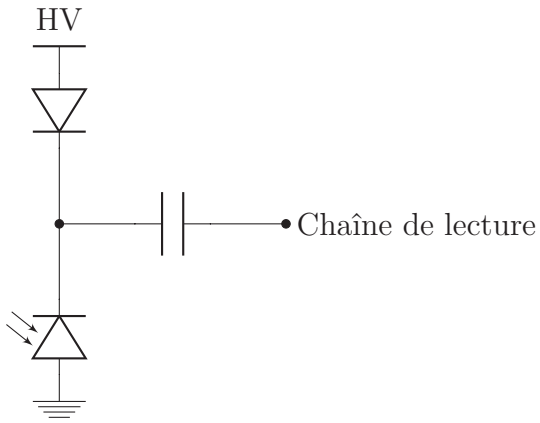

Figure 3: Schéma du nœud de collection permettant l'application de la désertion par la face avant du capteur. La polarisation est appliquée à la diode de collection au moyen d'une diode en direct. La chaîne de lecture est capacitivement couplée.

du pixel est adressé à la colonne pour être lu selon la méthode du volet roulant (*rolling-shutter*). La combinaison de petits pixels et de la lecture analogique a été guidé par l'optique d'application en imagerie X.
L'architecture a été fabriquée sur deux différents types de substrats de haute résistivité :

- une fine couche épitaxiale (18 µm) de résistivité supérieure à 1 kΩ cm dénommé HR18

- un substrat massif d'une épaisseur de 280 µm fabriqué selon la technique Czochralski présentant une résistivité supérieure à 600 kΩ cm dénommé CZ. Plusieurs capteurs fabriqués sur ce substrat ont été amincis à 50 µm dont environ 40 µm sont sensibles le restant étant composé des couches de métallisation. La face arrière amincie de ces capteurs ont ensuite été passivés selon la méthode PULSION® permettant l'obtention d'une fenêtre d'entrée limitée à quelques dizaines de nanomètres.

Les travaux présentés dans ce document se concentrent sur une seule architecture de pixel du capteur PIPPER-2. La diode de collection cylindrique d'un diamètre de 5 µm est connectée à un suiveur de source par couplage capacitif (21 fF). Un jeu de diodes, isolées du substrat afin de ne pas entrer en compétition pour la collection, après le couplage permet l'établissement du point DC en entrée de l'amplificateur.

Caractérisation du Prototype

Chaque version du capteur (HR18 et CZ aminci) a été connecté à son circuit imprimé dédié permettent l'illumination par les deux faces. L'ensemble circuit imprimé capteur est maintenu a température constante (environ 10 °C) pour garantir les mêmes conditions d'opération pour chaque variation de polarisation et d'illumination.

Avant toute illumination, les caractéristiques I-V ont été obtenues à l'aide d'une source de tension Keithley 237 faisant également office de pico-ampèremètre. La tension de polarisation inverse distribuée sur les 3 sous-matrices destinées à l'étude de la désertion étaient dans une gamme de 0 à 46 volt. La version du capteur fabriqué sur le substrat epitaxié était en phase d'avalanche à la limite du claquage à la tension la plus élevée de la gamme. Ainsi, une limite de 45 V pour toute étude s'est imposée et a également été appliquée pour le substrat CZ bien que la limite ait pu être repoussée.
Néanmoins, la forme des courbes obtenues ont permis de déterminer que le substrat HR18 est intégralement déserté pour des polarisations supérieures à 6 V et que le substrat massif ne l'est pas peu importe la tension appliquée.

Le capteur polarisé à différentes tensions en deçà de la limite imposée a été caractérisé en laboratoire :

- 30 000 trames consécutives sans illumination permettant la mesure du bruit
- 6 000 000 de trames avec illumination, par paquets de 30 000 permettant la prévention d'un goulot d'étranglement et la limitation de la taille des fichiers de données

Chaque trame est obtenue après un temps d'intégration de 40 µs et le signal analogique de chaque pixel est amplifié avant d'être converti en une valeur digitale sur 14 bits. Lors de l'analyse des fichiers de mesure, deux trames consécutives sont utilisées pour n'en former qu'une permettant du double échantillonnage corrélé hors ligne.

Les prototypes caractérisés ont été illuminés à l'aide de photons de différentes énergies issues de plusieurs sources:

- une source scellée de ^{55}Fe émettant deux raies caractéristiques : Mn-Kα (5.9 keV) et Mn-Kβ (6.49 keV) respectivement à hauteur de 90 % et 10 %

- Un générateur de rayons X Rigaku Geigerflex avec la possibilité d'utiliser trois différents tubes et de sélectionner des raies et leurs harmoniques à l'aide d'un monochromateur :
  - Cr: 5.4 keV
  - Cu: 8.05 keV
  - Mo: 17.48 keV

Grace à la lecture rapide du capteur, les impacts sur la matrice sont indépendants est discernables permettant ainsi l'étude des amas formés par l'étalement de la charge sur plusieurs pixels. Le pixel ayant le signal le plus élevé est appelé le pixel siège et les 8 pixels à proximité directe sont appelés les voisins. Les amplitudes des proportions de charge collectées sur le siège et sur les voisins à chaque impact sont utilisées pour reconstruire les spectres de la source. Ainsi avec une tension de polarisation suffisamment élevée et donc grâce à l'excellente collection de charge par champ électrique il est possible d'observer les raies caractéristiques des sources utilisées pour l'illumination sur le spectre du pixel siège. Les pics de calibration du ^{55}Fe sont discernables l'un l'autre et, dans le plateau aux basses énergies, les pics formés par la fluorescence et l'échappement du silicium sont observables. Les proportions de charges collectées par les voisins sont marginales confirmant ainsi l'excellente collection de charge par champ électrique.
Chaque pic de calibration obtenu par les sources a été ajusté à l'aide d'une fonction Crystal Ball, composée d'une partie Gaussienne et d'une partie en loi de puissance qui permet la modélisation du partage de charge. La position du pic ainsi que l'écart-type sont utilisés pour déterminer les paramètres de performance du capteur testé à une configuration énergie/polarisation donnée. Les performances communes aux deux types de substrats sont :

- Bruit équivalent charge : 24 électrons.
- Linéarité garantie jusqu'à 16 keV. La non-linéarité n'est pas expliquée.
- Gain de conversion : 17 µV/electron
- Capacité équivalente en entrée : 9 fF, limitée par la capacité inter-puits. La valeur établie est atteinte pour des polarisations plus faibles dans le substrat épitaxié que dans le substrat CZ en raison des différences de résistivités.

Des différences sont néanmoins observables dans la valeur moyenne de la proportion de charge collectée sur pixel siège, atteignant 90 % avec la fine couche épitaxiée et 86 % dans le substrat Czochralski illuminé par l'avant et 84 % en illumination par l'arrière, suggérant à nouveau une désertion partielle du volume.
L'autre principale différence entre les deux substrats concerne la résolution en énergie. Dans la fine couche de 18 microns, une résolution de 280 eV à 5.9 keV est atteinte et se révèle légèrement plus faible (288 eV) dans le substrat CZ aminci.
Une étude de la résolution en énergie a permis la mise en évidence de ses composantes :

- Le bruit équivalent charge, qui peut être mesuré
- Le bruit Fano causé par la dispersion sur la génération de charge, qui peut être estimé par calcul
- La dispersion de gain entre pixels obtenu avec l'aide des deux précédentes contributions. Cette dispersion moyenne a été estimée à 1.2 % dans le capteur PIPPER-2

A basse énergie, la résolution est limitée par le bruit équivalent charge. Ainsi, une architecture d'amplificateur bas bruit/basse dispersion est proposée ultérieurement.

Une des principales applications à la résolution en énergie, la spectroscopie, a été expérimentée. Des pilules destinées à la fluorescence ont été illuminés par des photons monochromatiques issus de la cible de cuivre dans le générateurs de rayons X. Les éléments ont tous été retrouvés ainsi que la source, mais également le pic de fluorescence du silicium et un élément supplémentaire pouvant correspondre au traitement du bois servant de support aux échantillons.

L'utilisation de capteurs désertés ne se limite pas uniquement aux applications des rayons X mous. Grace au champ électrique intense permettant la collection de charge en un temps très réduit, la tenue au radiation non ionisante, qui génère des pièges dans le cristal, peut être améliorée. Ainsi, un jeu de 5 capteurs fabriqués sur substrat épitaxié ont subi des radiations non-ionisantes à différentes fluences allant jusqu'à $5 \times 10_{14}$ n_{eq}/cm^2. Malgré un refroidissement du capteur à -20 °C pour limiter l'influence du courant de fuite, ce dernier se révèle supérieur à celui relevé dans des capteurs non-irradiés. Néanmoins, les excellentes performances de collection de charge par dérive avant recombinaison, le signal observé n'a été que peu impacté. Ainsi, le rapport signal à bruit se révèle suffisamment

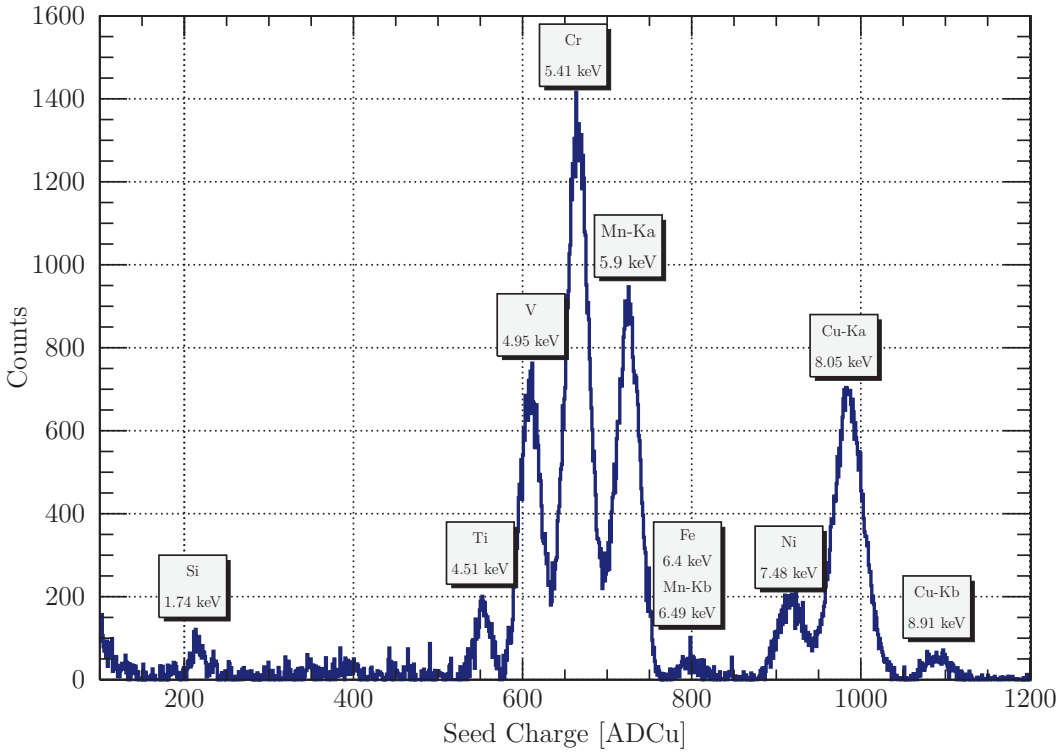

Figure 4: Spectre de fluorescence aux rayons X obtenu avec un prototype PIPPER-2 fabriqué sur couche épitaxiée et polarisé à 40 V. Des échantillons de Ti, V, Cr et Mn ont été illuminés par des rayons X monochromatiques obtenus avec un tube de Cu.

élevé (15) pour des applications de physique des hautes énergies en milieu radiatif.

Etude de la Profondeur de Désertion

La désertion dans PIPPER-2 fabriqué sur substrat épitaxié est considérée complète contrairement au substrat CZ. Afin d'estimer la profondeur atteinte, une étude analytique est effectuée, suivie de simulations et d'estimations par mesure.

L'équation de la largeur de la zone de charge d'espace donnée dans la littérature, en physique du semi-conducteur, est amplement surestimée. En effet, la solution obtenue dans le substrat CZ pour la résistivité garantie suggère un substrat intégralement déserté pour une polarisation au-delà de 25 V qui n'a pas été observé par mesure. Cette différence est expliquée par la condition initiale de l'équation employée qui considère une jonction pn infinie. Or, avec une diode de diamètre 5 µm dans un pixel carré de coté 22 µm, la jonction ne représente que 4 % de l'aire du pixel. Il a donc été nécessaire d'adapter l'équation pour cette condition.

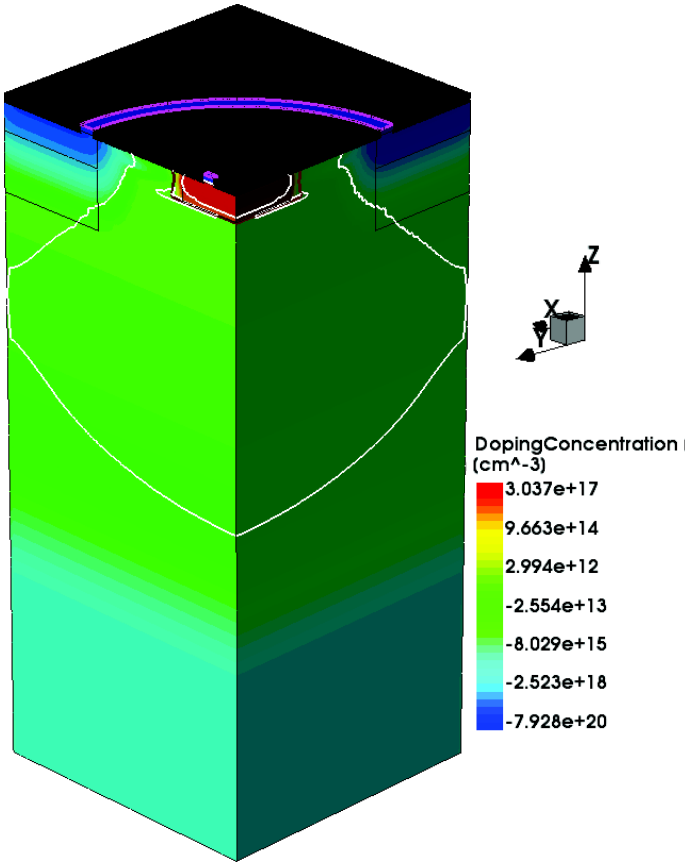

Figure 5: Structure réaliste du pixel PIPPER-2 étudié simulé par éléments finis polarisé à 20 V. La zone désertée est délimitée par la ligne blanche

En prenant en compte les contraintes de taille : petite diode et largeur finie, l'expression analytique suggère que la désertion n'atteint pas le fond du volume. Et est limitée entre 17 et 22 µm selon la résistivité considérée.

Pour confirmer ces profondeurs, des simulations par éléments finis ont été effectuées. En premier lieu, une structure simplifiée similaire à celle considérée pour l'expression analytique adaptée a été utilisée. Celle-ci est composée d'un puits cylindrique, de diamètre et profondeur correspondante à l'architecture du pixel de PIPPER-2 étudié, uniformément dopé de type n dans un substrat de type p uniformément dopé correspondant à des résistivités supérieures ou égales au minimum de 600 Ω cm. Les profondeurs obtenues par simulation surestiment celles obtenues par l'équation réécrite et suggère une désertion complète si le champ électrique est pris en compte.

Une seconde structure, réaliste, a donc été implémentée. Contrairement au modèle

simplifié, le puits n n'est plus uniformément dopé mais est défini avec un gradient issu des documentations de la technologie. Il en est de même avec les puits profonds de type p qui isolent les transistors du substrat. Ces puits n'avaient pas été pris en compte dans les études précédentes. La simulation du substrat CZ est effectuée dans des volumes uniformément dopés similairement au modèle simplifié. Concernant la couche épitaxiée, celle-ci n'est pas uniformément dopée et présente un gradient de dopage dont le profil a été implémenté pour la simulation.

Peu importe le type de substrat, l'extension du volume déserté est limitée par la présence des puits profonds de type p. Dans la couche épitaxiée, le gradient de dopage génère un champ électrique opposé qui limite la profondeur que peut atteindre le volume déserté. Ainsi cette couche est intégralement désertée mais pas sur les 18 µm saturant à 13 µm. Selon les résultats du substrat CZ, avec une résistivité de 600 Ω cm, une désertion atteignant 17 µm peut être espérée. 22 µm peuvent être atteints en considérant une résistivité supérieure (2 kΩ cm). Néanmoins, l'observation des simulations des volumes sensible montre que le champ électrique se révèle présente et intense au-delà de la zone déserté. Ainsi dans la version CZ de PIPPER-2 une excellente collection de charge par dérive est possible sur plusieurs microns au-delà du volume déserté. Une plus faible distance peut être espérée dans le volume épitaxié limité par le champ électrique opposé. Néanmoins, la profondeur maximale atteinte par ce champ est obtenu pour des polarisations moyennes (au-delà de 6 V) permettant une désertion complète.

Afin de confirmer ces résultats, une méthode de détermination de la profondeur de désertion est proposée. Le nombre de rayons X absorbés est proportionnel à l'épaisseur sensible et le nombre collecté par dérive dépend de la profondeur de la zone déserté. Ainsi, en comparant le ratio d'entrées de deux spectres obtenus pour différentes condition à une atténuation relative entre deux différentes épaisseurs il est possible, en fixant une profondeur, de déterminer la profondeur obtenue avec l'autre condition. L'épaisseur choisie correspond au point obtenu par simulation du modèle réaliste dans la couche épitaxiée polarisée à 40 V : 13 µm.
En premier lieu, les spectres ont été reconstruits en imposant un seuil sur la charge collectée sur le pixel siège et ses voisins directs. Ce seuil dépendant de l'énergie du photon utilisé

permet de séparer les impacts du bruit. Ainsi le nombre d'entrées dans ces histogrammes ont été comparés au nombre dans le spectre de la condition fixée. Il en ressort que la profondeur obtenue n'est pas la profondeur désertée mais la profondeur de bonne collection par le champ électrique. Ainsi, des charges générées jusqu'à 35 µm de profondeur dans le substrat CZ peuvent être collectées efficacement. Dans la couche épitaxiée, la profondeur sature pour des polarisations moyennes telles que suggérées dans les simulations du champ électrique. Afin de déterminer la profondeur de désertion, une seconde méthode a été introduite. Les spectres obtenus initialement sans coupure particulière sont utilisés. Le nombre d'entrées considéré est limité à une gamme d'énergie correspondant majoritairement au pic de calibration et de l'harmonique de la source utilisée. Cette méthode est similaire à reconstruire les spectres en sélectionnant des impacts dont la charge n'a été collectée que sur le pixel siège. Les tendances de l'évolution de la profondeur est similaire aux simulations atteignant 13 µm dans la couche épitaxiée et une vingtaine de microns dans le substrat CZ suggérant une résistivité du substrat aux alentours de 2 kΩ cm.
La méthode d'intégration dans une gamme d'énergie ne permet pas de retirer intégralement les coups dont les photoélectrons n'ont que partiellement ionisé le substrat. Ainsi en intégrant le nombre de coups dans le pic de calibration à $\pm$ 3σ, la résistivité du substrat est estimée à 1 kΩ cm suggérant une profondeur de désertion effective de 18 µm. Les méthodes employées pour déterminer la profondeur de désertion ne permettent pas la modélisation de la forme du volume et donc de la profondeur en n'importe quel point de l'aire du pixel. Un test sous faisceau serait ainsi nécessaire et permettrait également des mesures de résolution spatiale dans le cadre de la caractérisation du capteur.

Développements de Capteurs

Deux développements de capteurs sont présentés. Le premier est destiné aux applications utilisant les rayons X mous. L'architecture de pixel présentée pour PIPPER-2 ne permet pas la restauration rapide du nœud d'entrée en cas de flux important de photons. Après l'intégration d'une certaine charge, la diode de collection est saturée et n'est plus en mesure de fournir un signal correspondant à la charge obtenue. Lorsque la phase d'illumination est arrêtée, la décharge de la diode requiert un temps important incompatible avec des

contraintes de comptage allant jusqu'au méga coup par seconde et par pixel. Ainsi une architecture a été proposée qui ne nécessitant pas de modification de process. La diode en direct permettant le passage de la tension de polarisation est remplacée par un transistor PMOS utilisé comme interrupteur. Le substrat du transistor est connecté à une tension élevée (i.e. tension de polarisation ou tension du nœud d'entrée) et le signal de commande varie de la tension de polarisation (fermé) à la tension de polarisation 1.8 V (ouvert, pour remise à zéro). Ainsi la tension grille-*bulk* reste dans les limites acceptées par la technologie.
Lors des mesures de PIPPER-2, la résolution en énergie est dégradée à faible énergie en raison d'un bruit trop élevé. Afin de remédier à cela, une architecture d'amplificateur bas bruit et à faible dispersion de gain est proposée. Le bruit équivalent est divisé par deux et une résolution en énergie théorique de 160 eV à 5.9 keV a été simulée.
Les architectures de pixels décrites ont été conçues en technologie AMS 180 nm et envoyés en fabrication fin 2017. Les prototypes étaient prévus pour mai–juin 2018 mais ont été retardés. Ainsi aucun résultat de caractérisation n'est disponible.

Le second développement, n'utilisant pas la désertion, est destiné à des applications de neuroimagerie comportementale. Il est en effet devenu nécessaire pour le développement de médicaments d'observer les effets sur le cerveau sur des sujets (rats) éveillés et libres de leur mouvements afin de s'affranchir des effets dus aux anesthésiques. Cette liberté permet également des études comportementales couplées aux images des fonctions cérébrales.
Plusieurs approches utilisant l'imagerie TEP ont été proposés ne répondant que partiellement aux besoins. Ainsi, une approche invasive a été proposée. Celle-ci consiste à introduire une sonde pixellisée dans le cerveau de l'animal afin d'observer les amas de positrons à proximité. Etant donné l'utilisation des traceurs typiques en TEP qui sont utilisés comme émetteurs gamma, et que ces photons de haute énergie peuvent provenir d'autres organes tels que le cœur, les reins ou la vessie, la sonde se doit d'en être insensible.
Une première approche utilisant une sonde passive connectée à un circuit de lecture et un système de transmission sans-fil a été produite : le projet PIXSIC. Malgré la sensibilité importante aux photons d'annihilation et une fragilité de la sonde, l'approche s'est révélée efficace.

Afin de résoudre les défauts de PIXSIC, l'utilisation des CPS a été proposée. Grace à l'amplification à proximité du nœud de collection le rapport signal sur bruit est important. Egalement, le traitement des données peut être effectué dans la sonde pour minimiser l'électronique extérieure. Egalement, une sonde fabriquée sur une fine couche épitaxiée permet d'être insensible aux photons d'annihilation. Néanmoins, l'utilisation d'architecture active sous-entend dissipation d'énergie et donc échauffement de la sonde. Cette dissipation doit donc être minimisée pour satisfaire les besoins de l'expérience.
Une sonde pixellisée en forme d'aiguille nommée IMIC a été conçue et produite sur le substrat épitaxié. Grace à une architecture de pixel compacte dissipant une faible énergie, et avec une méthode de lecture lente, compatible avec le faible taux de coups attendu sur la matrice, la dissipation totale du capteur a été mesurée à 160 µW bien en-deçà de la limite fixée. Le fonctionnement de la sonde et son insensibilité aux gammas ont été validés en laboratoire.
Les sondes validées sont collées dos-à-dos afin d'augmenter l'acceptance et recouverte d'un polymère biocompatible pour être testées in-vivo.

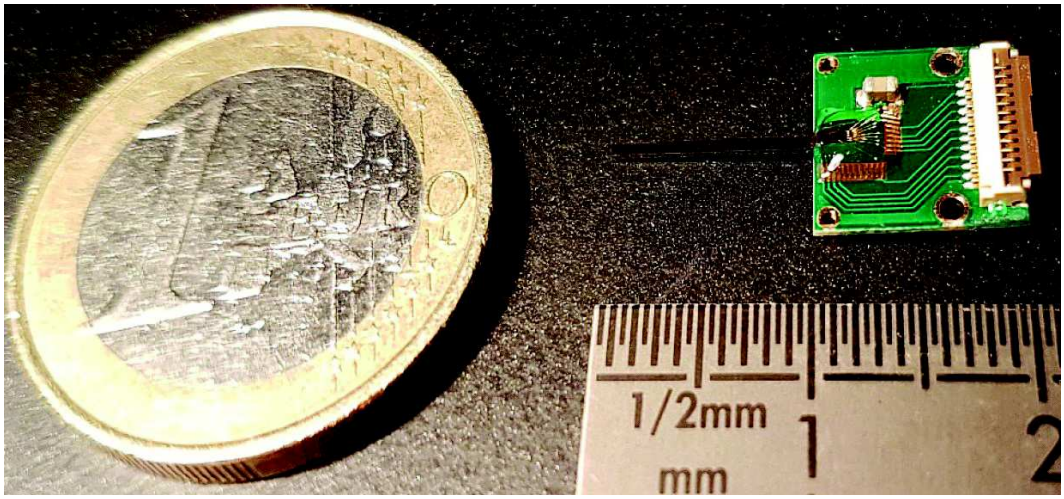

Figure 6: Sonde composée de deux capteurs IMIC collés dos-à-dos. (Photographie par F. Gensolen (CPPM)

Conclusions et Perspectives

Une méthode de désertion par l'avant de capteurs à pixels CMOS permettant l'utilisation de petits pixels et de minimiser la fenêtre d'entrée est présentée.
Un prototype fabriqué sur deux substrats différents utilisant la méthode a été caractérisé

et la profondeur de désertion a été évaluée. Le substrat épitaxié de faible épaisseur est intégralement déserté et le substrat épais ne l'est pas (limité par la présence de puits p profonds et par une résistivité pas suffisamment élevé). La méthode de détermination de la profondeur de désertion ne permet pas l'évaluation de la forme du volume déserté. Des mesures complémentaires sous faisceau se révèle donc nécessaire.

A l'issue des caractérisation, le substrat épitaxié a démontré une excellente tenue aux radiations pour des applications de physique des hautes énergies.
La méthode de désertion proposé est adéquate pour des applications aux rayons X mous mais nécessite l'utilisation de substrats de plus haute résistivités et des développements d'architecture permettant d'améliorer la résolution en énergie et de pouvoir compter au-delà du million de coups par seconde et par pixel.

Abstract

For various scientific applications especially in physics, depleted CMOS Pixel Sensors are being more and more considered. These semiconductors sensors allow the fast collection of charges generated by an ionizing particle.
To achieve depletion, high resistivity substrates or high reverse bias voltages can be applied on the pn junction that forms the collecting diode. Both methods can be used to increase the depleted volume.

In this work a method to deplete from the front-side of the sensor (on the electronics side) is proposed. The bias is applied through the collecting diode and the collecting node is AC-coupled to the readout chain. The capacitively coupled architecture allows biasing voltages on the collection node much higher than the breakdown limit of the technology used without process modification.

A prototype sensor named PIPPER-2 that uses this method is presented. It was designed in a 180 nm CMOS Image Sensor process and has been fabricated on two different high resistivity substrates: on a 18 µm thick epitaxial layer for high-energy physics tracking purposes and on a thick Czochralski bulk substrate that has been thinned for soft X-rays applications.

This prototype was characterized and demonstrated a low equivalent noise charge of 24 electrons, and thanks to the depleted operation an energy resolution of 280 eV at 5.9 keV is achieved in the thin epitaxial layer version. A slightly worse resolution of 288 eV is achieved in the bulk substrate. The epi version of the sensor is tested for non ionizing radiation hardness and demonstrates a signal to noise ratio high enough thanks to the depleted operation to be considered for high energy physics experiments in highly radiative environment.

The depletion depth is evaluated using analytical approaches, TCAD finite elements

simulations and measurements. The thin epitaxial layer is fully depleted up to 13 µm with bias above 6 V. The bulk substrate is depleted up to 18 µm and the electric field allows good charge collection up to 35 µm.

The proposed architecture for the application of the depletion from the front-side is not compatible for application requiring to count a high flux of photons. Thus a resetting architecture that can cope with such application requirements is proposed. An amplifier design is proposed to reach better energy resolution performance. The design is currently being fabricated.

An implantable needle shaped probe for in-brain positron neuroimaging in awake and freely-moving rats is presented. The low-power probe (160 µW) is validated in laboratory and being assembled to form a double sided needle shaped probe to be tested *in-vivo*.

Contents

List of Figures

List of Tables

Introduction: Applications Improvements with Depleted CPS

The success of scientific experiments, especially in physics, relies on dedicated sensors, among which pixelated ones play a crucial role. Consequently, advances in detector instrumentation usually turns into new steps ahead for science. Radiation sensitive detectors follow the same path, and in this work, the case of CMOS pixel sensors (CPS) is investigated. These devices undergo fast developments driven by cell-phone camera for the general public but also scientific applications.
The sensitive volume of sensors is of course of primary importance for the detection performance. In this respect, CPS are semiconductor based and require some level of depletion to operate properly. Until recent years, most CPS featured only a thin depletion depth of very few micrometers (and hence are tagged undepleted in the following). While the new generation of sensors offers much thicker depleted volume or even full-depletion (tagged depleted or fully-depleted later in this text), such detectors are appealing to a wide range of applications, from High Energy Physics to non-destructive-tests with electrons or X-rays.

Undepleted CMOS Pixel sensors (Mimosa-28 Ultimate [1]) have been successfully developed and used since 2014 for charged particle tracking purposes within the STAR experiment at RHIC. The STAR-PXL detector [2], which was the first vertex detector using CPS, is composed of 400 ULTIMATE sensors thinned to 50 µm representing a total sensitive area of 0.16 m^2 on two detection layers. During the three years of operation, the specific detector performance opened new achievements for the STAR experiment.
Because of their excellent single point resolution, low material budget, and easy integration for an attractive cost, CPS are being considered for present and future particle tracker projects: the upgrade of the ALICE Inner Tracking System (ITS) [3], the CBM[1]-Micro Vertex Detector (MVD) [4], the upgrade of the ATLAS ITk Pixel Detector [5].

Requirements on design might be satisfied using CPS designed in advanced technology nodes and a depleted sensitive volume. Due to the high level of optimisation, the requirements imposed by each experiment does not allow to re-use the sensors previously developed. Especially, these new projects generate constraints on time resolution and non-ionizing radiation hardness and require new sensors design.
Fast charge collection is a main advantage of depleted sensors giving a strong signal on

[1]Compressed Baryonic Matter

a few pixels to be treated in the sensor, thus improving time resolution. The ability to collect the generated charge before recombination in radiation-damaged sensors guarantees a sufficient amount of signal to partly satisfy radiation hardness requirements (very constraining for ATLAS).

In addition, the amount of charge deposited in matter (i.e. the sensor) and the resulting geometry give informations on the type and energy of the interacting ionizing particle. Ensuring full collection of the generated charge, with low noise performance, over a known sensitive thickness allows the determination of the type of an unknown ionizing particle by sampling the amount of charge deposited by unit length.

The use of thinned CPS for electron microscopy have proven good performance on one of the most important requirement for this application: the image definition, quantified by the modulation transfer function (MTF) [6]. The other main constraints of the application are the requirements on the readout speed which can be satisfied with CPS and on ionizing radiation hardness that can be optimized by design and by using fully-depleted backside illuminated sensors.
A large area detector is also required. By designing reticle size buttable sensors, the area can be increased to a desired field.

A large number of non-destructive-testing methods exploits X-rays produced by small-size generators or synchrotron beams (or FEL). All require imagers with high performance. Soft X-Rays are mandatory, but not limited to various biological applications (listed in [7]). With low energy photons, CCDs are a good choice for precise imaging under low fluxes (as long as the sensors are kept to low temperatures) while integrating hybrid pixel detectors, with their numerous embedded functionnalities are an excellent option under very high fluxes but need to be very large to compensate the large pixel (eg. LPD [8]).
CPS become relevant because of their performance (noise, spatial resolution) at room temperatures (or chilled) under a moderate flux for a reasonable price. To achieve good QE performance, the monolithic sensors are thinned to a few tens of microns (eg. 12 µm sensitive (fully depleted) requiring a support wafer [9], or $\approx$ 50 µm without handling wafer: this work).
As the charge generated by a soft X-ray photon is fully collected with excellent noise performance, depleted sensors can also be used for spectroscopy purposes. The resolution attained by CCDs under low temperature operation can not be reached but, the readout speed can allow higher fluxes.

Multiple applications can take advantage of the use of depleted CPS development. Depletion in CPS can be obtained by applying a depletion voltage on a sensor fabricated

on a high-resistivity silicon substrate. In this work, the depletion voltage is applied from the frontside (on the electronics side) through the collecting diode which does not require process modification.

The goal of this work is to evaluate the performance of such a depletion method, especially in terms of depleted depth and energy resolution for soft X-Rays. Therefore, the processes of the interaction of X-rays and electrons in matter are first described in chapter 1 to estimate the type and amount of signal expected in the sensor. The collection process of the generated signal is described with the physics of the pn-junction in chapter 2. The figures of merit that characterize the performance of silicon-based pixel detectors are detailed in chapter 3 which also review the performance of existing silicon based pixel detectors.
A depleted sensor prototype using the frontside biasing architecture developed at IPHC is characterized using various sources to determine its performance (chapter 5), and to estimate the achieved depletion depth (chapter 6) based on calculations and TCAD finite elements simulations (chapter 4).
The application of the depletion through the collecting diode constraints the sensor design and limits the detection capabilities of fast and repetitive hits. An architecture allowing to overcome this limit is proposed in chapter 7. A low power sensor design for neuroimaging is also presented in chapter 8.

Part I

Study of Depleted Pixelated Sensors

Chapter 1

Interaction of Radiation with Matter

A radiation interacting with matter is attenuated by the collisions with the atoms. The effect on the path of the incident radiation depends on its type, either a charged particle (heavy charged particle or electron), or a photon. During the attenuation processes, charges are generated within the medium and contribute to a signal proportional to the deposited energy.
In this chapter, the interaction processes in silicon are studied to find out the kind, and amount of signal expected to be generated from low energy electrons (<10 MeV), and soft X-rays (photons <10 keV).

1.1 Interaction of Electrons

1.1.1 Interaction Mechanisms

Similarly to heavy charged particles ($m_p c^2 \gg m_e c^2$), electrons mostly lose energy within matter through ionization. As soon as a charged particle enters an absorbing medium, it interacts with several shell electrons of the latter. For each interaction, the particle travels within the vicinity of the absorber atom, and a Coulomb force is perceived by an electron. For sufficiently close encounters, the felt impulse can be sufficiently high to displace an electron from the shell it occupies. It can either be raised to a higher lying shell of the atom (excitation, see figure 1.1a) or be expelled (ionization, see figure 1.1b).

The encounter leads to an energy transfer from the incident particle to the electron with which it interacts hence reducing the velocity of the charged particle. For a single collision between an heavy charged particle of energy E and mass m_p with an electron of mass m_e, the maximum energy transferred is $\frac{4Em_e}{m_p}$. With $m_e \approx 9.1 \times 10^{-31}$ kg, and $m_p \approx 1.7 \times 10^{-27}$ kg, less than 1 % of the energy of the incoming particle can be transferred per collision. Thus, to completely stop an incoming particle, multiple successive interactions have to take place to continuously diminish the velocity. Along its path, the heavy particle is almost undeflected by the encounters thus travelling in a straight line. The energy deposition creates a cloud of free electrons along its trajectory within the considered material.

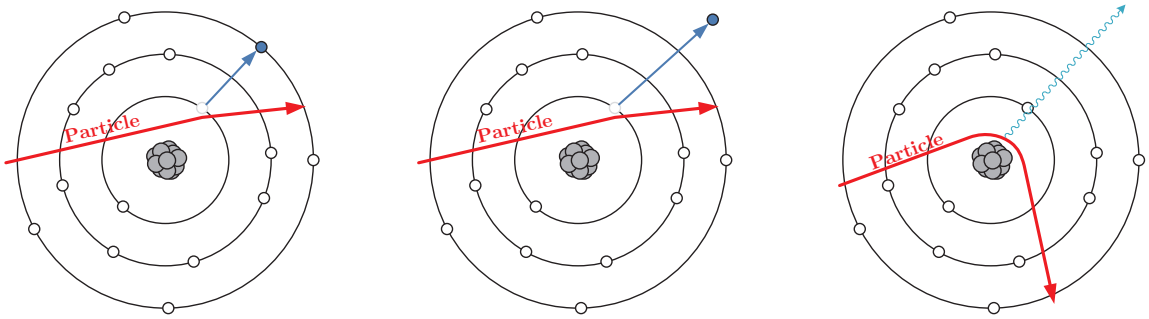

(a) (b) (c)

Figure 1.1: (a) Excitation: an electron is raised to a higher lying shell. (b) Ionization: an electron is expelled. (c) *Bremsstrahlung*: the incoming particle is deflected by the Coulomb field of the nucleus. A photon is emitted to satisfy the laws of conservation of energy.

Nevertheless, due to differences in mass, kinematics, and spin charge, an electron follows a sinuous path through the absorbing material while losing its energy at a lower rate than an heavy particle. The mass of the incoming electron being the same as the orbital electron with which it is interacting, larger deviations can happen. Also, an interaction with the nucleus of the atom can unexpectedly change the direction of the electron.

For highly energetic electrons, above the critical energy E_c (see 1.1.2), the energy loss is not dominated by ionization anymore but by *bremsstrahlung*. The incoming electrons are deflected by the Coulomb field of the nucleus of the absorber atom (figure 1.1c). The change in direction results in a loss of energy by deceleration. In order to satisfy the laws of conservation of energy, a photon is emitted.

These energy losses mechanisms of electrons crossing a medium can be expressed per unit length allowing an estimation of the amount of signal created.

1.1.2 Energy Loss

The energy loss rate of a charged particle in a given material is given by the *Bethe-Bloch formula*. A derivation of this equation describes the energy loss due to ionization and excitation induced by collision of electrons or positrons within a given material. With the quantities given in table 1.1, the loss rate is given by:

$$\left(-\frac{dE}{dx}\right)_{collisions} = K\frac{Z}{A}\frac{1}{\beta^2}\left[\ln\frac{m_e\beta^2c^2\gamma^2T}{2I^2} + F(\gamma-\delta)\right] \tag{1.1}$$

Ionization loss rates are rising logarithmically with the energy and are dominant over the *bremsstrahlung* induced rates below the critical energy (Energy for which $\left(-\frac{dE}{dx}\right)_{collisions} =$

$\left(-\frac{dE}{dx}\right)_{radiative}$). Nevertheless other processes are contributing to the energy losses at low energies.

For electrons, only half of the kinetic energy of the primary electron (the one with the highest energy) can be transferred [19]. The contribution to the energy loss rate (equation 1.1) is given by Møller scattering:

$$F(\gamma) = (1-\beta^2) - \frac{2\gamma-1}{\gamma^2}\ln 2 + \frac{1}{8}\left(\frac{\gamma-1}{\gamma}\right)^2 \tag{1.2}$$

For positrons, Bhabha scattering describes the interaction where all of its kinetic energy can be transferred. The contribution is given by:

$$F(\gamma) = 2\ln 2 - \frac{\beta}{12}\left(23 + \frac{14}{\gamma+1} + \frac{10}{(\gamma+1)^2} + \frac{4}{(\gamma+1)^3}\right) \tag{1.3}$$

Density corrections δ are added to the energy loss rates. It is more relevant at high energies. The electric field of the incoming particle polarizes the atoms of the target. A shielding of electrical field is generated far from the particle path thus decreasing the energy loss. Shell corrections developed for heavy particles are neglected for electrons [19].

The energy loss of electrons can take the form of radiative losses (*bremsstrahlung*). The contribution of radiative losses for electrons of energy E is given by:

$$\left(\frac{dE}{dx}\right)_{radiative} = \frac{1}{X_0}E \tag{1.4}$$

X_0 represents the radiation length. It corresponds to the distance after which a high energy electron has lost $1/e$ of its energy by radiation ($E(t) = E_0 e^{-\frac{t}{X_0}}$). The expression of the radiation length is:

$$X_0 = \frac{A}{4\alpha N_A Z^2 r_e^2 \ln\frac{183}{Z^{\frac{1}{3}}}} \tag{1.5}$$

The radiative energy loss becomes significant in high-Z materials (*e.g.* CdTe, CdZnTe for semiconductors), and for high energy electrons. The total energy loss rate is the sum of the rates induced by ionization, and by radiation:

$$\frac{dE}{dx} = \left(\frac{dE}{dx}\right)_{collisions} + \left(\frac{dE}{dx}\right)_{radiative} \tag{1.6}$$

Figure 1.2 shows the contribution of radiative and collisional stoping power of electrons in Silicon for energies between 10 keV and 1 GeV. Incident electrons of 1 MeV are at the minimum of ionization in silicon which can be also considered for incident electrons between 500 keV to 10 MeV. Outside this range, the stopping power is increased.

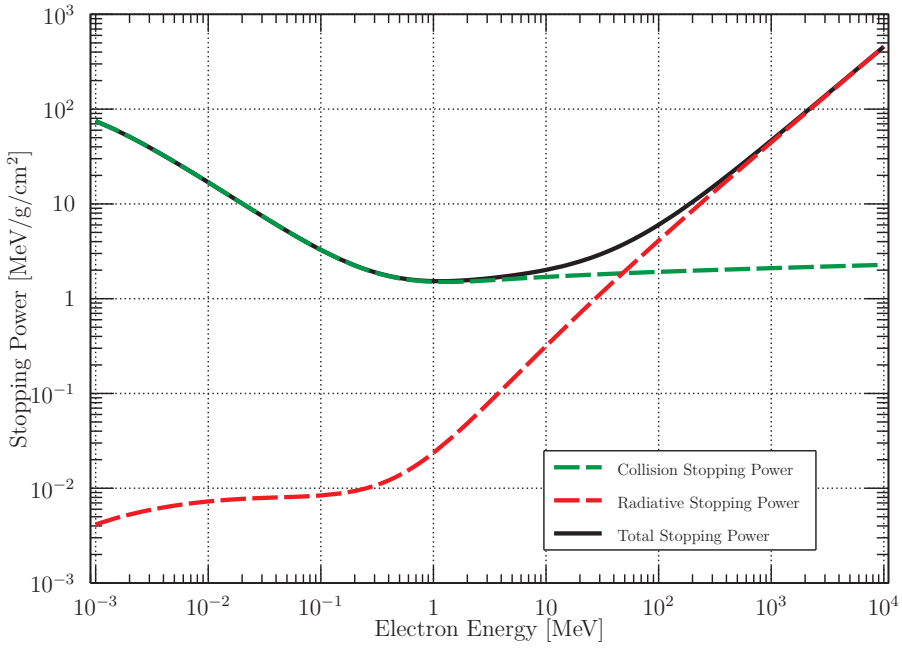

Figure 1.2: Energy dependence of the electron interaction processes in silicon. Data from [20].

The proportion of the energy loss rates is approximatively given by:

$$\frac{(dE/dx)_{radiative}}{(dE/dx)_{collisions}} \approx \frac{EZ}{700} \tag{1.7}$$

Energy losses by *bresmstrahlung* becomes valid for an incoming electron energy above a critical energy (E_c) depending on the medium where $\frac{dE}{dx}(E_c)|_{bremsstrahlung} = \frac{dE}{dx}(E_c)|_{ionization}$. The critical energy for silicon is $E_c(Si) = 39$ MeV. Such levels of energies are not reached for the further developments of this work

1.1.3 Energy Straggling

Equation 1.1 describes the mean energy loss in a given material. In a detector with thickness Δx, sufficiently thin not to stop the incoming particle, the amount of energy loss is continuously fluctuating because of the variation of energy transferred in a single collision (δE_n), and the number of collision (N). The second parameter fluctuates in accordance to the Poisson law (variation of $\sqrt{N}$ for N collisions). The deposited energy in a medium is:

$$\Delta E = \sum_{n=1}^{N} \delta E_n \tag{1.8}$$

Nevertheless this energy is statistically distributed and can be approximated by a Landau distribution from which the most probable value (MPV) of the energy deposition in a given thickness can be extracted. An experimental most probable value of energy loss per

micrometer of electrons in silicon of $\Delta E \approx 318.3$ eV is calculated from the values from [18].

It is more common in semiconductors to express the energy deposition in terms of electron-holes (e-h) pairs generated. The required energy (ionization energy) of an incoming charged particle to generate a single e-h pair in silicon, determined from multiple measurements [16], is $\epsilon = 3.63$ eV. Thus an electron generates ≈ 88 electron-hole pairs per micrometer travelled in silicon.

Nevertheless, most recent experimental results [19] determined that the charge deposition rate of a MIP (electrons at 500 keV–10 MeV) is approximatively 74 pairs/µm. At the minimum of ionization, the deposition of 1 keV requires ≈3.7 µm of silicon, and 37.3 µm for 10 keV.

1.2 Interaction of X-Rays and Gamma Rays

Among all the possible interactions of photons in matter, three major mechanisms are sufficient to characterize the effects of a photon beam in a medium. These processes transfer partially or totally the energy of an incoming photon to an electron of an atom composing the medium. The proportion of the contribution of each effects depends on the energy of the incoming photon. The photon is either completely stopped or is scattered through an angle depending on its energy after an interaction. The term X-ray will be used for photon energies between a few eV to 100 keV after which the term gamma-ray will be used for photon. Also, below 10 keV, photons are considered as soft X-rays.

1.2.1 Interaction Mechanisms

Photoelectric Effect

In photoelectric absorption mechanisms, an X-ray interacts with an atom as one, not with free electrons, to completely disappear. It is replaced by an energetic photoelectron from one of the bound shells of the atom. For sufficiently large energies of the incoming photon, the most probable electron emitted as the photoelectron in the photoelectric process is the most tightly bound or K-shell electron. The photoelectron arrives at an energy given by

$$E_{e^-} = h\nu - E_{binding} \tag{1.9}$$

where $E_{binding}$ is the binding energy of the photoelectron in its originating shell.

The energy of the photon increases the energy of an electron in the atom that can

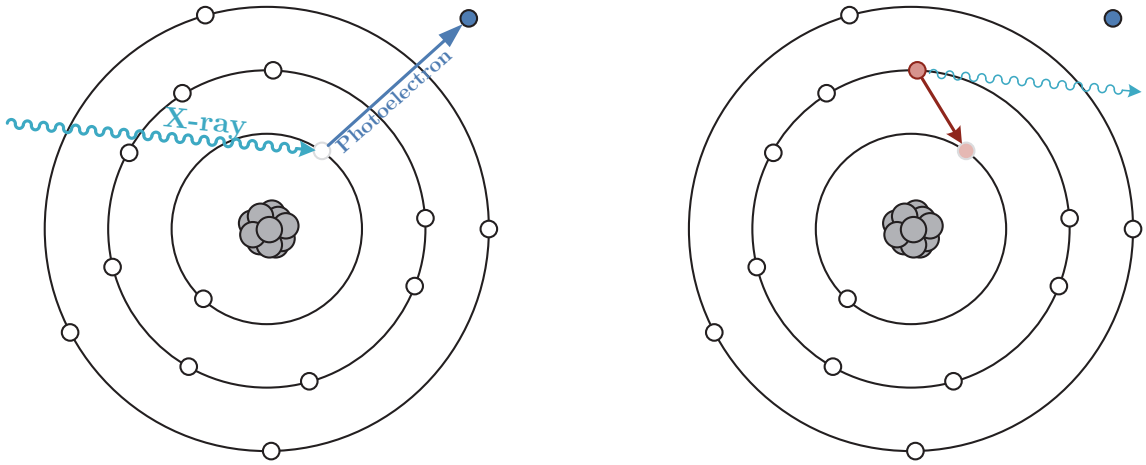

(a) (b)

Figure 1.3: (a) Genereation of a photoelectron by photoelectric effect, (b) De-excitation: generation of a characteristic fluorescence X-Ray.

be raised to an higher level or become a free electron. Thus, the interaction creates a photoelectron while ionizing the atom of the absorber. The vacancy in a bound shell is quickly filled by absorption of a free electron in the medium and/or by rearranging the electrons (de-excitation) from the other shells of the atom which results in the generation of one or more characteristic fluorescence X-rays photons that are reabsorbed closely to the original interaction site through photoelectric absorption implicating a less tightly bound shell of an atom. Their migration and possible escape from the detector can influence the response and is presented in chapter 3.1.2.

The amount of generated charge is proportional to the energy of the incoming photon divided by the ionization energy. The dispersion in the amount of charge generated by photons is the energy times the Fano factor (F). Its value for silicon, only obtained experimentally, found in literature is between 0.085, and 0.16. Nevertheless, the most commonly used value is F=0.11 [10]. Thus, the charge generated by a photon in silicon is

$$N = \frac{h\nu}{\epsilon} \text{ electron-hole pairs}, \quad < \Delta N^2 >= F \cdot N \tag{1.10}$$

Instead of generating a X-ray, the excess energy can be dissipated as an Auger electron which is expelled from the outer shell of the atom and takes up the excess energy. The atomic excitation energy is carried away.

An approximation for the probability of photoelectric interaction is given by

$$\sigma_{ph} = \text{constant} \frac{Z^n}{E^{3.5}} \tag{1.11}$$

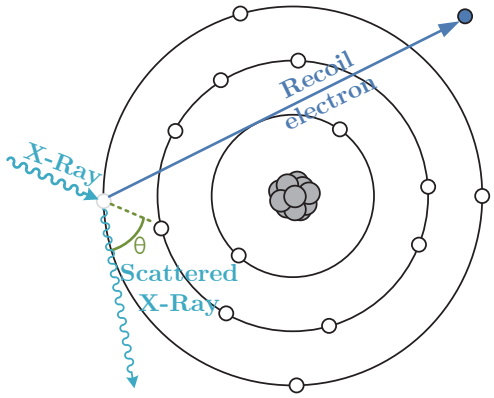

Figure 1.4: Compton Scattering: an incident photon is scattered through an angle θ after an elastic collision with an electron of the absorbing medium, which is ejected (recoil electron).

where n varies between 4 and 5 over the region of interest. The photoelectric absorption effect decreases rapidly with the energy ($E^{3.5}$ at the denominator) and is enhanced with high-Z materials. This effect is thus predominant for low energy photons.

At the lowest energies, discontinuities or absorption edges appear. They correspond to an interacting photon whose energy is similar to the binding energy of the electronic layers of the absorber atom. For silicon, the K-edge energy is 1.839 keV and is visible in figure 1.6. When the energy of the photon is slightly above the absorption edge energy, it is sufficient to withstand photoelectric interaction where a K-shell electron is ejected from the atom. However, photons with an energy below the edge can not undergo photoelectric absorption which drastically decreases the interaction probability. The same effect exist for the upper electronic layers of the atom.

Compton Scattering

At the typical gamma-ray energies, Compton scattering becomes predominant in the interaction processes of photons with an electron of the matter. This scattering is an elastic collision between an electron and the photon, deflecting the latter through an angle θ against its original direction. The resting electron gets a part of the energy of the photon and becomes a recoil electron (figure 1.4). The transferred energy varies from zero to a substantial amount of the photon energy depending on the scattering angle of the photon. An expression using the energy and momentum conservation gives:

$$h\nu' = \frac{h\nu}{1 + \frac{h\nu}{m_e c^2}(1 - \cos\theta)} \tag{1.12}$$

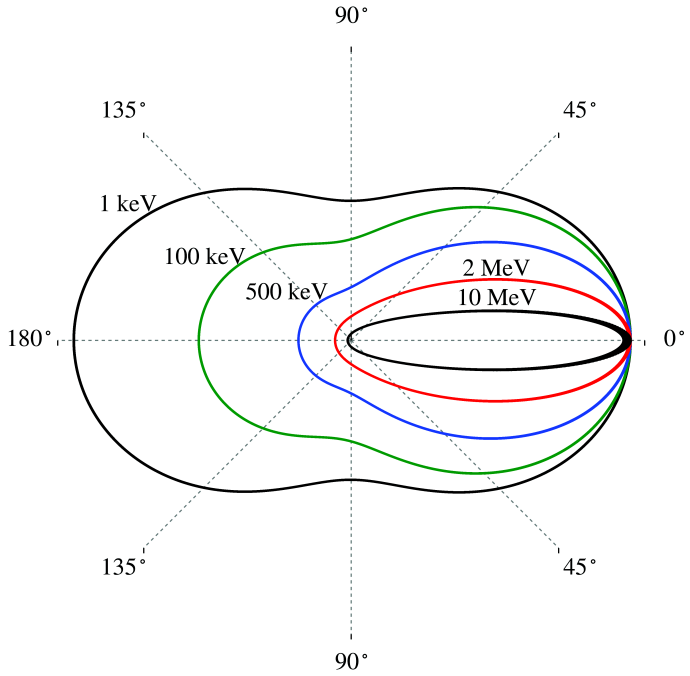

Figure 1.5: Polar plot of Compton scattered angles of photons of energies from 1 keV to 10 MeV

The amount of transferred energy is small for small scattering angles, and even for the largest scattering angle possible ($\theta = \pi$), the energy transfer is not full.

In the photon energy range where photoelectric interactions are dominant, Rayleigh scattering can occur. In this process, the photon coherently interacts with all the electrons of an atom without ionizing nor exciting it. The contribution of this effect is negligible.

The Klein-Nishina formula expresses the differential cross section for the Compton scattering into a solid angle $d\Omega$. It is considered that the gamma-ray interacts with a free electron, thus neglecting the atomic binding.

$$\frac{d\sigma_c^{e^-}}{d\Omega} = \frac{r_e^2}{2}\left(\frac{h\nu'}{h\nu}\right)^2\left(\frac{h\nu}{h\nu'} + \frac{h\nu'}{h\nu} - \sin^2\theta\right) \tag{1.13}$$

The angular distribution illustrated in figure 1.5 shows that for photon energies below 511 keV, the scattering is quite isotropic and back-scattering is almost as probable as forward scattering. At higher energies, the scattering is dominant in the forward direction. The total cross section can be obtained by integrating the Klein-Nishina formula over all

the angles

$$\sigma_c^{e^-} = 2\pi r_e^2 \left[\left(\frac{1+k}{k^2} \right) \left(\frac{2(1+k)}{1+2k} - \frac{1}{k} \ln(1+2k) \right) + \frac{1}{2k} \ln(1+2k) - \frac{1+3k}{(1+2k)^2} \right] \quad (1.14)$$

Also, simple and compact expression of the cross section for photon energies either much larger or smaller than the electron mass are obtained

$$\sigma_c^{e^-} = \begin{cases} \frac{8\pi}{3} r_e^2 \left(1 - \frac{h\nu}{m_e c^2}\right), & \text{if } h\nu \ll 511 \text{ keV} \\ r_e^2 \pi \frac{m_e c^2}{h\nu} \left[\ln\left(\frac{2h\nu}{m_e c^2}\right) + \frac{1}{2} \right], & \text{if } h\nu \gg 511 \text{ keV} \end{cases} \quad (1.15)$$

Compton scattering is dependent to the number of shell electrons (e.g. high-Z materials) of the atom composing the medium available as targets. Thus, the cross section per atom is

$$\sigma_c^{atom} = Z\sigma_c^{e^-} \quad (1.16)$$

Pair Production

For sufficiently high gamma-ray energies ($h\nu \gg 2m_e = 1.02$ MeV), pair production can occur. Still, if the incoming photon energy is only a few hundred of keV above the threshold, the pair production probability remains small.

Pair production can only occur in the Coulomb field of a nucleus in the medium which takes up the momentum of the incoming photon. When pair production occurs, the gamma ray disappears and is replaced by an electron and a positron each one sharing the excess energy of the photon above 1.02 MeV as their kinetic energy. The positron will annihilate after being slowed in the medium generating 2 annihilation photons as secondary product of the interaction.

The cross section corresponding to pair production rises after the threshold energy to saturate at a constant value at high energy, and is given by

$$\sigma_{pp} = \frac{7}{9} 4\alpha r_e^2 Z(Z+1) \ln\left(\frac{183}{3\sqrt{Z}}\right) \quad (1.17)$$

That expression echoes the quantity X_0 given by equation 1.5. It suggests that for high energy photons penetrating the medium, the quantity of high energy gammas that are unconverted decreases according to $\exp\left(-\frac{7}{9}\frac{dx}{X_0}\right)$. In one radiation length, there is a probability of 54 % to convert a high energy gamma-ray into an electron and a positron.

1.2.2 Attenuation

The interaction processes in a medium removes photons from a beam of intensity I_0 by absorption or by scattering. The process is characterized by the sum of probabilities that the photon is being removed from the beam and is given by the linear attenuation coefficient:

$$\mu = \sigma_{ph} + \sigma_c + \sigma_{pp} \tag{1.18}$$

The intensity of the beam in the medium is given by

$$\frac{dI(x)}{dx} = -I(x)\mu \tag{1.19}$$

The number of transmitted photons from a beam at a given thickness x is

$$I(x) = I_0 e^{-x/\lambda} \tag{1.20}$$

With λ representing the mean free path, or absorption length, of the photon in the medium. It is the average distance traveled before an interaction:

$$\lambda = \frac{1}{\mu} \tag{1.21}$$

The absorption length of photons of energies in the range 1 keV–100 MeV and the contribution of each cross section in a silicon medium is shown in figure 1.6. For photon energies below 30 keV, photoelectric absorption is the main contribution of photon interaction processes in silicon. Above, Compton scattering processes are contributing along the photoelectric effect. At typical gamma-rays energies (511 keV) Compton scattering is the main contribution to interaction processes in silicon. Pair production is added to Compton effect for the interaction processes of gamma-ray energies above several MeV.

To convert half of the incoming 1 keV X-rays into 276 electrons by photoelectric effect, 1.9 µm of silicon is required, while a thickness of 88 µm is needed to achieve 50 % conversion with 10 keV photons (2762 electrons).

For compounds, the attenuation coefficient is replaced by the mass attenuation coefficient which takes into account the density of the material and is given by μ/ρ. It allows the expression of an equivalent mass attenuation coefficient for mixtures of materials used. With w_i, the weight fraction of the element i the mass attenuation coefficient for compounds is:

$$\left(\frac{\mu}{\rho}\right)_{compound} = \sum_i w_i \left(\frac{\mu}{\rho}\right)_i \tag{1.22}$$

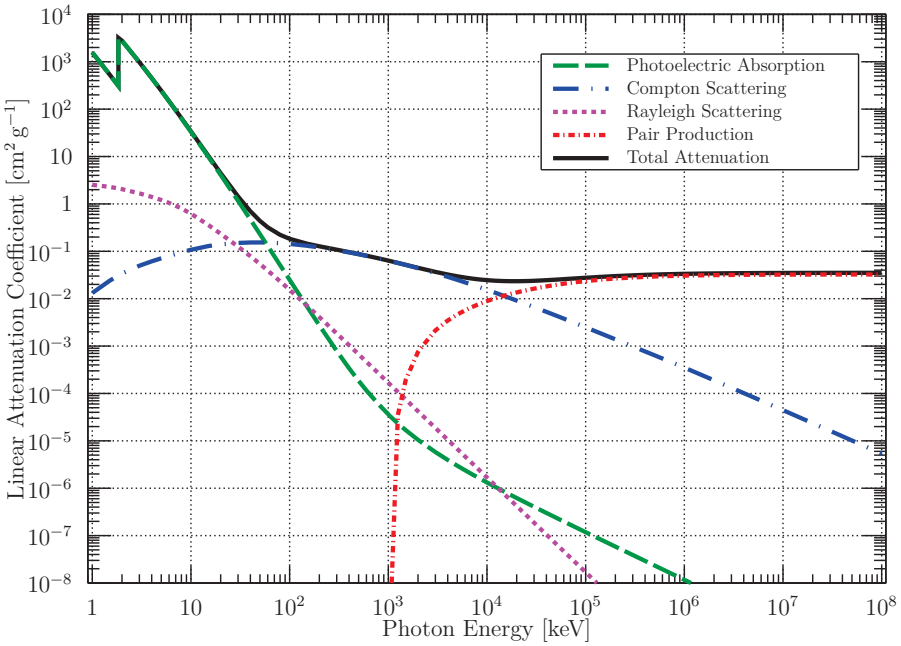

Figure 1.6: Energy dependence of the photon interaction processes in silicon. Data from [20].

1.3 Conclusions

The generated signal from either electrons or photons in silicon is electrons (and holes). These charges are generated along the path of the incoming particle for electrons and locally as a cloud for photons after absorption.

The amount of charge generated by an electron depends on its energy and on the thickness of the detection substrate. An electron at the minimum of ionization will generate 74 electron/hole pairs per micrometre.

Unlike electrons, photons below 30 keV are absorbed locally through photoelectric effect resulting in the generation of an electron cloud. The amount of generated charge is proportional to the energy of the incoming photon. The probability of absorbing a photon, and thus to generate a charge, increases with the thickness of the sensitive volume.

In any case, the detection volume must sufficiently thick and full charge collection must be guaranteed to maximize the signal.

Table 1.1: Summary of constants and variables used in chapter 1

Symbol	Value	Unit	Definition
$^{dE}/_{dx}$	-	$[\mathrm{eV\,g^{-1}\,cm^2}]$	Energy loss
K	0.307	$[\mathrm{MeV\,g^{-1}\,cm^2}]$	$4\pi N_A r_e^2 m_e c^2$
N_A	6.022×10^{23}	$[\mathrm{mol^{-1}}]$	Avogadro's number
r_e	2.818×10^{-15}	[m]	Electron radius
$m_e c^2$	511	[keV]	Electron mass
c	2.998×10^{8}	$[\mathrm{m\,s^{-1}}]$	Speed of light in vacuum
Z	$Z(Si) = 14$	-	Charge number of medium
A	$A(Si) = 28.855$	$[\mathrm{g\,mol^{-1}}]$	Atomic mass of medium
v	-	$[\mathrm{m\,s^{-1}}]$	Incident electron speed
β	$^{v}/_{c}$	-	Relative particle speed
γ	$^{1}/\sqrt{1-\beta^2}$	-	Lorentz factor
T	$m_e c^2(\gamma - 1)$	[MeV]	Kinetic Energy of the electron
I	$I(Si) = 172$	[eV]	Excitation energy of medium ($\approx 16Z^{0.9}$)
δ	-	-	Density correction
X_0	$X_0(Si) = 21.82$	$[\mathrm{g\,cm^{-2}}]$	Radiation length
α	$^{1}/_{137.03599974(44)}$	-	Fine structure constant ($^{e^2}/_{4\pi\epsilon_0\hbar c}$)
ϵ	$\epsilon(Si) = 3.63$	[eV]	Ionization energy
$\hbar$	$1.054571800 \times 10^{-34}$	[J s]	Reduced Plank constant $\left(\frac{h}{2\pi}\right)$
h	$6.626070040 \times 10^{-34}$	[J s]	Plank constant
ϵ_0	$8.854187817 \times 10^{-12}$	$[\mathrm{F\,m^{-1}}]$	Vacuum permittivity
μ_0	$4\pi \times 10^{-7}$	$[\mathrm{H\,m^{-1}}]$	Vacuum permeability
k	-	-	$k = {}^{h\nu}/_{m_e c^2}$

Chapter 2

Detection with Silicon Diodes

As soon as a charge is generated in the detector volume, it has to be collected to be treated as a signal. The charge collection processes in semiconductors (especially silicon) are developed. With particular focus on the charge transportation mechanisms, noise sources (intrinsinc charges), and generation-recombination processes, the integrity of the charge is discussed.

The collection of the charge is performed in a pn-junction. The range of action of the collection is determined by the depleted volume. The expected thicknesses of the latter is discussed.

2.1 Introduction to Semiconductors

Silicon exists as two solid states, amorphous and crystalline. The further discussions are focused on the latter. It is characterized by an organization of the atoms in a periodic lattice which results in an ordered set of nuclei and electrons linked by Coulomb interactions.
Such as the atoms found on the IV column in the periodic table of elements, silicon is a covalent crystal characterized by a covalent bond resulting from the sharing of the four peripheric electrons of the atom with the 4 direct neighbours.

2.1.1 Band Structure

Silicon has a valence and a conduction band separated by an indirect band-gap (E_g = 1.12 eV). At absolute zero temperature (O K), the valence band is full while the conduction band is empty and electrons can not be thermally excited to be elevated from the valence band to the conduction band which is the characteristic of an insulator. At room temperature, electrons can be thermally excited and their energy can be elevated from the valence band into the conduction band across the band-gap. Since the valence band is now incomplete, the electrons can travel within it and transport current. In the crystalline structure, an electron will move to an empty bonding orbital while the emptiness goes the other way: the hole. It characterizes the absence of electron but can be treated as an elementery quasi-particle positively charged ($+e$) with an elementary effective mass whose

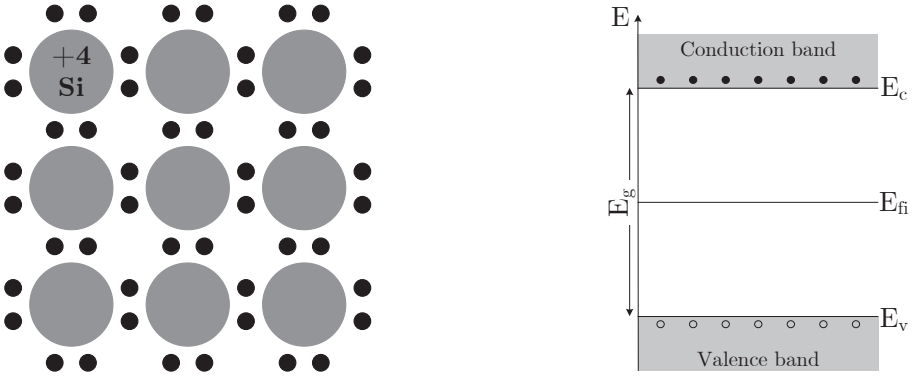

(a) (b)

Figure 2.1: (a) Schematic of the two-dimensional bond structure of a perfect silicon crystal. (b) Schematic energy band representation of an intrinsinc semiconductor.

value depends on which calculations they are used for (m_h^*/m_0 =0.386 for conductivity calculations and 0.811 for density of states calculations)[23]. Such as the hole, the electron can be considered as a quasi-particle with an effective mass (m_e^* =0.26 for conductivity calculations and 1.08 for density of states calculations)[23] negatively charged ($-e$). The potential energy of an electron at the bottom of the conduction band designated by E_c. E_v is the top of the valence band and is the potential energy of a hole. The fermi level E_f is the energy where the probability of occupation by an electron is 1/2.

The total density of electrons in the conduction band is n, and the hole density in the valence band is p. For non-degenerated semiconductor ($E_v < E_f < E_c$) the densities are:

$$n = N_c e^{-\left(\frac{E_c - E_f}{kT}\right)} \tag{2.1}$$

$$p = N_v e^{\left(\frac{E_v - E_f}{kT}\right)} \tag{2.2}$$

The product np is a constant at a given temperature

$$np = N_c N_v e^{-\left(\frac{E_g}{kT}\right)} \tag{2.3}$$

2.1.2 Intrinsinc Semiconductor

In a pure semiconductor, when no impurity can change the density of the carriers, the electrons in the conduction band can only be the result of thermal excitation of an electron

in the valence band. Thus, the product of densities in this condition is

$$np = n_i^2 \tag{2.4}$$

The density of intrinsinc carriers is

$$n_i = \sqrt{N_c N_v} e^{-\left(\frac{E_g}{2kT}\right)} \tag{2.5}$$

At room temperature (300 K), $n_i(Si) = 10^{10}$ cm^{-3}.

The intrinsinc fermi level E_{fi} is in the middle of of the forbidden band

$$E_{fi} \approx \frac{E_c + E_v}{2} \tag{2.6}$$

2.1.3 Doping

Donors and Acceptors

Adding a controlled quantity of impurities (specific atoms) in the lattice during the fabrication of the semiconductors allows the modification of electrical properties. The atoms used for doping are usually selected in the columns III and V of the periodic table. An example for each case is presented.

By adding arsenic (from column V) during the growth of the crystal, the dopant atom replaces a silicon atom in the lattice and creates covalent bonds with the four neighbours. Since the most external orbital of As is composed of nine electrons, eight saturate the orbitals while the ninth is in a more distance orbital. Its binding energy is small compared to E_g. At room temperature, the electron is liberated in the lattice by thermal excitation and occupies a state of the conduction band. Since the electron is missing from the As atom, it has an excess positive charge thus becoming As^+. Since an atom of the column V gives an electron to the lattice, it is named donor.

Doping with an atom from column III, such as boron creates a deficit of an electron in the structure of the lattice. This empty place is filled by an electron from the neighbouring binding which creates a hole in the valence band. Since there is an excess electron in the structure of the atom, it becomes B^-. An atom from column III is an acceptor.

Electrical neutrality is given by

$$p + N_a = p + N_d, \tag{2.7}$$

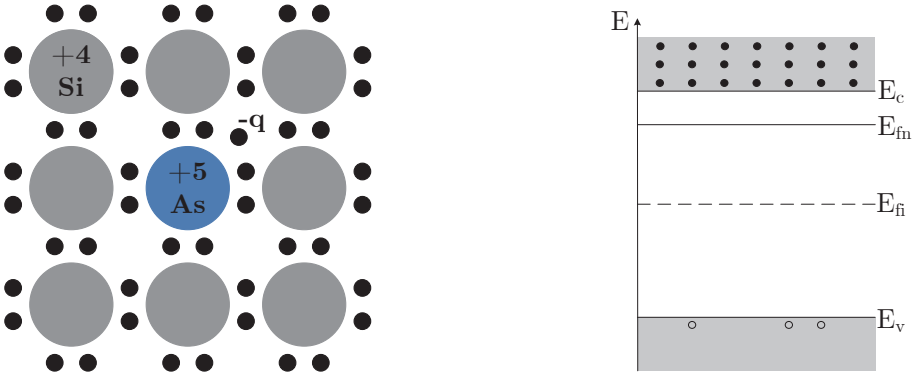

(a) (b)

Figure 2.2: (a) Schematic two-dimensional representation of n-type silicon with its donor (arsenic). (b) Schematic of the energy bands structure of a n-type semiconductor

with N_a the density of acceptors and N_d the density of donors.

N-type Semiconductor

When the donor's density is bigger than the acceptor's density, equation 2.7 shows that $n > p$. In this condition, electrons are named majority carriers and holes are minority carriers. Since the acceptors and donors densities, and $N_d - N_a$ exceed by far the intrinsinc carriers density n_i (e.g. from the *TowerJazz* documentation: $\mathrm{Nd_{n\text{-}well}} > 10^{18}$ cm^{-3}, and $\mathrm{Na_{epi}} \approx 10^{13}$ cm^{-3}),

$$n \approx N_d - N_a \tag{2.8}$$

and,

$$p \approx \frac{n_i^2}{N_d - N_a} \tag{2.9}$$

The Fermi levels of a n-doped semiconductor is given by

$$E_{f_n} = E_c - kT \ln\left(\frac{N_c}{N_d - N_a}\right) \tag{2.10}$$

P-type Semiconductor

When the acceptor's density is higher than the donor's density, electrons are named minority carriers and holes are majority carriers and,

$$n \approx \frac{n_i^2}{N_a - N_d} \tag{2.11}$$

and,

$$p \approx N_a - N_d \tag{2.12}$$

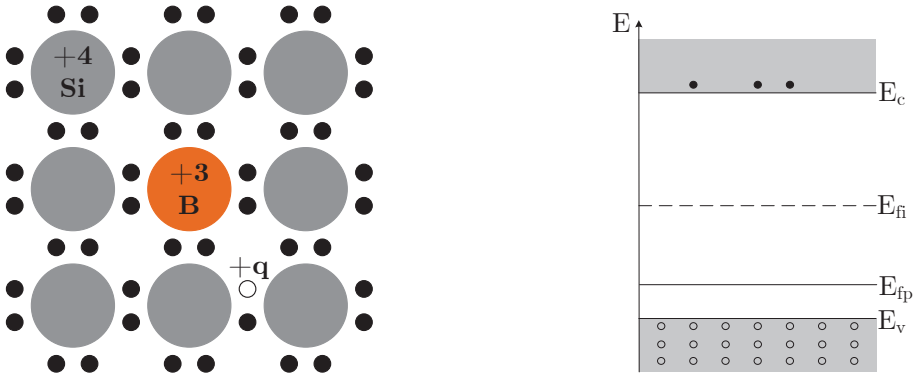

(a) (b)

Figure 2.3: (a) Schematic two-dimensional representation of p-type silicon with its acceptor (boron). (b) Schematic of the energy bands structure of a p-type semiconductor

The Fermi levels of a p-doped semiconductor is given by

$$E_{f_p} = E_v - kT \ln\left(\frac{N_v}{N_a - N_d}\right) \tag{2.13}$$

2.1.4 Carriers Transportation

Without any electric field applied, the carriers move in a Brownian motion. Between two collisions with the atoms of the lattice, the linear thermal speed of the carriers is

$$v_{th} = \sqrt{\frac{3kT}{m^*}} \tag{2.14}$$

With $m_e^* = m_0$, and $m_h^* = 0.5m_0$, at room temperature, $v_{th}(Si) \approx 10^7 \mathrm{cm\,s^{-1}}$.
It allows the determination of the free mean path of the carrier

$$l = v_{th}\tau_c \tag{2.15}$$

with τ_c the collision time, which depends on the purity of the medium, thus on the doping concentration (see section 2.1.5). The typical free mean path is between 100 and 1000 Å. Since the collisions are isotropic, the mean speed is zero.

With an electric field applied (e.g. generated by the presence of a voltage), a carrier with a charge q experiences a force $\overrightarrow{F} = q\overrightarrow{E}$ which allows the expession of the drift component of its speed

$$v_i(t) = \frac{qE}{m^*}t \tag{2.16}$$

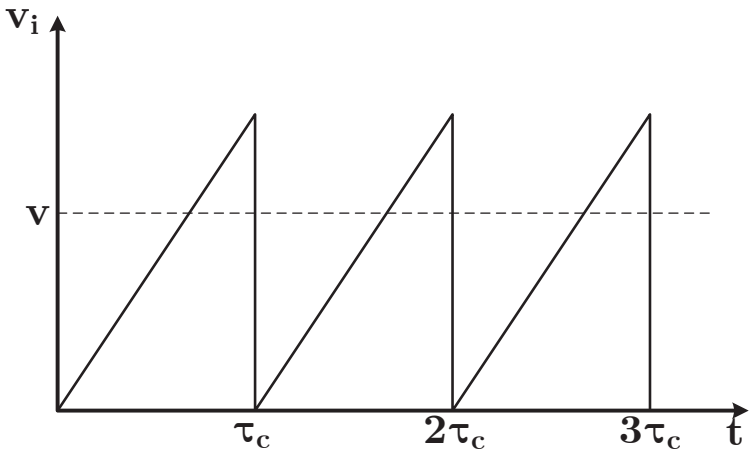

Figure 2.4: Time dependence of a free carrier's speed under with an electric field applied. The dashed line is the mean drift speed of a carrier in an electric field.

The speed increases linearly between two collisions and is statistically back to zero when colliding. Since $v_i(t)$ is periodic $\left(f = \frac{1}{v_{th}}\right)$, the mean drift speed of a carrier in an electic field is

$$v = \frac{1}{\tau_c}\int_0^{\tau_c} v_i(t)dt = \frac{1}{\tau_c}\frac{qE}{m^*}\frac{\tau_c^2}{2} = \frac{qE\tau_c}{2m^*} \tag{2.17}$$

It can also be written as

$$v = \pm\mu E \tag{2.18}$$

With $\tau = \tau_c/2$ the relaxation time and μ the mobility of the carriers expressed in $[\mathrm{cm}^2\,\mathrm{V}^{-1}\,\mathrm{s}^{-1}]$. This quantity expresses the aptitude of carriers to travel in a crystalline structure. The mobility is greater in the purest crystals with a low quantity of dopants. The value of the mobility is constant as long as the electric field is not too strong. The value of the mobility is temperature dependent and is different for each type of semiconductor which allows the expression of the velocity of the carriers

$$v_n = -\mu_n \overrightarrow{E} \tag{2.19}$$

$$v_p = +\mu_p \overrightarrow{E} \tag{2.20}$$

The conduction current resulting from the movement of electrons holes under an electric field is

$$\overrightarrow{J_c} = \overrightarrow{J_n} + \overrightarrow{J_p} = \sigma \overrightarrow{E} \tag{2.21}$$

with σ the conductivity of the medium given by

$$\sigma = nq\mu_n + pq\mu_p \tag{2.22}$$

Thus the resistivity of a medium is

$$\rho = \frac{1}{\sigma} \tag{2.23}$$

When the carriers are not uniformely distributed in a semiconductor, they diffuse in a direction tending to homogenize their spatial distribution. The flux is proportional to the gradient of carriers. With D_n, and D_p the diffusion constants for n-type and p-type semiconductors given by

$$D_x = v_{th}^2 \tau_c \tag{2.24}$$

leading to the estimation of the spread of the charge generated by an interacting particle.

The electron diffusion length for p-type semiconductors is given by $L_n = \sqrt{D_n \tau_n}$ and the hole diffusion length for n-type semiconductors is given by $L_p = \sqrt{D_p \tau_p}$.

The total diffusion current is expressed as

$$J_d = qD_n \overrightarrow{\nabla} n - qD_p \overrightarrow{\nabla} p \tag{2.25}$$

2.1.5 Generation and Recombination

The generation rate of carriers per unit volume and unit time (g' [$\mathrm{cm^{-3}\,s^{-1}}$]) is function of two contributions:

- g_{th}: Spontaneous generation due to thermal excitation
- g: External excitation of the semiconductor such as radiation interactions presented in chapter 1

The recombination rate of carriers per unit volume and unit time (r' [$\mathrm{cm^{-3}\,s^{-1}}$]) depends on the processes in the semiconductor.
With r the summary of recombination and thermal generation rates ($r' - g_{th}$), the variation of the number of carriers per unit of volume and unit of time is

$$\left(\frac{dn}{dt}\right)_{gr} = g - r \tag{2.26}$$

Direct Recombinations of Electrons and Holes

The rate of direct recombination is proportionnal to the amount of electrons and holes in the medium. Without external excitation,

$$r = k(np - n_i^2), \qquad \text{with } k = \frac{g_{th}}{n_i^2} \tag{2.27}$$

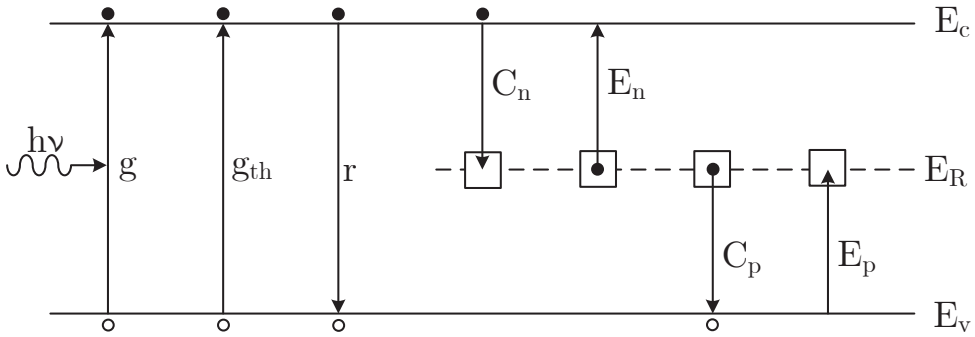

Figure 2.5: Generation and recombination processes under illumination

Under excitation ($n = n_0 + \Delta n$, and $p = p_0 + \Delta p$),

$$r = \frac{\Delta n}{\tau(\Delta n)} = \frac{\Delta p}{\tau(\Delta p)} \tag{2.28}$$

with $\tau(\Delta_n)$ the carrier lifetime in an excited semiconductor expressed by

$$\tau(\Delta_n) = \frac{1}{k(n_0 + p_0 + \Delta n)} \tag{2.29}$$

Under small injection, where the excess of carriers with respect to equilibrium is small compared to the density of majority carriers ($\Delta n = \Delta p \ll p_0$, or n_0), in a p-type silicon substrate, the recombination rate is:

$$r_n = \frac{\Delta n}{\tau_n} \tag{2.30}$$

with $\tau_n = {}^1/_{kp_0}$ the minority carriers lifetime.

The small injection condition is suited for the low energy photons and electrons interaction in thin silicon detectors since the deposited charge is small ($\Delta_n \approx 10^3$) compared to the majority density ($p_0 \approx N_a - N_d$, with $N_a \gg N_d$ in p-type semiconductors).

Recombination Center Assisted Recombinations

In high resistivity substrates, the carrier lifetime is theoretically very long because of the low probability of direct recombination. But, because of unwanted impurities inherent to the fabrication process, the effective lifetime is smaller than the theoretical one. Such impurities are trapping either an electron or a hole.

These traps are named *recombination centers* when the trapped electron has a greater

probability to capture a hole for recombination than to be reemited to the conduction band. When the probability of reemission of the elctron to the conduction band is bigger, it is a temporary *electron trap*. It plays a substantial role in the current in the medium. When the electron is temporary trapped, the free carriers density is reduced for a short time.

The recombination rate when assisted by recombination centers is expressed by the *Shockley-Read-Hall* (SRH) theory. With N_R the density of recombination centers, f_R the Fermi function that expresses the probability of occupation of the introduced energy level in the gap (E_R), and C_n, C_p, E_n, E_p the capture and emission coefficients of the centers for electrons and holes, the density of occupied and empty centers are respectively expressed by $N_{RO} = N_R f_R$, and $N_{RE} = N_R(1 - f_r)$. Three rates can be expressed depending on the doping of the substrate.

Lightly Doped Medium

$$r = \frac{1}{\tau_m} \frac{pn - n_i^2}{2n_i + p + n}, \quad \text{with } \tau_m = \frac{1}{CN_R}, \text{ and } C = C_n = C_p \tag{2.31}$$

Doped Medium

In a p-type semiconductor ($p_0 \gg n_i \gg n_0$) and under small injection ($p = p_0 + \Delta p \approx p_0$, and $n = n_0 + \Delta n \ll p_0$)

$$r = \frac{\Delta n}{\tau}, \quad \text{with } \tau = \frac{1}{kn_0 + CN_{R_i}} \tag{2.32}$$

Depleted Region (see section 2.2.1)

$$r = -\frac{n_i}{2\tau_m}, \quad \text{with } \tau_m = \frac{1}{CN_{R_i}} \tag{2.33}$$

The recombination rate is negative because the thermally generated carriers are greater than the recombinating carriers.

2.2 PN Junction

The PN junction is the juxtaposition of two doped semiconductor regions, one of each type, forming a diode (figure 2.6). The effects taking place in the device are used to collect the generated charge in a semiconductor detector.

The difference of the densities of donors and acceptors ($N_d - N_a$) is negative in the p-type region, and positive in the n-type region (figure 2.7 a). The difference switches

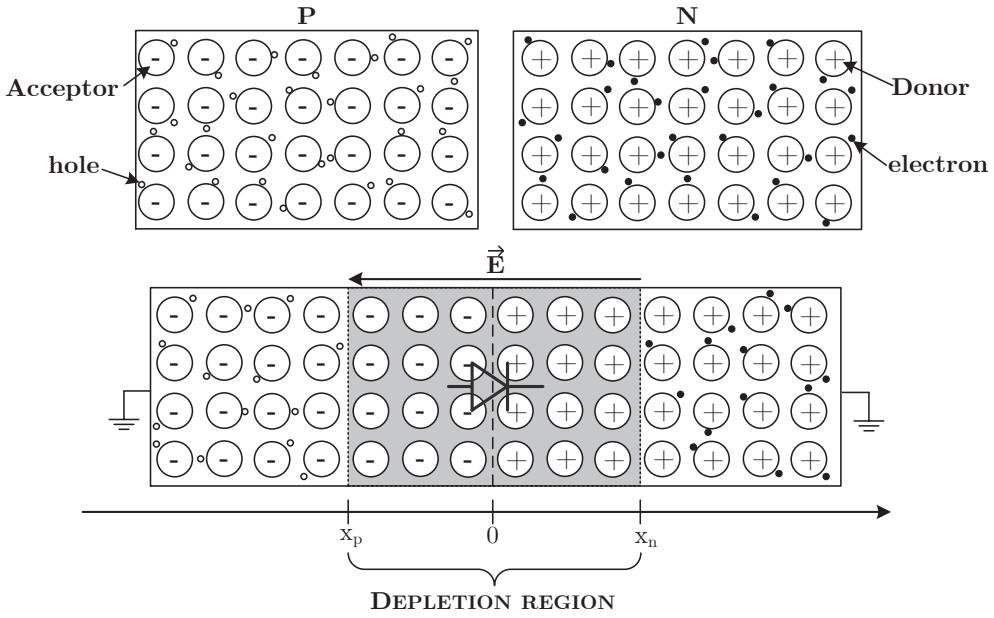

Figure 2.6: Uniformly doped p-type and n-type semiconductor before and after the pn junction is formed. In the pn junction, an electric field exists within the depletion region around the metallurgical contact. The pn junction forms a diode.

abruptely from the negative value to the positive value at the junction located at $x = 0$ in the abrupt model. The results obtained with the abrupt model are in accordance with the behavior of the pn-junction.

When the metallurgical PN junction is created, the holes in the p-type region diffuse towards the n-type region. The same happens for electrons but in the other way. The diffusion of the majority carriers from one side to the other creates a depleted region, also named space charge, composed of ionized acceptors and donors which are not compensated.

An electric field opposing the diffusion of majority carriers is created at the junction. The thermodynamic equilibrium is reached when the electric force compensates the diffusing force associated to the mobile carriers profiles. The density of mobile carriers is negligible within the depleted region.

2.2.1 Depleted Region

In extrinsinc semiconductor ($(N_d - N_a)_n \gg n_i$, and $(N_d - N_a)_p \gg n_i$), for simplification the excess of donors in the n-doped region can be expressed as

$$N_d = (N_d - N_a)_n \tag{2.34}$$

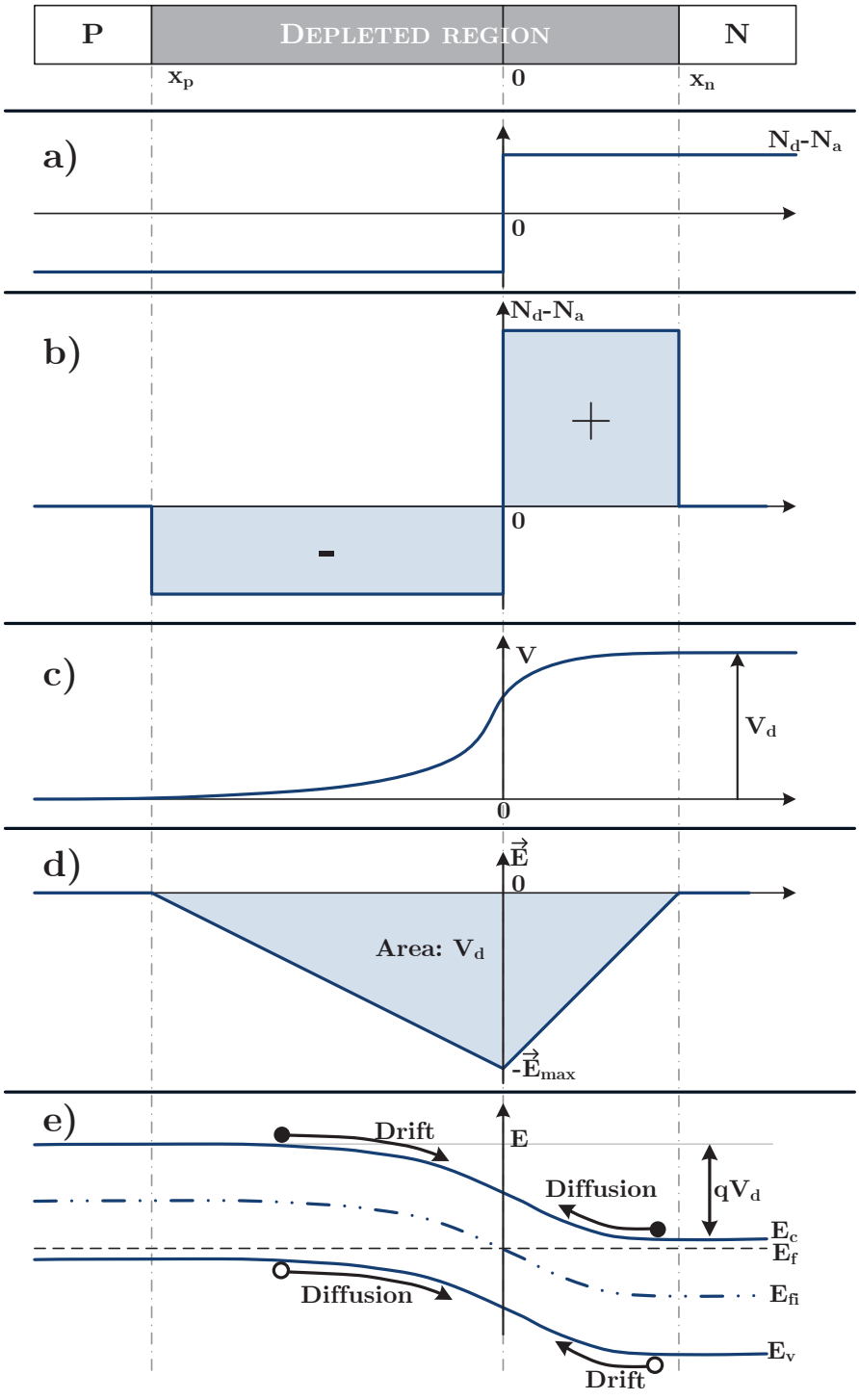

Figure 2.7: (a) Dopants
(b) Charge
(c) Potential. From 0 to the built-in potential accross the junction
(d) Electric field. The integration of the area represents the built-in voltage
(e) Band diagram and effect on electrons and holes

and the excess of acceptors in the p-doped region is thus

$$N_a = (N_d - N_a)_p \tag{2.35}$$

The density of electrons and holes in each region is

$$n_n = n_d, \quad p_n = \frac{n_i^2}{N_d}, \qquad n_p = \frac{n_i^2}{N_a}, \quad p_p = N_a \tag{2.36}$$

Supposing all the donors and acceptors left are ionized, the space charge is expressed as

$$\rho(x) = q[N_d - N_a + p(x) - n(x)] \tag{2.37}$$

On the n side of the junction, the charge is positive because of the ionized donors, while the charge is negative on the p side as a result of the ionization of the acceptors. The total quantity of charges on each side is equal. Outside the depleted region the space charge is zero. With the limit of the extension of the depleted region on each side marked as x_p and x_n the space charge can be expressed for each case

$$\begin{cases} \rho(x) = 0, & \text{for } x_p > x, \text{ and } x_n < x \\ \rho(x) = -qN_a, & \text{for } x_p < x < 0 \\ \rho(x) = qN_d, & \text{for } 0 < x < x_n \end{cases} \tag{2.38}$$

2.2.2 Built-in Voltage

The electric field generated in the space charge induces a potential varying from V_p in the neutral region of the p side to V_n in the neutral region on the n side. The potential barrier at the junction is the diffusion voltage, or built-in voltage

$$V_d = V_n - V_p \tag{2.39}$$

By considering the Fermi level being the same in the whole structure and from the density of electrons on both side of the structure, it is possible to determine the value of the diffusion voltage from difference of the potential energies of the conduction electrons between each region

$$V_d = \frac{kT}{q} \ln \frac{N_d N_a}{n_i^2} \tag{2.40}$$

In silicon, $V_d(Si) \approx 0.7$ V.

Potential and Electric Field

By integrating Poisson's equation with the densities from the previous section, the potential and electric field can be obtained for each side of the depleted region

$$\begin{cases} V = \frac{qN_a}{2\epsilon_{Si}}(x - x_p)^2 + V_p, & \text{and } E = -\frac{qN_a}{\epsilon_{Si}}(x - x_p), \quad \text{for } x_p < x < 0 \\ V = -\frac{qN_d}{2\epsilon_{Si}}(x - x_n)^2 + V_n, & \text{and } E = \frac{qN_d}{\epsilon_{Si}}(x - x_n), \quad \text{for } 0 < x < x_n \end{cases} \tag{2.41}$$

2.2.3 Width of the Depleted Region

In the depleted region, the amount of negative charges in the p region is equal to the amount of positive charges in the opposite side. With $W_p = |x_p|$ and $W_n = |x_n|$, the relation is expressed with

$$N_a W_p = N_d W_n \tag{2.42}$$

This equation also reveals that the depletion region is mostly extending on the less doped side of the pn junction. It can also be seen in the expression of the width developed from the continuity of potential at $x = 0$ given by

$$W_n = 2\left(\frac{\epsilon_{Si} kT}{2q^2 N_d}\right)^{1/2} \left(\frac{1}{1 + \frac{N_d}{N_a}} \ln \frac{N_a N_d}{n_i^2}\right)^{1/2} \tag{2.43}$$

$$W_p = 2\left(\frac{\epsilon_{Si} kT}{2q^2 N_a}\right)^{1/2} \left(\frac{1}{1 + \frac{N_a}{N_d}} \ln \frac{N_d N_a}{n_i^2}\right)^{1/2} \tag{2.44}$$

In a dissymetric junction ($N_a \gg N_d$, or $N_d \gg N_a$), the total width of the depletion region can be approximated by the width reached in the less doped region. For any region it can be expressed with

$$W = \sqrt{\frac{2\epsilon_{Si}}{q}\left(\frac{N_a + N_d}{N_a N_d}\right) V_d} \tag{2.45}$$

2.2.4 Polarized Abrupt Junction

By applying an external voltage on the junction to bias it, the potential barrier is modified thus changing the diffusion of carriers from a region to an other. The Fermi levels are not aligned anymore, but become shifted from the applied voltage in a direction depending to the polarization of the diode. With the ground set on the n-side and the biasing (V) applied on the p-side. The current through a diode is expressed by:

$$J = J_p + J_n = J_0 \left[e^{(qV/kT)} - 1\right] \tag{2.46}$$

Figure 2.8: Polarized pn junction

With J_0 the ideal diode law expressed by the Schockley equation

$$J_0 = \frac{qD_p n_i^2}{L_p N_d} + \frac{qD_n n_i^2}{L_n N_a} \tag{2.47}$$

Forward Biasing ($V > 0$)

The potential difference for positive voltages is

$$V_n - V_p = V_d - V \tag{2.48}$$

The main effect is the lowering of the potential barrier to $q(V_d - V)$. With sufficient biasing, the barrier is not high enough to block the diffusion of the carriers. Electrons are flowing from the n side to the p side of the junction, and holes diffuse to the other way. A forward current is thus flowing from the p region to the n region:

$$J_F \approx J_0 e^{qV/kT} \tag{2.49}$$

Reverse Biasing (V<0)

When a negative voltage is applied, the potential difference is

$$V_n - V_p = V_d + |V| \tag{2.50}$$

The height of the potential barrier is increased to $q(V_d + |V|)$. The diffusion of majority carriers, that are now not affected by the polarisation, is blocked making conduction current more valuable. Only the minority present in the depleted region can flow in the opposite region greatly helped by the stronger electric field.

The reverse current is:

$$|J_R| = J_0 \tag{2.51}$$

A reverse-biased diode allows the extraction of electrons from the p side to the n side of the junction. The same effects is true for holes on the other way. Thus, the electrons

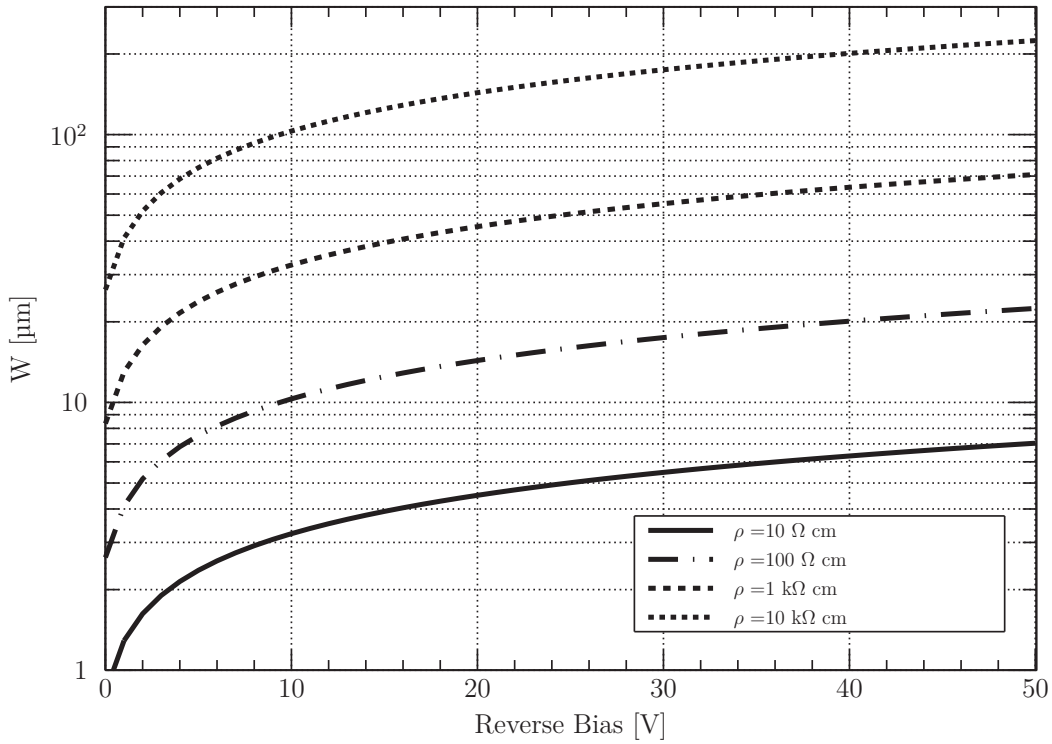

Figure 2.9: Theoretical depletion depth achieved with biasing voltages up to 50 V for various resistivities of silicon. W=70 µm can be reached with a 1 kΩ cm p-type substrate

generated from the interaction of radiation with p-type semiconductor can be collected in the N-side. It is the basic structure of the collecting diode.

The depleted width under reverse biasing is given by

$$W = \sqrt{\frac{2\epsilon_{Si}}{q}\left(\frac{N_a + N_d}{N_a N_d}\right)(V_d + |V|)} \tag{2.52}$$

In an assymmetric junction, with the n side highly doped ($N_d \gg N_a$), allowing the extension of the depletion in the p-side (electron collection), the total width can be limited to the size on the p region

$$W \approx W_p = \sqrt{\frac{2\epsilon_{Si}}{q}\frac{1}{N_a}(V_d + |V|)} \tag{2.53}$$

A variation dV_i of the inverse voltage creates a dQ variation of the space charge. The pn junction acts as a dynamic capacitor called transition capacitance. With S the section of the junction, the value of the transition capacitance is expressed by

$$C_t = \frac{S\sqrt{\frac{\epsilon_{Si} q N_a}{2}}}{\sqrt{V_d + |V|}} \tag{2.54}$$

2.2.5 Generation and Recombination in the Depleted Region

The recombination rate expressed by the SRH theory with a polarization can be expressed as

$$r = \frac{1}{\tau_m} \frac{n_i^2 \left(e^{qV/kT} - 1\right)}{2n_i + p + n} \tag{2.55}$$

The rate can be simplified to the equation 2.33 under reverse biasing condition. Since the rate is negative, thermal generation takes place in the depleted zone. The reverse current of the junction is

$$J_i \approx -\frac{n_i}{\tau_m} \left(\frac{q\epsilon_{Si}}{2N_a} V_d\right)^{1/2} \left(1 + \frac{|V|}{V_d}\right)^{1/2} \tag{2.56}$$

2.2.6 Breakdown

The maximum value of the electric field in the pn junction is at the metallurgical contact ($x = 0$). With biasing voltages greater than the built-in voltage ($V \gg V_d$) the value of the electric field is

$$E_0 \approx \sqrt{\frac{2qN_a}{\epsilon}} \sqrt{|V|} \tag{2.57}$$

The applied polarization could be continuously increased if there was not any limit for E_0. The limit is given by the maximum force applied on an electron by the electric field ($\overrightarrow{F} = -q\overrightarrow{E_0}$). If a valence electron experiences a force greater than its binding energy, it is liberated. The maximum electric field allowed is the one that could directly excite an electron in the valence band to a free state of conduction. In silicon, the maximum electric field is $E_{0_{max}} \approx 10^6$ V cm^{-1}. Nevertheless, in a pn junction the voltage limit depends on the width of the depleted region, and by extension, the doping concentration. In highly doped junction, with narrow space charge zone, the breakdown is governed by Zener effect or tunneling effect.

With greater depleted region, the breakdown is governed by the avalanche effect. The effects starts with electric fields approximatively ten times smaller than the Zener threshold ($E_{0_{max}} \approx 10^5$ V cm^{-1}). Under this strong electric field, the thermally generated electrons are accelerated. The transported reverse current becomes sufficient to create an electron-hole pair by ionization as a result of collisions with the atoms of the lattice. These pairs then accelerated to create more pairs and so on as long as the reaction is in the depleted region. The chain reaction is the so-called avalanche and is critical in very large depleted regions.

To increase detection performance in silicon based pixel sensors, the depleted volume must be extended as far as possible to optimize charge collection. The substrate must be lightly doped to allow the extension without applying too strong voltages. Also, the use

of high resistivity substrates will minimize the recombination rates such as the leakage current.

Table 2.1: Summary of constants and variables used in chapter 2

Symbol	Value	Unit	Definition
E_g	$E_g(Si) = 1.12$	[eV]	Band gap Energy
ϵ_0	8.8542×10^{-12}	$[\mathrm{F\,m^{-1}}]$	Vacuum Permittivity ($^{10^7}/_{4\pi c^2}$)
ϵ_r	$\epsilon_r(Si) = 11.68$	-	Relative Permittivity of Silicon
ϵ_{Si}	1.03417×10^{-10}	$[\mathrm{F\,m^{-1}}]$	Permittivity of Silicon
μ_0	12.56637	$[\mathrm{H\,m^{-1}}]$	Vacuum Permeability
k	1.38062×10^{-23}	$[\mathrm{J\,K^{-1}}]$	Boltzmann Constant
kT	0.02585	[eV]	Thermal Energy
N_c	$N_c(Si) = 2.7 \times 10^{19}$	$[\mathrm{cm^{-3}}]$	Density of states in conduction band
N_v	$N_v(Si) = 1.1 \times 10^{19}$	$[\mathrm{cm^{-3}}]$	Density of states in valence band
m^*	$m_e^* \approx m_0$, $m_h^* \approx 0.5m_0$	[kg]	Mass of carriers
m_0	0.910956×10^{-30}	[kg]	Electron mass
τ_c	10^{-13}–10^{-12}	[s]	Collision time
n_i	$n_i(Si) = 10^{10}$	$[\mathrm{cm^{-3}}]$	Intrinsinc carrier density
μ	$\mu_n(Si) = 1350$, $\mu_p(Si) = 480$	$[\mathrm{cm^2\,V^{-1}\,s^{-1}}]$	Carriers mobility
q	-1.602×10^{-19}	[C]	Electron charge

Chapter 3

Silicon-Based Pixelated Sensors

A pixelated sensor can be defined as a device embedding a highly segmented periodic two-dimensional array, the *matrix*, of collecting diodes with junction areas much smaller than the detector area. A *fill factor* (the ratio of sensitive area to the total area) of almost 100 % can be achieved. A sensor with a single junction covering the whole area is a pad detector. There are also strips detectors, where the diode length is approximately the length of the sensor while its width is much smaller. The pattern is repeated on the whole detection area making a one-dimensional array of collecting diodes. Double sided strips detectors with perpendicular strips can allow determining the two dimensional position of a hit as long as the hit rate is low enough.

Pixelated sensors can be divided in two main families:

- Hybrid Pixel Detector (HPD) where the detection is performed on one substrate while the readout electronics is on another. Each collecting point is connected to its own readout electronics via bump bonds, forming the imaging system. Depending on the application, HPDs exist as counting, or integrating detectors. The detection substrate being independent of the readout electronics, can be made in semiconductors material other than silicon (e.g. Ge, GaAs, CdTe, CdZnTe, and other compounds according to the application) and is operated fully depleted.

- Monolithic Pixel Sensors where the detection and the readout is performed on the same substrate. The signal obtained by the diode can either be carried out of the sensor to be amplified and processed on an ASIC (monolithic passive pixel sensor), or be amplified on the sensor closely to the diode before readout (Monolithic Active Pixel Sensor[1]). The detection volume can be partially depleted or fully depleted. When the partial depleted volume is very small (close to the collecting diode), the detection volume can be considered as undepleted.

After a brief description of the parameters that can be used to compare the performance of pixelated detectors, existing silicon based HPDs and monolithic sensors are reviewed. Other detecting materials than silicon for HPD are deliberately avoided to have references with a common material.

[1] MAPS

3.1 Pixelated Detectors

3.1.1 Generalities

For low energy radiations such as soft X-rays, some energy loss can happen outside the sensitive volume, therefore reducing the *quantum efficiency*. The loss can either happen with *Frontside Illumination (FSI)* and be stopped in the SiO_2-metalization layers, or with *Backside Illumination (BSI)* in a metallic electrode for backside contact and/or in a dead layer of silicon due to doping gradients, surface defects, undepleted region, etc. causing charge collection inefficiencies. These interacting layers that are not the sensitive volume are the *entrance window* and have to be kept as thin as possible for low energy radiation detection. For this reason, BSI is preferred requiring a thin backside contact that can also be removed and replaced by a thin passivation layer. The thickness of the detection volume is determined by the application.
An interacting radiation will generate a charge in the substrate either along its path (electrons, MIP) or locally. However, if the incident electron is not perpendicular with respect to the sensor surface, the deposited charge will be shared over multiple pixels. More pixels collect the charge if the *pitch* (the distance between the repetition of the same structure) is smaller. Also, a charge generated between two pixels can evenly be collected by both. The same *charge sharing* behaviour exist for photons where the charge generation forms a cloud which expands because of electrostatic repulsion and diffusion effects. The standard deviation of the Gaussian distribution estimating the spatial extent caused by diffusion only is given by

$$\sigma = d\sqrt{\frac{2kT}{qV}} \tag{3.1}$$

In a d=40 µm thick fully depleted substrate biased at V=30 V at room temperature (T=300 K), with q the elementary charge and k the Boltzmann constant, the charge cloud is extending 1.7 µm away from the interaction point. However, the generated charge cloud is larger because of the electrostatic repulsion. The effects of charge sharing for a back side illuminated sensor is presented in figure 3.1. The electrons generated along the path of an electron (or a MIP) outside the depleted volume are diffused and might reach the depleted volume to be collected before being recombined (Figure 3.1a). Every charge generated in a depletion region is collected and, the ones at the border between two pixels are shared between two pixels (Figure 3.1b). The same effect is true for the locally generated charge cloud by a photon (Figures 3.1c, 3.1d).

The maximum amount of charge a pixel can hold is limited by the capacitance of the pixel. The limit is the *full well* and is given in electrons. The capacitance of the pixel also determines the noise of the preamplifier. It is the sum of the backplane capacitance, the interpixel capacitance, and other small contributions. The backplane capacitance in

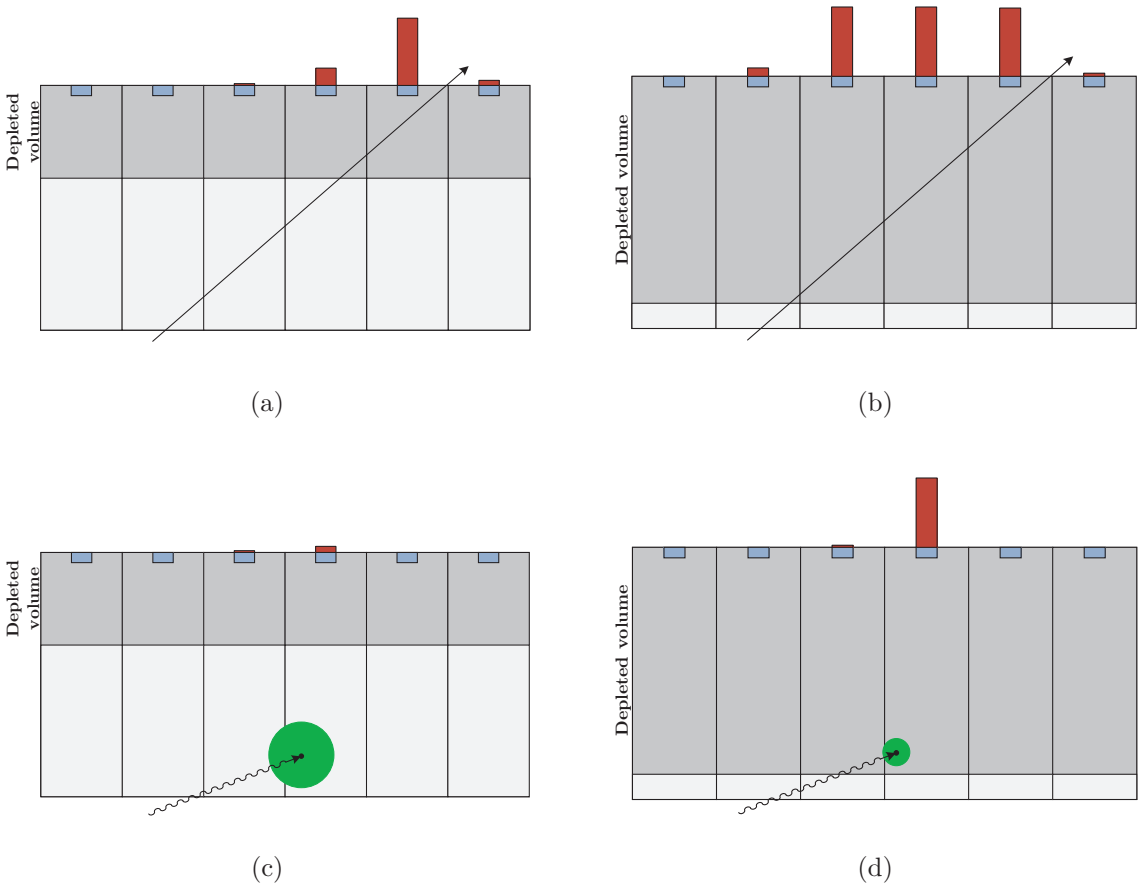

Figure 3.1: Amount of charge collected by an array of pixels after generation by a MIP or an electron in an undepleted (a), and depleted (b) substrate. The path can be identified in the depleted substrate since full collection is achieved.
A photon interacting at the bottom of the matrix in an undepleted substrate generates a bigger charge cloud (c) while a low amount of the generated charge is collected. In a depleted substrate, the charge cloud is smaller and full collection is achieved giving a strong signal on the seed pixel (d).

a silicon substrate is given by

$$C = \epsilon_{Si} \frac{A}{d} \tag{3.2}$$

with A the area of the pixel, d the thickness of the sensor, and ϵ_{Si} the permittivity of silicon. The interpixel capacitance in depleted sensors is the main contribution to the pixel capacitance. It is proportional to the perimeter of the pixel, to the gap between implants, and the biasing voltage of the junction.

The capacitance also has a role on the voltage resulting from the amount of charge collected by the diode. The signal (in volts) obtained from the collected charge is given by:

$$V_{signal} = \frac{Q}{C} \tag{3.3}$$

This relation shows that for low energy photons, which generate a small charge, the capacitance must be minimized to guarantee a sufficiently high signal with respect to the noise.

A significant source of noise comes from the *leakage current* that exist when a reverse bias is applied on a junction. One of its components is the bulk leakage current where majority carriers diffusing from a p- or n-doped region towards the depleted region are repelled by the intense electric field. Minority carriers that are continuously generated on any side of the junction are attracted and diffused across the pn junction creating a current proportional to the area of the junction. Another source comes from the thermal generation of electron hole pairs within the depletion region thus generating a current.

Obviously the current is proportional to the volume of the depleted volume and is temperature dependant. Silicon-based sensors can be operated at room temperature thanks to the sufficiently high band gap energy. Cooling the sensor decreases the contibution of this source to the leakage current. Another input to the leakage current is the surface leakage where large voltage gradients at the edges of the junction exist. This contribution can be reduced by design with guard rings.

The noise performance is important to keep the *signal-to-noise ratio* (SNR) sufficiently high for small input signals (e.g. low energy photons, thin sensitive volumes, undepleted sensors). Noises can not be completely removed, and aside from the leakage current, other sources of noise inherent to pixel design exist such as *1/f noise*, *shot noise*, and *fixed pattern noise*. The latter is due to the non-uniformities in doping, mismatch in the MOSFETs, variation of mobilty, threshold voltages, etc. from pixel to pixel.

Data acquired in each pixel is readout at a given frequency, the *frame rate*, which

also determines the *integration time*. The data can either be integrated to obtain a signal proportional to the collected charge or the signal hits can be counted provided that the electronics is fast enough with respect to the application to discriminate single events.

The data can be readout using *rolling shutter*, where a token activates the readout of the selected row while the other rows are integrating, and in *global shutter* mode, the integration is stopped while the matrix is readout thus creating a longer dead-time operation. A new trend for tracking applications emerges: *data-driven readout* where the information of the hit only is fetched via complex digital circuitry.
The more complex the circuit is, the more power is dissipated into heat. The heating of the sensor will cause a degradation of the signal-to-noise ratio and thus requires cooling. But, specific applications require low material budget resulting in near impossibility to add radiators or active cooling systems, thus requiring efficient designs to minimize the dissipated power.

3.1.2 Figures of Merit

To evaluate the performance of a given detector, three major figures of merit will be used: the energy resolution, the spatial resolution, and the radiation tolerance. The three main parameters driving these quantities are discussed in detail below. Also quantum efficiency can be cited. It is strongly dependant to the sensitive thickness, and will not be discussed further.

Energy Resolution

The main interaction process with low energy photons is photoelectric absorption. The response on the sensor is a full energy peak. Since the charge generation in the sensor is proportional to the energy, with sufficient biasing, all the generated charge is collected before trapping or recombination resulting in the observation of the full energy peak (i.e. spectroscopy) widened by noise contribution such as the Fano noise, and readout noise. A broadening can be seen on the low energy side of the peak caused by partial charge loss in the insensitive volume or by trapping, and by charge sharing effects.

Typical characterization are performed with an ^{55}Fe soft X-ray source. This source emits two rays: the Mn-Kα ray at 5.9 keV (emission probability: 24.4 %), and the Mn-Kβ at 6.49 keV (emission probability: 2.86 %). The full width at half maximum (FWHM) of the calibration peak is the energy resolution of the sensor. It is the quadrature sum of

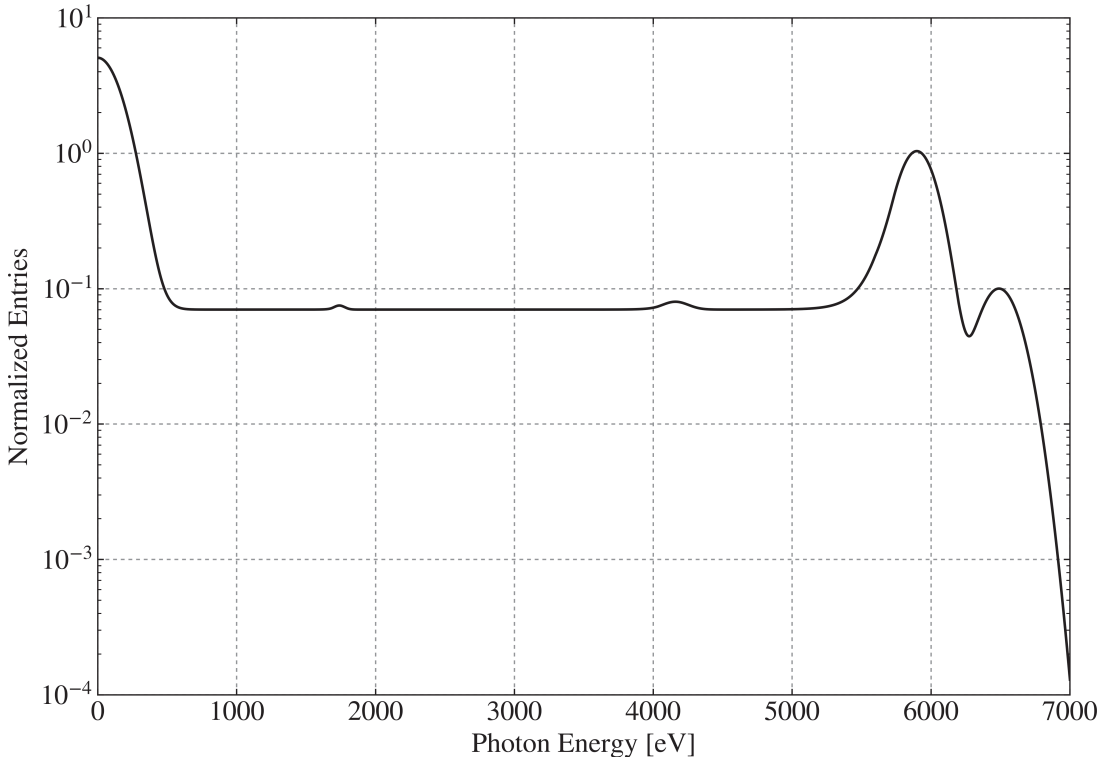

Figure 3.2: Representation of a theoretical spectrum of ^{55}Fe acquired with a silicon sensor achieving an energy resolution of 300 eV. The Mn-Kα and Mn-Kβ calibration peaks are clearly separated. The main calibration peak is thicker on the low energy side because of partial charge loss and charge sharing effects. At zero energy, the noise forms another peak. In between, a plateau exists on which the escape and fluroescence peaks can be observed, especially the silicon fluorescence peak at 1.74 keV, and the escape peak at the energy of the fluorescence peak below the calibration peak

independant components.

$$FWHM = 2.355\sigma_T = 2.355\sqrt{\sigma_{ENC}^2 + \sigma_D^2 + \sigma_X^2} \tag{3.4}$$

The first contibution is σ_{ENC} the equivalent noise charge of the signal processing chain,

$$\sigma_{ENC}[\text{eV}] = \epsilon\sigma_{ENC}[e^-] \tag{3.5}$$

The second contribution, σ_D is the equivalent spread of the charge generation statistics given by the fano factor (section 1.2)

$$\sigma_D^2 = \epsilon FE \tag{3.6}$$

with ϵ the ionization energy in silicon, F the Fano factor ($F = 0.11$), and E the energy of the incoming photon.

The last contribution σ_X is the result other sources of noise such as gain spread.

$$\sigma_X = E\sigma_g \tag{3.7}$$

with σ_g the gain spread as a proportion of the photon energy E.

The best achievable resolution (i.e. with noiseless electronics and perfect collection), the energy resolution is limited by the Fano noise. Thus, for a 5.9 keV soft X-ray ^{55}Fe source, the minimum energy resolution achievable is:

$$FWHM(5.9\text{ keV})_{min} = 2.355\sqrt{\epsilon FE} \approx 114.3\text{ eV} \tag{3.8}$$

In silicon, a characteristic peak exists 1.74 keV below the main calibration peak (*Si K-escape peak*). On the low energy side of the spectrum, another peak is formed by noise fluctuations. Between both ends, a continous plateau caused by photoelectrons and Auger electrons travelling from the sensitive volume to the insensitive volume. Additional peaks can be visible, coming from the interaction fluorescence X-rays (e.g. Si-Kα at 1.74 keV). At energies above the calibration peaks, double counts can be seen.
An estimation of a ^{55}Fe spectrum acquired in a silicon pixelated sensor with $\sigma_{ENC} \approx$ 25 electrons and achieving an energy resolution of 300 keV is shown in figure 3.2.

Spatial Resolution

Spatial resolution is the ability to distinguish details. A way to determine the spatial resolution consists of applying a mask on a part of the sensor. Under uniform illumination,

the edge of the mask is visible. In an ideal sensor with infinite spatial resolution, the edge would be abrupt. Actually the result is a gradient of grey levels, the *Edge Response Function* (ERF). The 10 %–90 % distance is a good approximation of the spatial resolution.

The derivative of the ERF is the *Line Spread Function* (LSF) which represents the generated image by a straight line source. In the case of the perfect sensor, the LSF would be a Dirac peak while actually being a Gaussian. Its FWHM quantifies the spatial resolution (in unit of a distance).

The image resolution can also be expressed by its *Modulation Transfer Function* (MTF) which is the spatial frequency response of a sensor. The sensor is characterized with a sinusoidal input with variable spatial frequency. It can either be determined by the Fourier transform of the LSF, or by using a mask with alternating openings at given spatial frequency. This frequency is given in line pairs per millimeters (lp/mm). The input on the sensor is thus not sinusoidal but a squared function which slightly overestimates the resolution.

A matrix of pixels with binary readout where the detection threshold is set to allow single pixel detection is illuminated. The fired pixel of pitch p centered around 0 is considered. With an uniform density of particles ($D(x) = 1$) the average difference between the real impact position within the pixel area (x_r) and the measured position (x_m) is given by:

$$\sigma^2 = \frac{\int_{-p/2}^{p/2} (x_r - x_m)^2 D(x_r) \mathrm{d}x_r}{\int_{-p/2}^{p/2} D(x_r) \mathrm{d}x_r} = \frac{\int_{-p/2}^{p/2} x_r^2 1 \mathrm{d}x_r}{\int_{-p/2}^{p/2} 1 \mathrm{d}x_r} = \frac{p^2}{12} \tag{3.9}$$

Meaning that for a simple configuration, the minimum spatial resolution achievable is $\sigma = \frac{p}{\sqrt{12}}$. This value can be improved with charge sharing and algorithms. With analog readout where the sample is proportional to the collected charge, interpolation algorithms can be used to enhance the resolution. Nevertheless for single pixel hits, the resolution remains limited to pitch/$\sqrt{12}$.

Radiation Hardness

A sensor under irradiation is degraded by two types of defects which affect the electrical properties of the sensor in various ways.

Bulk damage is the outcome of the interaction of particles with the nuclei of the atoms of the substrate. A silicon atom is displaced from the lattice with a recoil energy

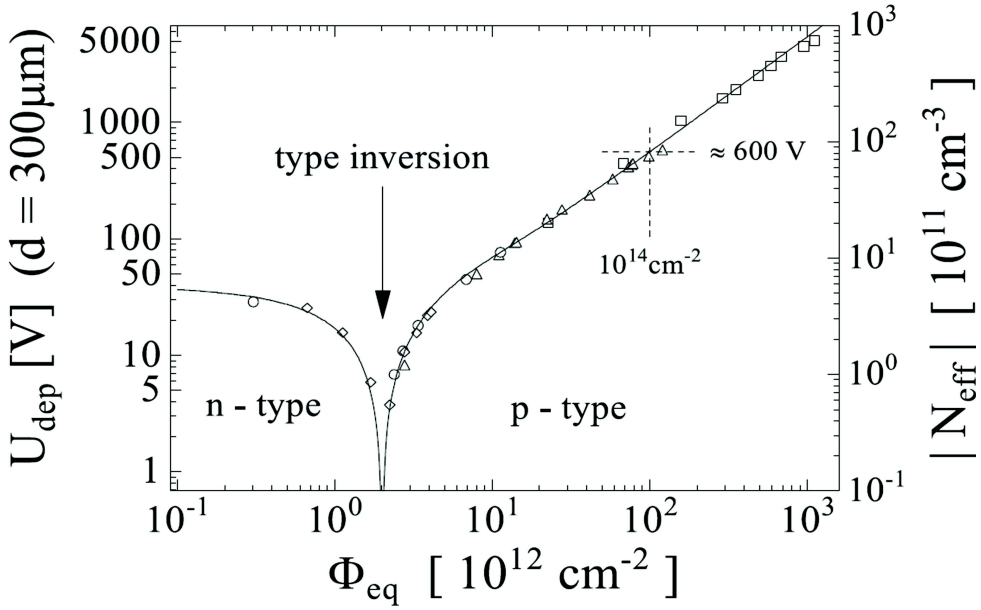

Figure 3.3: Change of the full depletion voltage of a 300-µm-thick silicon sensor and its absolute effective doping versus the normalized fluence, immediately after the irradiation. Figure from [11].

of 25 eV which can be provided by electrons above 290 keV. The recoiling atom can cause secondary defects when enough energy is transferred to it. Nevertheless, electrons and photons of a few MeV only create point defects while heavy charged particles create clusters. Such defects are not reversible since the crystalline structure is damaged. Bulk radiation damages is scaled with *Non Ionizing Energy Loss* (NIEL) which summarizes the deposited energy which has not been used for ionization, given as a fluence of 1 MeV equivalent neutrons.

The induced defects add energy levels in the band gap. They act as generation or recombination centers reducing the generation lifetime, and increasing the generation current added to the initial leakage current proportionaly to the fluence. Nevertheless, this added leakage source is partially annealed with time and/or heating.

Also, the space charge of the depleted volume can be modified by charged defects. The effective doping of the substrate is modified with the fluence. The effective doping of a n-doped silicon bulk is reduced with the fluence which also decreases the space charge until it disappeares. With further increase of the fluence, the effective doping increases with acceptor like defects thus creates a negative space charge. The doping type changed, and becomes more p with the fluence. The type inversion is shown in figure 3.3.

For initially p-type doped substrates, the effective doping increases which reduces the depleted volume. To compensate the diminution of the space charge, the operating voltage can be increased as long as it is below the breakdown voltage. Nevertheless, increasing

the biasing voltage, along with the increase of the leakage current by irradiation raises the dissipated power and thus the temperature of the sensor requiring cooling which may not cope with the experiment requirements. For tracking purposes with constant biasing voltages, the diminution of the amount of collected charge because of the reduction of the depleted volume and trapping effects, can be compensated by design as long as the SNR remains sufficiently high. Also, the use of oxygen enriched substrates reduces the effect of the defects.

Surface defects are caused by ionization and charge accumulation in regions such as the silicon oxide, and the interface between the silicon and the dielectrics. When an electron-hole pair is generated in oxide, the electron will be swept away thanks to its high mobility. On the other hand, holes have a very low mobility in oxide because of shallow hole traps and will move very slowly with the electric field. If these holes get to transition region between silicon and oxide, they might encounter deep hole traps and be constantly kept. The positively charged oxide influences the electric field next to the surface inducing an accumulation of electrons in a n-type layer, thus modifying the electrical properties of PMOS transistors. In p-type silicon, a depletion layer is created.

Due to the generation of interface states, a surface generation current exists when the depleted volume reaches the surface and contributes to the leakage current of the sensor. The damages can be annealed with sufficient heating.

3.2 Hybrid Pixel Detectors

Hybrid pixel detectors were first developed at CERN for tracking experiments closely to the interaction point at the LHC (Large Hadron Collider). The foreseen specifications of the experiments lead to requirements such as a micrometer range spatial resolution, small time resolution to separate events from each bunch crossing, low material budget to minimize the disturbance induced on a crossing particle for which the power dissipation must be reduced, and high radiation tolerance. Each experiment at the LHC is equipped with such detectors until the ALICE ITS upgrade, planned in 2019–2020, where the innermost pixelated detector will be replaced using MAPS (see 3.3.2). The technology of HPDs has been transferred to imaging purposes. A representation of a hybrid pixel detector is shown in figure 3.4.

The detection substrate embedding an array of sensitive elements (diodes) is bump bonded (or connected via *Through Silicon Vias(TSV)*) to its readout ASIC. Because of the development and fabrication costs of the detector and the ASIC that require to be connected by bump bomnding, such a detector remains expensive.

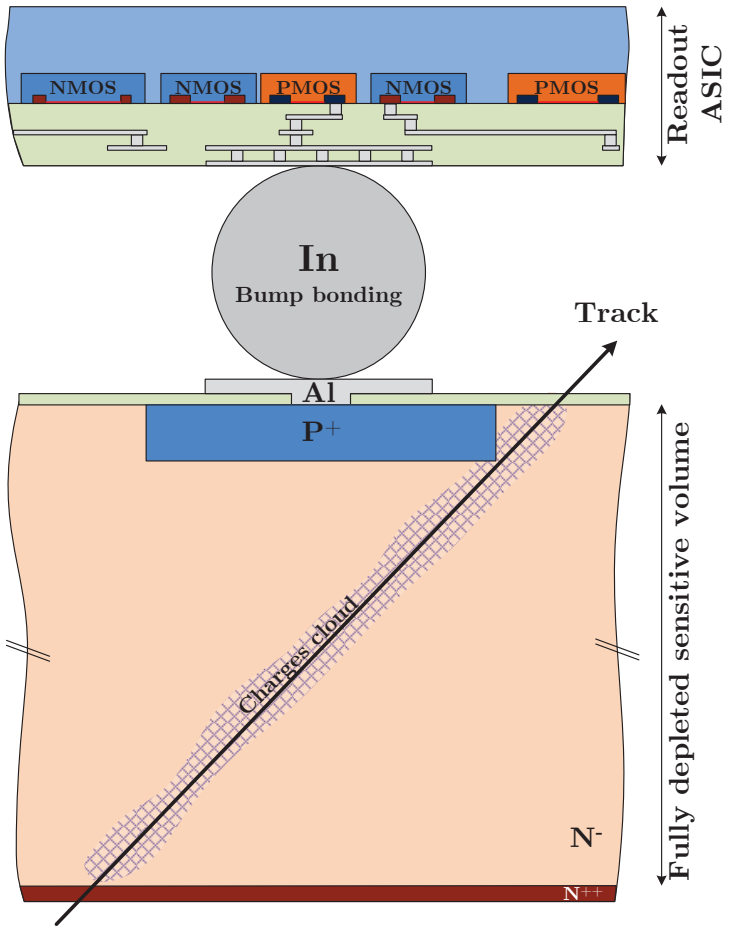

Figure 3.4: Schematic cross section of an hybrid pixel detector. The p+ implant in a high resistivity n type substrate is bump bonded to a readout ASIC (Application-Specific Integrated Circuit).

Although the detection substrate can be composed of any adapted semiconductor material, the further sections reviewing readout ASICs will be focused on silicon based detectors.

3.2.1 Counting HPD

A charge generated in the detection volume of HPDs is collected in a few tens of ns, thanks to the depleted operation, which allows the detection of single events with respect to the photon flux. The generated signal, proportional to the amount of charge collected, is read out and amplified by a CSA (Charge Sensitive Amplifier). It is followed by a shaper which modifies the time constant of the response and thus the maximum hit rate that can be processed by the front-end. The output of the shaping stage is compared to thresholds to digitize the informations from the current hit. A global threshold is applied over the whole readout chip but, in order to minimize the dispersion effects between the pixels, the threshold can be adjusted in each pixel using trim DACs. The digital information of the hit resulting from the comparison is used to increment a counter allowing *single photon counting*. A schematic of the readout chain of a counting hybrid pixel detector is shown in figure 3.5.

The digital information can also be used for in-pixel digital processing such as communication with the neighbouring pixels to assign the hit to the pixel which holds the highest charge (MEDIPIX 3 SPM[32]).

The characteristics and performance of various counting hybrid pixel detectors are summarized in tables 3.1, and 3.2 and have been partially adaptated from [31].

Because of the size of the indium ball used for the bump bonding and the amount of elements embedded in the pixel, the pitch can not be minimized which is a limitation

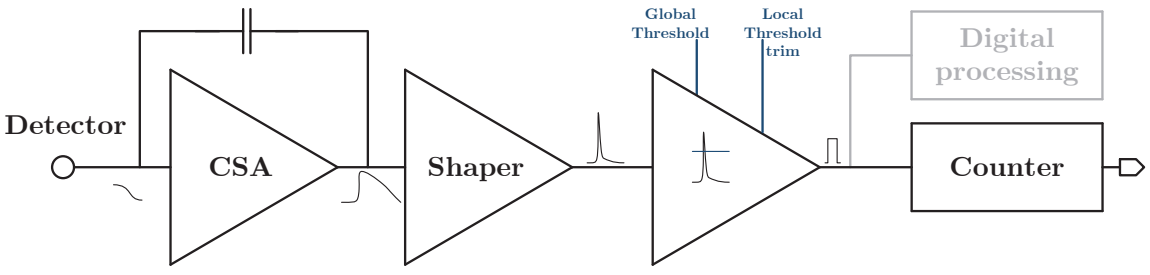

Figure 3.5: Block schematic of a counting hybrid pixel detector. The collected signal is amplified, shaped and compared to a threshold to have a digital information of the presence of a hit to increment a counter. The digital data can be used by other digital processing techniques.

for the spatial resolution performance. Also, to achieve very high count rates, the peaking time at the shaper is minimized at the expense of higher noise limiting the energy resolution and the minimum energy threshold that can be applied for the detection.

3.2.2 Integrating HPD

With bursts of photon arriving on a given area of a sensor, the count rate of counting HPDs may not be sufficient to distinguish two separate photons. Thus, an other method is needed for imaging. Instead of counting each incident photon, the amount of charge generated by multiple encounters is stored in a given amount of time, *the integration time*. The signal is then amplified and either carried out of the sensor, before or after filtering, or can be stored in analog memories array within the pixel. Also, on-chip ADCs can be implemented. In order to satisfy requirements on the signal to noise ratio, the gain of the amplifier can be adjusted, either on the whole sensor or on the pixel level. The gain can also be auto adaptative (see AGIPD). Thus, for a sufficient amount of signal integrated, the gain can be reduced, increasing the noise but also increasing the saturation limit.

The DSSC (Depfet Sensor with Signal Compression) embeds an intrinsic compression mechanism directly on the sensor level. The collected electrons are accumulated in an internal gate which results on a positive image of the amount of charge on the PFET channel. Since a clearing is required to remove the charge from the internal gain, the signal can be readout multiple times allowing sub-electron noise performance by averaging. The internal gain compression is achieved by the presence of an overflow region where the internal gate is extended beyond the transistor channel towards the source region.

The performance of integrating hybrid pixel detectors are summarized in tables 3.3, and 3.4. Since the analog data can be readout directly, there is less area required for embedding within the pixel allowing finer pitch (down to 25 µm for MÖNCH with which a spatial resolution of the order of 1 µm is achieved using charge sharing to interpolate the hit position [33]). The integration method is necessary on XFEL experiments, where a very large amount of photons arrives in a very short time over the sensor. The bunch train structure of the European XFEL provides 2700 bunches of up to 10^{12} photons at 12 keV in less than 100 fs every 220 ns at a 10 Hz rate [34]. Thus, the sensor used at this facility takes a series of images (with integration times « 220 ns) during the 600 µs train of pulses while the remaining 99.4 ms of the bunch structure is used to read the acquired data. The HPD developped for this application can achieve very high frame rates by storing successive frames between two readouts (AGIPD, LPD, DSSC).

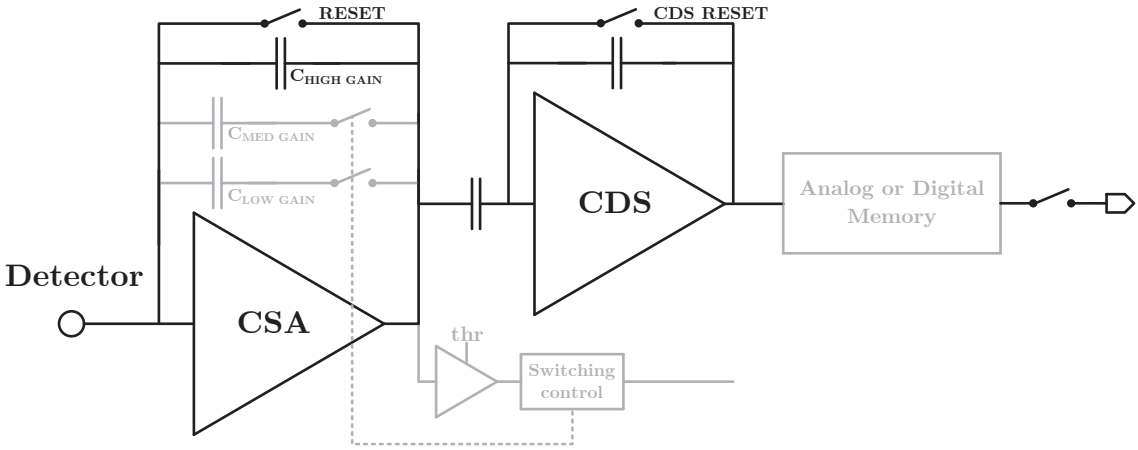

Figure 3.6: Block schematic of an integrating hybrid pixel detector. The signal is amplified before being filtered and either stored or read out. The gain of the amplifier may be self adapted to the amount of integrated charge.

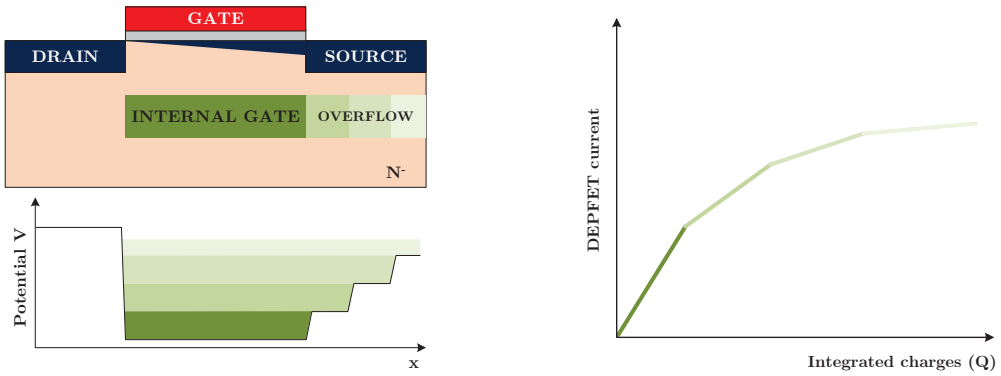

(a) (b)

Figure 3.7: (a) Principle of the DSSC. An internal gate in the PFET stores the charge. An overflow region extending towards the source allows internal signal compression. (b) The resulting current available at the output of the DEPFET versus the integrated charge

3.3 Monolithic Pixel Sensors

The frontier between monolithic sensors and hybrid pixel sensor can be very blurry. Here, the proposed definition for monolithic sensor is :

The signal resulting from the charge collection is not directly sent to an external readout ASIC. It is adressed, directely or indirectely, either to amplifiers at the periphery of the matrix or to the output to be readout on an external ASIC, or directely amplified in the pixel area before readout.

When the amplification is not performed in the pixel area, the chip is a *passive detector*, while a *monolithic active pixel sensor* has at least an active transistor embedded within the pixel.

3.3.1 Passive Sensors

Passive pixel sensors can be separated in two different subcategories, the *Charge Coupled Devices (CCDs)* and the passive pixel sensor.

Charge Coupled Devices

The charge collected by a diode in the CCD array has to be physically transferred through every CCD cell to the edge of the array. This charge transfer method implies sensitivity to bulk radiation damage and prohibits very high photon rates applications whose are also limited by the low frame rates achieved. To increase the latter, methods are used such as frame store, where the charge is transferred to a CCD array outside the matrix the be readout or amplified. CCDs also suffer from a high sensitivty to leakage current requiring low temperature operations. Nevertheless from the performance presented in tables 3.5, and 3.6, CCDs achieve good spatial resolution and, with very low noise operation, excellent energy resolution close to the Fano limit. CCDs are very common for spatial applications and its technology is mastered and relatively low-cost.

Passive Pixel Sensors

The XAMPS sensor is a passive pixel sensor. The signal generated from the charge collection in each pixel is adressed at the output of the sensor over a connection. Each row is sequentially adressed and a JFET switch allows the propagation of the signal on the column as shown in figure 3.8a. It is then amplified on an ASIC. The performances are reported in tables 3.5, and 3.6. The propagation of a low unamplified signal over relatively long lines limits the noise performance and the frame rates. Also the relatively

(a) (b)

Figure 3.8: (a) Pixel structure schematic of a passive pixel sensor. The diode is connected to the column through a JFET switch when the row is selected. (b) Pixel structure schematic of a MAPS. The signal at the diode is amplified before being adressed on the column by a row selection switch.

large pitch, with respect to the smallest ones in HPDs, CCDs, and MAPS, limits the spatial resolution of the sensor.

3.3.2 Monolithic Active Pixel Sensors

The most basic application of a monolithic active pixel sensor is similar to the XAMPS sensor except that the signal is amplified within the pixel before being adressed to the column (figure 3.8b). The amplification can be simple (3T architecture) where the amplification stage is a source follower composed of a single transistor (gain < 1) or to more complex amplifier architectures along with in-pixel data processing.

The rise of the CMOS sensors market for consumer applications opens technologies that can be used for scientific applications while standard CMOS processes can also be used with slight adaptations. By assuming a sensor can be produced on a high resistivity P type substrate, either epitaxial or bulk, notable features of the available technologies can be described. The use of commercial processes reduces the cost for prototyping and production of *CMOS Pixel Sensors (CPS)*.

With standard or OPTO CMOS (*AMS-0.35 µm, 0.18 µm*)[2] technologies that embed only two or three levels of wells (N-wells, P-wells and sometimes deep N-wells), the sensor design is limited to the use of NMOS in the pixel area (figure 3.9a). Using PMOS that are composed of a highly doped N-well would indeed compete in the charge collection process with the N-well used as a diode. Also such technologies generally do not allow direct access to the bulk which limits the reduction capabilities of the sidewall capacitance as

[2]http://ams.com

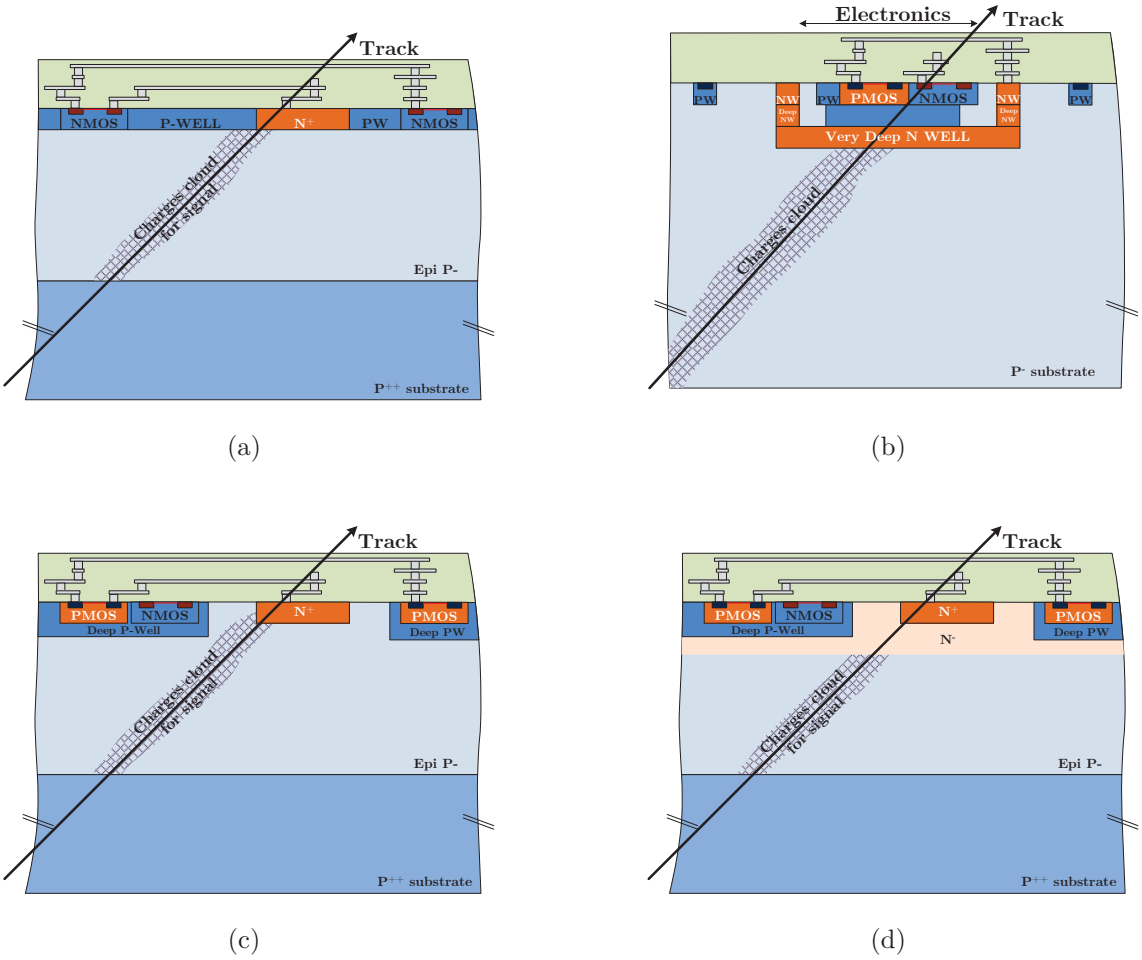

Figure 3.9: (a) Cross section schematic of a pixel designed with a twin well process. Only NMOS can be used since the PMOS would compete with the diode for charge collection. This technology is used for the design of the prototype presented in chapter 7.(b) Cross section schematic of a DMAPS pixel. The CMOS process is enclosed in a deep p well surrounded by a N-type structure acting as the collecting diode. (c) Cross section schematic of the standard TowerJazz CIS process. Both NMOS and PMOS can be used because of the isolation provided by the deep P well structure. An opening in the substrate is allowed to reduce sidewall capacitance. This technology is used for the design of the PIPPER-2 and IMIC sensors respectively presented in chapter 4.1 and in chapter 8. (d) Modified TowerJazz CIS process. A N- layer is added in the opening and below the deep P well region. It helps the depletion of the volume and improves bulk radiation hardness.

the N-well (collection diode) is next to the P-well. The capacitor's plates formed by each well are barely separated, this increasing the capacitance.

The *0.18 µm CMOS Image Sensor (CIS)* process proposed by *TowerJazz*[3] includes two well levels (standard and deep) for each type. This feature allows the isolation of the PMOS within a deep P-well which removes the restriction of PMOS usage in the design of the pixel. The technology also permits an absence of well (figure 3.9c) for direct substrate access and sidewall capacitance reduction by the separation of the plates represented by the wells (N-well from the collecting diode and P-well containing the CMOS circuitry).

A modified version of the standard process is explored with the CERN. A N- layer is deposited below the deep P-wells and in the opening region around the N-well to enhance the depletion in the epitaxial layer and to improve the tolerance to non ionizing radiation effects [36] (figure 3.9d).

The *LFoundry 150 nm*[4] process is composed of up to three levels of wells. Using a very deep N-well under the deep P-well that isolates the CMOS process as a diode, and with high voltage biasing, the formed structure is a *Depleted MAPS (DMAPS)* thanks to the high resistivity P-type substrate.

The performance of selected MAPS using various processes are summarized in the tables 3.7, and 3.8. With very large matrices of small pixels, the spatial resolution performance are below one micrometre. Also, the noise performance can be improved thanks to optimized designs and amplification close to the collecting point. The capacity to use the full CMOS process unlocked the high frame rate performance with data sparsification and compression. Nevertheless, despite almost perfect collection efficiency (see references in table 3.7) within epitaxial layers, full depletion is required to reach those performances with thicker substrates.

To increase depletion in CMOS pixel sensors, the resistivity of the substrate must be maximized which does not require process modifications. Nevertheless, a negotiation is needed with the foundry if they do not propose the substrate wanted. On the other hand, the substrate can be thinned to a thickness corresponding to full depletion which might require handling wafer (<50 µm thinning).
Another method to increase the depleted volume in CPS is to raise the diode bias voltage. The maximum value allowed without process modification is limited by the constraints of the technology. Also, very high bias values require specific board design which might not

[3]http://www.jazzsemi.com/cmos-image-sensor.html
[4]http://www.lfoundry.com/

cope with the experiment requirements.
Increasing the area of the diode with respect to the pixel area eases to increase the depleted volume at the expense of higher capacitance and thus, lower signal. It is either possible with the standard process, as *LFoundry* with the very deep N-wells enclosing the CMOS circuitry, or with process modifications, as the N- layer from the modified *TowerJazz* process.

Table 3.1: Characteristics of counting hybrid pixel detectors

Name	Technology	Matrix size	Pitch [µm^2]	Si type	Thickness [µm]	Resistivity [kΩ cm]	Depletion voltage [V]	Max counts [/pixel]	References
MEDIPIX 1	SACMOS 1µm	64×64	170×170	N	300	10	100	32768	[37–41]
MEDIPIX 2	IBM 0.25µm	256×256	55×55	P or N	300, 700, 1000	2–5	100, 200, 240	11810	[41–46]
TIMEPIX	IBM 0.25µm	256×256	55×55	P or N	300	2–5	200	11810	[45–49]
MEDIPIX 3 (FP)[5]	IBM 0.13µm	256×256	55×55	P or N	300	13	90	4096, 16777216	[32, 50–52]
MEDIPIX 3 (SM)[6]	IBM 0.13µm	128×128	110×110	P or N	300	13	90	-	[32, 50–52]
TIMEPIX 3	IBM 0.13µm	256×256	55×55	P or N	300	13	90	-	[53, 54]
PILATUS 1	UMC 0.25µm	60×97	172×172	P	320	8	80	1048574	[55]
PILATUS 2	UMC 0.25µm	60×97	172×172	P	320	8	80	1048574	[56]
PILATUS 3	UMC 0.25µm	60×97	172×172	P	450	8	80	1048574	[56–58]
EIGER	UMC 0.25µm	256×256	75×75	N	320	-	-	4096	[59–61]
XPAD 2	AMS 0.8µm	25×24	330×330	P or N	500	-	200	65536	[62–64]
XPAD 3	IBM 0.25µm	120×80	130×130	P or N	500	-	200	4096	[65–69]
PIXIE III	0.16µm	512×402	62×62	-	750	-	-	32768	[70–73]

Table 3.2: Performances of counting hybrid pixel detectors

Name	Energy thresholds	Peaking time [ns]	ENC [e$^-$]	Threshold dispersion [e$^-$]	Energy resolution (FWHM)	Max count rates [Mcps/mm^2]	Spatial resolution
MEDIPIX 1	1	150 ns	142	350	1.15 keV at 5.9 keV	69	1.81 lp/mm
MEDIPIX 2	2	150 ns	110	95	1.6 keV at 8 keV	330	8.5 lp/mm
TIMEPIX	13 bits	40 ns	100	35	< 5 % above 3.6 keV	-	80 µm FWHM
MEDIPIX 3 (FP-SPM)[7]	2	120 ns	60	55	1.37 keV at 10 keV	826	10 lp/mm
MEDIPIX 3 (FP-CSM)[8]	2	120 ns	130	110	2.03 keV at 10 keV	164	-
MEDIPIX 3 (SM-SPM)	8	120 ns	80	-	1.43 keV at 10 keV	376	-
MEDIPIX 3 (SM-CSM)	8	120 ns	130	-	-	28	-
TIMEPIX 3	10 bits	30 ns	62	35	2.58 keV at 10.5 keV	0.43	-
PILATUS 1	1	110 ns	123	16	863 eV at 8 keV	8	2.91 lp/mm
PILATUS 2	1	110 ns	123	16	1 keV at 8 keV	203	-
PILATUS 3	1	110 ns	123	16	1 keV at 8 keV	507	PSF: 1 pixel FWHM
EIGER	1	30 ns	121	20	-	747	-
XPAD 2	2	-	175	75	1.5 keV above 8 keV	22.95	-
XPAD 3	2	150 ns	127	57	960 eV at 8 keV	118	4.4 lp/mm
PIXIE III	2	125 ns	50	30	1.31 keV at 20 keV	260	8 lp/mm

Table 3.3: Characteristics of integrating hybrid pixel detectors

Name	Technology	Matrix size	Pitch [µm^2]	Si type	Thickness [µm]	Resistivity [kΩ cm]	Depletion voltage [V]	ADC	References
CSPAD	TSMC 0.25µm	185 × 194	110 × 110	N	500	5	120	Single slope 14b	[74–78]
KECKPAD	TSMC 0.25µm	128 × 128	150 × 150	N	500	7.5	250	Off chip	[79–83]
MMPAD	TSMC 0.18µm	128 × 128	150 × 150	N	500	-	150	Off chip[9]	[84–86]
ePix100	TSMC 0.25µm	352 × 384	50 × 50	-	-	-	-	Off chip[10]	[87–91]
ePix10k	TSMC 0.25µm	176 × 192	100 × 100	-	-	-	-	Off chip[10]	[87–91]
JUNGFRAU	UMC 0.11µm	256 × 256	75 × 75	N	320	-	120	Off chip	[92–96]
JUNGFRAU 0.4 (low noise)	UMC 0.11µm	48 × 48	75 × 75	N	500	-	240	Off chip	[97]
MÖNCH	UMC 0.11µm	400 × 400	25 × 25	-	320	-	70	On chip	[33, 98–101]
AGIPD	IBM 0.13µm	64 × 64	200 × 200	-	300–500	-	120	Off chip	[102–106]
LPD	-	128 × 32	500 × 500	N	500	-	300	SAR 12b	[8, 107–110]
DSSC	DEPFET + IBM 0.13µm	64 × 64	204 × 236[11]	N	450	-	-	Single slope 8b	[111–114]

Table 3.4: Performances of integrating hybrid pixel detectors

Name	Number of gains	ENC [e$^-$]	Saturation	Energy resolution (FWHM)	Spatial resolution	Frames stored	FPS
CSPAD	2	350 (HG[12]), 1000 (LG[13])	840 ke$^-$ (HG), 5.97 Me$^-$ (LG)	-	-	1	120
KECKPAD	2	1550 (HG)	2.65 Me$^-$ (HG), 17.68 Me$^-$ (LG)	-	-	1	10000
MMPAD[14]	2	394 (HG), 1443 (LG)	86.6 Ge$^-$	-	21.9 µm FWHM	1	1160
ePix100	1	50	220 ke$^-$	-	-	1	500
ePix10k	2	176 (HG), 3000 (LG)	220 ke$^-$ (HG), 22.1 ke$^-$ (LG)	-	-	1	1000
JUNGFRAU	3+1[15]	53 (HG0[16]), 83 (HG), 1105 (MG[17]), 13260 (LG)	33 ke$^-$ (HG/HG0), 2.32 Me$^-$ (MG), 36.5 Me$^-$ (LG)		61 µm FWHM	16	2400
JUNGFRAU 0.4	1	27	13.8 ke$^-$	400 eV at 1.2 keV	1–5 µm	1	500000
MÖNCH	2	37	14.9 ke$^-$	-	1–5 µm	1	6000
AGIPD	3	363	247 ke$^-$ (HG), 6.85 Me$^-$ (MG), 30.5 Me$^-$ (LG)	-	-	352	4.5 M
LPD	3	1900	>165.75 Me$^-$	-	-	512	4.5 M
DSSC	Internal signal compression	12	6.63 Me$^-$	160 eV at 5.9 keV	-	800	4.5 M

Table 3.5: Characteristics of monolithic passive pixel detectors

Name	Technology	Matrix size	Pitch [µm^2]	Si type	Thickness [µm]	Resistivity [kΩ cm]	Depletion voltage [V]	References
XAMPS[18]	JFET technology (sensitive) TSMC 0.25µm (ASIC)	$n \times n$ (sensitive), 16×16 (ASIC), n=16, 32, 64, 128, 256	90×90	N	400	4–6	110	[115–118]
MOSCCD[19]	-	4000×4000	24×24	P	600	11.4	155 (≈430 µm depleted)	[119]
FASTCCD[19]	0.25 µm (readout chip), 0.35 µm HV-CMOS (Voltage buffer)	1920×960 (Frame store), 1920×1920 (Full frame)	30×30	-	300	-	-	[120, 121]
MPCCD[19]	-	1024×512	50×50	P	Epi 50	-	10.5 (40 µm depleted)	[122, 123]
pnCCD[19]1	-	264×264 264×66 (window mode)	48×48	-	450	-	-	[124]
pnCCD[19]2 (VERITAS)	AMS 0.35 µm	128×256	48×48	-	-	-	-	[125]
pnCCD[19]3 (CAMEX)	-	384×384	75×75	N	450	-	-	[126]

Table 3.6: Performances of monolithic passive pixel detectors

Name	ENC [e$^-$]	Saturation	Energy resolution (FWHM)	Spatial resolution	Operation temperature [K]	FPS
XAMPS	650	7000×8 keV	-	90 µm	-	3900
MOSCCD	373	373×13.5 keV	-	40 µm FWHM at 8 keV 22 µm FWHM at 17.5 keV	205	1.6–3.2
FASTCCD	25	900 ke$^-$	589 eV at 21.99 keV	5 µm FWHM	223.15	200
MPCCD	300	1200×6 keV	-	3.3 µm FWHM	238.15	30
pnCCD 1	3.7	-	-	1 µm FWHM	243.15	1200 (window mode)
pnCCD 2 (VERITAS)	3.3	-	142 eV at 5.9 keV	-	213.15	1000
pnCCD 3 (CAMEX)	8.2	5.6–1433.6 eV	195 keV at 8.041 keV	-	213.15	<200

Table 3.7: Characteristics of monolithic active pixel detectors

Name	Technology	Matrix size	Pitch [µm^2]	Si type	Thickness [µm]	Resistivity [kΩ cm]	Depletion voltage [V]	References
LDRD2-RH	AMS 0.35µm	96×96	20×20 (subdivised in $2 \times (20 \times 10)$)	N	Epi 14	-	-	[127, 128]
TEAM	AMS 0.35µm	1024×1024	9.5×9.5	N	Epi 14	-	-	[129, 130]
LePix	IBM 0.09µm	32×32	50×50	P	300 (thinned to 50)	>0.4	<100	[131–135]
PERCIVAL	TowerJazz 0.18µm	1408×1484 (2 Mpix) 3520×3710 (10 Mpix) 160×210 (Prototype)	27×27 25×25 (Prototype)	P	Epi 5 or 18 (thinned to 12 µm)	>1	-	[136, 137]
LF-MONOPIX	LFoundry 0.15µm	36×129	250×50	P	-	>2	100–280[20]	[138, 139]
ALPIDE	TowerJazz 0.18µm	512×1024	29.24×26.88	P	Epi 18–50	1–8	6	[140, 141]
INVESTIGATOR	TowerJazz 0.18µm[21]	$134 \times (8 \times 8)$	25×25, 28×28, 30×30, 50×50	P	Epi 25	>1	6	[36]
MIMOSA-5	AMS 0.6µm	1020×1024	17×17	P	Epi 14	-	-	[142, 143]
MIMOSA-18	AMS 0.35µm	512×512	10×10	P	Epi 14	>0.4	3.3	[144]
MIMOSA-22	AMS 0.35µm	576×136	18.4×18.4	P	Epi 14	>0.4	-	[145, 146]
MIMOSA-26	AMS 0.35µm	576×1172	18.4×18.4	P	Epi 14	>0.4	-	[146–148]
MIMOSA-28	AMS 0.35µm	928×960	20.7×20.7	P	Epi 14	>0.4	-	[1]
MISTRAL, ASTRAL[22]	TowerJazz 0.18µm	-	22×33	P	Epi 18	>1	-	[149, 150]

Table 3.8: Performances of monolithic active pixel detectors

Name	ENC [e$^-$]	Saturation	Energy resolution (FWHM)	Spatial resolution	FPS
LDRD2-RH	67	-	-	8.1 µm FWHM (10 µm pixel) 10.9 µm FWHM (20 µm pixel)	-
TEAM	28	-	-	2.72 µm FWHM	380000
LePix	28	-	340 eV at 5.9 keV	-	200000
PERCIVAL	14	3.94 Me$^-$	-	20–30 lp/mm	1–120
LF-MONOPIX	191 (+ 27 from threshold dispersion)	-	-	-	-
ALPIDE	10	-	-	5 µm	33333[23]
INVESTIGATOR	-	-	200 eV at 5.9 keV	9 µm	-
MIMOSA-5	20.74	-	-	1.7µm	125
MIMOSA-18	10	-	-	0.95 µm	250
MIMOSA-22	10–14	-	-	3.5 µm	10000
MIMOSA-26	14	-	-	5.3 µm	8680
MIMOSA-28	11.6	-	-	3.5–4 µm	5388
MISTRAL/ASTRAL	12–25	-	-	5 µm	33333–50000

[5]Fine Pitch Mode
[6]Spectroscopic Mode
[7]Single Pixel Mode
[8]Charge Sharing Mode
[9]Integrated in final detector
[10]Sigma Delta in final detector
[11]Hexagonal
[12]High-Gain
[13]Low-Gain
[14]Mixed-mode: integration and counting in parallel. Achieves counting up to 4444 Mcps/mm^2
[15]High gain can be switched to very high gain
[16]Gain>HG
[17]Medium-Gain
[18]Passive Pixel Detector
[19]CCD
[20]100 µm depleted
[21]CERN modified process
[22]Performances from multiple individual test chips: MIMOSA32, MIMOSA34, SUZE, AROM 0
[23]Required, achieved by asynchronous readout and priority encoders

Part II

Characterization of a Depleted CMOS Pixel Sensor

Chapter 4

Expectation for Depletion Depth in CPS

With the possibility to produce CMOS sensors with dedicated design kits on high resistivity substrates, CPS have become attractive for the detection of soft X-rays with small pixel pitch. To achieve low noise operation, good quantum efficiency performance (which requires minimum substrate thicknesses of a few tens of micrometers), and good resolution (both spatial and energy), the dedicated CPS must be depleted.

A method to apply the depletion voltage from the frontside of the sensor is proposed. The sensitive volume is biased from the top of the sensor through the collecting diode using a forward bias diode. In a standard pixel architecture (e.g. 3-T pixel), the amplifier is DC-coupled to the collecting node. With this configuration, the breakdown limit of the technology imposes the maximum bias voltage that can be applied on the input node. Here, to allow higher bias voltages, the readout chain is AC-coupled. The readout chain can be composed of transistor whose breakdown limit is lower than the bias applied on the collecting node and does not require any process modification. A schematic of an AC-coupled collecting node is shown in figure 4.1.

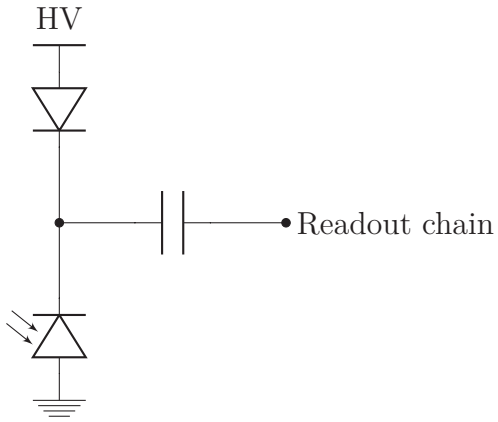

Figure 4.1: Schematic of the input node for the application of the depletion voltage from the frontside of a CPS. The bias is applied to the collecting diode through a forward bias diode. The readout chain is AC-coupled to the collection node

Since the bias is applied from the top of the sensor, there is no need for a backside

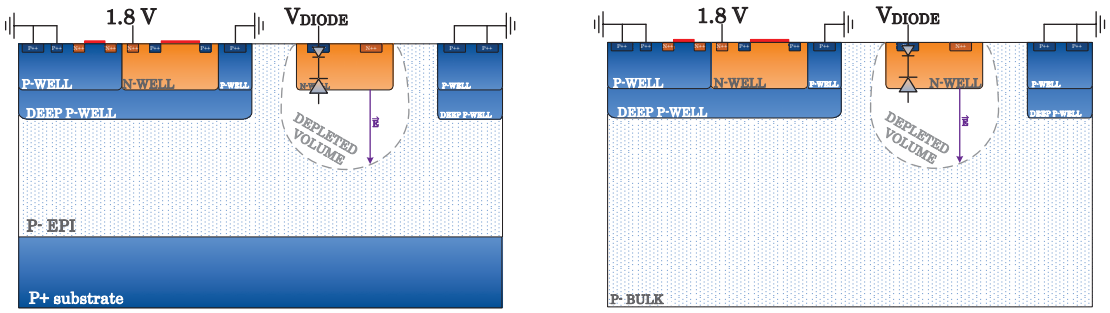

(a) (b)

Figure 4.2: Cross section schematic of a depleted pixel with frontside biasing on an epitaxial layer (a), and on a bulk substrate (b)

contact, allowing the minimization of the entrance window with backside illumination. A cross-section illustration of a pixel with frontside biasing in each type of susbtrate is shown in figure 4.2.
The collecting diode composed of a N-well is biased through a P++ implant forming a forward bias diode structure. The depleted volume is formed around the diode and is extending in the sensitive volume, creating an electric field.

The calculations for the depletion depth reached in a pn-junction (equation 2.52) is only valid for a planar junction. Here the area of the diode in CPS is small with respect to the pixel area resulting in invalid conditions for the application of the equation.

An equation based on the same assumptions but with point-like diodes must be evaluated. The expression results must be compared with simulations to assess its validity. The junction parameters to evaluate the depth reached with each methods are based on an existing sensor: PIPPER-2.

4.1 The PIPPER-2 Sensor

PIPPER-2 (*P*ixelated sensor for *I*onizing *P*article and *P*hotons *E*nergy *R*esolved detection) is a monolithic active pixel sensor aiming to study charge collection by drift using depletion with the bias applied from the top side of the sensor.

It was designed by Maciej Kachel in the microelectronics group at IPHC in 2015 in *TowerJazz* 180 nm CMOS Image Sensor process. The prototype was fabricated on two different substrates: an 18 µm high resistivity (>1 kΩ cm) p-type epitaxial layer dubbed HR18 in the following, and a high resistivity (>600 Ω cm) p-type Czochralski, noted CZ, substrate thinned to 280 µm at the foundry.

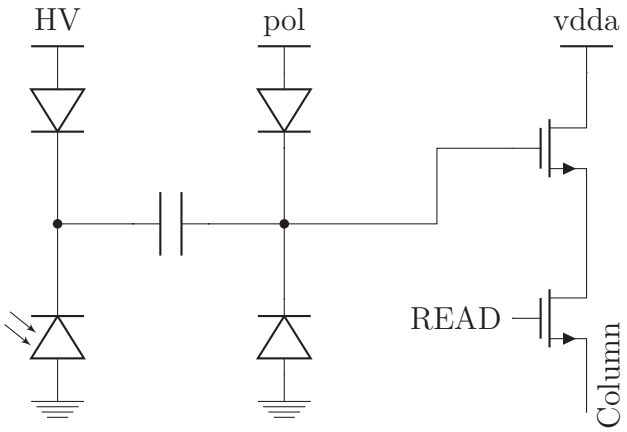

Figure 4.3: Schematic of the PIPPER-2 pixel. The substrate is biased from the top through a forward bias diode and the collecting diode. The collection node is AC-coupled to a source follower. A set of diodes after the coupling at the input of the amplifier is used to set the DC point.

A few CZ sensors have then been thinned to 50 µm which represents ≈ 40 µm thick sensitive volume. The remaining 10 µm is occupied by the metallization layers of the CMOS process. The backside of the thinned sensors is passivated through the PULSION® process [151], allowing to keep a thin entrance window (≈20–50 nm).

This sensor prototype is composed of four independant submatrices each organized in 8 columns and 128 rows of square pixels with 22 µm pitch. The submatrix selected for acquisition is read out using rolling-shutter, and each column is independently connected to an output of the sensor. Three submatrices are designed to explore collection performance with various collecting diode configuration while the fourth submatrix embeds an amplifier design that will not be discussed. The diode configurations used for the depletion studies are presented in table 4.1. Each diode is AC-coupled to a source follower using a 21 fF fringe capacitor which has been preferred over MIM capacitors because of better leakage current performance, and higher breakdown voltage.

The DC point after the coupling is set using a set of diodes that are isolated from the sensitive volume with deep P-wells. A pixel version with a transistor used as a switch to set the DC point has been developed in a most recent prototype: PIPPER-3. The architecture and performance of the latter will not be discussed here.

A schematic of the pixel is shown in figure 4.3. The further studies will focus on the submatrix 1 which features a 5 µm round N-well acting as the collecting diode.

Table 4.1: Summary of the PIPPER-2 pixel parameters variants for depletion studies

Submatrix	Number of diodes	Diameter [μm]	Coupling capacitance [fF]
1	1	5	21
2	1	3	21
3	4	4	4×5.7

4.2 Analytical Approximation of the Depletion Depth in a Point-like Diode

4.2.1 Adaptation For Small Diodes

The depletion depth (equation 2.52) is given assuming that the junction area represents an infinite area of the semiconductor (planar device) which is not valid in our biasing scheme (see figure 4.2). The area of the collection node in a pixel is indeed much smaller than the area of the pixel itself. For instance, the area covered by a 5 µm diameter round diode represents only 4.06 % of the total area of a 22 µm pitch squared pixel. An analytic equation for small diodes with respect to the pitch can be derived under simplification assumptions. For instance, J. Lincelles [152] considered a 3-dimensional ellipsoid, but the study is limited to low voltages.

Here, a simplified geometry of a pixel is assumed to estimate the depletion depth in such structures. A highly doped N-well represented by a n-sides prism of radius r and depth z sits in a high resistivity p type substrate ($N_D \gg N_A$). No additional wells representing the CMOS process is present within the substrate. A non-conductive layer of SiO_2 is on the top of the pixel where any effect is neglected. The geometry is displayed in figure 4.4.

The volume of the collecting diode $\mathcal{V}_{diode}$ and the junction area $\mathcal{A}_{PN}$ can be computed with respect to the three parameters r, z, and n depending on the shape assumed for the diode. For a n-sides prism (figure 4.5a), we get:

$$\mathcal{V}_{diode} = nzr^2 \tan\frac{\pi}{n} \tag{4.1}$$

$$\mathcal{A}_{PN} = nr \tan\frac{\pi}{n}(r + 2z) \tag{4.2}$$

Thus, the volumes and area for a squared diode, n=4, (figure 4.5b):

$$\mathcal{V}_{diode}(n = 4) = (2r)^2 z \tag{4.3}$$

$$\mathcal{A}_{PN}(n = 4) = 2r(2r + 4z) \tag{4.4}$$

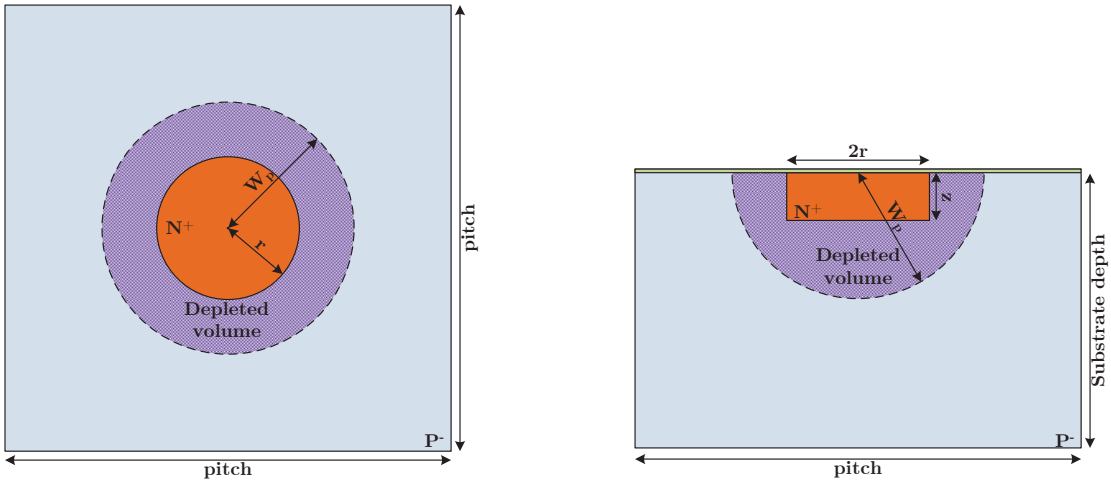

(a) (b)

Figure 4.4: Schematic of the simplified structure for analytical approximation of the depletion depth in a point like diode. (a) Top view. (b) Side view.

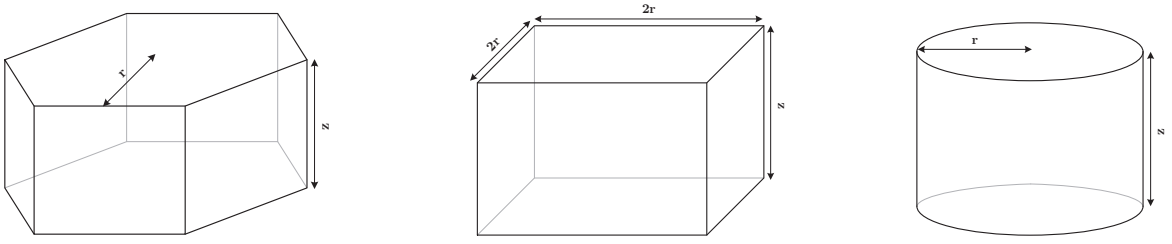

(a) $n = 6$ (b) $n = 4$ (c) $n \to \infty$

Figure 4.5: Geometry of diodes for the analytical approximation of the depletion depth. The diode is represented by a n-sides prism with $n \to \infty$ resulting in a cylinder.

In a round diode, $n \to \infty$, (figure 4.5c):

$$\mathcal{V}_{diode}(n \to \infty) = \pi r^2 z \tag{4.5}$$

$$\mathcal{A}_{PN}(n \to \infty) = \pi r(2z + r) \tag{4.6}$$

Next, the same development as in the unidimensional case is followed (section 2.2.4).

On each side of the junction, the amount of charges in a depleted volume $\mathcal{V}$ is:

$$\begin{aligned} Q &= \rho \mathcal{V}_{depl} \\ &= qN_{eff}\mathcal{V}_{depl} \end{aligned} \tag{4.7}$$

Inside the N-well where there is an excess of donors, $N_{eff} = N_D$ and, with W_N the depletion depth over the contact area of the junction $\mathcal{A}_{PN}$ the depleted volume is:

$$\mathcal{V}_N = \mathcal{A}_{PN} W_N \tag{4.8}$$

Thus the amount of charges on the n side of the junction is:

$$Q_N = qN_D \mathcal{A}_{PN} W_N \tag{4.9}$$

On this side of the junction, the thickness of the depletion depth is given in [22] and expressed by:

$$W_N = \sqrt{\frac{2\epsilon_{Si}}{q}\frac{N_A}{N_D}\left(\frac{1}{N_A + N_D}\right)(V_d + |V|)} \tag{4.10}$$

The amount of charges can thus be rewritten:

$$\begin{aligned} Q_N &= qN_D \mathcal{A}_{PN}\sqrt{\frac{2\epsilon_{Si}}{q}\frac{N_A}{N_D}\left(\frac{1}{N_A + N_D}\right)(V_d + |V|)} \\ &= \sqrt{2\epsilon_{Si} q \left(\frac{N_A N_D}{N_A + N_D}\right)\mathcal{A}_{PN}^2 (V_d + |V|)} \end{aligned} \tag{4.11}$$

With the N implant sitting in the P type substrate, one can assume a hemispherical extension of the depleted volume. This space charge volume with the volume of the N-well, $\mathcal{V}_{diode}$, removed can be expressed with:

$$\mathcal{V}_P = \frac{2}{3}\pi W_P^3 - \mathcal{V}_{diode} \tag{4.12}$$

Thus, the amount of charges in the depleted volume on the P side, where there is an

excess of acceptors ($N_{eff} = N_A$), is:

$$\begin{aligned} Q_p &= qN_A\mathcal{V}_P \\ &= qN_A\left(\frac{2}{3}\pi W_P^3 - \mathcal{V}_{diode}\right) \end{aligned} \tag{4.13}$$

The amount of charges from each side of the pn junction are equal:

$$Q_P = Q_N \tag{4.14}$$

$$qN_A\left(\frac{2}{3}\pi W_P^3 - \mathcal{V}_{diode}\right) = \sqrt{2\epsilon_{Si}q\left(\frac{N_A N_D}{N_A + N_D}\right)\mathcal{A}_{PN}^2\left(V_d + |V|\right)} \tag{4.15}$$

By considering a highly doped N well in a low doped P substrate implies $N_D \gg N_A$, and $(N_A + N_D) \approx N_d$, which allows to express the depletion radius for a small collecting diode with respect to the pixel pitch:

$$W_P = \sqrt[3]{\frac{3}{2\pi}\left(\sqrt{\frac{2\epsilon_{Si}}{qN_A}\mathcal{A}_{PN}^2\left(V_d + |V|\right)} + \mathcal{V}_{diode}\right)} \tag{4.16}$$

4.2.2 Merging of the Depleted Volume with the Neighbours

The previous approximation (equation 4.16) of the depletion depth does not take the pitch into account. If the distance of the depleted volume becomes greater than half the pitch ($W_p > {}^{pitch}/_2$) the space charge will merge with the ones from the four adjacent pixels. Also, if the depth becomes greater than half the diagonal of the pixel area ($W_p > \sqrt{{}^{\text{pitch}^2}/_2}$), the depleted volume will merge with the eight surrounding pixels. If the depleted volume of two adjacent pixels are shared, the equality of charges condition is no longer respected.

The part of the depleted volume extending to the neighbouring pixel can be estimated as two spherical caps (four halves). With a, the radius of the base and h the height of the spherical cap shown in figure 4.6, from the volume of a spherical cap[153], the volume shared is given by:

$$\mathcal{V}_{merged} = \frac{2}{3}\pi h^2(3W_P - h) \tag{4.17}$$

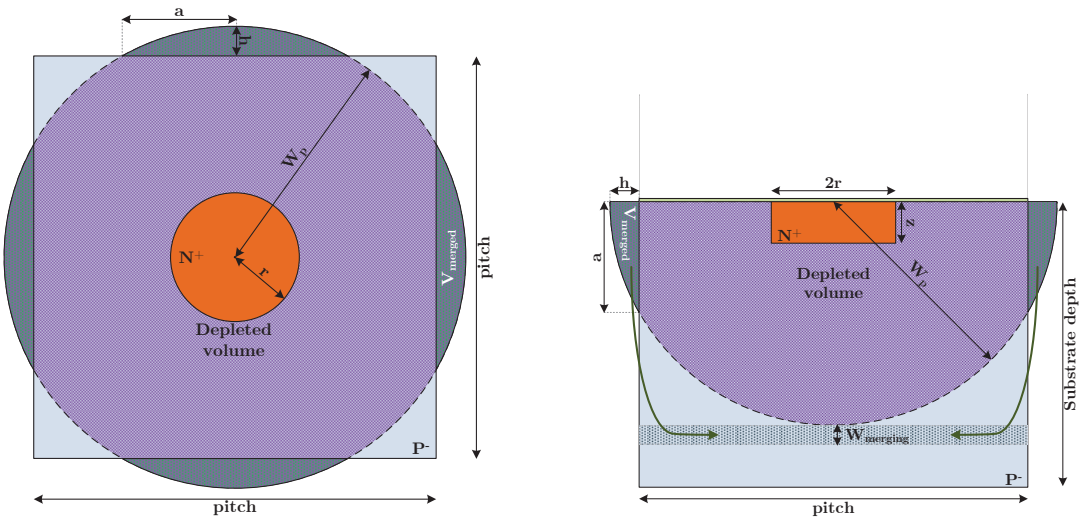

(a) (b)

Figure 4.6: Schematic of the simplified structure for analytical approximation of the depletion depth in a point like diode. (a) Top view. (b) Side view.

With a and h expressed by:

$$\begin{aligned} h &= W_P - \frac{\text{pitch}}{2} \\ a &= \sqrt{h(2W_P - h)} \end{aligned} \tag{4.18}$$

To evaluate the depth added, the merged volume is added as a cuboid tangent to the bottom of the depletion hemisphere. The added volume is not wrapped around the hemisphere and, thus only the tangent point can be used to evaluate the total depth. The depth is $W_{P_{TOT}} = W_p + W_{merging}$, the latter being given by:

$$W_{merging} = \frac{\mathcal{V}_{merged}}{\text{pitch}^2} \tag{4.19}$$

The radius of curvature increases with the extension of the total depletion depth thus flattening the bottom of the total volume.

4.2.3 Comparison of Analytical Approximations of the Depletion Depth

The analytical equation of the depletion depth for a planar device and for a point like diode are plotted in figure 4.7 for two values of resistivity in the p-type substrate, respectively 10 Ω cm, and 2 kΩ cm. The planar equation does not take any geometry into account while the proposed equations in the previous sections do. For this figure, the considered

pixel has a 22 µm pitch and a 5 µm diameter round n-well[1] sitting in the p-type substrate.

In a low resistivity substrate, the approximated depth of the depleted volume at the center of a pixel with a point like diode is greater than in planar devices. The value of the depth reaches very modest values (below 10 µm) and is more or less constant with the increase of the biasing voltage, and for high biasing values, the approximation for each device is almost the same.

With a high resistivity substrate, the planar approximation reaches a 100 µm thick depleted volume while the point like diode approximation only reaches $\approx$ 20 µm, up to $\approx$ 30 µm by considering the pitch of the pixel and the merging of the volumes with the adjacent pixels.

This result strongly points to the limitation of the strategy to deplete the volume through small diodes and already indicates that thick depletion volumes will probably stay out of reach. However, depletion depths of few tens of micrometres seem achievable, with a strong dependence on the resistivity of the p-type substrate.

To confirm the validity of these approximations, TCAD simulations are conducted with the same considerations of structure (i.e. single implant in a substrate), and with realistic structures, based on the foundry documentation.

4.3 TCAD Simulations

Finite elements simulations were performed using the *Synopsis Sentaurus TCAD*[2] tools. These tools allow exploration of processes and predictions of the performance of a structure to determine their capabilities without having to produce a prototype.

To explore a structure, such as a pixel, a 2D or a 3D model must be first implemented to represent the pixel structure (dimensions, relative position of structures, doping profiles, contacts). A mesh for the simulation is created in the structure and can be refined in the regions of interest, such as the pn junction formed by the collecting diode in the substrate.

Simulations are performed with various controlled input parameters such as the resistivity (doping profile), the bias applied, pitch, thickness of the sensitive volume etc.
Once simulated, a wide range of results is available for the evaluation of the structure (electron concentration, hole concentration, electric field, space charge, potential etc.)

[1] The thickness is taken from the *TowerJazz* datasheets.
[2] https://www.synopsys.com/silicon/tcad.html

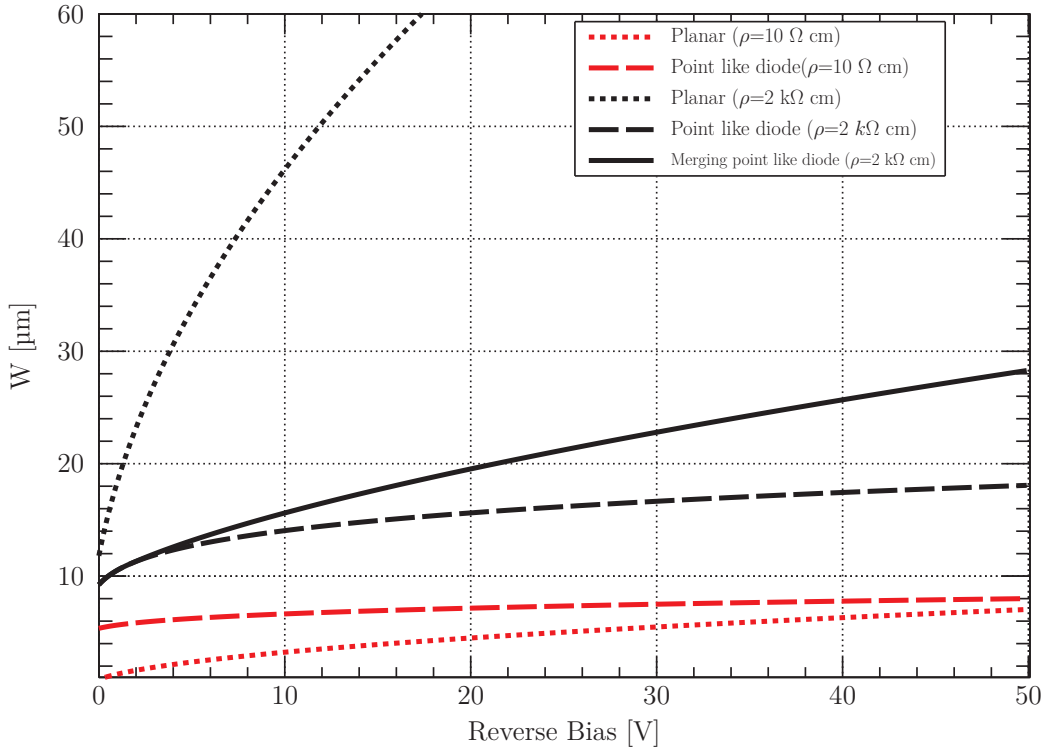

Figure 4.7: Analytical estimation of the depletion depth using the planar equation (dashed line, equation 2.52), the point like diode equation (equation 4.16), and the point like diode equation with merging of the volume from the adjacent pixels (equation 4.19) for two resistivities: 10 Ω cm and 2 kΩ cm There is no merging observed with the low resistivity substrate.

that can be probed at will.

4.3.1 Model Implementation

Two different models have been implemented to explore the possibilities of model simplifications to reduce the meshing and simulation times.

Simplified Model

The simplified model represents the simplified geometry previously presented for the analytical approximations. An uniformly doped round diode represented by a cylindrical n-well sits at the center of the top of a uniformly doped p-type substrate (figure 4.8a). When an abrupt junction is created, TCAD generates a very steep gradient to facilitate the continuity during the simulation (figure 4.8b).

The diameter of the cylinder is 5 µm and the thickness is extracted from the doping profiles of the implants from the foundry documentation. The pixel pitch is 22 µm and the total thickness of the substrate is 60 µm to limit the amount of meshing nodes with acceptable mesh refinements within the volume.

On the top of the pixel area, a SiO_2 layer is added with an opening at the middle for the biasing contact. The ground contact is set at the bottom of the substrate. The 3 dimensional structure is cut along the z-axis to keep a quarter of the initial structure to allow finer meshing. The mesh is set finer around the diode area to facilitate the first points. During simulations, the interfaces are considered as mirrors, which results in same outcomes than for a full pixel structure, and even as in an infinite matrix of pixels.

Realistic Model

The realistic model design features a centered 5 μm diameter round N-well with a doping profile extracted from the foundry's documentation. This collecting diode sits directly in the P– epitaxial layer or Czochralski substrate. Deep P-wells are representing the CMOS structures isolated from the detection volume.

The forward bias diode composed of a P++ implant placed in the N-well through the oxide with the bias contact is implemented. A circular P++ implant also sits in the deep P-wells structure through the oxide with the ground contact. The doping profiles considered are taken from the *TowerJazz* process documentation.

A measured doping profile shown in figure 4.9 (the exact concentrations are not displayed) is used for the generation of the realistic HR18 model.

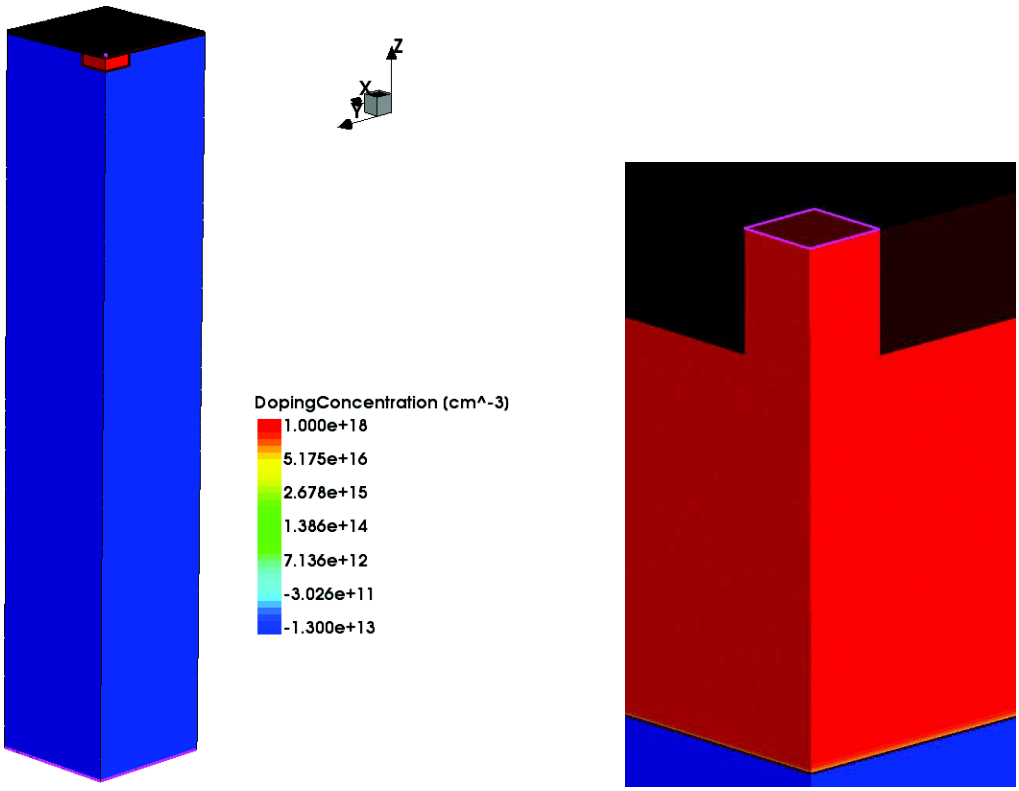

(a) (b)

Figure 4.8: Simplified structure for TCAD simulations. (a) Quarter of a 22 µm pitch pixel with a 5 µm round diode visible on the top. (b) Zoom on the implantation area at the top center of the pixel. The junction assumed as abrupt has a very steep gradient generated by the software. The bias connection is on the top through the oxide and is delimited by the pink square.

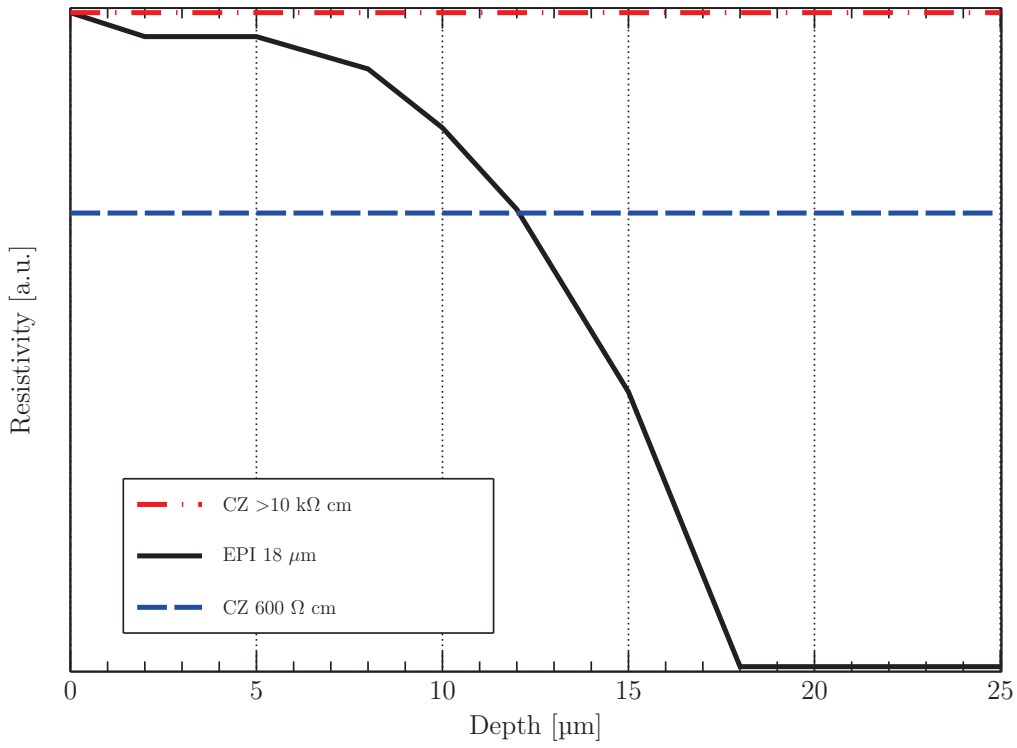

Figure 4.9: Shape of the doping profile of the 18 µm thick epitaxial layer (HR18): black solid line. Examples of two different constant doping profiles applied for the CZ model with resistivities of 600 Ω cm (blue dashed line) and above 10 kΩ cm, corresponding to the maximum value set in the HR18 model (red dashed-dotted line).

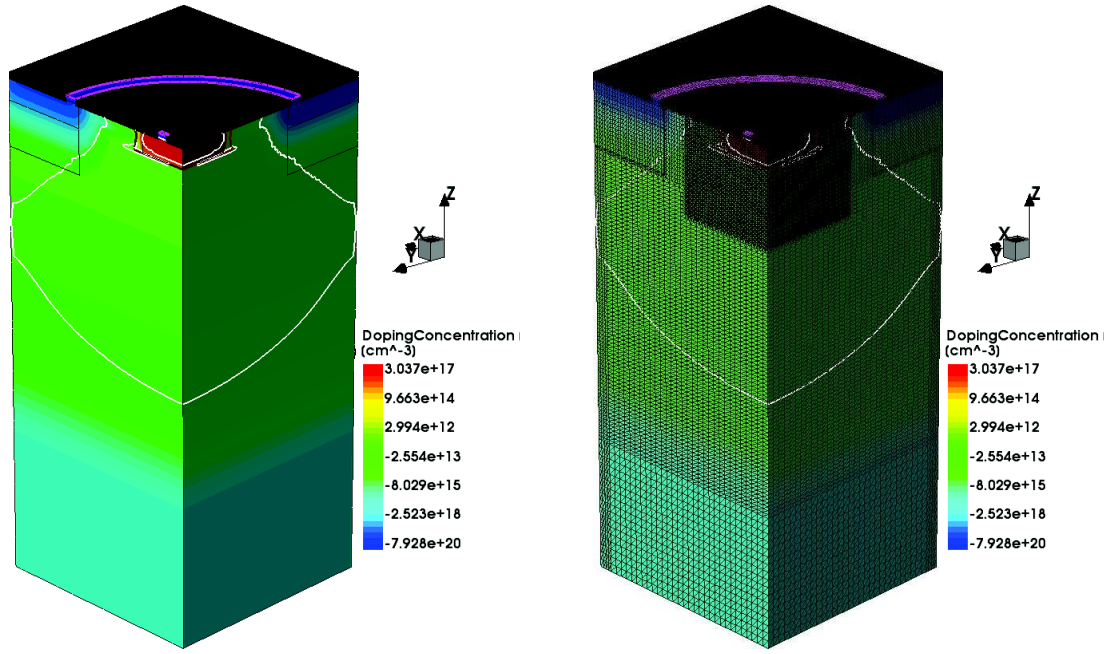

(a) (b)

Figure 4.10: Realistic HR18 structure for TCAD simulation biased at 20 V. Both the depletion voltage and the ground are set from the top of the pixel. (b) Meshing of the structure. The structure is thinner around the interfaces and especially around the n-well. The displayed color scale represents the doping concentration. The p-type wells are shown in dark blue while the collecting diode, being a n-well, is shown in red. The low doped p-type substrate is in green and becoming more p with the depth.

The maximum value of the resistivity is above 10 kΩ cm at the top of the sensitive volume. The value decreases to reach the 1 kΩ cm limit at ≈11 µm and merges to the p-type substrate at 18 µm. Four different constant doping profiles are used for the generation of the realistic CZ model. The corresponding resistivities are 600 Ω cm (minimum guaranteed by the manufacturer of the wafer), 1 kΩ cm, 2 kΩ cm, and 10 kΩ cm (exact value of the maximum of the HR18 doping profile). The total thickness of the CZ model is 60 µm.

Figure 4.10a shows the described architecture with the HR18 configuration simulated for a biasing voltage of 20 V. The same structure with the meshing is presented in the figure 4.10b. The mesh is finer around the diode and on the interfaces. The border of the depletion volume (read below for the definition) is shown by the white line which is automatically calculated and shown by TCAD.

4.3.2 Depletion Depth Measurement Methods

A single quasistationary simulation is carried out for each structure where the biasing voltage is progressively increased up to 45 V. The results of the simulated 3-dimensional

structure are saved when biased at 2, 4, 6, 8, 10, 15, 20, 30, 40, and 45 V. Post-simulation analysis allows the extraction of the depletion depth.

Various parameters are available to be plotted in the TCAD environment. The Q_{SC} variable echoes the equation 2.37 and is given by [154]:

$$Q_{SC} = (p - n - N_D - N_A) + \frac{\rho_{trap}}{q} \tag{4.20}$$

The space charge along the z-axis for a section in the middle of a simulated simplified structure in a 600 Ω cm substrate biased at 45 V is shown in figure 4.11b. In the depleted volume, the value of Q_{SC} equals the doping concentration of the substrate.

The depleted zone can be extracted from the doping profile by writing, with N_{eff} the effective doping, in the p-type region where $N_{eff} = N_A$:

$$V_D = \frac{|Q_{SC} - N_{eff}|}{|N_{eff}|} \approx \frac{|Q_{SC} - N_A|}{|N_A|} \tag{4.21}$$

The result with the Q_{SC} input of figure 4.11b is shown in figure 4.11c. At the diode side, the boundary between depleted and undepleted region is sharp while a slope is visible on the substrate side spreading over almost 10 µm.

To make the evaluation of the boundary more precise, the slope becomes steeper by considering only the values above 95 % of V_D and given by:

$$D = -0.5\,(1 - \mathrm{erf}\,[(V_D - 0.05) \times 100]) \tag{4.22}$$

The outcome is shown in figure 4.11d, where the depleted region is more precisely defined. The value extracted at $D = -0.5$ on the substrate side of the step is the depth reached by the depleted volume at the center of the pixel area, and is very close to the value displayed by TCAD.

A more direct method consists of probing the hole density curve along the z-axis at the center of the pixel area (figure 4.11a). On the p-side region, outside the depleted volume, the hole density equals the density of acceptors. Inside the depleted region, the hole density is much smaller than the density of acceptors. Thus, the limit can be set to a proportion of N_A.

The result of probing using both methods is presented in figure 4.12. The limits used for the hole concentration method are $0.1 \times N_A$, and $0.05 \times N_A$. The latter gives similar results than the depletion method while the higher limit tends to be overestimating the achieved depth.

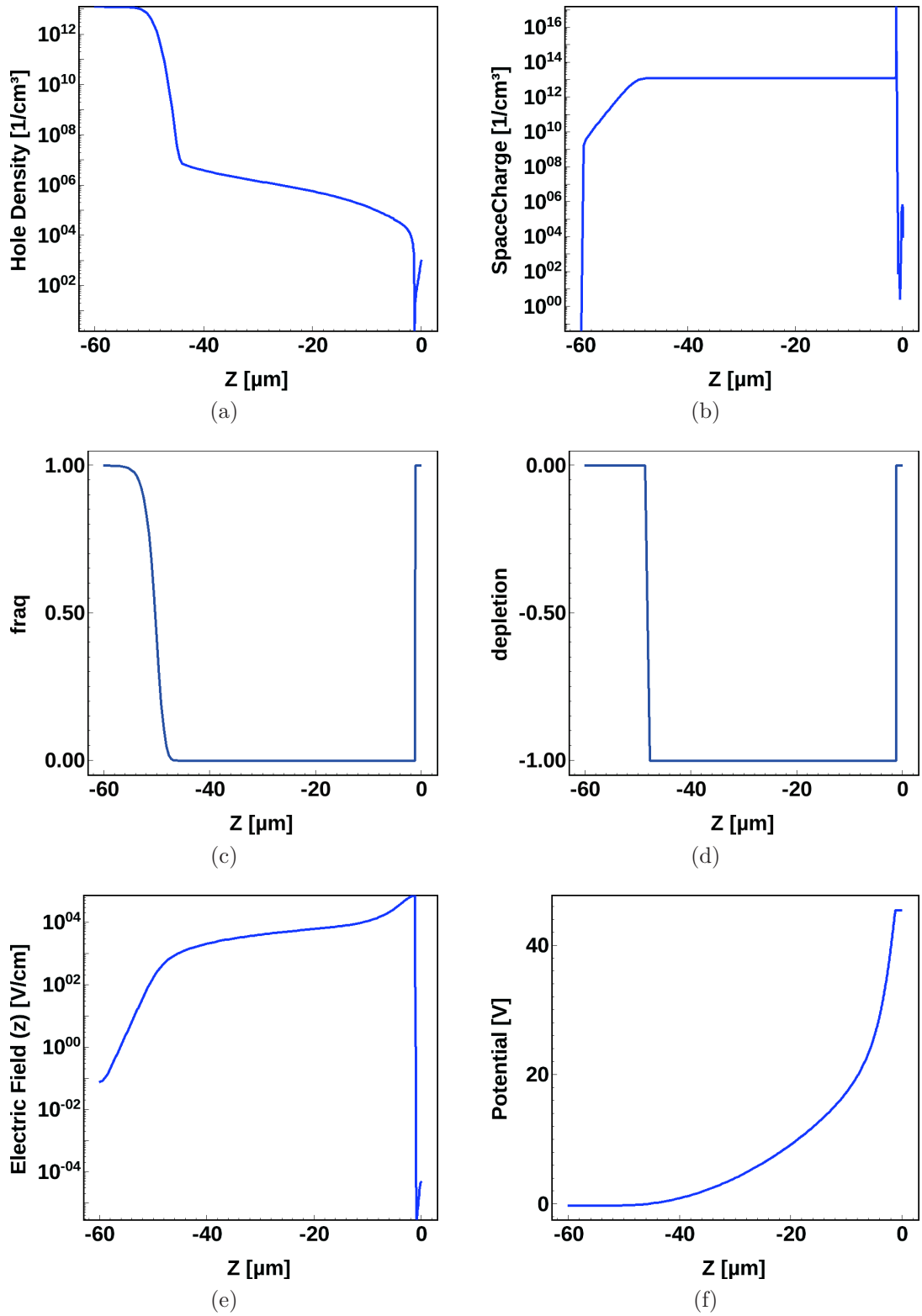

Figure 4.11: Simulation results of a simplified structure with a substrate resistivity of 600 Ω cm biased at 45 V. The collecting diode is between 0 and -1.5 µm. (a) Hole density. (b) Q_{SC} (equation 4.20). (c) V_D (equation 4.21). (d) D (equation 4.22). (e) Electric field. (f) Potential

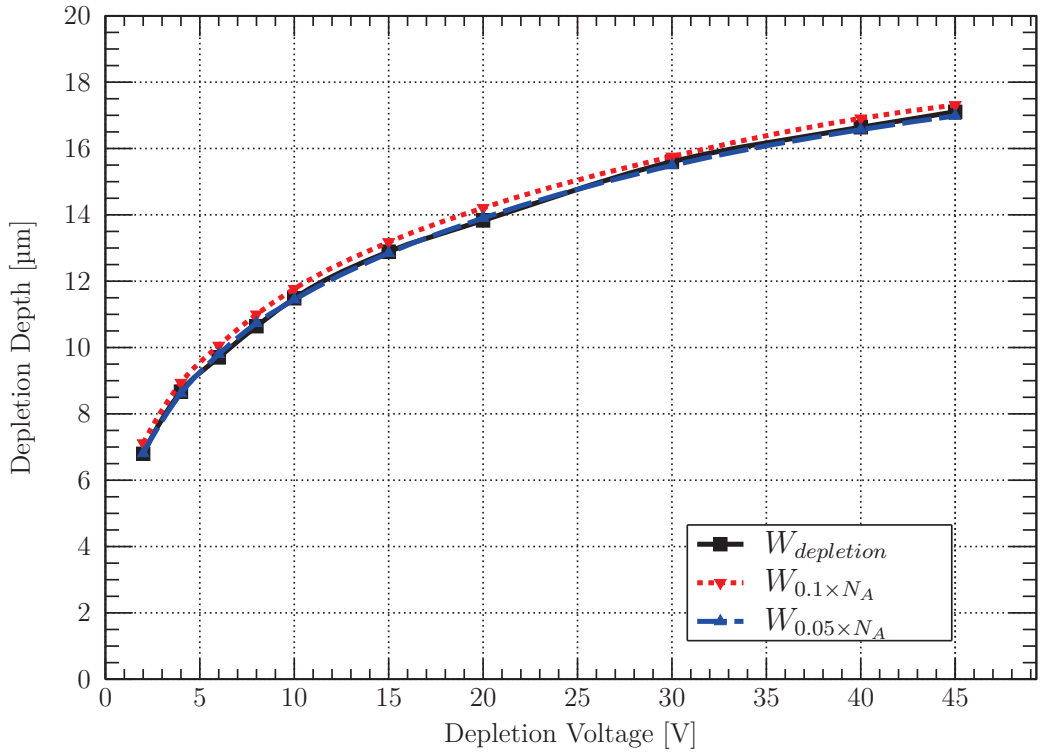

Figure 4.12: Comparison of depth determination methods for TCAD simulations of the realistic model

Because the determination using the hole concentration is more direct and gives results similar to the one displayed by TCAD, it is chosen for the further analysis of finite elements simulations with the limit at $0.05 \times N_A$.

The determination of the depth is also sensitive to the input of the model and to the meshing size. From the discrepancies observed between the determination methods, an uncertainty of a micrometer can be considered for the depth reached by the depleted volume. Also, only the maximum depletion depth reached is probed which can also provide an estimation on the lateral extension. For small values of depth attained with respect to the pixel pitch, the edges of the pixels can be considered as undepleted.

4.3.3 Simulations Results

Computing Times

The time used for the generation of the structure, and the simulations of simplified and realistic structures are compared. During the structure generation, the meshing process can be performed using multiple threads as well as the simulations. In table 4.2, the times are given for processes using up to 24 threads of a couple of Intel Xeon E5-2670 at 2.60GHz CPUs.

Table 4.2: Computing times for the meshing and simulation of simplified, and realistic CZ configurations with various resistivities

Resistivity [Ω cm]	Structure generation time [s]		Simulation wallclock time [s]	
	Simplified	Realistic	Simplified	Realistic
600	485	728	6480	16070
1000	514	732	6390	14088
2000	521	730	16957	23980
>10000	523	682	11384	21762

The time taken for the generation of the structure is relatively small compared to the simulation times. The amount of time taken to simulate a realistic structure is 1.5 to 2.5 times longer than for a simplified structure.

Simplified Model

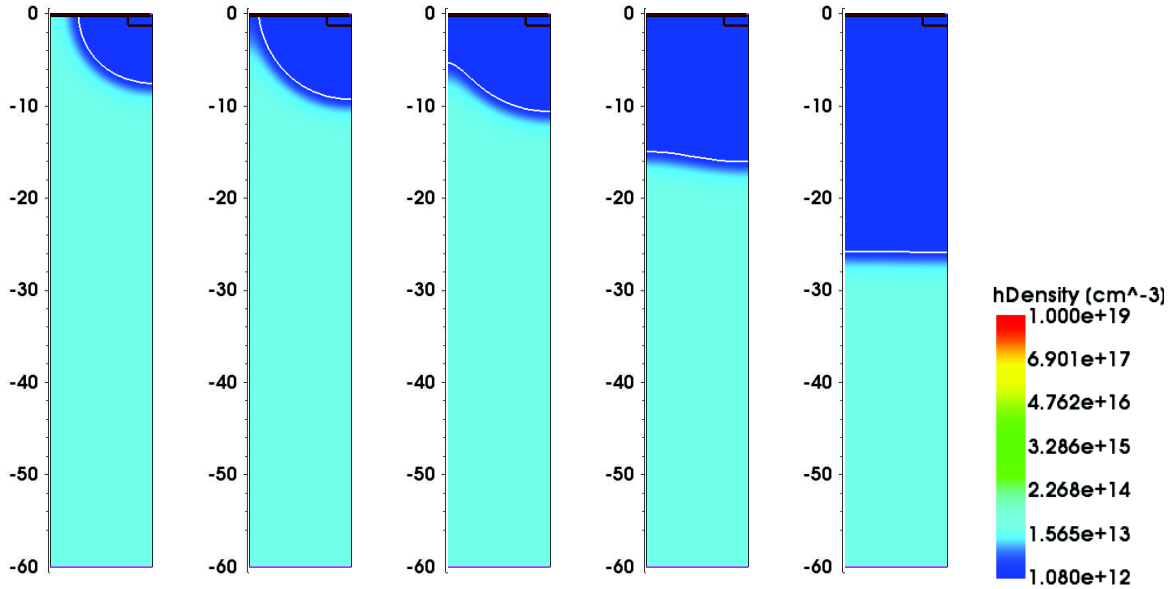

Figure 4.13: Behaviour of the depletion depth with the simplified model using a 600 Ω cm substrate biased at (a) 2 V, (b) 4 V, (c) 6 V, (d) 15 V, and (e) 30 V. The simulated substrate is 60 µm thick with a 22 µm pitch (half of the pitch is displayed since only a quarter of the pixel is simulated). The diode located at the center of the pixel area is visible on the top right corner of each cross-section. The dark blue area is where the density of holes is below 5 % of the acceptors concentration.

Selected cross sections of the quarter of the same simplified architecture biased at various reverse bias values are shown in figure 4.13. At low biasing voltages, the depleted

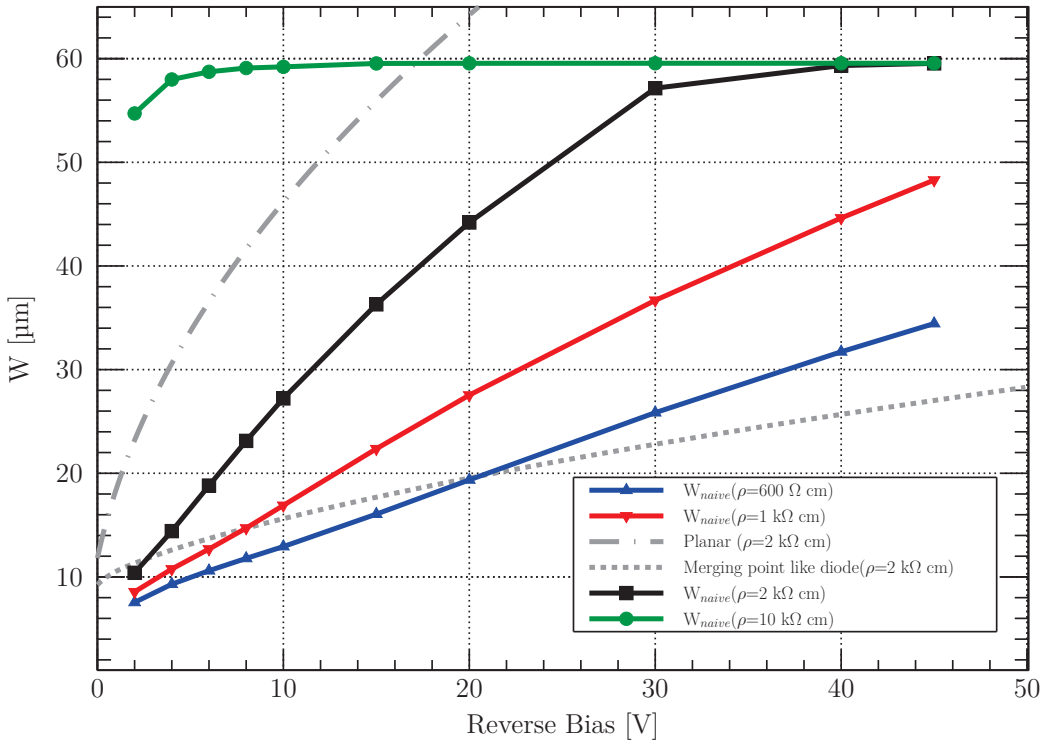

Figure 4.14: TCAD simulated depletion depth reached in a simplified PIPPER-2 structure at various resistivities: 600 Ω cm, 1 kΩ cm, 2 kΩ cm, and >10 kΩ cm compared to the depth calculated for a 2 kΩ cm with the planar equation (equation 2.52) and with the merging point like-diode equation (equation 4.19).

volume is hemispherical until reaching the edge of the pixel when the bias is increased. As soon as the volume reaches the edge of the pixel (figure 4.13c), the shape of the depleted region becomes flatter until being a cuboïd at high biasing values (figure 4.13e).

The depth reached by the depleted volume with various resistivities set for the simplified structure are plotted in figure 4.14 versus the biasing voltage. The resistivities used are 600 Ω cm, corresponding to the known doping concentration of the substrate for the fabricated CZ PIPPER-2 sensor, 1 kΩ cm, 2 kΩ cm, and >10 kΩ cm, corresponding to the minimal doping concentration of the epitaxial layer (figure 4.9).

Since the volume simulated was limited to a thickness of 60 µm for meshing purposes, the simulation with the highest resistivity quickly increases to saturate at the thickness limit. The depth reached by the bottom of the depleted volume for the other doping configuration increase linearly with the bias voltage of the junction, and reaches the limit. The simulated depth using the simplified structure significantly overestimates the analytical expression of the point like diode.

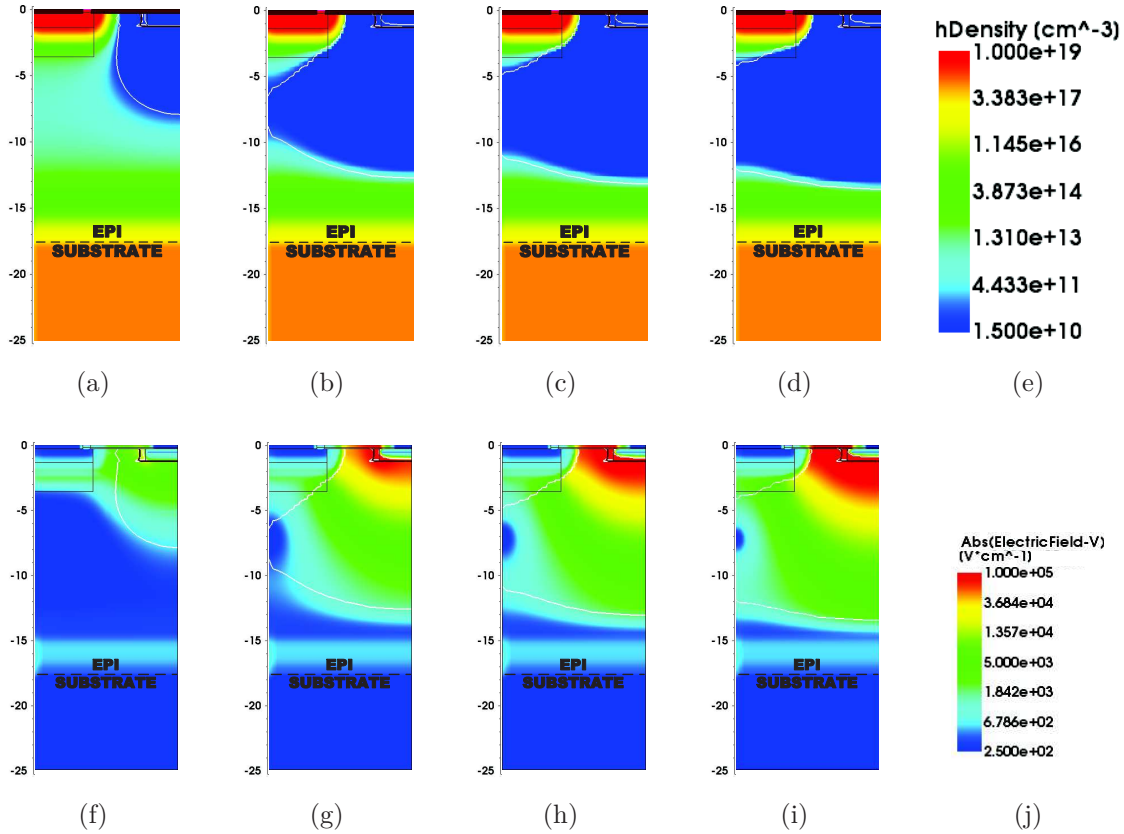

Figure 4.15: Behaviour of the depletion depth with the realistic HR18 model biased at (a) 2 V, (b) 20 V, (c) 30 V, and (d) 45 V. The 25 µm thick substrate is defined using the doping profile presented in figure 4.9. The total thickness is 25 µm thick with a 22 µm pitch (half of the pitch is displayed since only a quarter of the pixel is simulated). The diode located at the center of the pixel area is visible on the top right corner of each cross-section. The dark blue area in (a–d) is where the density of holes is below 5 % of the acceptors concentration. The electric field in the epitaxial layer for the same conditions as (a–d) are (f–i)

Realistic Model

The realistic structures of the HR18 using realistic doping profiles, and the CZ substrate with the resistivities noted above have been simulated for the same biasing values. The cross section of the quarter pixels for each type of sensitive volume are respectively presented in figure 4.15, and figure 4.16.

The shape of the depletion volume differs from the simplified simulations results. The deep p-well structure that embeds the CMOS process limits the lateral expansion of the space charge zone. Thus the depleted volume is shaped like a light bulb with the socket plugged in the inter-well region. The volume also extends towards the edges of the pixel to merge with the adjacent one when the bias is sufficiently increased (figure 4.16c). The volume becomes flatter with sufficiently large bias voltages as seen previously with the

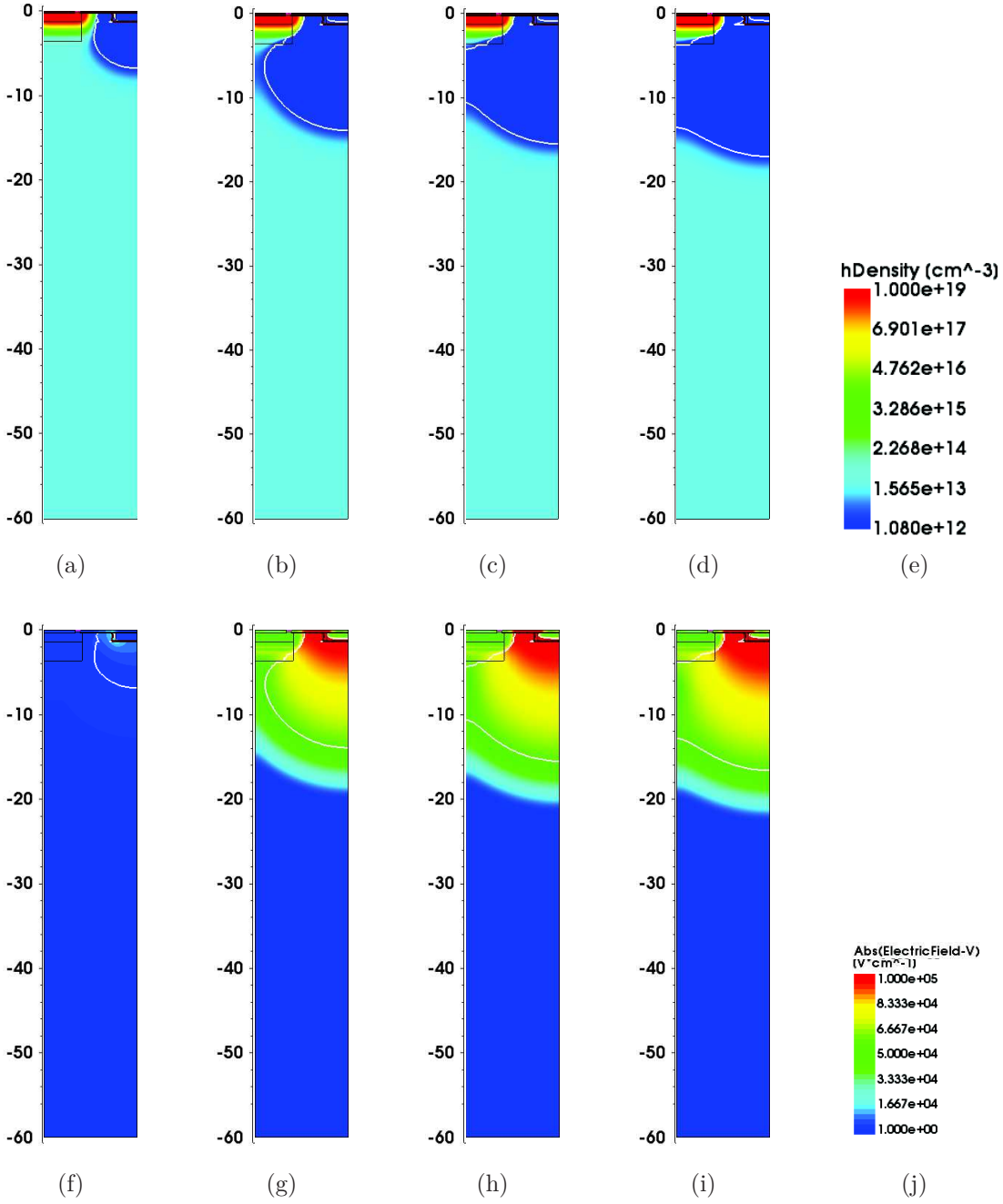

(a) (b) (c) (d) (e)

(f) (g) (h) (i) (j)

Figure 4.16: Behaviour of the depletion depth with the realistic CZ model using a 600 Ω cm substrate biased at (a) 2 V, (b) 20 V, (c) 30 V, and (d) 45 V. The simulated substrate is 60 µm thick with a 22 µm pitch (half of the pitch is displayed since only a quarter of the pixel is simulated). The diode located at the center of the pixel area is visible on the top right corner of each cross-section. The dark blue area is where the density of holes is below 5 % of the acceptors concentration.
The electric field in the bulk substrate for the same conditions as (a–d) are (f–i)

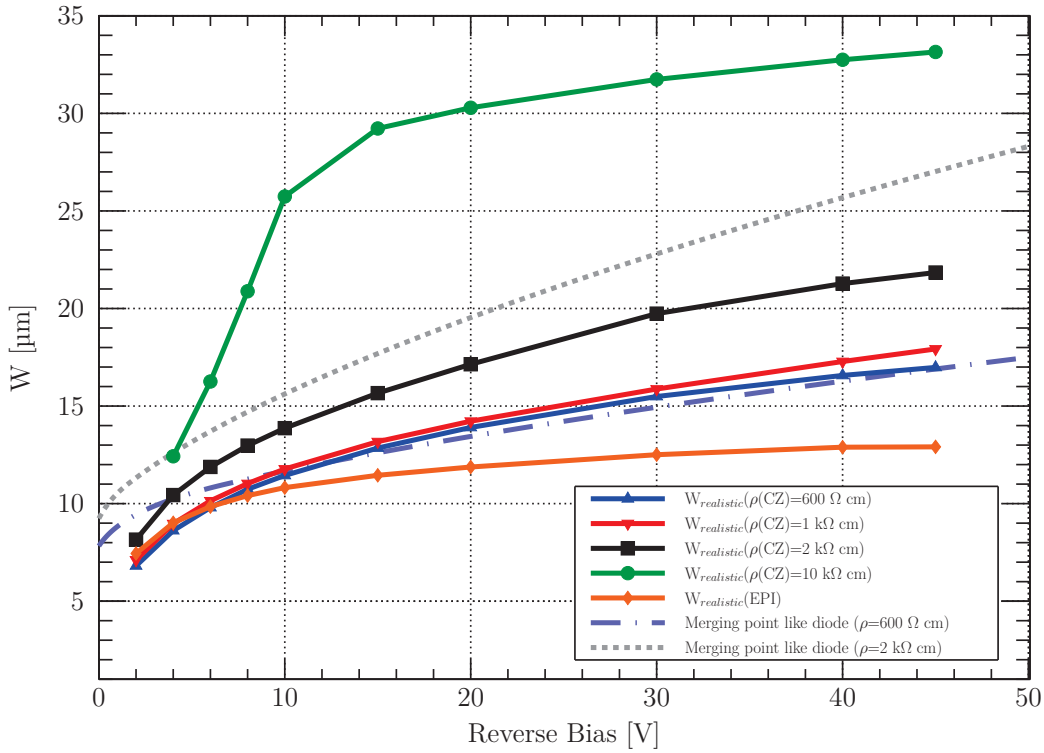

Figure 4.17: TCAD simulated depletion depth reached in a realistic PIPPER-2 bulk structure at various resistivities: 600 Ω cm, 1 kΩ cm, 2 kΩ cm, and >10 kΩ cm and in the HR18 structure. The simulations are compared to the point like diode equation for a bulk resistivity of 600 Ω cm, and of 2 kΩ cm

simplified structure.

The extension of the depleted volume in the HR18 configuration is similar but is limited by the doping profile of the epitaxial layer on the substrate, and is not able to reach the bottom of this grown layer (figure 4.15d).

The obtained depth for each simulated device are presented in figure 4.17. Despite the fact that the simplified structure is similar to one considered for the point-like diode expression, the behaviour of the latter is alike the realistic structure simulations results. The discrepancy can be explained by the more complex set of equations and considerations used by the TCAD simulator. Nevertheless, the analytical approximation with merging seems to overestimate the reached depth at low biasing values while being underestimated at higher voltages caused by the presence of deep P-wells that limits the expansion at higher biases.

At the minimal guaranteed resistivity of 600 Ω cm of the fabricated CZ chip, the depletion depth reaches 17 µm in the substrate at the highest biasing values. The value

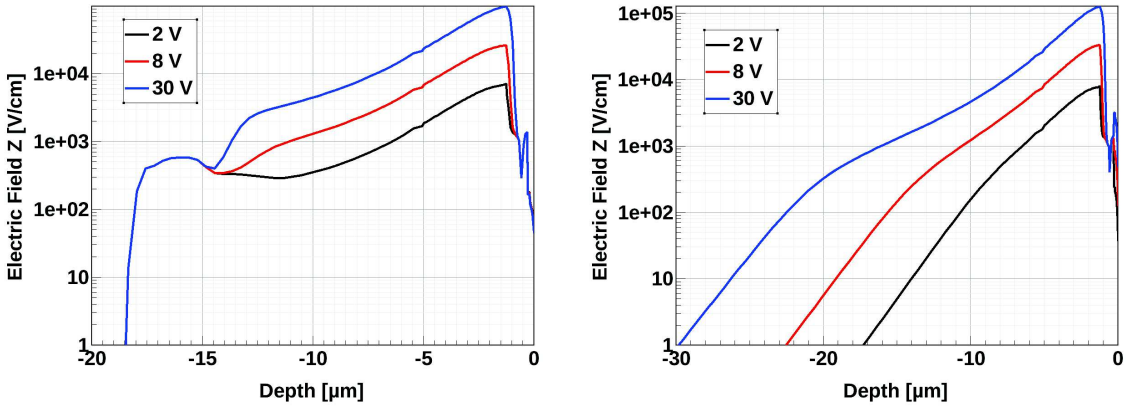

(a) (b)

Figure 4.18: Simulations of the electric field along the Z-axis for different diode bias voltage (2 V, 8 V, and 30 V) in the (a) HR18 structure, and the (b) realistic CZ with a 2 kΩ cm structure

reached in the 1 kΩ cm substrate is similar with respect to the uncertainties. The difference is more noticeable with a 2 kΩ cm substrate, where the volume reaches 22 µm along the z-axis. At very high resistivity values, which is probably very optimistic, the volume is expanding very quickly with voltages in range 2–15 V followed by a much smaller slope. At 20 V, a 30 µm thick depleted volume is achieved, reaching 33 µm at 45 V.

The depth reached in the HR18 model, even at low biasing voltages, does not follow the trend of the one using the CZ model with the highest resistivity. At low biasing voltages (2–6 V), the trend is similar to the CZ with a 2 kΩ cm uniformly doped substrate model, then saturates around 13 µm. As suggested by the cross sections, this constrained behaviour of the expansion of the depletion volume is caused by the doping profile of the epitaxial layer above the substrate.

The electric field in the bulk substrate (figures 4.16f–4.16i) is present outside the boundaries of the estimated depleted volumes for each bias applied suggesting that charges generated close to the limit can be collected thus increasing the sensitive volume with respect to the depleted volume.

The same effect exists in the epitaxial layer (figures 4.15f–4.15i) but is limited to the direct neighbouring of the depleted volume. The inferior limit of the electric field scale is set higher in the HR18 version than in the CZ version to expose the presence of an electric field caused by the doping profile of the epitaxial layer which limits the extension of the depleted volume up to the estimated limit of 13 µm.

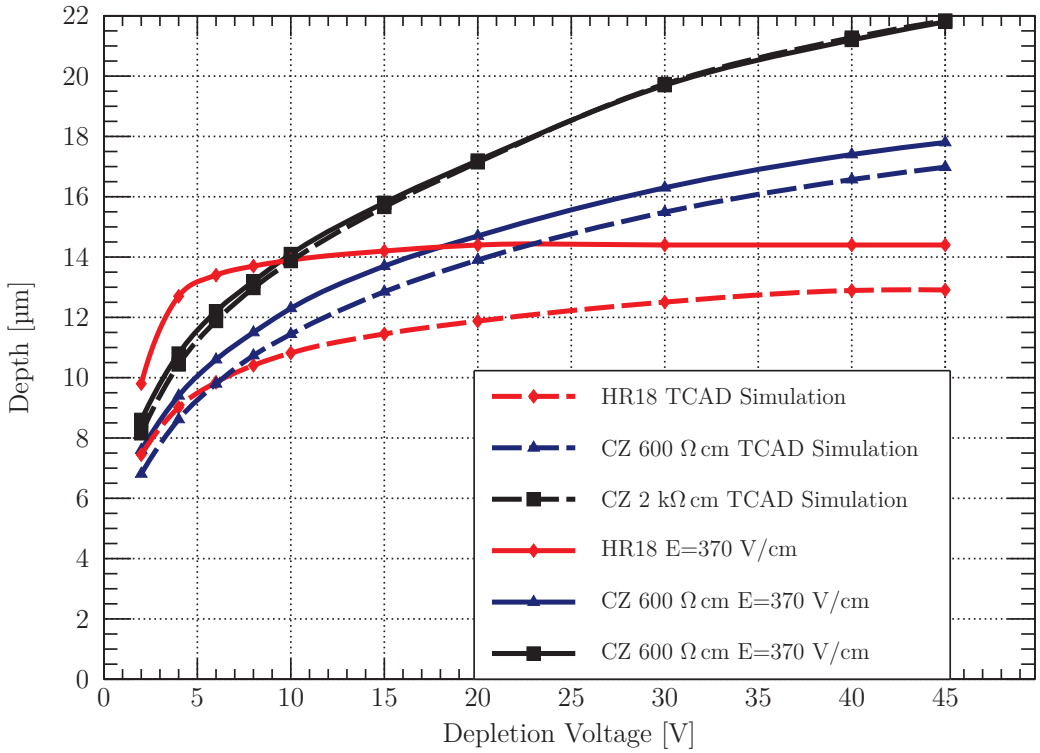

Figure 4.19: Depth where the electric field along the Z-axis is above 370 V cm^{-1} in the HR18 structure and in the CZ structure with resistivities of 600 Ω cm and 2 kΩ cm

The electric field along the Z axis using the HR18 and the realistic CZ (2 kΩ cm) models is presented in figure 4.18. In the bulk version (figure 4.18b), the strongest electric field is located next to the diode and fades with the depth. The reduction of the intensity of the electric field with the distance starting from the diode is also visible in the epitaxial layer model (figure 4.18a). Nevertheless, the intensity of the electric field rises at the bottom of the epitaxial layer in the doping profile (figure 4.9) after reaching a minimum which will lead to a limitation of the distance where charge collection can be performed. Also the doping at this depth is very high and thus increases the recombination rate.

An electron collected 40 µm away from the diode in 10 ns or less requires a constant electric field above 370 V cm^{-1}. By probing the position where the electric field is above this limit, a distance of good collection can be evaluated. The resulting depth is shown in figure 4.19 for the HR18 model, the CZ model with a resistivity of 600 Ω cm and the CZ model with a resistivity of 2 kΩ cm.

The intensity of the electric field in the HR18 model is higher than the considered limit for biasing values above 30 V. The depth is thus evaluated to the bottom of the electric field basin in the doping profile of the epitaxial layer. Still, the distance evaluated using the electric field in the epitaxial layer increases quickly with the bias, allowing good charge collection up to 4 µm deeper than the evaluated depletion depth for low bias volt-

ages. The sensitive thickness reaches a steady value while the depleted volume continues its expansion. The difference in the evaluated distances is reduced to less than 2 µm with a diode biased at 45 V.

Using the CZ models, the difference between the distances evaluated remains similar for any bias applied. With the limit on the electric field set at 370 $\mathrm{V\,cm^{-1}}$, the good collection depth is 1 µm bigger than the evaluated depletion depth in the 600 Ω cm bulk substrate. The evaluated depth are similar in the 2 kΩ cm bulk volume. However, the electric field remains quite strong below the evaluated depth. A deep electron can still be accelerated by the electric field to be collected before recombination, thus increasing the good collection depth. By considering a minimum electric field of 100 $\mathrm{V\,cm^{-1}}$, the good collection depth is evaluated 3 µm deeper than the depleted depth in the 2 kΩ cm substrate.

Because of the worse performance of the simplified model, it cannot be recommended and its lower demand on ressources cannot be taken advantage of. Thus, a realistic model using doping profiles and structures representing the CMOS process must be used to simulate the depletion in a pixel.

For the PIPPER-2 sensor, in the HR18 model, the depleted volume extends up to 13 µm limited by the doping profile of the epitaxial layer. From the observation of the electric field, a charge generated outside the space charge zone could be collected up to 2 µm away from the depleted volume. In the bulk model at the minimum resistivity guaranteed, the depletion volume extends up to 17 µm within the substrate with good charge collection performance possible up to 3 µm deeper.

Chapter 5

Measurements with Depleted CPS

In this chapter, a PIPPER-2 prototype sensor fabricated on both version of high-resistivity substrate, the 18 µm thick epitaxial substrate, which is estimated to be sensitive over 15 µm due to its doping profile, and the thinned bulk substrate (50 µm) is tested. The experimental setup and analysis methods are first presented. The figures of merit resulting from characterization using various X-ray energies are then shown along post neutron-irradiation results. Finally, the spectroscopic capabilities of the prototype are revealed.

5.1 Experimental Setup

A PIPPER-2 sensor (presented in chapter 4.1) is wirebonded to its own PCB (see figure 5.1a), denominated as proxy board. An opening in the PCB is present under the sensor to allow backside illumination (see figure 5.1b). The proxy board is connected to an auxiliary board in charge of the steering of the sensor, and of the distribution of the data to the external analog to digital converter.

Each analog output of the sensor (see chapter 4.1) is amplified on the proxy board by a non-inverting amplifier with a gain of 3.91 ± 0.04. The analog signal is digitized using a 14-bit, 50 MS/s digitizer in a National Instruments PXIe-1071 crate, and the acquisition is controlled with a LabView software. The frame is read out in 40 µs.

The proxy board is enclosed in an aluminum box coupled to a watercooling system to perform measurements on a chilled sensor to guarantee constant operating conditions for the characterizations. The temperature of the coolant is set to +5 °C which sets the PCB at +11 °C.

The high voltage biasing is provided by a Keithley 237 High Voltage Source which also acts as a picoammeter allowing to perform IV-curves. Despite that only one submatrix is selected for readout at a time, the high voltage biasing is distributed over the 3 submatrices designed for the depletion studies, representing 3072 pixels.

The sensor is either frontside or backside illuminated using an ^{55}Fe soft X-Ray sealed source, providing two characteristic rays at 5.9 keV, and 6.49 keV. A source holder was

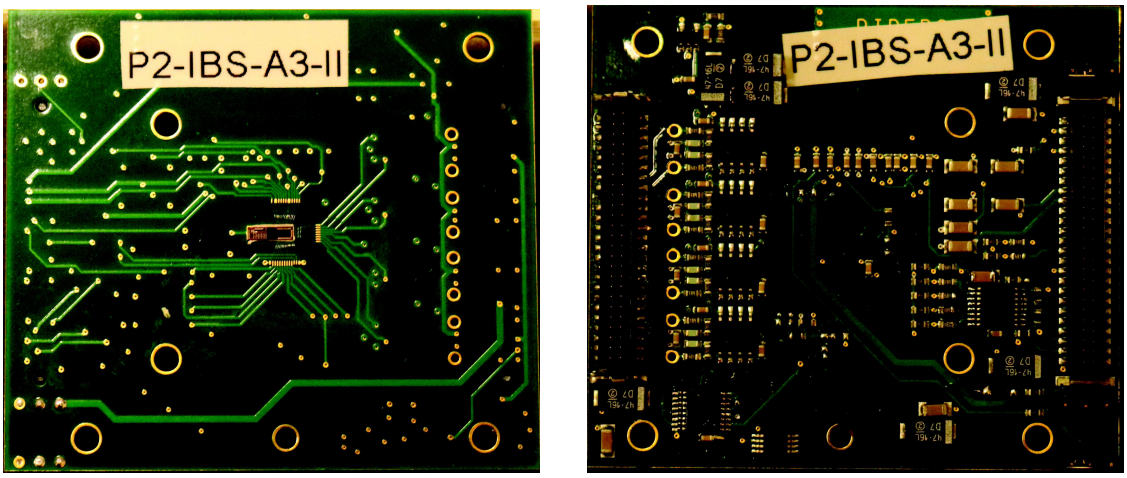

(a) (b)

Figure 5.1: (a) A PIPPER-2 sensor wirebonded to its PCB. (b)Backside where an opening allows illumination through the PCB

3D-printed for each configuration (frontside and backside) to allow the same distance between the emitter and the sensor. The prototype is also illuminated using a *Rigaku D/MAX-B* X-ray generator (see figure 5.2) with three different tubes to perform characterization at various energies, respectively 5.4 keV (Cr), 8.05 keV (Cu), and 17.48 keV (Mo) along with their own harmonics up to $\approx$ 20 keV. The X-ray generator was set to 20 kV and 20 mA for the measurements presented in this chapter.

The range of the applied depletion voltage for the further developments are limited to the breakdown threshold of the thin epitaxial layer version of the PIPPER-2 sensor. The sweep is thus performed from 0 V to 45 V (see section 5.3.1).

For each depletion voltage applied, 6 000 000 frames are acquired under illumination conditions in bunches of 30 000 consecutive frames to prevent data bottleneck, and to keep the data files from being too large. Without illlumination, 30 000 frames are acquired to determine the noise performance.

5.2 Analysis Techniques

During the analysis of the data, the difference between two consecutive frames (correlated double sampling) is used to determine the amplitude of the signal in each pixel giving 15 000 frames of noise, and 3 000 000 frames under illumination.

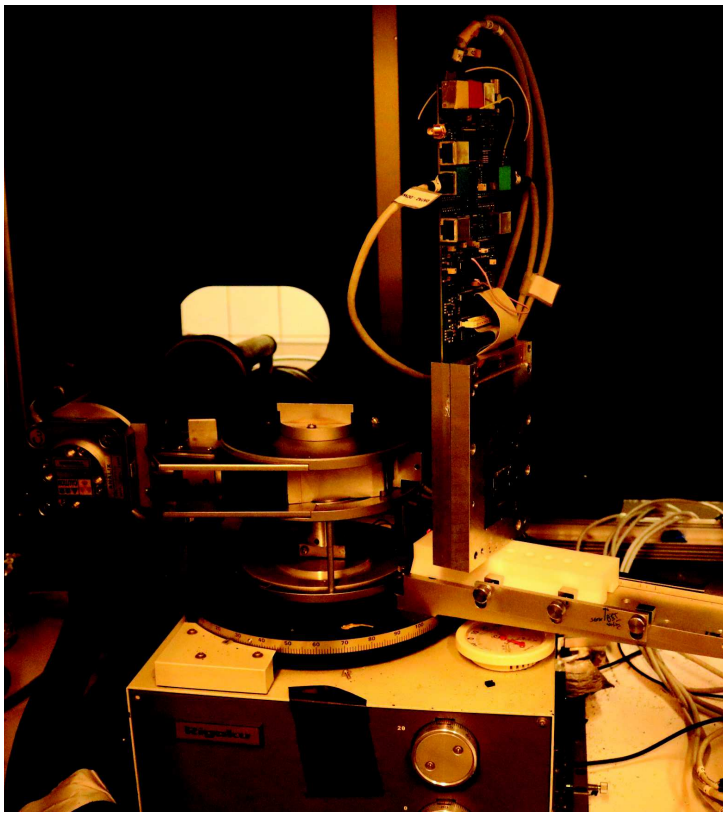

Figure 5.2: A PIPPER-2 proxy in its watercooled aluminum box coupled to its auxiliary board installed in the X-ray generator with a copper tube installed.

5.2.1 Noise

The total signal of a single pixel k in a MAPS at a frame n can be expressed as the sum of different terms:

- $q_k^{phys}(n)$: a signal generated by the interaction of an ionizing particle or a photon,
- $q_k^{random}(n)$: a random charge (noise contribution),
- $p_k(n)$: the pedestal,
- $cms(n)$: a common mode shift.

Since the noise of the sensor is acquired without illumination in darkness, $q_k^{phys}(n)$=0. Also, offline Correlated Double Sampling (CDS) is used, thus removing any common mode displacement ($cms(n)$=0) giving:

$$r_k(n) = q_k^{random}(n) + p_k(n) \tag{5.1}$$

The pedestal, for N frames, is expressed with:

$$p_k = \frac{1}{N}\sum_{i=1}^{N} r_k(i) \tag{5.2}$$

This expression represents the value around which the noise fluctuates. Similarly to the common mode shift, CDS operation sets the pedestal to 0. A distribution of the pedestal of the 1024 pixels of a PIPPER-2 sensor on an 18 µm epitaxial layer is shown in figure 5.3a. Similar pedestal figures are obtained for each voltages applied on each type of PIPPER-2.

For each individual pixel, the standard deviation of the fluctuations around the pedestal, caused by the random charge, is the estimation of the *pixel noise* expressed by:

$$\sigma_k^2 = \frac{1}{N-1}\sum_{i=1}^{N}(r_k(i) - p(k))^2 \tag{5.3}$$

5.2.2 Under Illumination

For the analysis under illumination, the pixels index are stored in decreasing order of the amplitude signal. Clustering algorithm around the seed pixel (pixel with the larger signal in the cluster) takes place using the 8 surrounding pixels. A single frame acquired with a PIPPER-2 fabricated on a 18 µm thick epitaxial layer biased at 20 V is shown in figure 5.4. The signal corresponding to a single hit over the matrix is collected in a single pixel as the direct neighbours are within the fluctuations. The flux of the used sources is

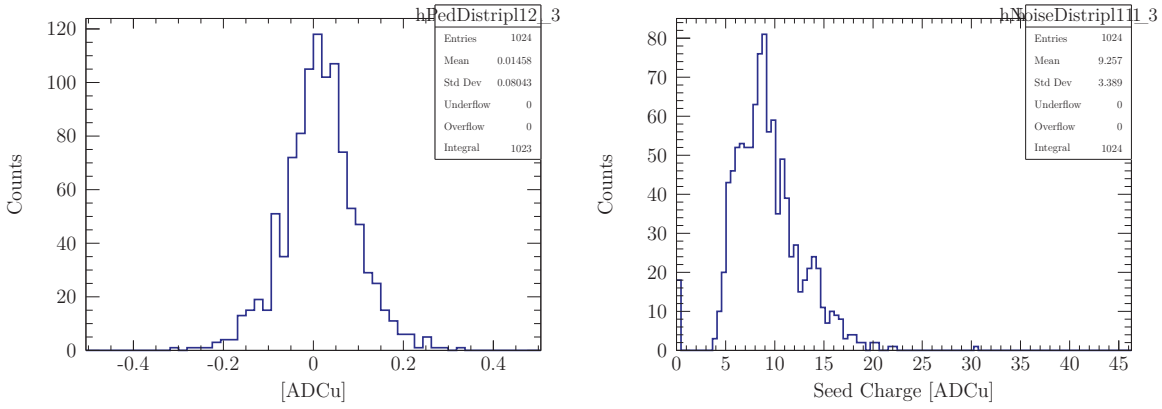

(a) (b)

Figure 5.3: Pedestal distribution (a), and noise distribution (b) obtained for individual pixels with a PIPPER-2 sensor biased at 30 V. The mean pedestal is very close to 0. The observed mean noise is 9.257 ADC units.

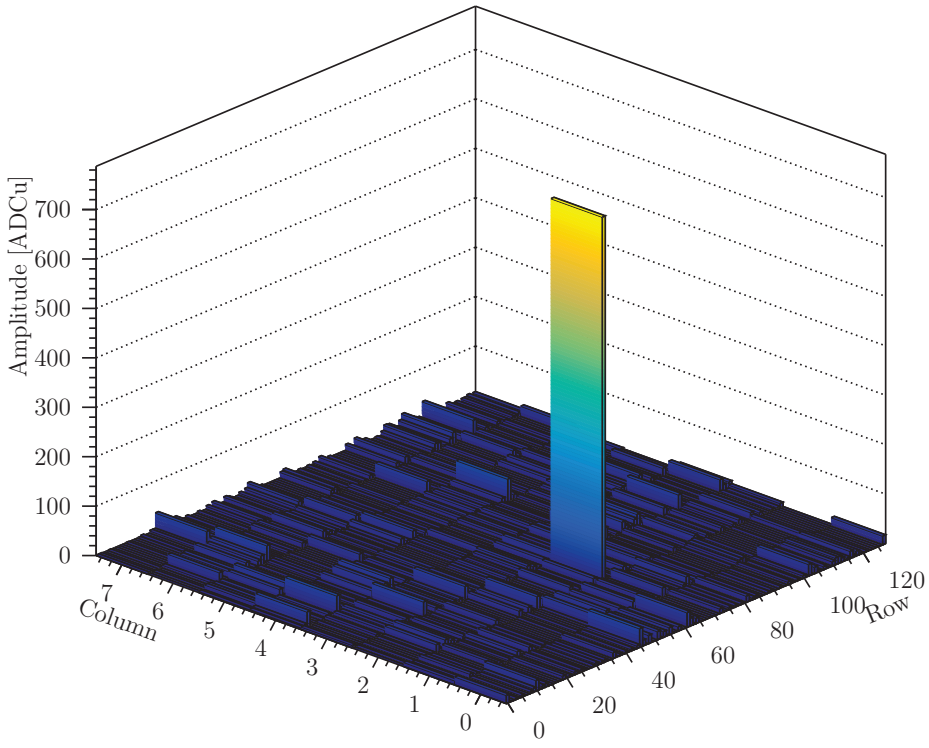

Figure 5.4: Single frame of PIPPER-2 HR18 biased at 20 V under ^{55}Fe illumination. A single hit is distinguishable among the noise fluctuations.

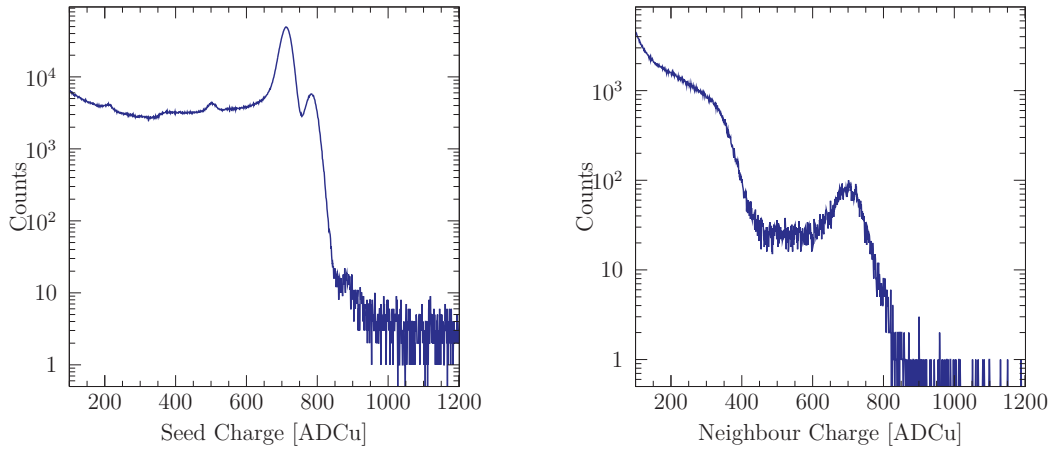

Figure 5.5: (a) Seed charge spectrum and (b) neighbour charge spectrum (sum of 8 pixels surrounding the seed) obtained from frontside illumination with ^{55}Fe of a PIPPER-2 sensor fabricated on a thin epitaxial layer and biased at 30 V

sufficiently low to distinguish hits from each other. The highest flux has been observed on the bulk substrate biased at 45 V front-side illuminated with ^{55}Fe with a mean value of 2.98 $\pm$2.108 hits per frame.

The spectrum of the used source is reconstructed using the seed pixel charge. The amplitude in Analog to Digital Converter unit (ADCu) is proportional to the amplitude of the signal at the output of the pixel, thus to the amount of collected charge. The seed pixel charge histograms resulting from the illumination with each available sources of the HR18 sensor biased at 30 V are presented in figure 5.5a. The Silicon escape peaks (see chapter 3.1.2) are easily visible (1.74 keV below the calibration peak) as well as the silicon fluorescence peak (1.74 keV).
The remaining charge in cluster (neighbour charge) histogram for the same condition is shown in figure 5.5b. A peak corresponding to the calibration peak is discernable in a continuous spectrum resulting from double hits within the clusters. One being considered as the seed and the second in the neighbour. From the observation of the amount of entries, such event is marginal.

The determination of the peak position and resolution parameters of the response are obtained by fitting each characteristic peak. Since the response is not purely Gaussian, being asymmetric on the low energy side, a Crystal Ball function [155] is used because of its power-law that allows the modelisation of the charge sharing. The function is given

by:

$$f(x,\alpha,n,\mu,\sigma) = N \cdot \begin{cases} \exp\left(-\frac{(x-\mu)^2}{2\sigma^2}\right) & \text{for } \frac{x-\mu}{\sigma} > -\alpha \\ A \cdot \left(B \cdot \frac{x-\mu}{\sigma}\right)^{-n} & \text{for } \frac{x-\mu}{\sigma} \leq -\alpha \end{cases} \tag{5.4}$$

With,

$$A = \left(\frac{n}{|\alpha|}\right)^n \cdot \exp\left(-\frac{|\alpha|^2}{2}\right) \tag{5.5}$$

$$B = \frac{n}{|\alpha|} - |\alpha| \tag{5.6}$$

$$C = \frac{n}{|\alpha|} \cdot \frac{1}{n-1} \cdot \exp\left(-\frac{|\alpha|^2}{2}\right) \tag{5.7}$$

$$D = \sqrt{\frac{\pi}{2}} \cdot \left(1 + \text{erf}\left(\frac{|\alpha|}{\sqrt{2}}\right)\right) \tag{5.8}$$

$$N = \frac{1}{\sigma(C+D)} \tag{5.9}$$

With α, n, μ, and σ free fit parameters. The factor N allows the normalization of the two components to provide a continuous transition between the power-law part and the Gaussian part (see figure 5.6).

Both the Mn-Kα (5.9 keV) and the Mn-Kβ (6.49 keV) rays from the ^{55}Fe source are fitted. The three other sources being monochromatic, the Kα rays are fitted and, except for Molybdenum, the first harmonics (2 $\times$ Kα) are also fitted. The fit result is shown on the spectra in figure 5.7 and the fits results parameters for the main calibration peaks are summarized in table 5.1. When the fit is not efficient, such as the 2 $\times$ Cu-Kα, the Gaussian part of the peak is manually fitted to extract μ, and σ.

Table 5.1: Crystall ball fits results for the main peak of the spectra shown in figure 5.7

Source	μ	σ	α	N	n	χ^2	ndf
Cr	656.7	14.83	1.11	1.434×10^7	1.014	15280	982
^{55}Fe	711.3	14.72	1.221	2.68×10^7	1.011	9355	244
Cu	976.2	18.74	1.038	2.886×10^6	1.073	5133	1179
Mo	1694	35.8	1.192	6.881×10^5	1.036	1251	583

The reduced χ^2 indicates bad fit results mostly caused by the large fit range. Reducing the latter to the calibration peaks could improve the fit results. Nevertheless, the main parameters obtained (i.e. μ and σ) from the current configuration are not influenced by the high reduced χ^2.

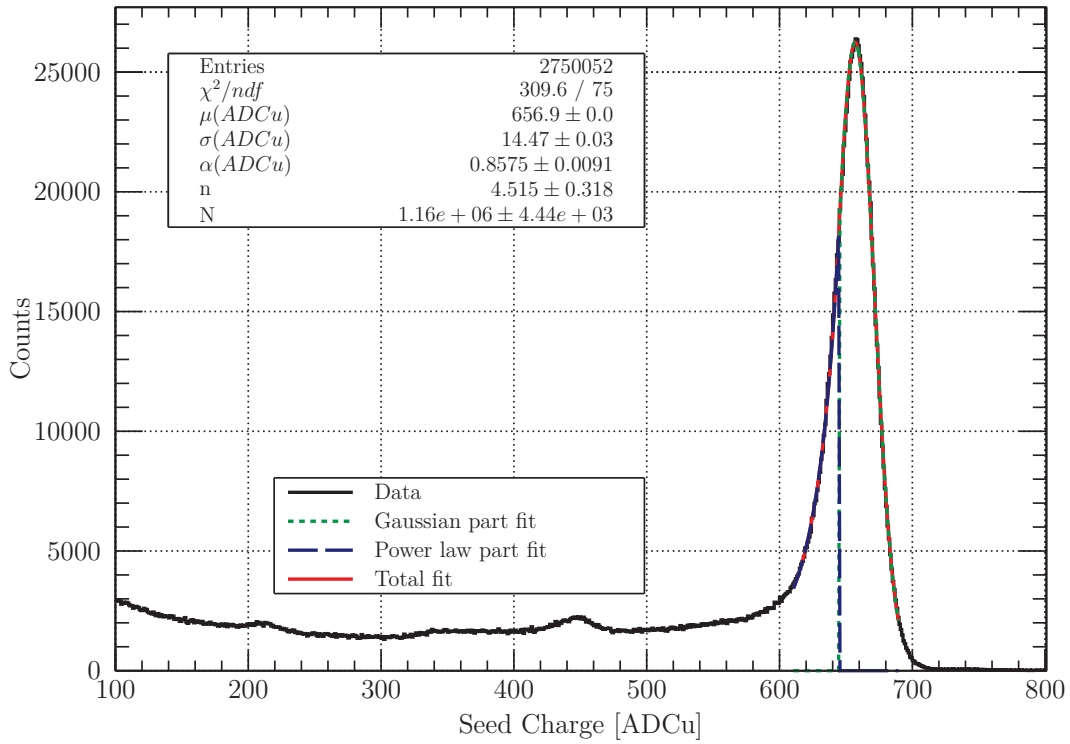

Figure 5.6: Crystal Ball fit of a Cr calibration peak obtained with PIPPER-2 fabricated on the epitaxial layer biased at 30 V. The power-law and the Gaussian parts are individually shown.

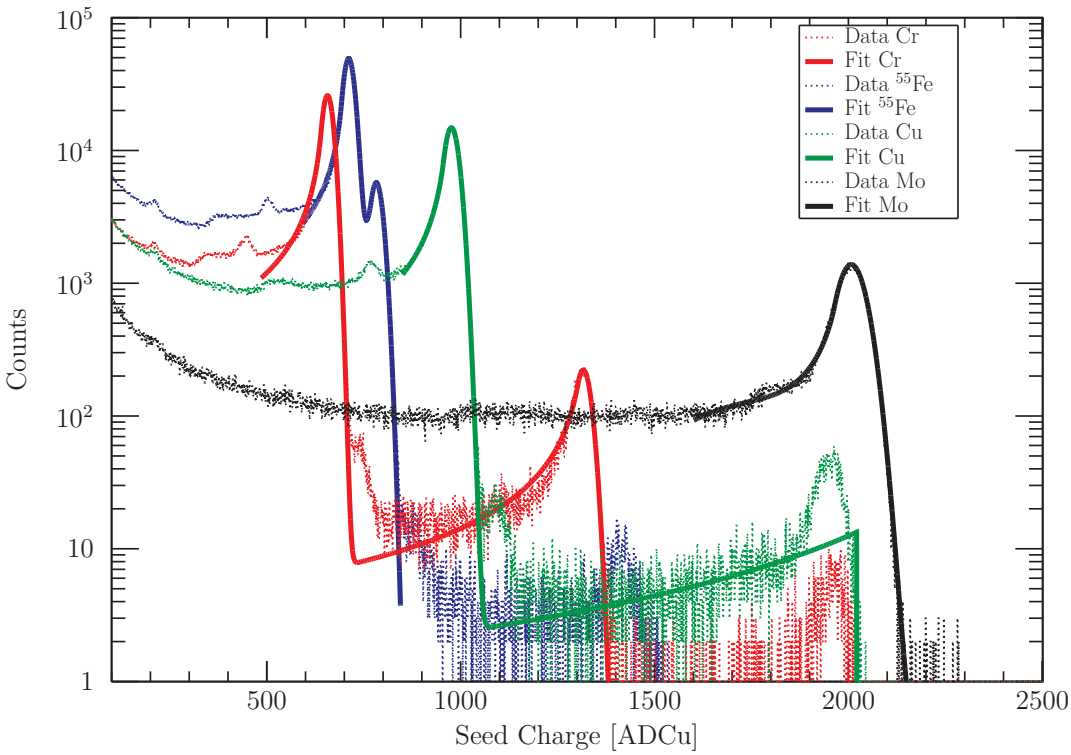

Figure 5.7: Spectra obtained with PIPPER-2 HR18 biased at 30 V illuminated with Cr (red), ^{55}Fe (blue), Cu (green), and Mo (black). The calibration peaks of each source are fitted using a Crystall Ball function (equation 5.4)

The spectra acquired for each bias were fitted in the same way for each illumination configuration of each sensor. The position of the calibration peak increased with the applied depletion voltage as shown in figure 5.8. The left column is the HR18 version, the center column is CZ 50 µm with frontside illumination, and the right column is CZ 50 µm with backside illumination. The biasing values are 0 V (first line), 10 V (second line), 30 V (third line), and 45 V (fourth line). The source used was ^{55}Fe.

Without biasing, at 0 V, the calibration peak (Mn-Kβ is merged with Mn-Kα) emerges from a prominent background suggesting that the sensor is not depleted at all. The calibration peak at 0 V bias is around 500 ADCu and moves to a steady value of 700 ADCu with the bias increasing. Also the background becomes flatter, and the escape and fluorescence peaks becomes visible. The proportion of integrated entries in the background with respect to the amount in the calibration peaks is bigger in the CZ version of the sensor.
Also, a difference is noticeable for each biasing voltage between frontside and backside illumination: the proportion of the integrated counts between the calibration peak and the flat shelf is different, being worse in the BSI condition suggesting that the response of the sensor is not the same. The sensor is thus not fully depleted because of the mean free path of the charge. Charge loss at the back surface due to passivation might also worsen the response.
With a 45 V bias applied the calibration peak becomes broader on the high energy side, lowering the amount of entries in the calibration peak while the integrated counts in the peak with the tail is increased with respect to the lower biases. This effect is especially pronounced in the epitaxial layer (figure 5.8j), and the cause is discussed in section 5.3.7.

Charge sharing can also be observed with the reconstructed spectra by correlating the seed pixel charge spectra with the spectra made from the 8 neighbouring pixels. The resulting maps are shown in figure 5.11

With a depletion voltage applied, the seed pixel spectrum without sharing can be seen along the X-axis for 0 neighbour charge. The majority of a non-zero neighbour charge is located in a diagonal where the sum of the seed charge with the neighbour charge equals the position of the calibration peak on the seed pixel spectrum. On a seed charge spectrum (figure 5.7), the sharing can be observed starting from the shoulder at half the position of the calibration peak.

The more discernable and sharp is the distribution around 0 neighbour charge, the better is the collection (HR18).

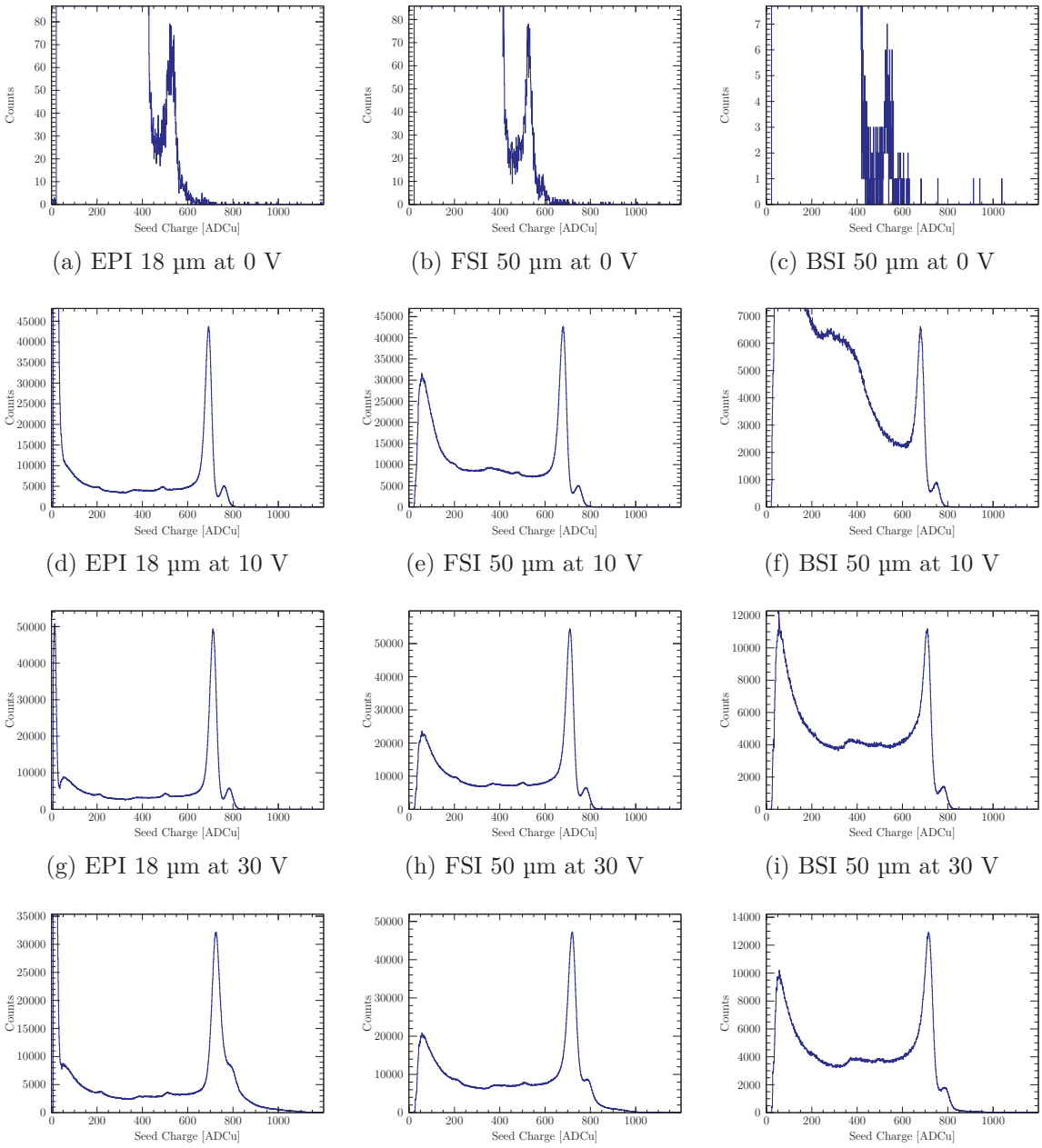

(a) EPI 18 µm at 0 V (b) FSI 50 µm at 0 V (c) BSI 50 µm at 0 V

(d) EPI 18 µm at 10 V (e) FSI 50 µm at 10 V (f) BSI 50 µm at 10 V

(g) EPI 18 µm at 30 V (h) FSI 50 µm at 30 V (i) BSI 50 µm at 30 V

(j) EPI 18 µm at 45 V (k) FSI 50 µm at 45 V (l) BSI 50 µm at 45 V

Figure 5.8: Seed pixel charge spectra of ^{55}Fe using PIPPER-2 HR18 (a, d, g, j), CZ 50 µm FSI (b, e, h, k), and CZ 50 µm BSI (c, f, i, l) for different biasing values (0, 10, 30, and 45 V) under same running and illumination conditions.

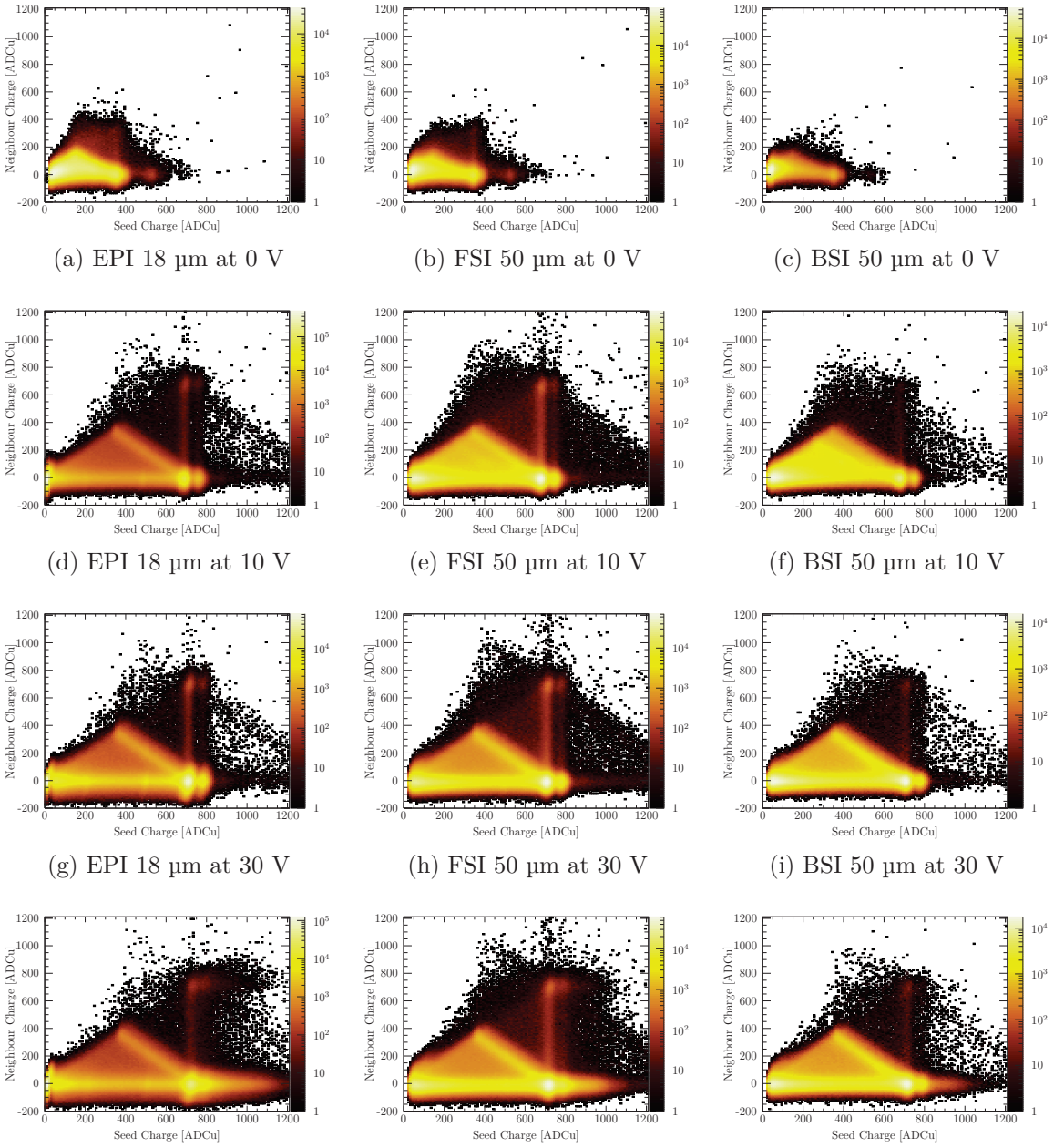

(a) EPI 18 µm at 0 V (b) FSI 50 µm at 0 V (c) BSI 50 µm at 0 V

(d) EPI 18 µm at 10 V (e) FSI 50 µm at 10 V (f) BSI 50 µm at 10 V

(g) EPI 18 µm at 30 V (h) FSI 50 µm at 30 V (i) BSI 50 µm at 30 V

(j) EPI 18 µm at 45 V (k) FSI 50 µm at 45 V (l) BSI 50 µm at 45 V

Figure 5.9: Maps of the distribution of charge in the seed and its neighbours on recorded hits

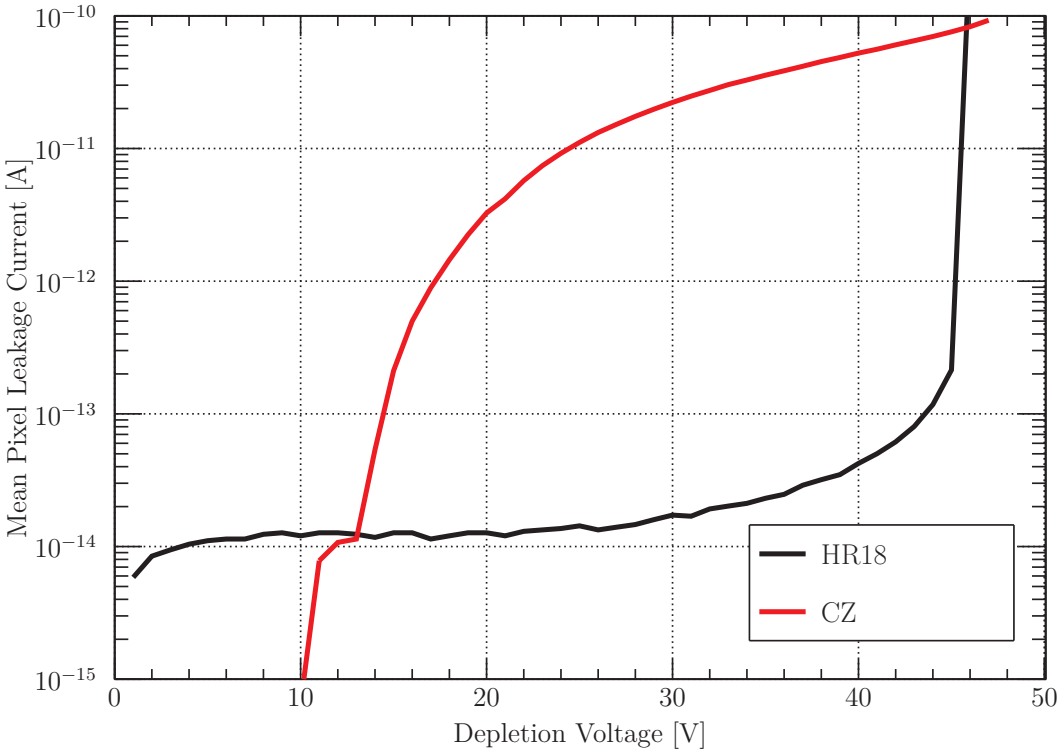

Figure 5.10: Mean pixel leakage current measured with a Keithley 237 High Voltage Source/picoammeter in both PIPPER-2 version in the 18 µm thick epitaxial layer (black) and in the 50 µm thick bulk substrate. The sensors were chilled ($T_{coolant}$=+5 °C, $T_{PCB} \approx$ +11 °C)

5.3 Analysis Results

The results presented in this chapter were acquired on the first submatrix of the sensor whose diodes have a diameter of 5 µm, which is the model used for the depletion studies in chapter 4.

5.3.1 Leakage Current

IV curves have been acquired in the different sensors configuration to set a limit on the maximum bias value that can be applied on the matrix before breakdown. The measurement of the leakage current is performed over three submatrices (3072 pixels) and is presented as a mean pixel leakage current in figure 5.10. The dispersion of the leakage current over the matrices can not be measured nor estimated.

The mean leakage current in the HR18 version of PIPPER-2 is constant (a few tens of fA) for bias below 40 V before rising and reaching the avalanche limit. The mean leakage current in the bulk version is higher than in the HR18 version.
From 12 V to below 45 volt the measured leakage current in the thinned bulk substrate continuously rises to reach three orders of magnitudes higher values than in the epitaxial

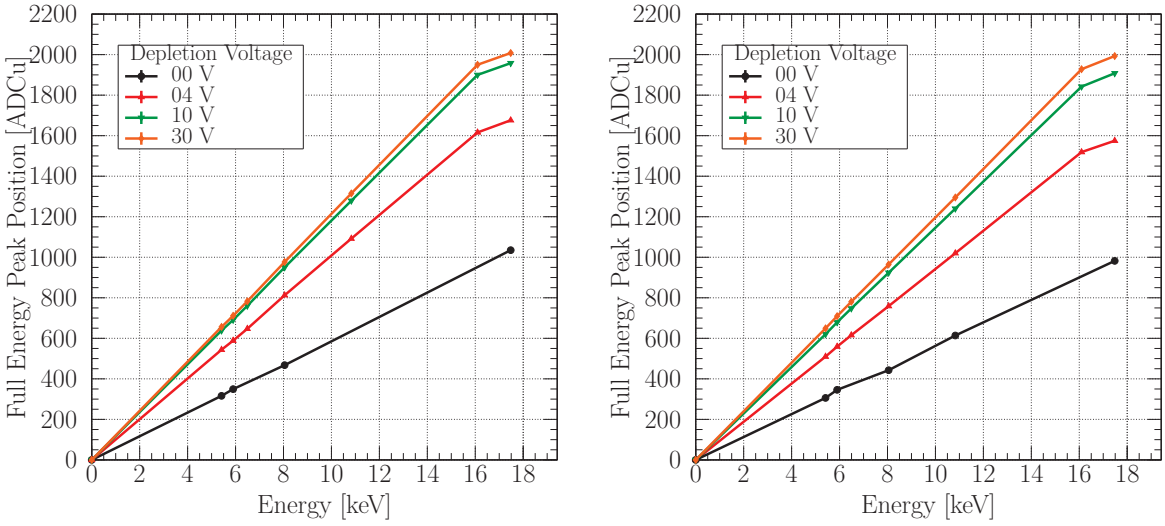

(a) HR18 (b) CZ 50 µm

Figure 5.11: Measured peak position versus the energy of the incoming photon for a PIPPER-2 sensor produced on an 18 µm thick epitaxial layer (a) and on a 50 µm thick bulk substrate (b).

device.

The saturation before breakdown in the thin epitaxial layer version of PIPPER-2 shows that full depletion is reached as explained in [11]. The continuously growing leakage current in the bulk substrate indicates that full depletion is not reached and that the depleted volume is pursuing its expansion with the augmentation of the bias voltage.

5.3.2 Energy Calibration and Linearity

The position of the calibration peaks with various illumination conditions on different sensors have been obtained from the fits and allows to check the response of the linearity of the PIPPER-2 sensors. The results for selected biasing voltages in each substrate are presented in figures 5.11a and 5.11b.

The sensors are linear up to $\approx$ 16 keV for any value of depletion voltage applied in each configuration. The cause of the non-linearity is not yet explained as it might not be caused by any kind of saturation in the chain (for higher bias, non-linearity would appear at lower energies). The slope of the linear region gives the calibration factor of the sensor in ADCu/keV which are reported versus the depletion voltage in figure 5.12a.

Without bias applied, the calibration factor on each sensor is similar. They both increase with the application of the bias and then stabilize around 120 ADCu/keV.

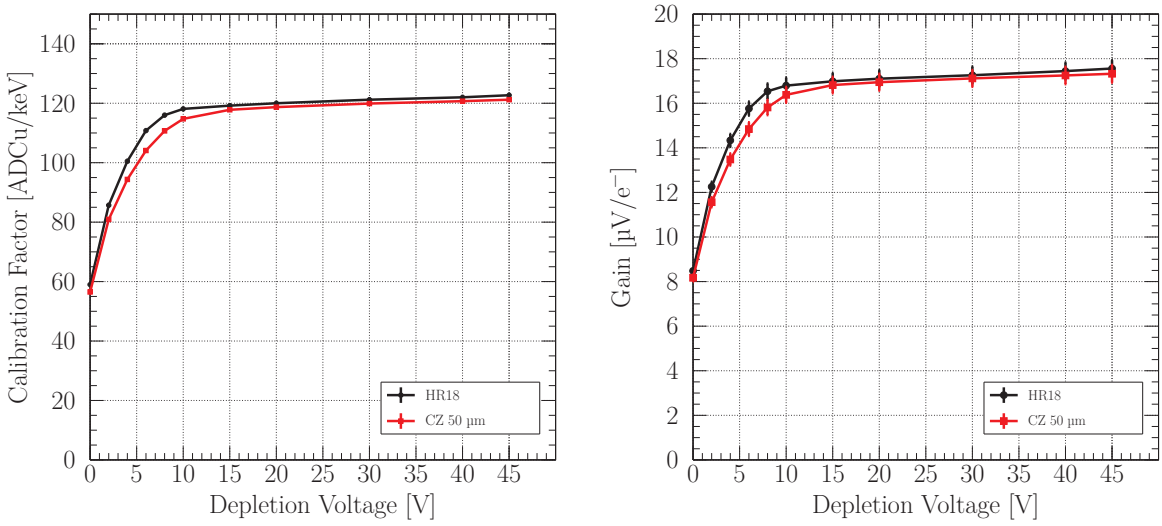

(a) (b)

Figure 5.12: (a) Calibration factor in ADC units per keV of each PIPPER-2 substrate type obtained from the slope of the linearity presented in figures 5.11a and 5.11b. (b) The calibration factor shown in figure 5.12a is converted to a gain in units of µV/electron

5.3.3 Detector Capacitance

Since the value in ADCu is proportional to the collected charge, the calibration factor can be converted to a gain in Volts per electron. The voltage span of the used 14 bit ADC is 2 V. Thus, its resolution is:

$$Q = \frac{2}{2^{14}} = 122 \text{ µV/ADCu} \tag{5.10}$$

Also, the signal is amplified at the output of the sensor on the proxy board by a gain A_{proxy}=3.91 ± 0.04. By varying the polarization voltage (pol) of the input node of the source follower of the pixel, the gain at the output of the pixel is evaluated to $A_{SF} \approx 0.78$. Thus the total gain of the readout chain is $A_{TOT} \approx 3.05$. The conversion of the calibration factor to the gain is thus expressed by:

$$Gain = \frac{\text{Calibration Factor} \cdot Q}{A_{TOT}} \cdot \frac{1}{1000/\epsilon(Si)} \tag{5.11}$$

Figure 5.12b presents the gain versus the depletion voltage applied on the sensor.

The gain corresponding to the highest value of stabilized calibration factor over the matrix is around 17 µV/e$^-$ after rising from a similar value of gain without biasing (≈8 µV/e$^-$).

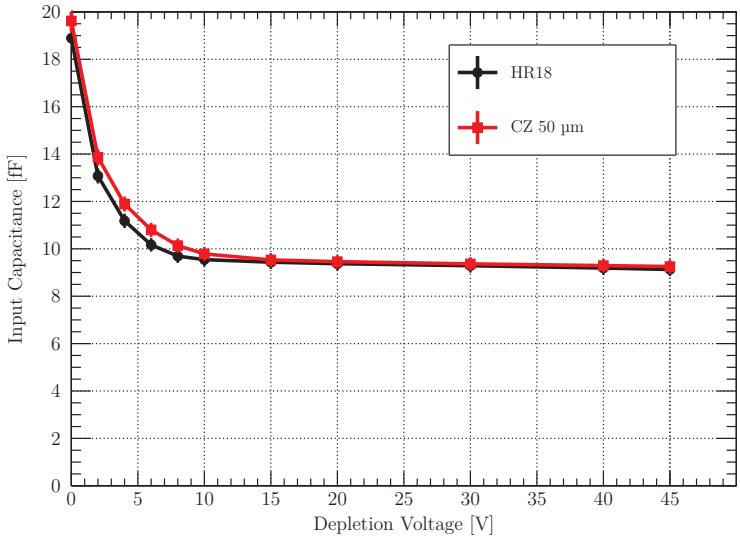

Figure 5.13: Input capacitance as a function of the depletion voltage applied on each substrate-variant of PIPPER-2

The gain is converted to an equivalent input capacitance using:

$$C_{input} = \frac{|q|}{\Delta V} \tag{5.12}$$

With ΔV the voltage corresponding to the ADCu value of the peak position, the reference being 0.

The result of the conversion is shown in figure 5.13.

The equivalent input capacitance decreases from 19 fF without applied bias to 9 fF for biasing voltages above 10 V. The input capacitance in the HR18 version of PIPPER-2 decreases quicker to its stable value than in the CZ version, which can also be seen with the gain (or calibration factor) increasing faster to its steady state.

The input capacitance decreases as the depleted volume in the sensor extends until it reaches the closest well (in this case, the deep P wells containing the CMOS circuits). The stabilized limit corresponds to the inter-well capacitance. The limit being reached quicker in the epitaxial layer suggests that the extension of the depletion to a given distance requires lower biasing value, which is consistent regarding the known values of resistivity in each version, >1 kΩ cm in the epitaxial layer version and 600 Ω cm in the bulk version of the sensor.

5.3.4 Noise Performance

The distribution of the noise for the whole matrix of an HR18 version of PIPPER-2 is shown in figure 5.3b. The mean value of the distribution is the mean readout noise over the whole sensor which can be converted to electrons, or energy, using the calibration

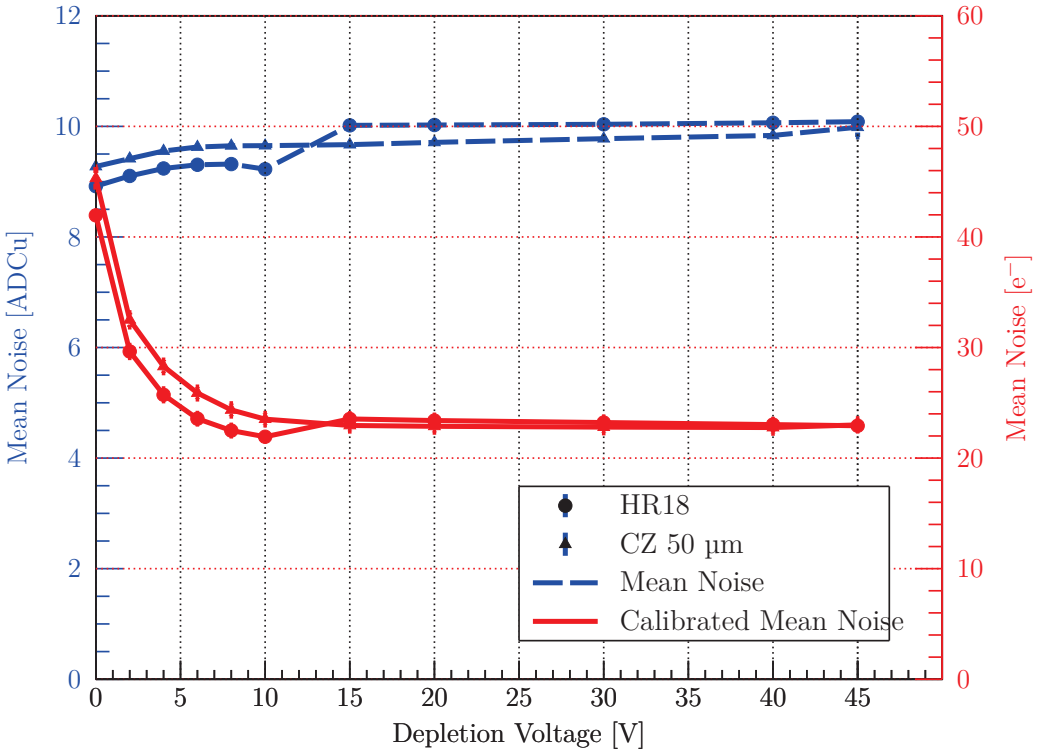

Figure 5.14: Mean noise measured with each version of PIPPER-2 as a function of the applied depletion voltage. In ADCu (blue), and converted to an equivalent noise charge (in electrons) using the calibration factors.

factor. The measured mean noise, in ADC units and in electrons, for various bias values in each type of substrate is displayed in figure 5.14.

Similar behaviour and values between both versions are observable with the calibrated noise. The noise is above 40 electrons without depletion voltage applied and decreases to a plateau of around 24 electrons. The calibrated noise is smaller in the epitaxial version of the sensor for bias below 10 V. Above 15 V, the calibrated noise is similar in both versions.

The evolution of the equivalent noise charge with the depletion voltage applied is correlated to the equivalent input capacitance. It suggests that a contribution proportional to the input capacitance is added to the leakage current in the total noise and is dominant when undepleted.

5.3.5 Charge Sharing

It is expected that a charge generated within the pixel area, in a fully depleted sensitive volume, is not shared with any neighbouring pixels. The worst case should happen when the charge is generated at the corner of four pixels. Nevertheless charge sharing effects exist leading to a distribution of the charge over multiple pixels.

To determine the proportion of charge collected by the seed pixel, the distribution of the amount of charge collected in the seed pixel within a nine-pixel cluster is computed. Figure 5.15 displays the distribution resulting from the acquisition with ^{55}Fe in the epitaxial layer version and the 50 µm thick Czochralski with frontside and backside illumination with 2 V and 30 V bias.

With the lowest biasing voltage (2 V) the ratio distribution starts above 25 % in each version. Since the charge generated outside the thin sensitive epitaxial layer can not be collected, the spread of the charge moving by thermal diffusion will be smaller for HR18 than in the bulk version sensor. Also, the most distant generated charge is less likely to be collected before recombination processes. These effects are visible on the proportion of charge collected within the epitaxial layer being higher (figure 5.15a, $\approx$ 82 %) than in the frontside illuminated bulk sensor (figure 5.15c, $\approx$ 74 %).

In a similar way, since the depleted volume resulting from a low voltage biasing is small with respect to the sensitive thickness, the charge generated with backside illumination close to the entrance window will have to travel and spread over a larger distance before being collected, heading to a smaller ratio of charge collected by the seed pixel (figure 5.15e, $\approx$ 65 %).

Under higher biasing conditions, with the extension of the depleted volume, the majority of the charge is collected by the seed pixel. Also, under similar illumination condition, the amount of entries is approximatively 1.8 times higher in the bulk version than in the epitaxial layer. The shoulder at 50 % suggests that charge sharing exists mostly between two adjacent pixels.
In HR18, any charge generated outside the epitaxial layer, in the P-type substrate, is not collected at all.
With the backside illuminated CZ sensor, the proportion of charge collected by the seed pixel (figure 5.15f, $\approx$ 84 %) is smaller, but close to the proportion obtained under frontside illumination (figure 5.15d, $\approx$ 86 %).

The ratio of charge collected by the seed pixel (figure 5.16) in the thin epitaxial layer rises quickly with the biasing voltage, starting at 75 % up to a steady plateau close to 90 %. The stabilization is reached with biasing values above 10 V. The variation of the ratio Seed Charge/Hit Charge with the biasing voltage is not energy dependant in the epitaxial layer.

In the bulk substrate (figure 5.17), the proportion of charge in the seed pixel rises with the biasing voltage from $\approx$ 65 % to slightly lower values than the ones reached in the

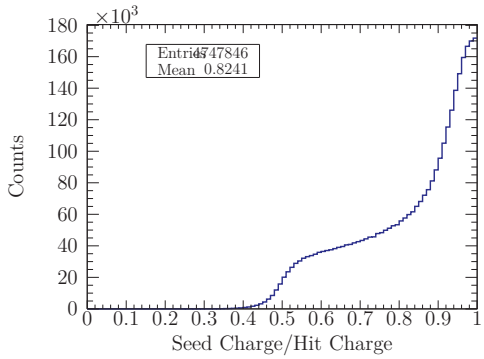

(a) Epi 18 µm at 2 V

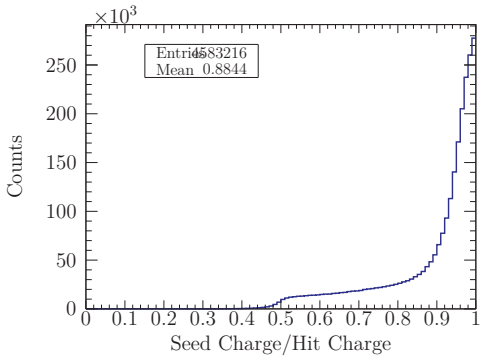

(b) Epi 18 µm at 30 V

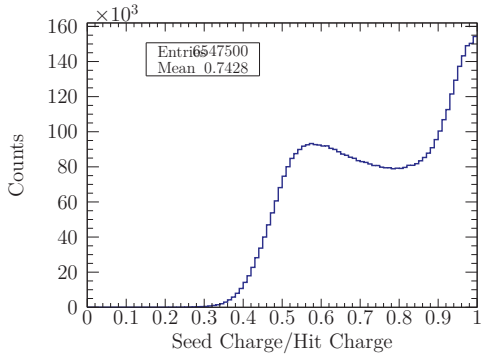

(c) FSI 50 µm at 2 V

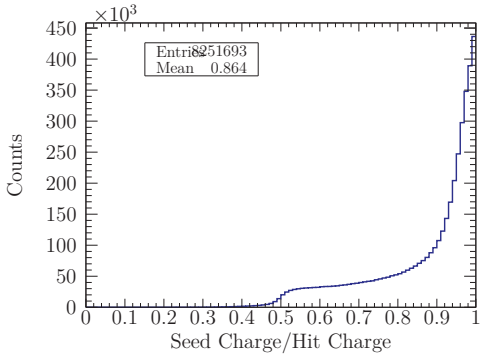

(d) FSI 50 µm at 30 V

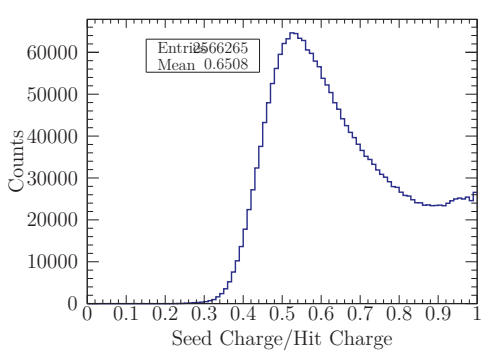

(e) BSI 50 µm at 2 V

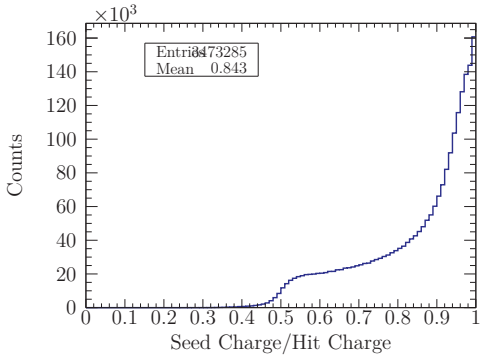

(f) BSI 50 µm at 30 V

Figure 5.15: Ratio of hit charge collected by the seed pixel for various configurations of PIPPER-2 sensors.

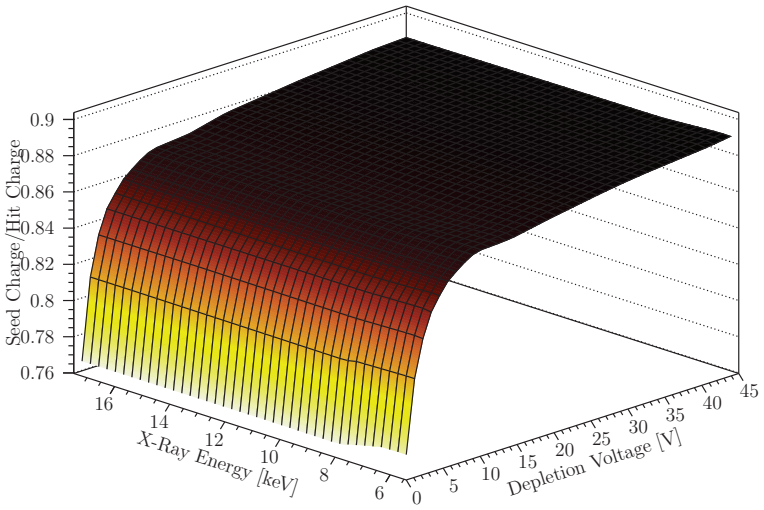

Figure 5.16: Map of the proportion of hit charge collected by the seed pixel versus the energy of the incoming photon and the applied depletion voltage in the 18 µm thick epitaxial layer.

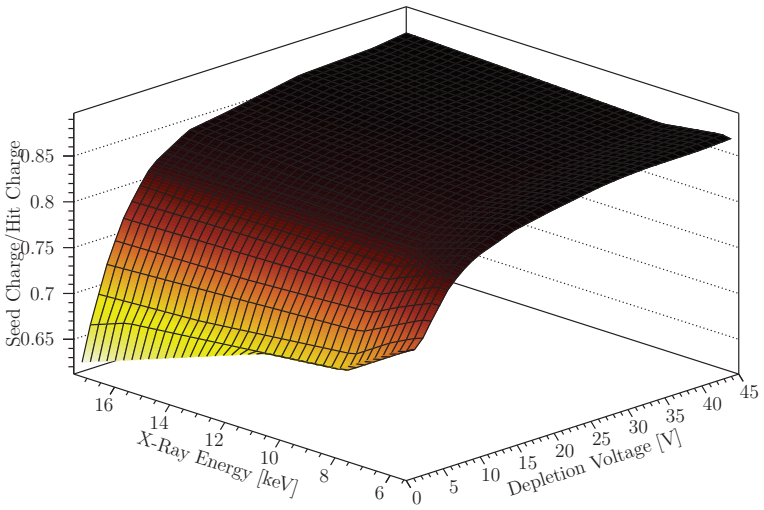

Figure 5.17: Map of the proportion of hit charge collected by the seed pixel versus the energy of the incoming photon and the applied depletion voltage in the thinned bulk substrate.

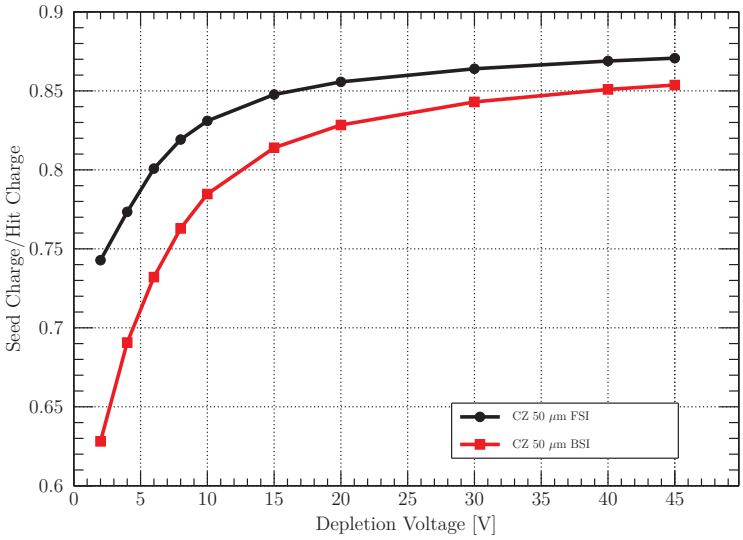

Figure 5.18: Proportion of hit charge generated by a ^{55}Fe source collected by the seed pixel versus the depletion voltage using a frontside illuminated, and backside illuminated 50 µm thick bulk PIPPER-2 sensor.

epitaxial layer (87 % at 45 V). At low biasing values, the proportion of charge collected by the seed pixel that have been generated by low energy photons is higher (75 %) than with photons of higher energies (60 %). This discrepancy is not present at higher biasing values (above 15 V).

The comparison between frontside and backside illumination of the bulk substrate using ^{55}Fe is presented in figure 5.18.

The ratio of charge collected by the seed pixel with backside illumination is smaller than with frontside illumination for any bias applied. With a 2 V bias, 63 % of the charge is collected by the seed pixel under backside illumination conditions while 74 % of the charge collected is in the seed pixel with frontside illumination. With increasing values of the depletion voltage, the difference tends to decrease: at 45 V, 85 % of the charge is collected by the seed pixel in backside illumination condition when 87 % is achieved with frontside illumination.

The discrepancy observed between frontside and backside illumination suggests that the sensor is not fully depleted. A charge generated in the undepleted volume will diffuse until being collected by the electric field of a depleted volume, which results in charge sharing. A small proportion of the electrons might recombine with a hole resulting in partial charge collection.

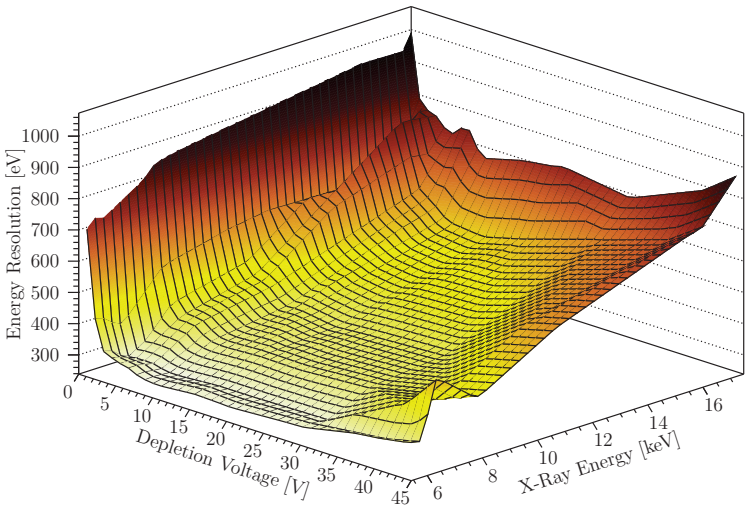

(a) Epi 18 µm

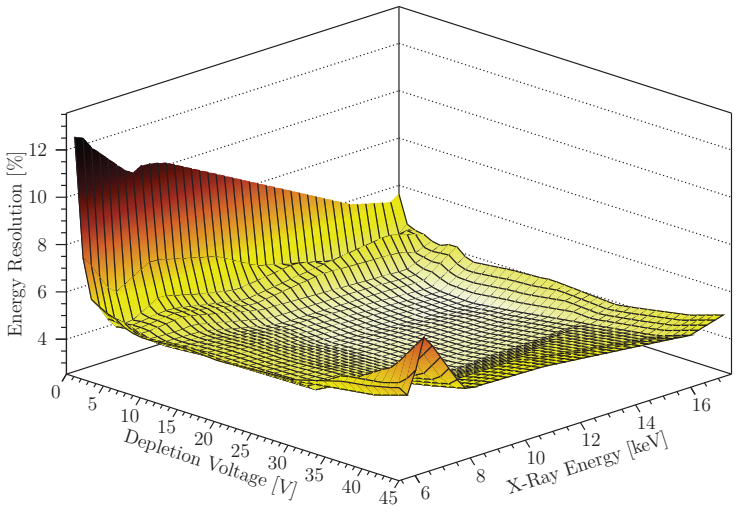

(b) Epi 18 µm

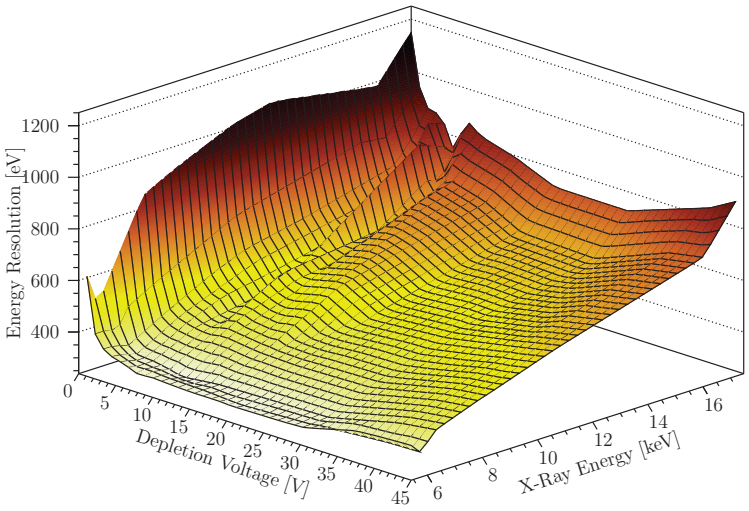

(c) Bulk 50 µm

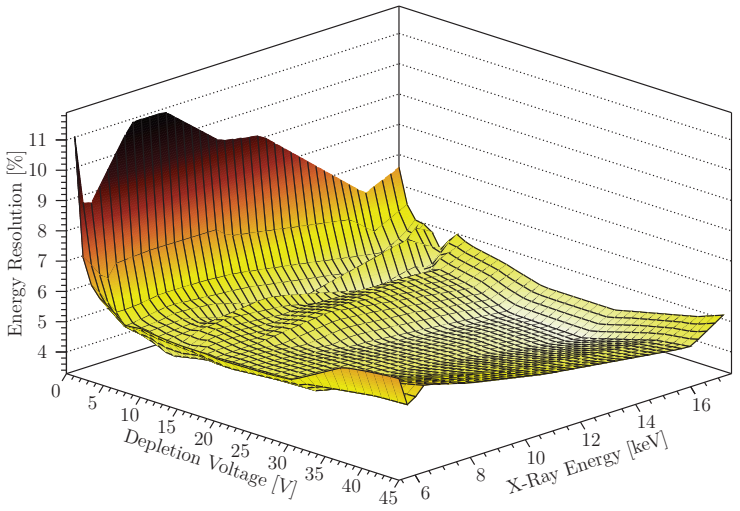

(d) Bulk 50 µm

Figure 5.19: Map of the measured energy resolution versus the energy of the incoming photon and the applied depletion voltage on each version of PIPPER-2 in eV (a, c) and as a proportion of the energy of the photon (b, d).

5.3.6 Energy Resolution

Readout noise is one of the components of the energy resolution (see chapter 3.1.2). With 24 electrons of noise, an energy resolution of 234 eV FWHM should be achieved.

Using the standard deviation σ of the Gaussian part of the Crystall Ball fits, the energy resolution is computed (FWHM= $2.355 \cdot \sigma$). For each type of substrate, the extracted values in eV are plotted versus the applied depletion voltage and the energy of the incoming photon (HR18 in figure 5.19a, and CZ 50 µm in figure 5.19c). The energy resolution with respect to the incoming photon energy is also shown (HR18 in figure 5.19b, and CZ 50 µm in figure 5.19d).

A resolution of 280 eV FWHM at 5.9 keV is achieved using the epitaxial layer version of PIPPER-2 biased at 8 V. For photon energies below 16 keV, with depletion voltages applied between 6 V and 30 V, the energy resolution reaches its best value (3–5 %) reaching its best value over the energy range at a bias of 10 V. Above 30 V applied, the energy resolution performance is degraded.

The same effect is visible in the bulk version of the sensor. Nevertheless, the best performance, slightly worst than in the thin epitaxial layer (4.5–6%), are obtained for voltages above 20 V limiting the range of operating voltages. An energy resolution of 288 eV FWHM at 5.9 keV is achieved at 30 V.

Using equation 3.4, the gain fluctuations are quantified. As an example, with the sensor fabricated on the thin epitaxial layer and biased at 8 V, the energy resolution achieved with illumination from ^{55}Fe is 280 eV FWHM with an equivalent noise charge (σ_{ENC}) of 22.5 electrons. With a Fano noise (σ_D) of 13.4 electrons, the remaining noise (σ_X), supposed to be caused by gain fluctuations in chapter 3.1.2 represents 20 electrons.

Since 5.9 keV photon generates 1640 electrons without considering the fluctuations from the Fano noise, the gain fluctuates by $\sigma_X/1640$ =1.2 %. With a measured mean gain of 16.5 µV/e$^-$, the fluctuation per electron is approximatively 200 nV, which is within the measurements uncertainties of the gain. The theoretical components of the energy resolution with the noise and gain fluctuations measured with the measured energy resolutions with PIPPER-2 fabricated on the epitaxial layer and biased at 8 V, value for which the best energy resolution is measured, are shown in figure 5.20.

The full resolution with the parameters allows the representation of the data up to 16 keV. Above (17.48 keV), the worsening of the energy resolution is linked to the non-

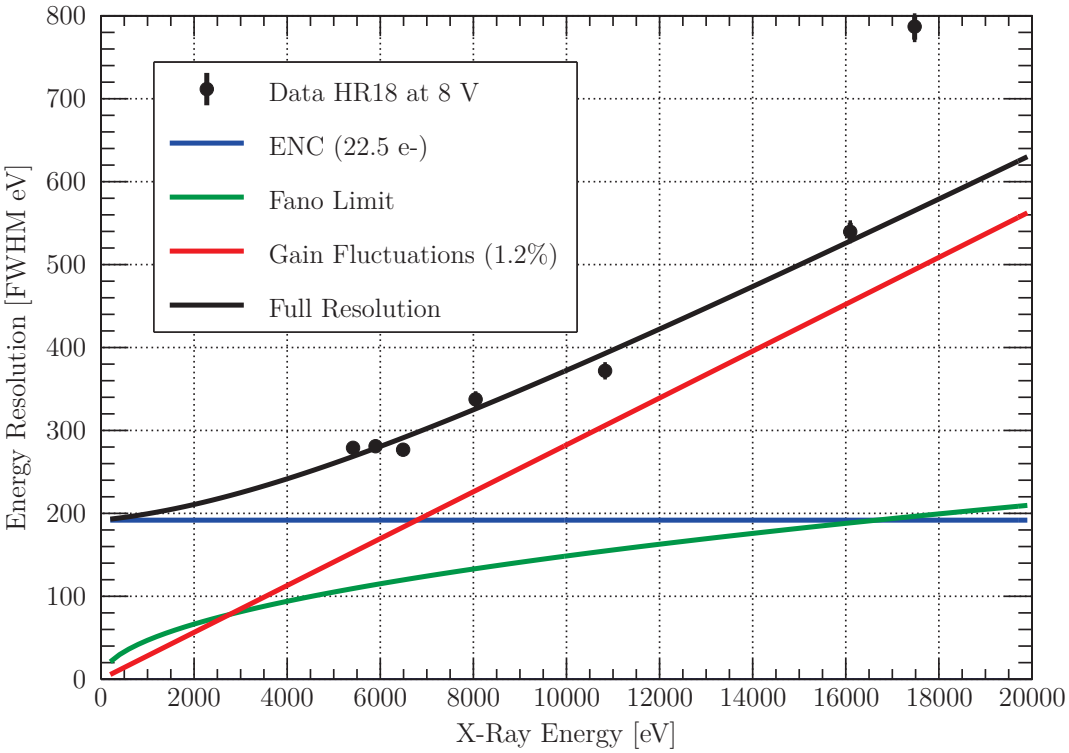

Figure 5.20: Energy resolution and its components versus the photon energy with an ENC of 22.5 electrons, and 1.2 % gain fluctuations. Measured energy resolution for PIPPER-2 built on the thin epitaxial layer and biased at 8 V

linearity. Below 7 keV, the energy resolution is driven by the equivalent noise charge while the gain fluctuations become the main component above this photon energy.

To reach the Fano limit for the lowest energies, the ENC must be reduced which can be achieved by increasing the gain of the amplifier in the pixel with the gain fluctuations kept as low as possible.

5.3.7 Effects of High Bias

With high bias, a tail is present on the high energy side of the calibration peaks which become broader and even merge (figures 5.9j, 5.9k, 5.9l, 5.8j, 5.8k, and 5.8l). More electrons than those generated by photons are collected suggesting an avalanche effect. Furthermore, if an additional gain from avalanche appears, its fluctuation will generate a new term in the energy resolution, which will get worse. The resolution indeed tends to increase beyond 40 V, as seen of figure 5.19.

5.3.8 Performance of Neutron Irradiated Sensors

A set of five HR18 PIPPER-2 sensors have been irradiated with neutrons at fluences from 10^{13} to 5×10^{14} $n_{eq}cm^{-2}$. The study was conducted by A. Perez Perez and the results

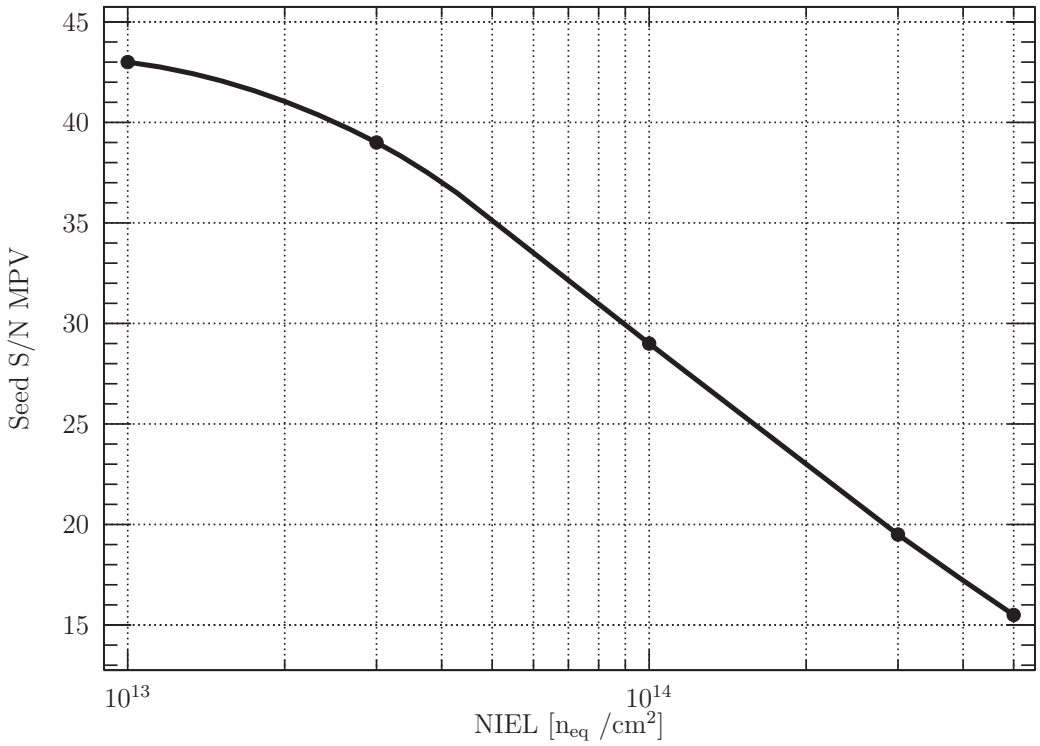

Figure 5.21: Seed signal to noise ratio MPV versus neutron fluence of PIPPER-2 fabricated on an 18 µm thick epitaxial layer biased at 20 V and cooled at -20 °C. Reproduced from A. Perez Perez in [156]

have been presented in [156]. A figure of the signal to noise ratio of the seed pixel versus the neutron fluence is reproduced in figure 5.21.

Although cooling to -20 °C, the noise after irradiation increases with respect to the noise before irradiation due to the contribution of the leakage current, while almost no signal loss was reported thus influencing the signal to noise ratio. The latter can be improved with faster readout to ensure that the charge is collected before recombination. For fluences up to 5×10^{14} $n_{eq}cm^{-2}$, the signal to noise ratio remained acceptable (≥ 15) for tracking purposes.

5.4 Example Application: X-Ray Fluorescence

Fluorescence tablets samples (Ti, V, Cr, and Mn) provided by the SOLEIL synchrotron have been used in the X-ray generator equipped with a copper tube. The resulting spectrum from the frontside illumination of a PIPPER-2 sensor fabricated on the 18 µm thick epitaxial layer is shown in figure 5.22.

With the background removed, the fluorescence peaks are easily discernable thanks to the good energy resolution of the sensor. From the position of the Cu calibration

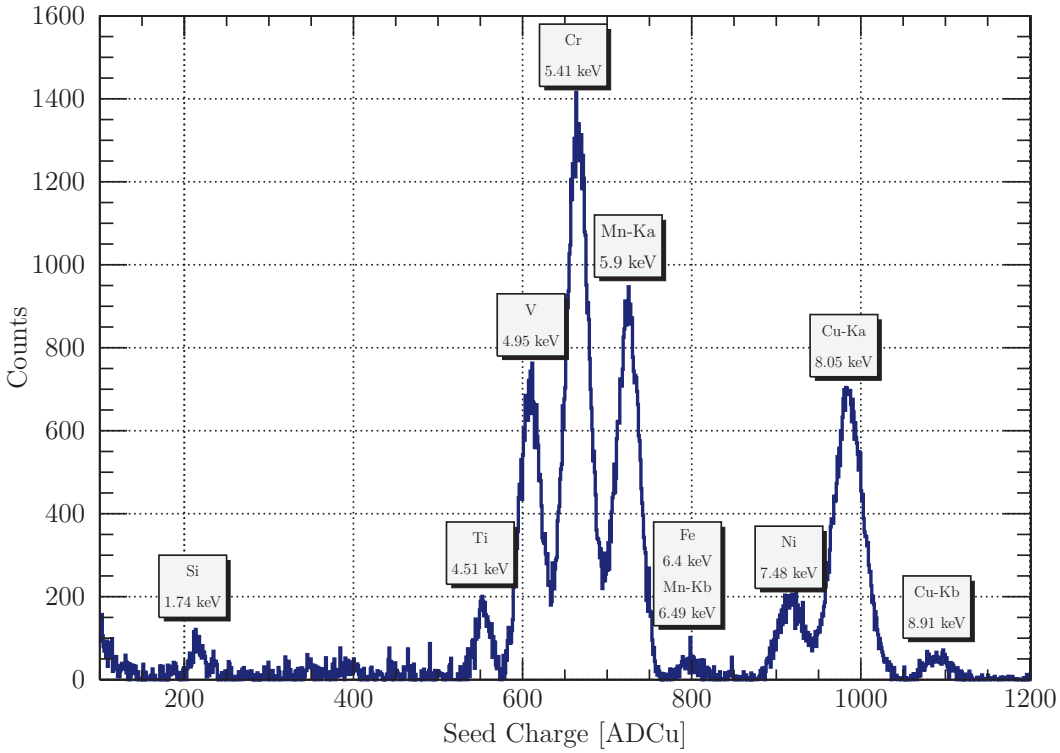

Figure 5.22: X-Ray fluorescence spectrum acquired with a HR18 PIPPER-2 prototype biased at 40 V. A Cu tube was used with Ti, V, Cr, and Mn samples. The peaks are labeled with the related element.

peak, the peaks corresponding to the samples are retrieved. The element corresponding to each peak is mentionned on the figure and the fit results are presented in table 5.2. The linearity is evaluated to 122.4 ± 0.247 ADCu/keV.

Table 5.2: Peak identification and energy resolution of the X-ray fluorescence spectrum (figure 5.22)

Element	E [eV]	μ [ADCu]	FWHM [eV]
Si	1740 ± 29.9	216.8 ± 0.4	[1]
Ti	4510.8 ± 29.9	554.1 ± 0.2	[1]
V	4952.2 ± 21.1	609.2 ± 0.1	250.9 ± 4.2
Cr	5514.7 ± 84.2	665.2 ± 0.1	267.2 ± 4.6
Mn-Kα	5898.8 ± 18.3	724.8 ± 0.1	269.7 ± 3.4
Mn-Kβ	6490.5 ± 8.7	796.1 ± 0.4	[1]
Ni	7478.2 ± 16.9	918.1 ± 0.3	299.9 ± 7.72
Cu-Kα	8047.8	985.8 ± 0.2	331.3 ± 6.3
Cu-Kβ	8905.3 ± 31.3	1087 ± 0.3	[1]

[1]Bad fit for the determination of σ

5.5 Conclusions

The PIPPER-2 sensor was characterized on each version of detection volume: an 18 µm thick epitaxial layer, and a ≈ 50 µm thick bulk substrate (40 µm sensitive with 10 µm process).

A small discrepancy in performance is observed between both versions of the characterized sensors, being slightly better in the epitaxial layer version. Nevertheless, with a mean noise of approximatively 23 electrons, and more than 90 % of the charge collected on the seed pixel, an energy resolution of 280–288 eV FWHM at 5.9 keV is achieved allowing soft X-Ray spectroscopy applications.

The comparison between frontside and backside illumination suggests that the bulk version is not fully depleted. The important study of the depleted depth and the sensitive thickness, driving the quantum efficiency for the detection of X-rays, is described in the next chapter.

Chapter 6

Discussion on the Depletion Depth Reached

The number of entries in a given spectrum, as presented in chapter 5, reflects the number of X-rays detected by the sensor, which is driven by the attenuation factor.
As the attenuation factor is driven by the sensitive thickness, the amount of entries obtained in a partially depleted sensor must be different with different biasing voltages of the diode. Thus, under the same illumination conditions, the ratio of entries obtained at two different biasing voltages of the diode is equal to the ratio of the two attenuations. If one thickness is known, the other can be indirectly determined.

6.1 Evaluation of the Depletion Depth Using TCAD Simulations as Reference

Attenuation of X-Rays in matter follow the exponential law described by equation 1.20 where μ, the attenuation power depends only on the energy. At fixed energy, the relative attenuation R of any sensitive depth x_1 compared to a reference depth x_0 can be computed.

$$R = \frac{1 - e^{-x_1 \mu \rho}}{1 - e^{-x_0 \mu \rho}} \tag{6.1}$$

This ratio corresponds to the ratio of entries in the corresponding spectra. Under the same illumination and readout conditions, at two biasing voltages, with N_0 the amount of entries in the reference spectrum and N_1 the amount in the spectrum of the condition to evaluate, the ratio is:

$$\frac{N_1}{N_0} = R \tag{6.2}$$

Equations 6.1 and 6.2 allow the determination of a depth from the ratio of counts and from a reference value:

$$x_1 = -\frac{\log\left(Re^{-x_0 \mu \rho} - R + 1\right)}{\mu \rho} \tag{6.3}$$

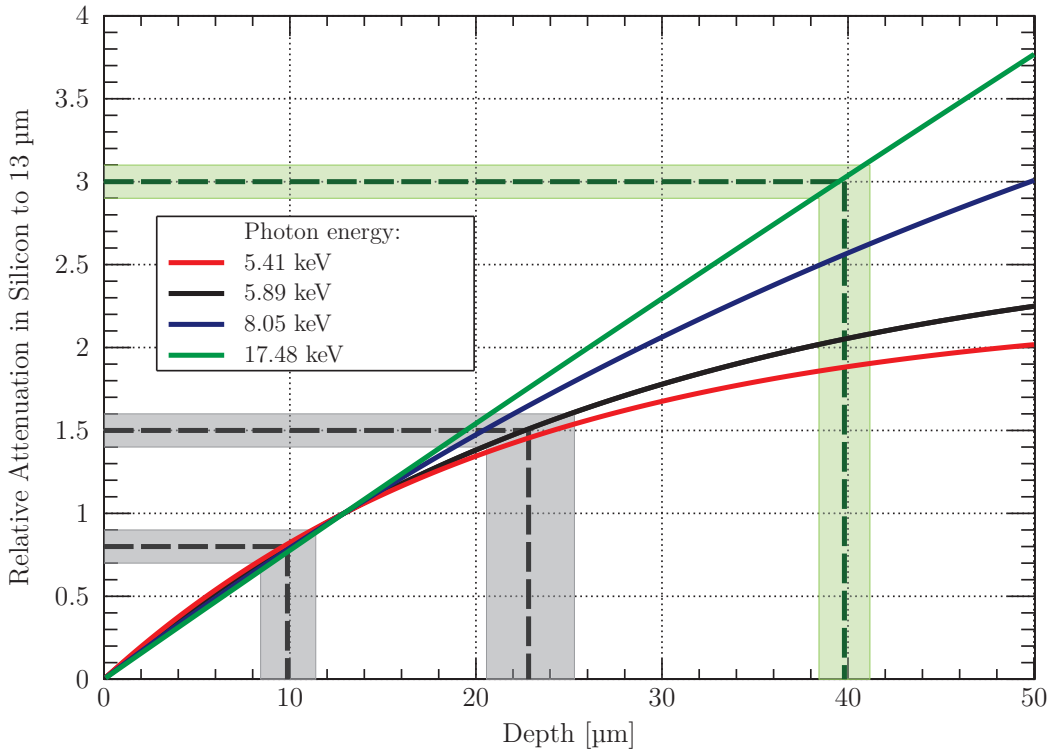

Figure 6.1: Relative attenuation to a fixed thickness (x_0=13 µm) for each sources used to characterize the sensitive thickness of the PIPPER-2 sensor. A relative attenuation below 1 between two different measurements suggests a sensitive depth below the fixed thickness while a relative attenuation above one between two measurements suggest a thicker depleted volume. With ^{55}Fe (μ(5.9 keV) =154.82 cm^2 g^{-1}), a relative attenuation of 0.8 evaluates the sensitive depth to x_1=10 µm when an attenuation of 1.5 gives a thickness of $x_1 \approx 23$ µm

Figure 6.1 shows the calculated curves for the relative attenuation of photons of four different energies (μ(5.41 keV) =194.92 cm^2 g^{-1}, μ(5.89 keV) =154.82 cm^2 g^{-1}, μ(8.05 keV) =62.64 cm^2 g^{-1}, and μ(17.48 keV) =6.17 cm^2 g^{-1}) to a reference depth of x_0=13 µm in silicon (ρ=2.33 g cm^{-3}).

The chosen reference for the sensitive thickness (x_0=13 µm) corresponds to the simulated value achieved in the epitaxial layer version of the sensor at a bias value of 40 V. The simulated depletion depth for a bias of 45 V was not considered because of the degradation of the collection by avalanche breakdown.

In the given example, a ratio of counts from ^{55}Fe illumination of 0.8 leads to an equivalent depth of x_1=10 µm. Twice the amount of entries with respect to the reference yields a thickness of $x_1 \approx 38$ µm.

With a relative attenuation value below 1, the relation between the ratio and the

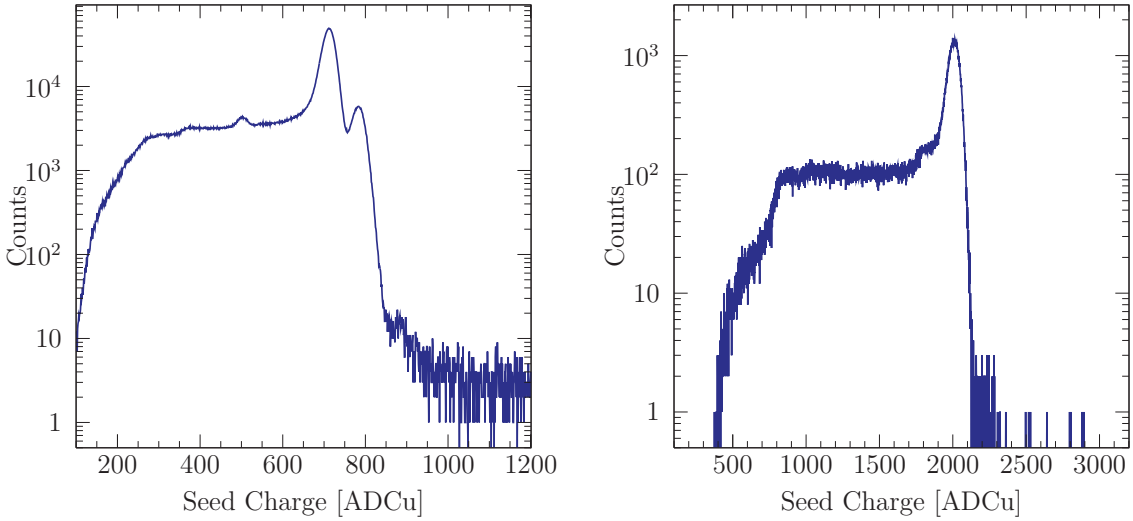

Figure 6.2: Seed charge histograms for selected hits on PIPPER-2 fabricated on the 18 µm thick epitaxial layer, diode biased at 30 V. (a) ^{55}Fe, hits above 250 ADCu, (b) 17.48 keV, hits above 800 ADCu

equivalent depth is relatively similar with each source. Also, the trend is more or less linear. For attenuations above 1, with decreasing photon energies, the equivalent depth is extending further for a given ratio, but the uncertainties also become greater since the curves tend to saturate. The trend of the relation between the ratio and the depletion depth with respect to the fixed value using 17.48 keV photons illumination is nearly linear. The use of higher photon energies reduces the uncertainty to probe the depletion depth over a longer distance.

6.1.1 Evaluation Using Selected Hits

For each configuration of sensor, voltage, and photon energy used, the seed charge spectra have been reconstructed (see chapter 5.2.2) with selected hits. Only hits where the total charge on the 3 × 3 cluster is above a limit in ADC units were selected (250 ADCu for ^{55}Fe, and 800 ADCu for 17.48 keV). Examples of seed charge spectra acquired with hits selected on PIPPER-2 HR18 are shown in figure 6.2.

The cut on the total charge allows a selection of hits generated by the source against noise, and against charges coming from the undepleted parts of the sensor (steering circuits, pads, edges of the matrix, etc.). Since the whole spectrum is used for the evaluation, shared charges are taken into account which might have been generated from undepleted regions. The evaluation thus gives an estimation of the distance up to which good collection occurs. The good collection distance corresponds to the depleted depth with the addition of a distance of undepleted region over which a large amount of the generated

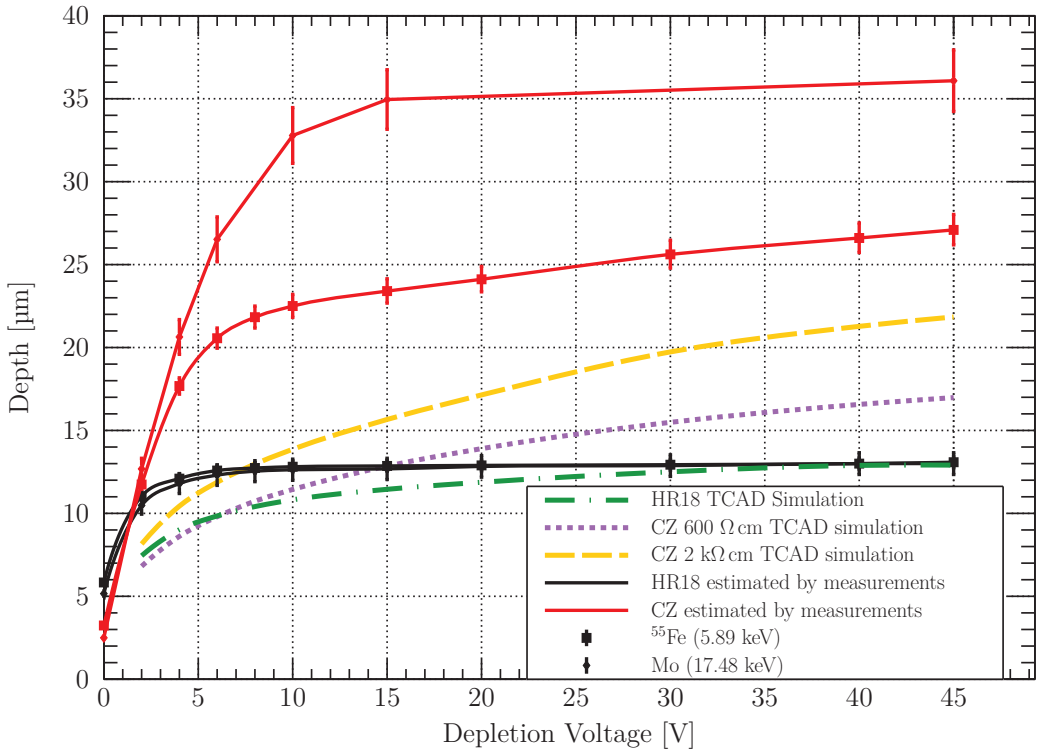

Figure 6.3: Estimated depth reached for good collection performance, using ratios of the total amount of entries in the seed spectrum for selected hits (above a minimum charge must be deposited) with a TCAD simulation result as a reference point: EPI 18 µm at 40 V evaluated at 13 µm.

charge is collected by the lower electric field and/or by diffusing into the depleted volume. The estimated good collection depths from the ratio of attenuations with a fixed depth (13 µm) as exposed in the previous section are shown in figure 6.3 and compared to the depleted depth simulated by TCAD (see chapter 4.3.3).

The behaviour of the depth estimated by measurement using ratio of the entries in the seed charge spectra for selected hits do not match the one expected from the TCAD simulations for the expansion of the depleted volume. The behaviour matches the behavior of the good collection depth where the electric field is estimated to be sufficiently strong to allow charge collection by drift before recombination (figure 4.19).

Since the collection depth saturates with voltages above 6 volts, good charge collection performance is achieved in the epitaxial layer even with moderate diode biasing voltages.

In the 50 µm thick sensor ($\approx$ 40 µm thick bulk substrate), a good collection of the charge generated by 5.9 keV photons up to 27$\pm$1 µm away from the collection point is observable.

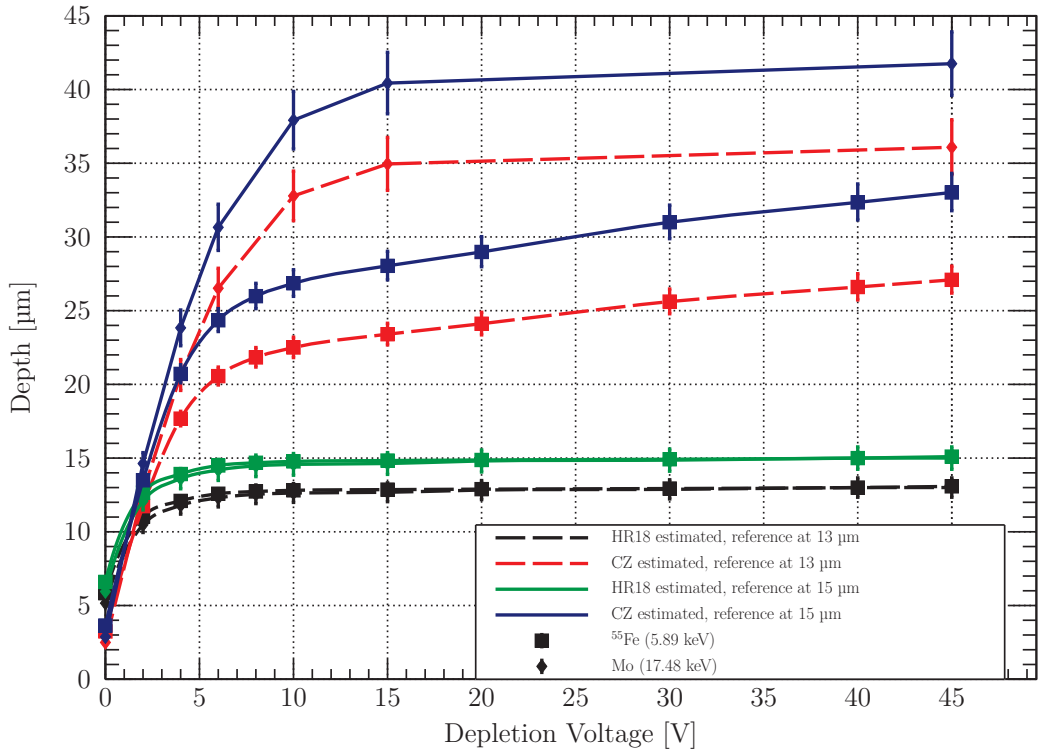

Figure 6.4: Estimated depth reached for good collection performance using ratios of the total amount of entries in the seed spectrum for selected hits (above a minimum charge deposited), reflecting a ratio of attenuations, with a TCAD simulation result as a reference point: EPI 18 µm at 40 V evaluated at 15 µm.

The estimated depth recalculated with a reference point at 15 µm is shown in figure 6.4.

In the epitaxial layer, the estimated depth is shifted from the previous values by 2 µm. Nevertheless, the thickness reached in the bulk substrate is shifted by 6 µm from the one obtained with the reference at 13 µm, reaching 42 µm, which is impossible as the thickness of the bulk is approximately 40 µm.

The reference must then be chosen wisely to prevent overestimation of the collection distances. For this reason, an other estimation method is proposed with the initial reference point at 13 µm.

6.1.2 Entries Count in a Finite Range of the Spectrum

For each depletion voltage applied on a PIPPER-2 sensor, the calibration peak on the seed pixel spectra resulting from a frontside illumination with a monochromatic X-Ray (examples in figure 5.8) is fitted using the Crystal Ball function (see figure 5.7), providing the peak position and thus the calibration factor. The integration in a given energy range (the limits are obtained with the calibration factor) of the peaks is performed, providing the number of entries in the calibration peaks to compare. This method is similar to the selection of single pixel hits which can only be possible for charges generated within the

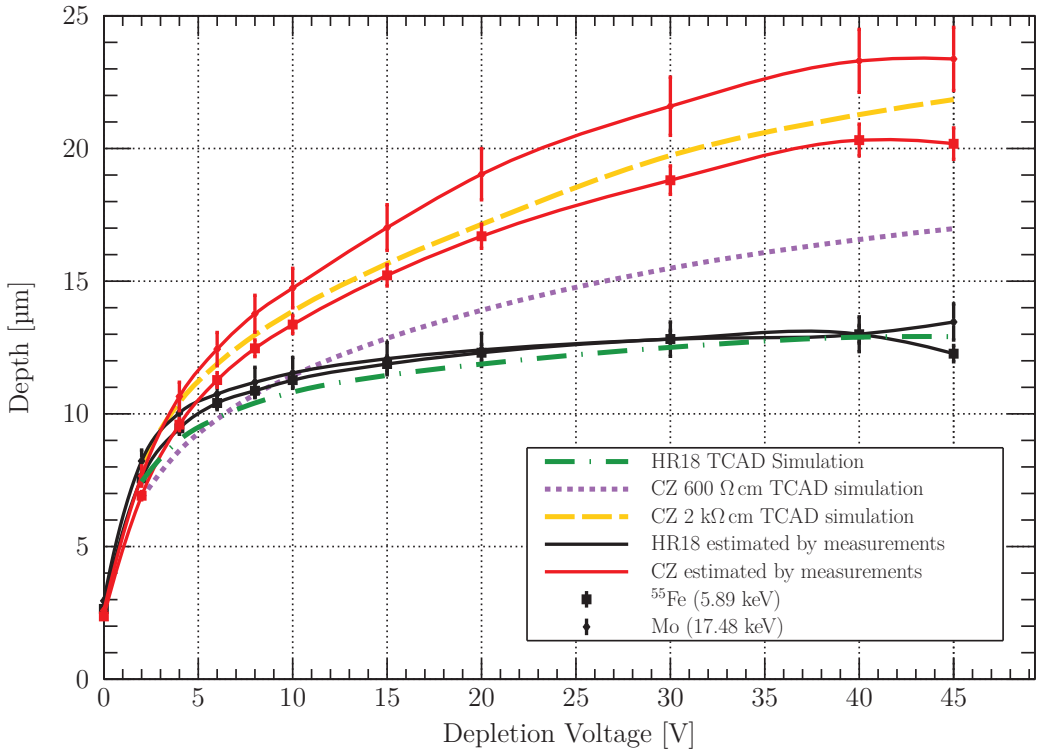

Figure 6.5: Estimated depletion depth using ratios of the amount of entries of the calibration peaks in the seed spectrum with a TCAD simulation result as a reference point: EPI 18 µm at 40 V evaluated at 13 µm. The behaviour of the extension in the epitaxial layer follows the TCAD predictions. The estimated depth in the bulk version reaches ≈20 µm suggesting that the effective resistivity of the substrate is around 2 kΩ cm.

depleted volume or at its close boundary. The integration ranges considered, that contain the calibration peaks (emission lines and harmonics), are:

- Cr: 4–13 keV
- ^{55}Fe: 4.9–7 keV
- Cu: 7–18 keV
- Mo: 14–20 keV

These ranges also set the limits of the Crystal Ball fits presented in figure 5.7.

The evaluated thickness of the depletion depth using the entries count in the calibration peaks is presented in figure 6.5.

The behavior of the extension of the depleted volume with increasing values of diode bias is much alike the simulated one for both types of substrate.
In the epitaxial layer version of PIPPER-2, a maximum discrepancy within uncertainties is observed for polarization voltages up to 10 V and becomes smaller with higher bias.
The extension of the depletion depth in the bulk substrate, guaranteed to be above

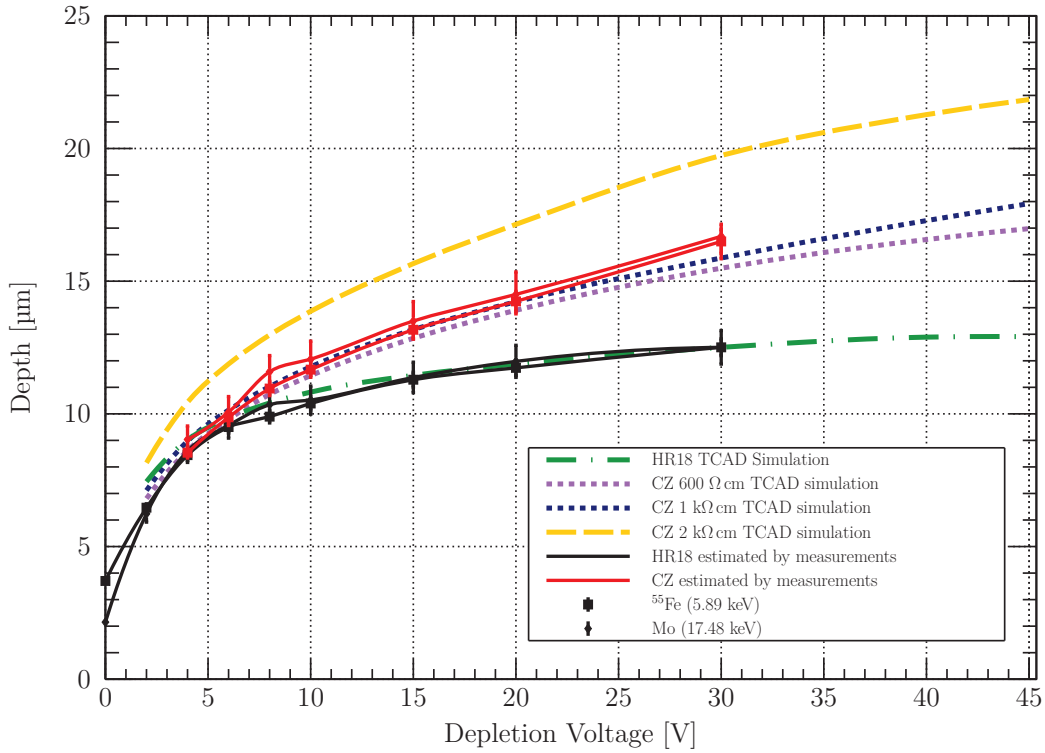

Figure 6.6: Estimated depletion depth in PIPPER-2 using the entries in the calibration peak ($\pm 3\sigma$)

600 Ω cm, from measurements with a ^{55}Fe and a molybdenum source surrounds the curve obtained from the simulation of a 2 kΩ cm bulk substrate. The thickness of the depletion depth obtained for measurements with an ^{55}Fe source reaches 20±1 µm. The value reaches 23±2 µm using the more energetic photons from the molybdenum source.

Due to the fact that charges generated in the undepleted volume at the edge of the depleted one have a high probability to be collected, the estimated depth is probably greater than the effective depletion depth. This conclusion is also sustained by the higher resistivity needed to reproduce these results (2 kΩ cm, which is much higher than the expected 600 Ω cm.

6.1.3 Entries in the Calibration Peak

The method presented in the previous section takes into account entries from partial charge deposition either between the main peak and its harmonic or below main line. Another method consists on integrating the entries under the calibration peak ($\pm$ 3σ). The obtained depth with a new reference (TCAD simulations of HR18 at 30 V: 12.5 µm) are presented in figure 6.6.

This method suffers from a high sensitivity to the charge sharing effects at lower voltage and from the avalanche effects at the highest biases. For these reasons, some

voltage points have not been considered. Nevertheless, the trend of the curves for each photon energy in each substrate types are similar and match simulations results.
In the CZ bulk substrate, the estimated depletion depth is lower than the one computed with the energy range method. As the curve matches the 1 kΩ cm simulation results, more inline with the expected 600 Ω cm, the depletion depth at 45 V is estimated to 18±1 µm.

6.2 Conclusions and Proposals to Map the Shape of the Depleted Volume

Various methods have been presented to evaluate the depletion depth reached in the bulk substrate from measurements using lab sources. Using the TCAD simulation results, and the amount of entries in the calibration peaks from various X-Ray sources, the depth reached is estimated to ≈ 18±1 µm. Unlike the epitaxial layer version, the bulk sensitive volume is not fully depleted, but feature collection close to the full depth.

The calculated values presented in this chapter depict the maximum depth reached and do not give indications on the shape of the depleted volume. Using a synchrotron pencil beam (in the micrometre range), with various energies, a single pixel area can be scanned to reconstruct the map of the collected charge. A three-dimensional map could be reconstructed to observe the shape of the depleted volume. It could also be performed using a telescope with excellent spatial resolution and a beam using MIPs.

Part III

Sensor Development

Chapter 7

Design Oriented For High Counting Rate

Beyond the standard figures of merit, such as energy resolution, and quantum efficiency, high-performance X-ray detectors are required to cope with a high photon flux. To benefit from the energy resolution provided by the depletion strategy followed in the PIPPER concept implies to shorten the CDS readout scheme.
The challenge to overcome the limitations of the current design for fast repetitions of hits are discussed. Also, a proposition of an architecture to achieve better energy resolution is presented. The designs presented in this chapter have been studied using the AMS 180 nm design kit.

7.1 Limitations of Fast Repetition on AC-Coupled Pixels

The application of the depletion voltage at higher values than the breakdown limit imposed by the foundry from the frontside of the sensor inhibits the use of a reset transistor such as in a three transistors pixel architecture. For this reason, the bias is applied through a forward biased diode (figure 7.1).

The presented architecture is the one used in the PIPPER-2 sensors. Nevertheless, the main limitation caused by the absence of a resetting device is visible with hits with high repetition rate. The simulated behavior of the collecting node under highly repetitive rates is presented in figure 7.2.

From ≈ 820 µs to ≈ 935 µs, 1 000 electrons are injected every microsecond. The pixel is read-out every 10 µs. The pixel can integrate approximatively 50 000 electrons before reaching its full well capacity indicated by the flat shelf. The hits beyond this limit are not seen by the collecting diode.

As a result of charge transfer through the coupling capacitor, successive voltage drops of same magnitude than on the collecting node (IN) are visible on the gate of the source follower. The DC-point set by V_{pol} complies with the requirements on breakdown voltage

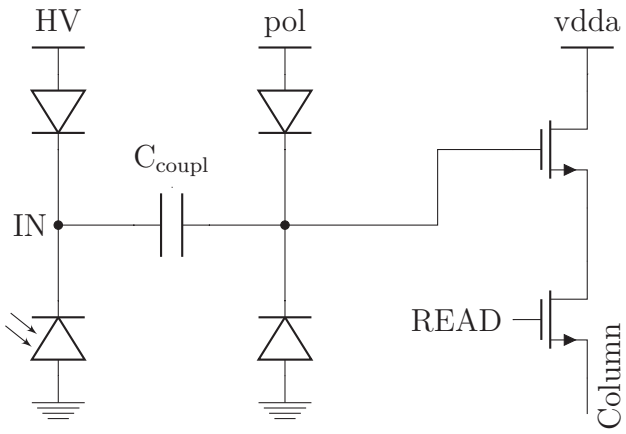

Figure 7.1: Schematics of the PIPPER-2 pixel. The substrate is polarized from the top through a forward bias diode and the collecting diode. The collection node is AC-coupled (C_{coupl}) to a source follower. A set of diodes after the coupling at the input of the amplifier is used to set the DC point.

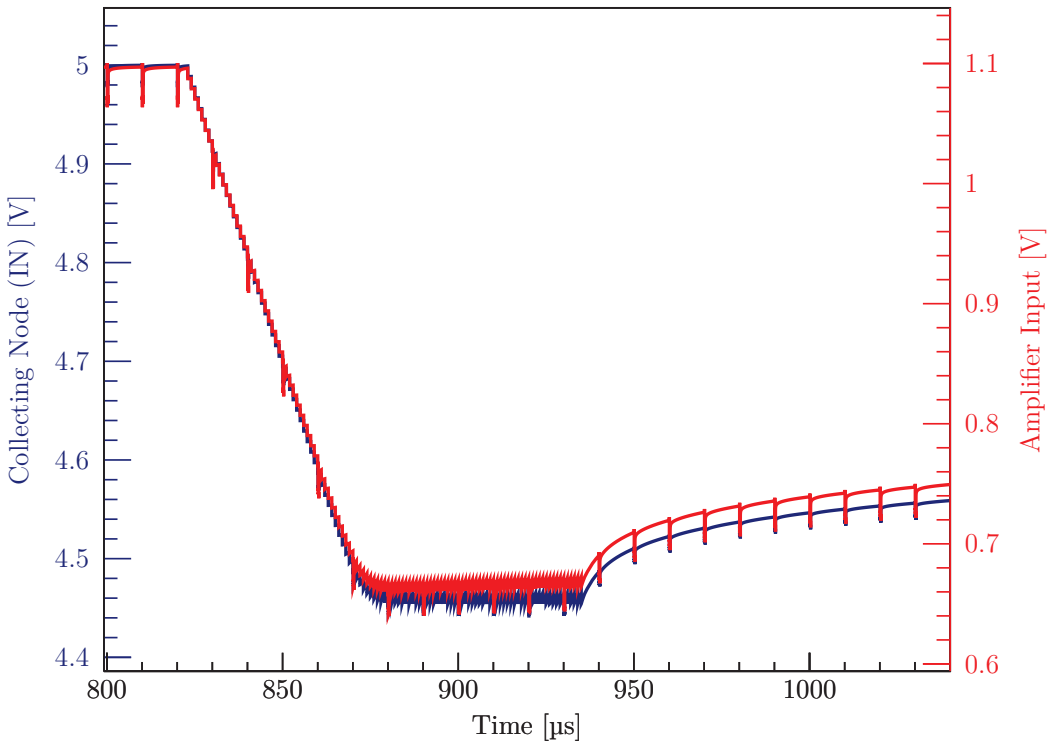

Figure 7.2: Simulated voltage variations of the input node of the PIPPER-2 (HV=5 V) pixel with successive hits (1000 electrons every microsecond). In the absence of reset techniques, full well (see chapter 3.1.1) is reached for 50 000 electrons. When the illumination is stopped, the node starts its slow reset

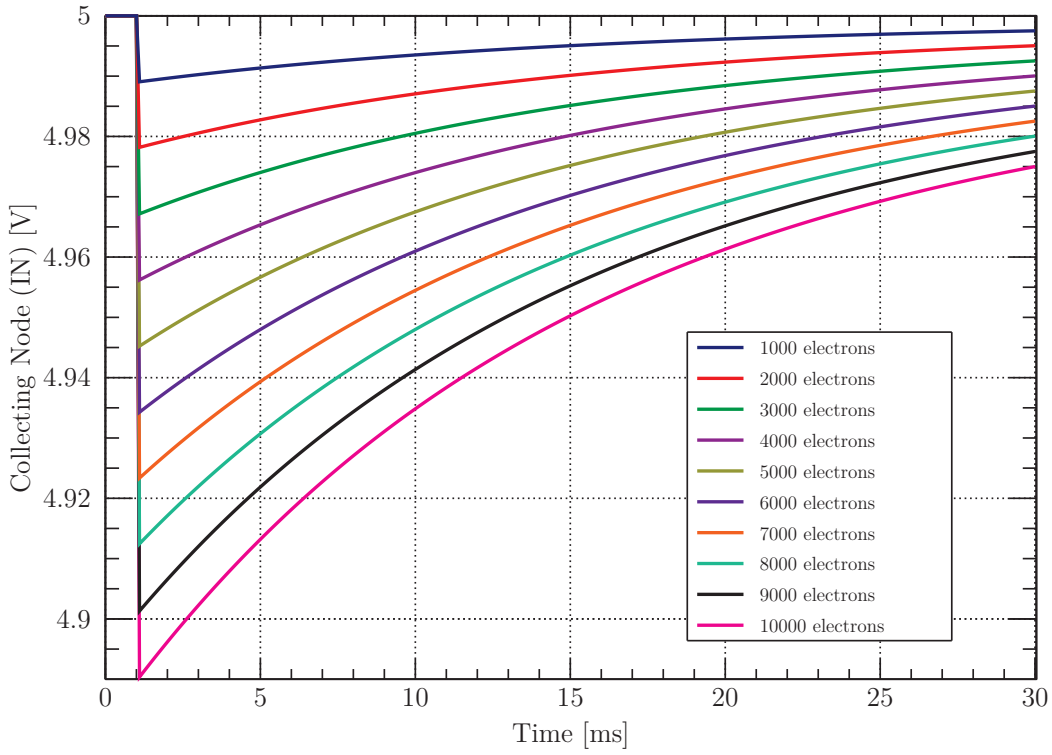

Figure 7.3: Discharge of the collection node after a single injection of charges (1000–10000 electrons)

of the technology.

Once the illumination is stopped, the baseline of the pixel gets restored at a very slow rate which becomes incompatible with very high rates. A simulation of the collection node (IN) discharge for different quantities of charges injected is shown in figure 7.3.

Once the charge is injected (at 1 ms), the node is slowly discharges and requires several tens of milliseconds to reach its initial value. A time constant of ≈ 18 ms is evaluated. A resetting method has to be introduced to overcome this limitation.

7.2 Diode Reset with High Voltage Bias

The standard architecture of a 3T pixel is only composed of NMOS transistors. With the quadruple well technologies offering the possibility to use PMOS transistors within the pixel area without competing with the collection node, the architecture of an AC-coupled 3T pixel with a PMOS as the reset transistor is presented in figure 7.4.

The main particularity of the presented schematic is the bulk connection of the reset transistor. Instead of being connected at the vdda value (1.8 V in 180 nm processes), it is either set to the depletion voltage bias (HV) or to the input node (which is equivalent

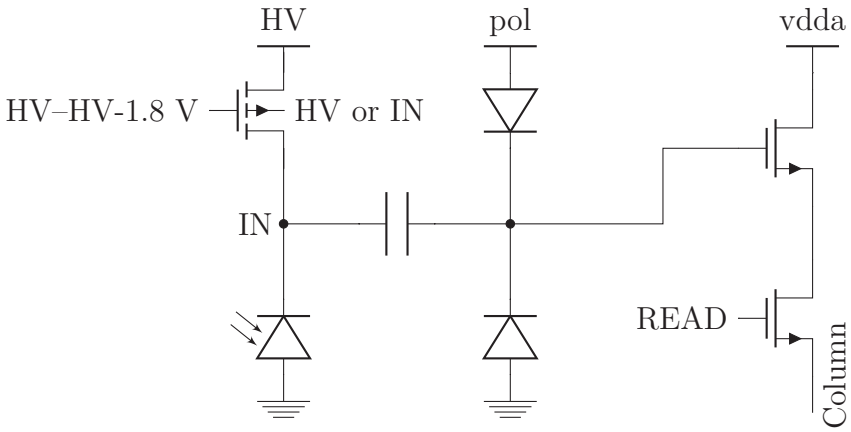

Figure 7.4: Schematics of a pixel with reset capabilities while biased from the top. The collection node is AC-coupled to a source follower. The forward bias diode is replaced by a PMOS acting as a reset switch. The bulk of the transistor is connected to a high voltage either HV or IN. The gate voltage swings between HV and (HV-1.8 V).

to HV before illumination).

When the gate of the reset transistor is connected to HV, the equivalent structure is a reverse biased diode. The resetting operation makes the switch to close, which in the present case can not be performed by applying the gate voltage to 0 V because gate–bulk voltage will be above the breakdown limit imposed by the technology. Thus, the gate of the reset transistor must swing between HV and HV-1.8 V.

The command can not be generated nor propagated in the sensor during the rolling shutter readout. Such signal can only be used for a global reset of the sensor once in a while, introducing a dead time, which might not be a serious issue with the application (eg. between two bunches of X-Rays).

Simulated behaviours of the input node for both bulk connection configuration with the same hit rate as in figure 7.2 is shown in figure 7.5.

In both configurations, a behavior comparable to the forward biased diode structure is observed. With the accumulation of hits, the input node is saturated and discharges slowly (at different rates with each connection arrangement) when the injection is stopped. At 1 ms, a reset signal is sent to the pixel. The input node immediately returns to its baseline allowing the detection of a new bunch of photons. Nevertheless, an overshoot exists, which might cause observation of fake hits depending on the threshold, and must return to its initial and stabilized value. The input node of the amplifier requires its individual resetting system.

With a reset every microsecond, from the simulation results, a flux of 70 000 photons of

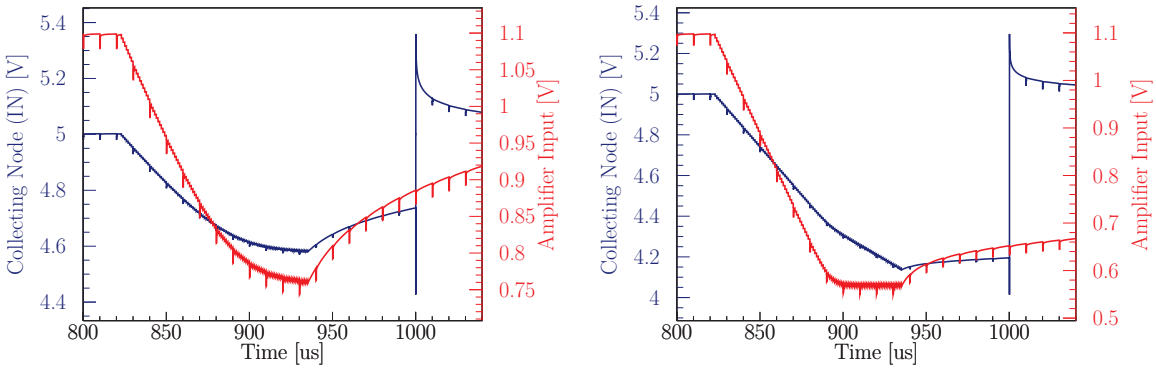

Figure 7.5: Simulation of the input node of the PIPPER like pixel with reseting capabilities. The bulk of the PMOS is connected to HV in (a) and to IN in (b). Such as the PIPPER-2 pixel version, full well is reached after a large amount of electrons have been collected, and the diode discharges slowly when the illumination is stopped. When the reset transistor is opened, the diode is quickly reset.

1 keV per pixel per second can be considered. Higher rates can be reached with higher reset frequencies.

7.3 Low Noise, Low Dispersion Amplifier

Another important parameter for low energy radiation detection at high rate is the capability to perform the detection operation while keeping a low level of equivalent noise charge when amplifying the signal. For soft X-rays spectroscopy purposes, achieving excellent energy resolution performance requires low noise structures and low gain dispersion as described in chapter 5.3.6. The schematic of a proposed low noise, low gain spread amplifier with resetting possibilities is shown in figure 7.6.

The AC-coupled collection node of the proposed architecture is similar to the PIPPER-2 sensor. It is followed by a cascode-based CSA [11] whose feedback capacitor is kept as low as possible ($\approx$ 1 fF) by using the parasitic value of a small custom fringe capacitor to achieve high gain.

The feedback capacitance can be discharged using a reset transistor that connects the output and the input of the integrator. The cascode stage is only powered when in use to minimize the power dissipation over a full-scale sensor. The high gain stage is followed by a source follower as a buffer to the column readout bus.

Particular care to the scaling of the input transistor is necessary to minimize the gain dispersion. The simulation results of the input node of this amplifier is shown in figure 7.7 for similar hit rates than previously presented.

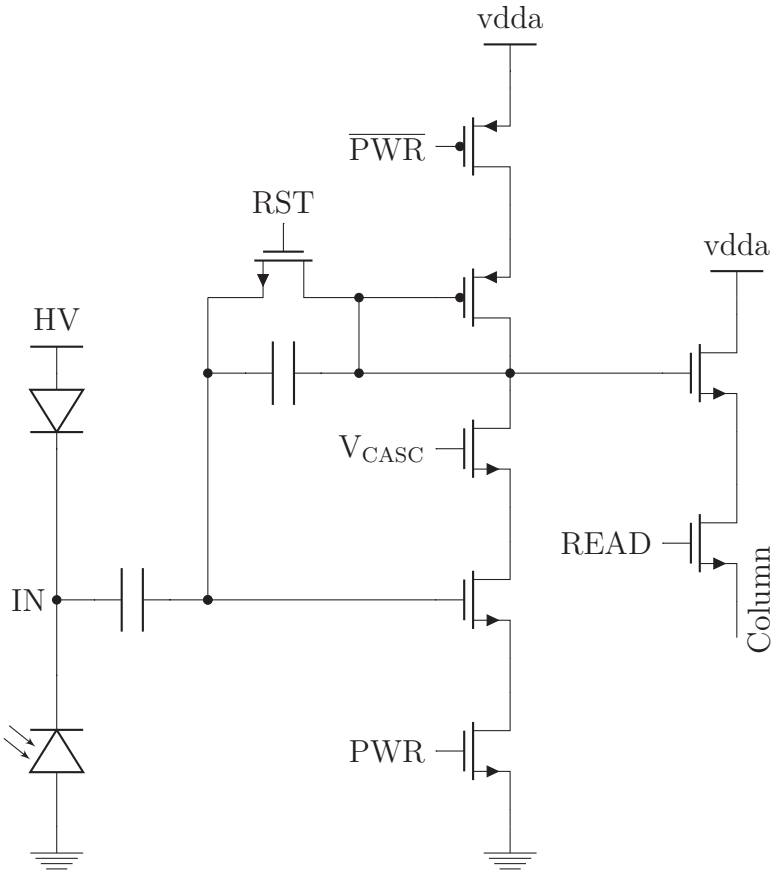

Figure 7.6: Schematics of a low-noise, low dispersion pixel architecture. The substrate is polarized from the top through a forward bias diode and the collecting diode. The collection node is AC-coupled to a CSA composed of a cascode stage with power pulsing. The feedback capacitor can be shorted to reset the input node. The integrator is followed by a source follower to perform impedence adaptation.

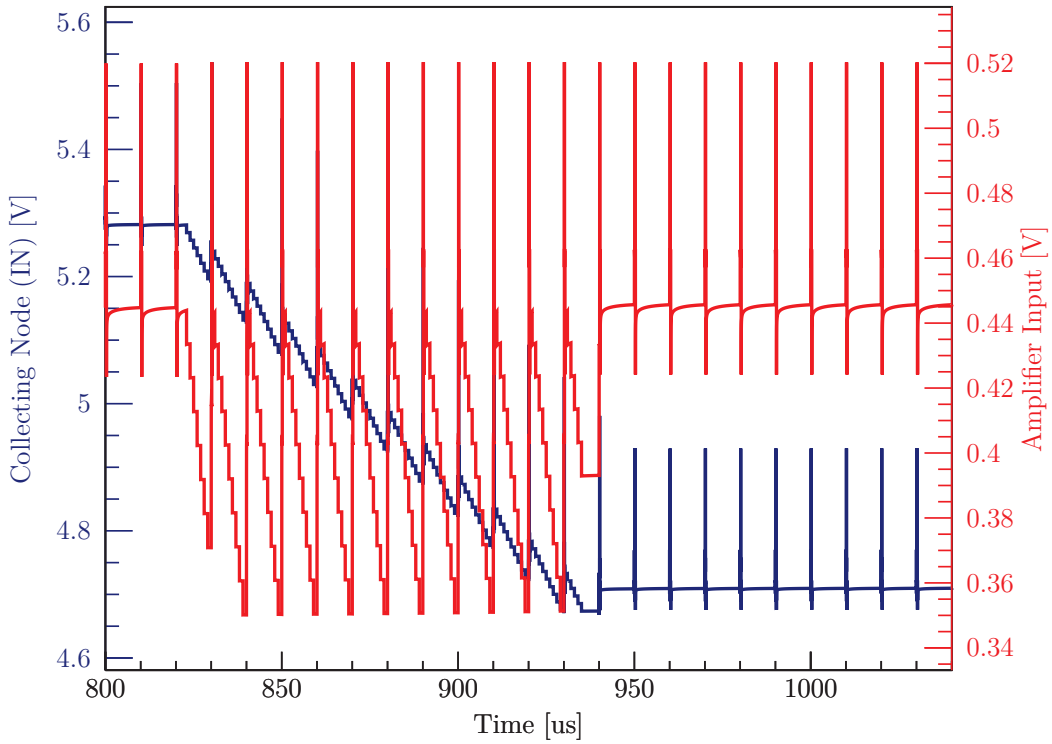

Figure 7.7: Input node of the low noise, low dispersion pixel architecture based on a CSA.

During the reset process of the feedback capacitance, the fast voltage change of the input node of the amplifier allows charge transfer to the collecting node which is partially restored. In the absence of hits, the reset on the amplifier side has no effect anymore on the input node of the detector and the input node discharges slowly as in the current PIPPER-2 architecture (figure 7.3) and does not cope with high photon flux. The input node reset method presented in section 7.2 could be implemented to overcome the limitation. The spikes every 10 µs, corresponding to the reset with small contributions from the pixel selection and powering of the amplifier, can be safely ignored as the sampling operations are performed on stabilized signals (shown in figure 7.8).

7.4 Simulated Performance of the Architectures

The proposed architecture have been designed by myself (with punctual help from Maciej Kachel, Frederic Morel, Grégory Bertolone and Isabelle Valin), in standard AMS-180 nm technology. The equivalent noise charge has been extracted along with the gain spread using Monte Carlo distribution on the post-layout extracted view.

The PIPPER-2 equivalent architecture present as a reference has a simulated equivalent noise charge of 26 electrons with an energy resolution of 250 eV at 5.9 keV. These simulated values are not far from the characterization results from the TowerJazz proto-

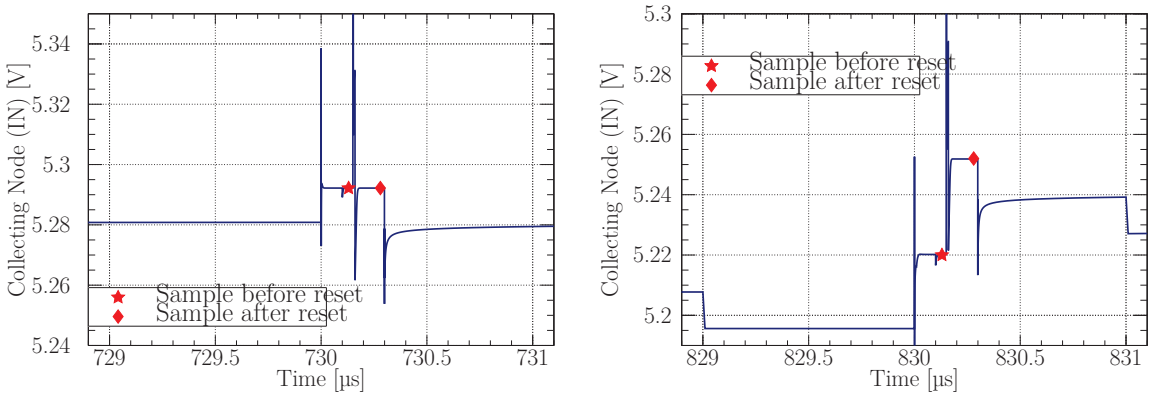

Figure 7.8: Sampling around the resetting operation of the CSA with no charge integrated (a) and after charge integration (7000 electrons) (b)

type. Nevertheless, simulations results does not give a precise value on the noise that can be measured and the uncertainties can not be estimated from previous designs as it is the first attempt for such architecture using the AMS 180 nm process.

The pixels using active reset demonstrate a simulated noise of 50 (bulk connected to HV) and 28 electrons (bulk connected to IN) with an achieved energy resolution of respectively 430 and 270 eV. The discrepancies can be explained with a higher current consumption in the architecture where the bulk is connected to HV (higher resistance). These architectures have not been designed to achieve good performance but to prove the possibility of resetting the input node with frontside depletion.

The high gain architecture has a simulated noise of 11 electrons, that with the restrained gain dispersion, allows a simulated energy resolution of 160 eV. A fast amplifier with excellent detection performance (and linearity) can be used either in a integrating sensor or in a counting architecture. The latter would require additional features to the proposed architecture (shaper, discriminator etc.).

7.5 Prototype Production

With a 5 mm^2 free AMS-180 nm miniasic run granted through the EUROPRACTICE First User stimulation programme (along 10 selected projects in Europe), the presented architectures are being produced. The layout of the pixels are shown in figure 7.9.

Unfortunately, the prototype is being produced on a standard p-type substrate, and the pixels will not be tested with depletion. Also there is no opening between the wells around the collecting diode, and the PMOS transistor is not isolated from the substrate

by a deep P-well as in the TowerJazz version.

The four pixel variations have been included in a PIPPER floorplan to use the existing PCBs and testbenches. At the time this chapter is written, the sensors are being produced and are expected to arrive in September 2018.
Although no depletion will be applied to the pixels, the figures of merit of each version, with particular care on the low-noise, low-dispersion amplifier will be characterized to evaluate the influence of the proposed structures (the PIPPER-2 like pixel as the reference). The reset technique will be tested by illuminating the sensor with a laser to reach full well.

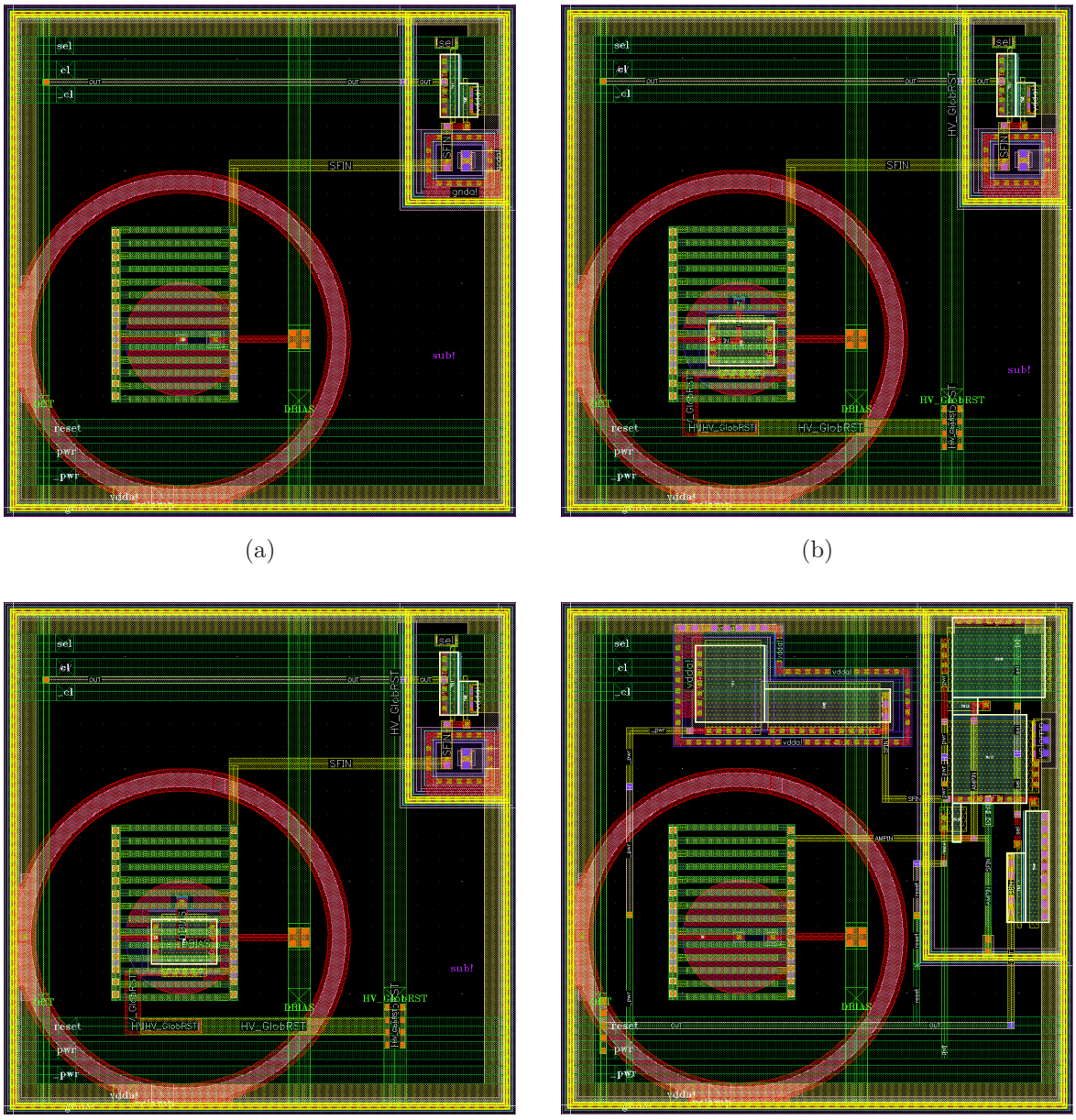

(a) (b)

(c) (d)

Figure 7.9: Layout of each pixel presented in this chapter in AMS-180 nm. (a) PIPPER-2 equivalent, (b) Source follower pixel with a resetting PMOS whose bulk is connected to the input node, (c) Source follower pixel with a resetting PMOS whose bulk is connected to HV, (d) Low noise, low dispersion amplifier variant.

Chapter 8

Low Power Sensor Design

The previous chapter discussed the optimization of designs for soft X-rays applications. In this chapter, an application on beta imaging is discussed: neuroimaging on an awake and freely moving rats.
A needle-shaped probe will be inserted in the brain of the rodent leading to strong constraints on the shape of the sensor to limit invasivity, and on the dissipated power. The motivations and constraints are first discussed followed by the detector development and validation. The integration of the final setup is finally presented.

8.1 Neuroimaging on Awake and Freely Moving Rats

Precautions have to be taken when translating functional neuroimaging results acquired in anesthetized animals to conscious humans [157]. The effects of anesthesia on the functions are beyond a simple loss of consciousness to permit easy manipulations of the subject. Anesthesia has considerable effects on multiple physiological processes and also affects neural and vascular responses. Also, positron emission tomography (PET) imaging on an unanesthesized but highly restrained rodent may result in non-awaken brain functions [158]. Furthermore, PET imaging combined with behavioural studies may be the key to increase knowlegde on functional processes in the brain [159]. Real time monitoring of molecular processes of neuronal communication during behavioural studies will assess the validity of preclinical studies in drug development [160] by being able to compare animal to human behaviour.

Multiple approaches have been developed to partially achieve these goals using PET imaging:

- The easiest method consists of conducting anesthesized imaging preceeded by behavioural experiments, prohibiting real time analysis without being able to overcome all the limitations [161].

- A second method uses motion tracking techniques to follow the movements of the rodent position inside a PET gantry limiting behavioural studies possibilities to be performed in the field of view area [162].

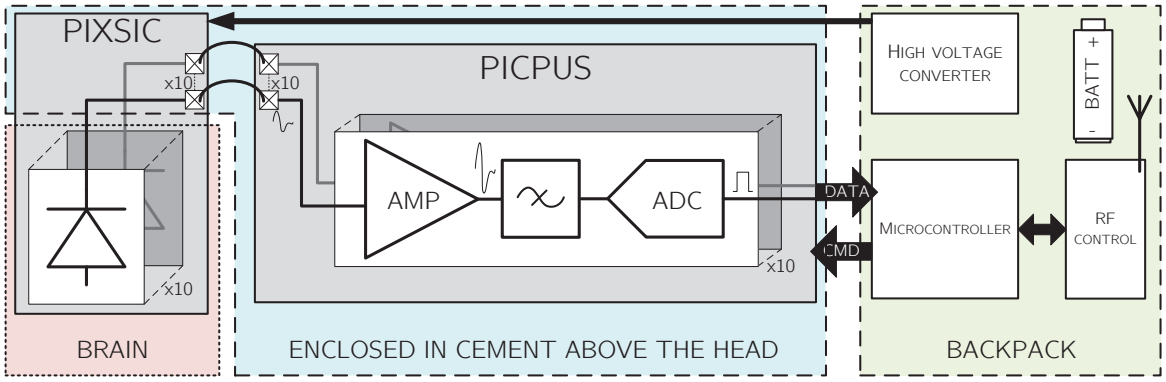

Figure 8.1: Schematic of the PIXSIC setup. The needle probe implanted in the brain is composed of 10 passive pixels, each directly wire-bonded to one channel of the readout chip: PICPUS. This chip embeds amplifiers, filter, digitisation, and memories, and is enclosed in dental cement above the skull. A micro-controller steers and gathers data from the readout chip. It is located on a backpack carried by the rodent during experiments. It also embeds active and passive circuits for the polarisation of the sensor and readout chip, and a battery for full autonomy.

- The *RatCAP* is a wearable PET scanner scaled to the size of the rodent's head and capable of performing full brain images on awake and freely moving subjects. However, the weight and the size of the device requires to be held by an articulated arm therefore limiting the movements of the rodent within a limited area [163].

Another approach is to get rid of PET imaging by performing invasive measurements using a positron sensitive probe implanted in specific regions in the brain by stereotaxic surgery. Two variants of probes have been developed:

- SIC (*Sonde Intra-Crânienne*) [164, 165] is an implanted scintillator which is either a plastic scintillator developed at IMNC and at the PET center of University Hospital of Zurich (β-probe) [166], or a LSO crystal developed at the Brookhaven National Laboratory (NY, USA) [167]. An optical fiber connects the scintillating probe to a photomultiplier tube operated in single photon counting mode. The presence of the physical connection is still resticting the possibilities of behavioural studies.

- PIXSIC (PIXelated *Sonde Intra-Crânienne*) [168, 169] is the first attempt of using a pixelated needle-shaped silicon probe in the brain. A scheme of the setup is shown on figure 8.1. The system is composed of an implanted silicon probe with 10 passive pixels of 200 $\times$ 500 µm^2 arranged in a single column. It allows direct detection of positrons and thus localisation of the clusters of radiotracers close to the sensor. A second probe is implanted in a non-specific region to monitor the response in absence of radiotracers as a reference. The principle is shown in figure 8.2. However, the 511 keV γ-rays resulting from electron-positron annihilation are also detected by

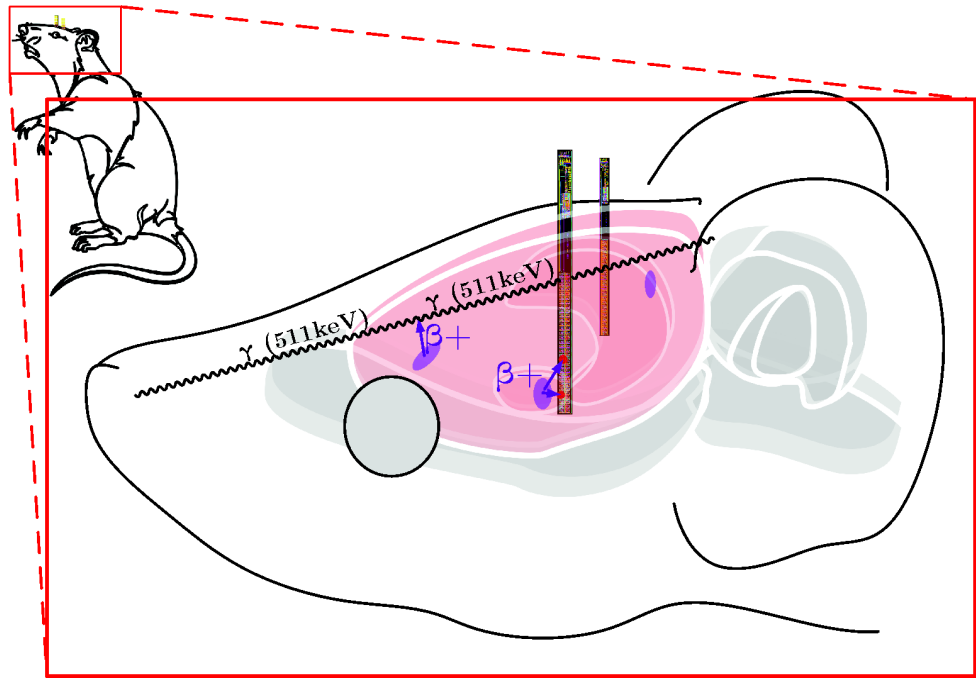

Figure 8.2: Principle of invasive measurements using positron sensitive probes. A sensor close to the radiotracers clusters can detect positrons while a second sensor away from the clusters, in a non-specific region, allows the monitoring in absence of close positrons. Usually, the radiotracers are used as a 511 keV annihilation photons emitter. The sensors must remain insensitive to these gamma-rays.

the sensor producing an unwanted signal especially when arriving from non specific regions such as the bladder. To minimize the detection of the γ-rays, the sensor is thinned down to 200 µm. But, it still exhibits too high sensitivity while becoming quite brittle making manipulation and implantation challenging [170, 171]. The sensor is readout using an ASIC named PICPUS which is enclosed in dental cement above the head of the rodent. Both the probe and the PCB holding the ASIC are coated in a biocompatible polymer.

While invasiveness of this technique is a major point of concern, no impact from the small-size probe direct implantation was observed. However, the PIXSIC setup suffers from two main limitations: first the length of the metallic lines that connect pixel sensors to their pre-amplification stages on the PICPUS readout chip induces EM pickup, which reduces signal over noise ratio and hence the overall probe sensitivity. The second weak point of PIXSIC pertains to the thickness of the passive sensor, which is constrained by antagonist requirements. On the one hand, mitigating the sensitivity to γ-rays generated by electron-positron annihilations, whose positions are not necessarily near the probe, requires a thickness as small as possible. On the other hand, a relatively thick sensor is beneficial to mechanical stiffness. A compromise of 200 µm thickness was chosen for PIXSIC, though it was not really

satisfactory for neither the constraints.

The usage of monolithic active pixels sensors (MAPS) was proposed [172] to improve the implanted probe concept. MAPS can embed an amplification and digitisation stage in each pixel, basically replacing the PICPUS chip and suppressing *a priori* sensitivity to electromagnetic environment. Since the amplification allows a small primary signal, the sensitive thickness can be thinner than the overall sensor thickness. Hence a depth of typically a few tens of micrometers generate enough signal for efficient detection and does not need to extent to the full sensor thickness also limiting its sensitivity to γ-rays. The thickness can be optimally set with respect to invasiveness and stiffness. In addition, the probe integration is simplified due to the absence of an additional circuit on the rodent head, as depicted in figure 8.3.

However, the usage of an implanted active sensor can only be effective under the condition that the local temperature is marginally affected by the probe operation (typically ΔT <1°C). Consequently, a key design feature is the power dissipated by the sensor.

Following the ideas developed in [172] along with the requirement to minimize the power consumption, a first MAPS based on the CMOS pixel sensors technology has been developed. The chip is named IMIC (*Imageur Moléculaire Intra-Cérébral*) and is part of the MAPSSIC (MAPS *Sonde Intra-Crânienne*) project to develop and exploit the first MAPS-based intracerebral positron probe.

8.2 Sensor Requirements

Neuroimaging exploits a variety of radioactive isotopes, typically ^{18}F, ^{15}O and ^{11}C, which emit $\beta+$ at energies from 0 to 1.7 MeV. The probe ability to measure activities by counting local events depends obviously on what energy range the sensor is sensitive to. Consequently an important figure of merit is the detection threshold, which should be as low as possible (this requirement is an outcome of the study in [172]) and depends on the signal-over-noise ratio of the sensing element. The threshold value will be discussed in section 8.3 with respect to the sensitive thickness and noise level of the designed sensors. As previously mentionned, the usage of MAPS for this kind of probe intends to both enhance the overall robustness and simplify the system beyond the implanted part of the probe. Thus, we have included into the requirements the digital conversion of the signal inside the pixels hence facilitating further data transmission. It is also expected that the readout architecture of the sensor optimises data throughput to the micro-controller embedded on the animal backpack with respect to the measured activity.

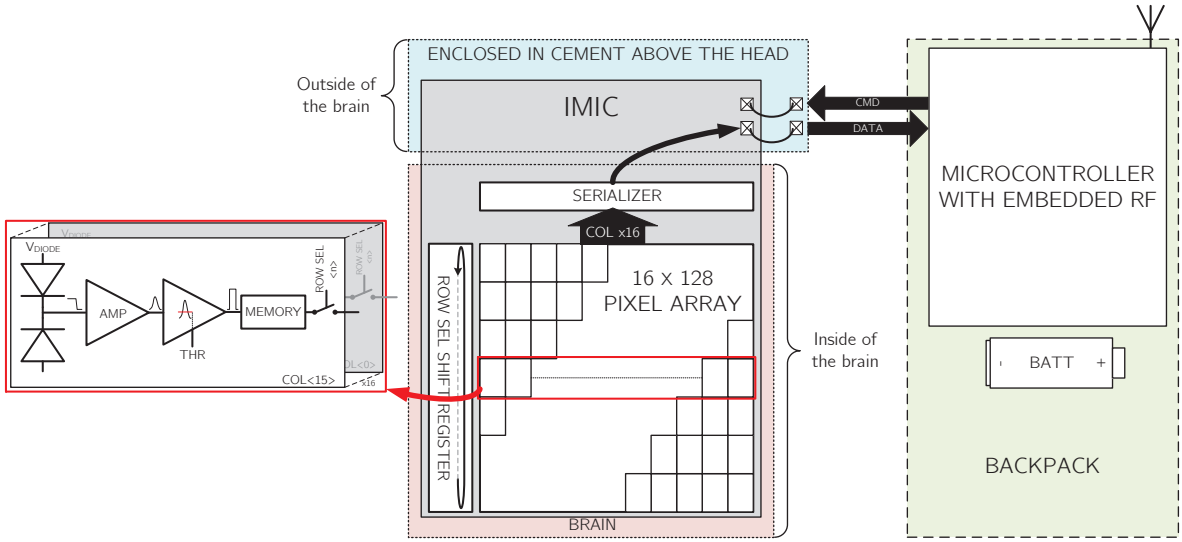

Figure 8.3: Schematic of the MAPSSIC setup. The monolithic active pixel sensor IMIC is a needle shaped probe composed of 16 × 128 pixels of 30 × 50 µm^2, which provide binary information whether a pixel has been hit or not. IMIC is wire bonded to a PCB acting as an interface to the connector and is enclosed in cement on the head of the rodent. The chip is steered and read out only through digital signals by using a micro-controller located on the backpack together with a battery, which is embedding wireless transmission with the data acquisition PC.

Regarding the sensors dimensions, we follow the ones of the PIXSIC sensor (15 mm long, 500 µm wide and 500 µm thick), compatible with the requirements on invasiveness [169] yet providing mechanical stifness.
Imaging the source and evaluating its activity require some level of segmentation, especially along the (vertical) implantation direction. The size of the pixels of the PIXSIC probe were 200 × 500 µm^2, with no segmentations but along its length. Such a segmentation proved to be granular enough to map subcortical brain activity [169] and therefore should be matched quite easily by MAPS, which can feature much higher granularity.

According to first positron count rate observations with the PIXSIC probe [169], an average positron flux of about 100 hits/sensor/s is expected over the required dimensions. This level of positron flux corresponds to at least three orders of magnitude less than standard achievements of CMOS pixel sensors used for charge particle detection. However, a stringent constraint arises from operation in a living animal brain.

As a matter of fact, active architectures involve power consumption and thus heat dissipation, which could locally overheat brain tissues in contact with the sensor. To avoid behavioural impact or worst, tissue damage, from excess heat dissipation, finite element computations were performed in order to set a limit on the dissipated power.

The simulated geometry includes a volume of silicon representing the implanted part of the probe (10 mm × 500 µm × 600 µm) in a spheric medium representing the brain at a constant temperature of 37 °C. The highest temperature gradient at the direct probe contact stays below the required 1 °C for a dissipated power below 4 mW. Considering the possible implantation of multiple probes composed of 2 to 4 sensors, a limit of 1 mW dissipated per sensor has been set. Due to the simplistic nature of the above calculation, the power of 1 mW per sensor is taken as an indicative limit. The actual guideline chosen for the sensor design follows the requirement to achieve the lowest possible power dissipation.

8.3 IMIC sensor design

8.3.1 Technology choice and overall geometry

The sensor was designed in 2015 by Maciej Kachel and myself (with punctual help from Grégory Bertolone) in *TowerJazz* 180 nm CIS technology. The sensitive volume consist of the 18 µm thick low-doped epitaxial layer (HR18), which has demonstrated 100 % detection efficiency for minimum ionising particles for various pixel sizes below 50 µm [173]. Such realization guarantee *a priori* excellent detection performances for $\beta+$ within the energy range of interest *without depletion applied*.

In addition, the thin detection layer presents two key advantages. First, it mitigates the sensitivity to the annihilation photons as recommended in [172]. Secondly, it allows thinning the sensor down to thicknesses from 100 to 300 µm, thus achieving an optimum between invasiveness and mechanical stiffness.

Regarding segmentation, a rectangular shape pixel was opted, within the dimensions known to yield excellent charge collection: 30 µm wide and 50 µm along the vertical dimension of the probe. A matrix of 16 (horizontal) × 128 (vertical) pixels then covers a sensitive area of 480 × 6400 µm^2, meeting the objective to create a needle-shape probe.

The overall sensor dimensions reach 610 µm width and 12 mm length. The vertical extension beyond the active matrix serves to implement the readout and control micro-circuits as well as the connection pads. The sensor is thinned by the foundry to 280 µm and hence presents three different layers along its thickness: first 10 µm of electronic process insensitive to particles, secondly 18 µm of sensitive epitaxy and lastly roughly 250 µm of silicon substrate that provides mechanical support.

The produced sensor layout is shown on the top of figure 8.4.

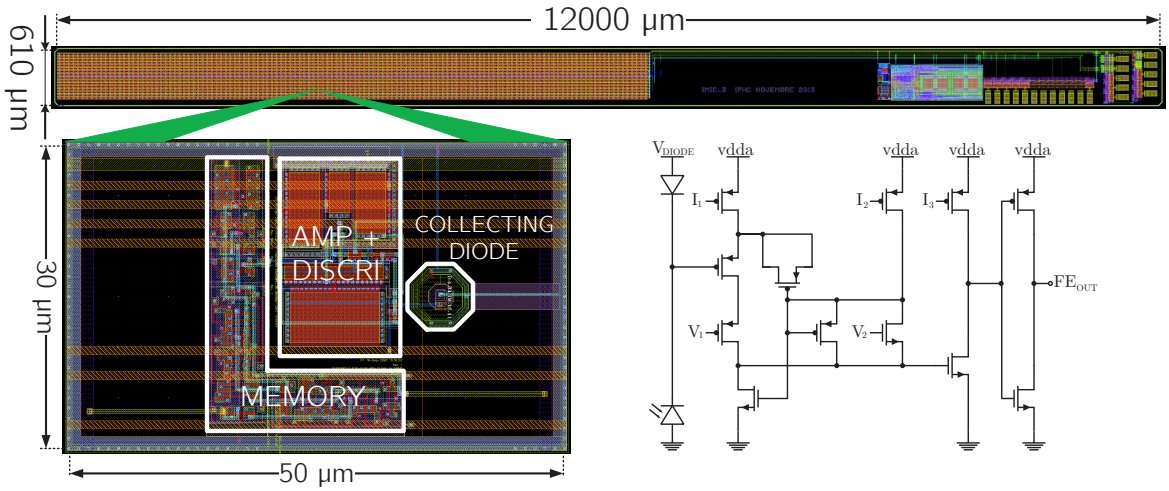

Figure 8.4: Top: layout of the 12000 µm long and 610 µm wide IMIC sensor. Bottom left: magnified layout of a single pixel underlying the location of its main functional components. Bottom right: Pixel circuit schematic derived from the ALPIDE sensor [174].

8.3.2 Pixel design

To satisfy simultaneously the main requirements on the pixel functionalities and performances (digital output, low data-throughput, low detection threshold and low power), a modified version of the ALPIDE (ALice PIxel DEtector) [174] circuit developed for the ALICE experiment is implemented. The initial compact pixel architecture amplifies, shapes (with clipping to prevent saturation), and discriminates the signal collected by the diode using only 12 transistors, as depicted on the bottom of figure 8.4).

Pixels integrate any incoming charge between two consecutive readouts. Since the binary output of the front-end indicating the presence of a hit is only available for a few tens of µs, a 1-bit memory was added per pixel to keep this information until the pixel readout time. The memory is reset after the pixel is read out, so that if a second particle hit the same pixel before readout, the 1-bit memory cannot account for it. The matrix readout strategy is detailed in the next sub-section.

Simulations of the pixel architecture using Cadence Virtuoso Analog Design Environment have evaluated the equivalent noise charge (ENC) at the collection node below 10 electrons, hence allowing to set discriminators for the digitisation at an equivalent level of ≈ 100 e^-. The corresponding energy threshold for the detection equals ≈ 360 eV, well below the maximum probability value of energy loss in 18 µm of silicon by $\beta+$ with energies within 0 to 2 MeV.

Finally, these simulations predict that the overall front-end dissipates about 55 nW

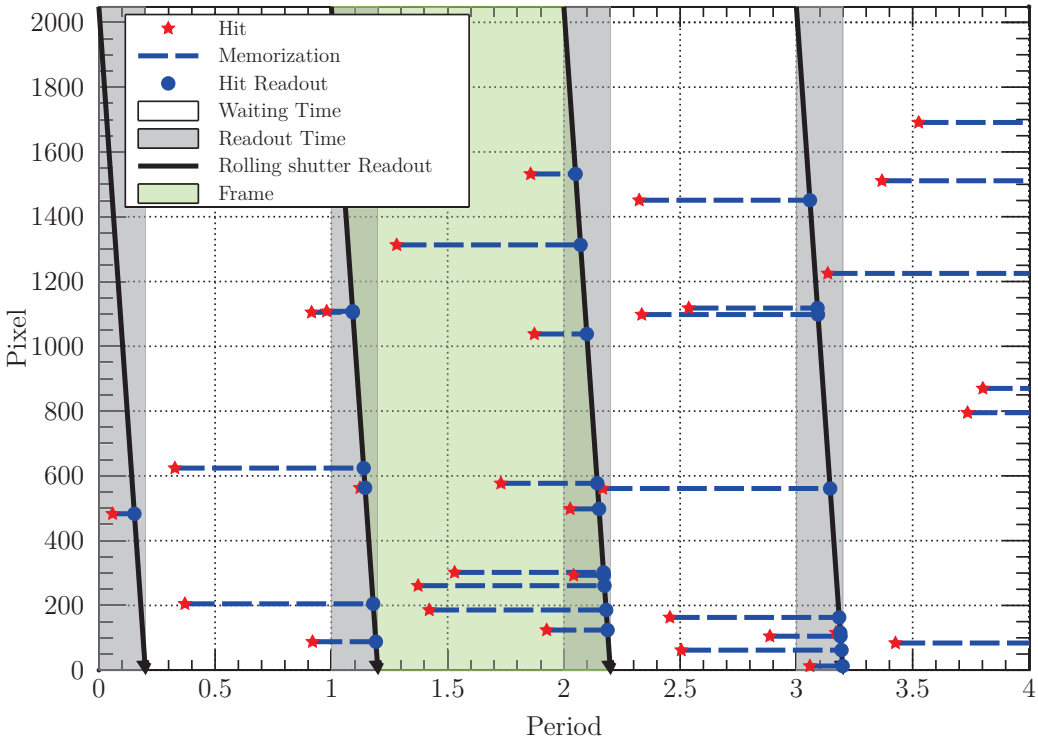

Figure 8.5: Readout strategy for IMIC. When a pixel detects a hit, the event is memorised until rolling-shutter readout. A frame is composed of an adjustable waiting time and the readout time. During the readout, the data of each pixel is sent outside the sensor bit after bit. The data of the memory is reset after readout to allow the detection and memorisation of a new hit.

per pixel (or 113 μW for the whole matrix), well below the upper limit of 1 mW. The schematic of the pixel and its layout are shown in figure 8.4.

8.3.3 Readout strategy

IMIC readout mechanism is kept simple for the sake of space and power dissipation, which does not depend on the hit rate, and relies on the rolling-shutter principle. A token is propagated through the matrix in a shift register at a fixed clock rate to select one line. The 16-bits word formed by all the pixel memories in the line is serialised towards the output of the sensor at a higher clock rate (at least 16 times), which defines f_{clock}. This operation is repeated 128 times to gather data from the entire pixel array, thus the time $t_{readout}$ needed for this full readout cycle amounts to

$$t_{readout} = \frac{2048}{f_{clock}} \quad [\text{s}]. \tag{8.1}$$

Pixels integrate particle hits during the time t_{wait} between two readout cycles, plus the readout time itself:

$$t_{integration} = t_{readout} + t_{wait} \quad [\text{s}]. \tag{8.2}$$

For each readout cycle, data are provided to the micro-controller as a vector of 2048 bits to be sent further away through a wireless protocol. In view of limiting the data rate defined by equation 8.3 and hence the overall power consumption of the MAPSSIC setup, it is better to maximise the waiting time t_{wait} during two readout cycles. However, avoiding pile-up of hits during the same integration period requires to minimise t_{wait}.

$$Data\ rate = \frac{2048}{t_{integration}} \quad [\text{bits/s}] \tag{8.3}$$

The foreseen average hit-rate of about 100 hits/matrix/s in our experiments, leads to an optimisation for the integration time of around 50 milliseconds. In such conditions the data rate stays at a few tens of kilo-bits per second while keeping the pile-up probability at the per mil level. Figure 8.5 depicts the principle of operation of the IMIC readout.

8.3.4 A fully programmable needle shaped sensor

In order to minimize the complexity of the external circuitry, IMIC limits the number of required connections by using a command decoder controlled through Serial Peripheral Interface (SPI) protocol. This controller also allows the parametrisation of on-chip digital-to-analog converters (DACs) used for the polarisation of the front-end. The steering signals (and the data) are sent independently between the micro-controller located on the rodent backpack and the sensor. The micro-controller connects to the external world through a wireless protocol.
The digital block driving IMIC is located on the sensor edge near the few connection pads located outside of the brain, opposite to the pixel matrix deeply implanted in the tissues. This block adds a power consumption of approximately 2 µW. The simulated total IMIC power consumption amounts to approximately 115 µW. This dissipation does not depend on the activity measured but is entirely driven by the number of pixels populating the matrix.

The main characteristics of the IMIC sensor are summarised in table 8.1.

Table 8.1: Summary of the simulated characteristics of the IMIC sensor.

Feature	Value
Sensor size [µm^3]	610 × 12000 × 280
Pixel pitch [µm^2]	30 × 50
Sensitive depth [µm]	18
Det. threshold [eV deposited]	≈ 400
Pixel power consumption [nW/pixel]	≈ 55
Matrix size	16 × 128
Sensitive area [µm^2]	480 × 6400
Total power consumption [µW]	≈ 115

8.4 IMIC characterisation

8.4.1 First images

A few IMIC sensors were bonded to a printed circuit board (PCB) in order to facilitate the first tests. After adjustment of the various polarisations through the on-chip DACs driven by the SPI protocol, the bonded chips were confirmed to be fully functional. All results reported below were obtained with these sensors at room temperature and under relative obscurity.

The measured dissipated power by the whole sensor is 160 µW, rather close to the value expected from simulations in table 8.1 considering the low absolute value for a complete chip.

Three types of sources have been used to characterise the IMIC sensor. Single frames from each source type are displayed in figures 8.6a–8.6d. Soft X-rays (5.9 and 6.4 keV rays) from the ^{55}Fe source (figure 8.6a) generate small clusters of mainly two pixels, while the β particles, either from β- (^{90}Sr: figure 8.6b) or from β+ (^{18}F: figure 8.6c) yield clusters about ten times larger in average. This difference comes from the relatively long ionising path of β-rays in silicon. In contrast, X-rays undergo point-like conversion through photoelectric effect.

Images from 511 keV γ-rays were obtained by placing the ^{18}F source far away (see sub-section 8.4.3) from the sensor. The cluster size observed for these γ-rays is similar to the one for positrons (see figure 8.6d). This indicates that the cluster size information cannot be used to identify (and suppress) the unwanted γ-rays hits on an individual basis information.

To demonstrate that the sensor internal readout performs as expected, an image of a metallic washer was acquired using the ^{55}Fe source (as shown in figure 8.6e). The ring is

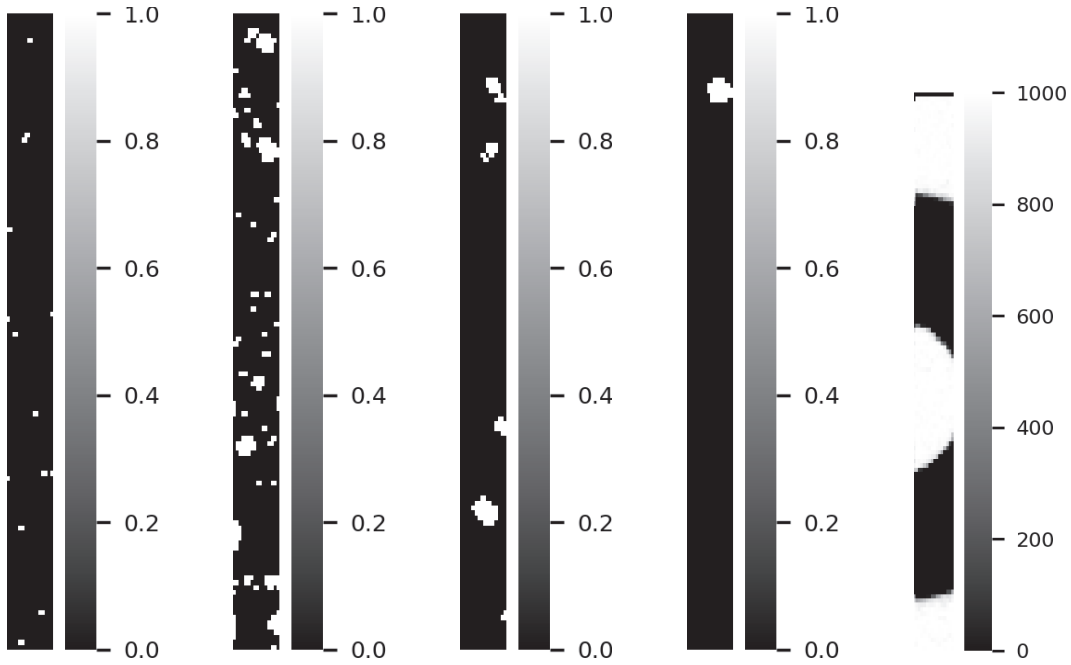

(a) (b) ^{90}Sr (c) (d) (e)

Figure 8.6: Images acquired with the IMIC sensor. Single frame aquired with a ^{55}Fe soft-X-ray source (8.6a), a ^{90}Sr β source (8.6b), and a ^{18}F positron source (8.6c). A single gamma hit (8.6d). Image composed of 1000 accumulated frames of a metallic spacer acquired with ^{55}Fe (8.6e).

approximately 500 µm thick with an external diameter of 5 mm and an opening diameter of 2 mm. The ring structure can easily be recognized on the image as it completely stops the soft X-rays.

8.4.2 Validation of long integration times

As explained in section 8.3, the modest awaited activities of the radiotracers allow running the IMIC sensor with a long integration time in the order of 100 ms, which in turn reduces the data flow and simplifies the whole system. This readout strategy is made possible by the in-pixel memory and was tested by measuring a range of activities at integration times varying from 20 ms to 1 s.

For this test, the IMIC sensor was indirectly illuminated with a ^{90}Sr β source through an aluminium shield. The activity was modulated using three different aluminium thicknesses: 1, 3 and 7 mm. Additional measurements were performed without the source in order to monitor dark count rate. For each combinations of shield and integration time, 1000 frames were acquired with the same detection threshold. Results are presented in figure 8.7. The mean entries per integration time were converted into a mean activity

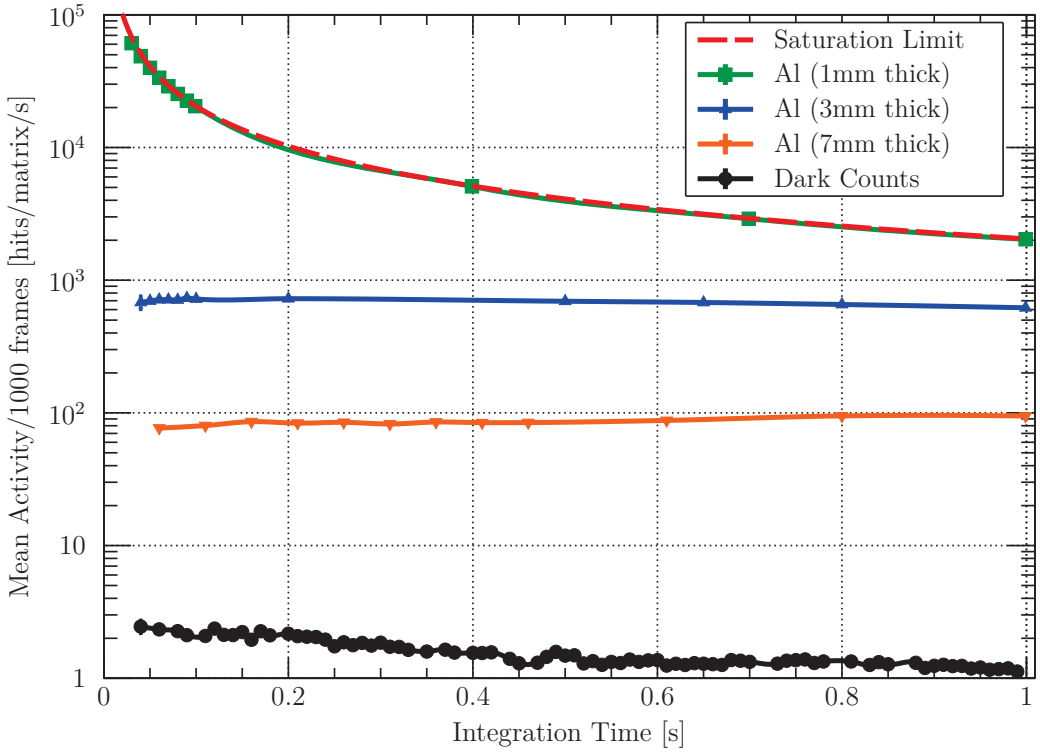

Figure 8.7: Mean activity seen by the sensor for integration times between 20 ms and 1 s of the IMIC sensor dark counts, and with various activities of ^{90}Sr β-rays modulated by using various aluminum shielding thicknesses.

measured over the whole matrix:

$$\overline{\mathcal{A}(t_{int})} = \frac{\overline{entries}}{t_{int}} \quad \text{[hits/matrix/s]}. \tag{8.4}$$

The saturation limit corresponds to the situation where every pixel over the matrix has been fired. This limit depends on the integration time through the simple relation:

$$\mathcal{A}_{sat}(t_{int}) = \frac{2048}{t_{int}} \quad \text{[hits/matrix/s]}. \tag{8.5}$$

The analysis of the dark count map revealed that a few pixels (denominated noisy pixels in the following) dominate the production of fake hits, which explains the dark count rate evolution with the integration time. As there are one to two noisy pixels systematically firing during one integration period, it follows that the dark count rate simply decreases as $1/t_{integration}$ along with equation 8.4.
The low level for the dark count rate means that the IMIC sensor can measure robustly activities down to approximately 10 hits/matrix /s.
With the ^{90}Sr source attenuated by only 1 mm of aluminum, the mean activity follows the saturation limit curve. As the primary radiation is stopped by 1 mm of aluminum, the observed counts are from the interaction of ^{90}Y (2.283 MeV) [13]. At $t_{int} = 10$ ms,

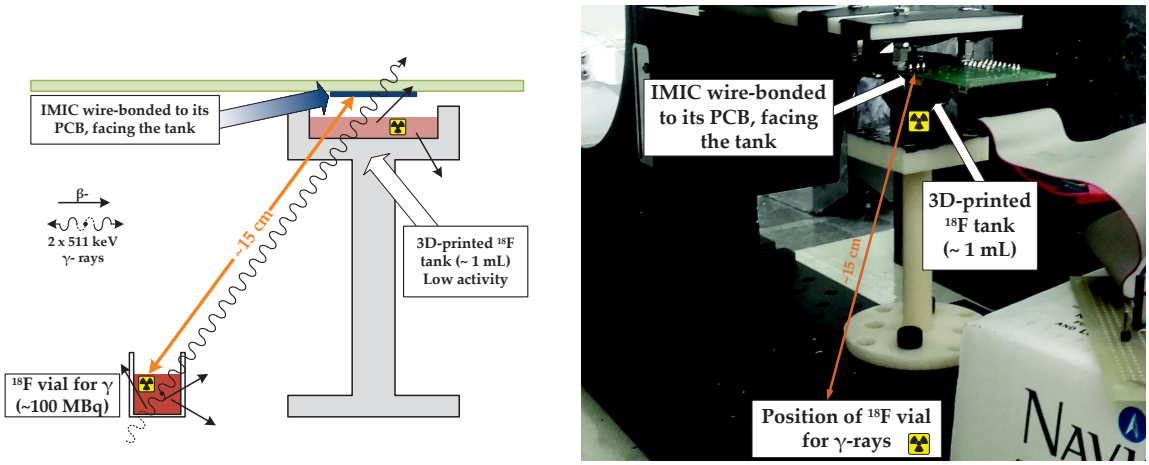

(a) (b)

Figure 8.8: Experimental setup dedicated to measurements with ^{18}F. The IMIC sensor wire-bonded to its PCB is closely oriented towards a first tank containing an aqueous solution of ^{18}F. A vial of the same radiotracers with an higher activity was put on demand 15 cm away from the sensor in order to mimic the presence of a parasitic γ-ray source.

the mean activity seen by the sensor is approximately 60000 hits /matrix/s.

Using thicker shielding, the mean activity on the sensor remains below the saturation limit and is constant for every integration time. Thus, in the ballpark of expected average activities (100 hits/matrix/s), integration time up to 1 s can be chosen without information loss and with a safety margin against activity fluctuation of one order of magnitude. This read-out condition allows low data rates, and limits the power consumption of the overall system.

8.4.3 Preliminary sensitivity study

Measurements using ^{18}F radioisotope, produced at the CYRCé cyclotron at IPHC, in a non-sealed aqueous solution were performed in view of studying the differential sensitivity to prompt $\beta+$ and annihilation photons.

A first 3D printed tank contained a diluted solution of ^{18}F presenting an activity of about 1 MBq. The tank was designed to precisely position the sensor bonded to its PCB 5 mm away from the solution. Since the source was dissolved in saline solution, the sensor was protected by plastic wrap.

Another vial filled with the same isotope but featuring a much higher activity of 100 MBq was disposed on demand 15 cm away from the sensor. This second tank served as a parasitic source of 511 keV γ-rays, since the air distance and the glass of the vial (the opening needed to fill the vial is not oriented towards the sensor), fully attenuates positrons. This setup presented in figure 8.8 intends to reproduce roughly the head–bladder relative positions in a rat.

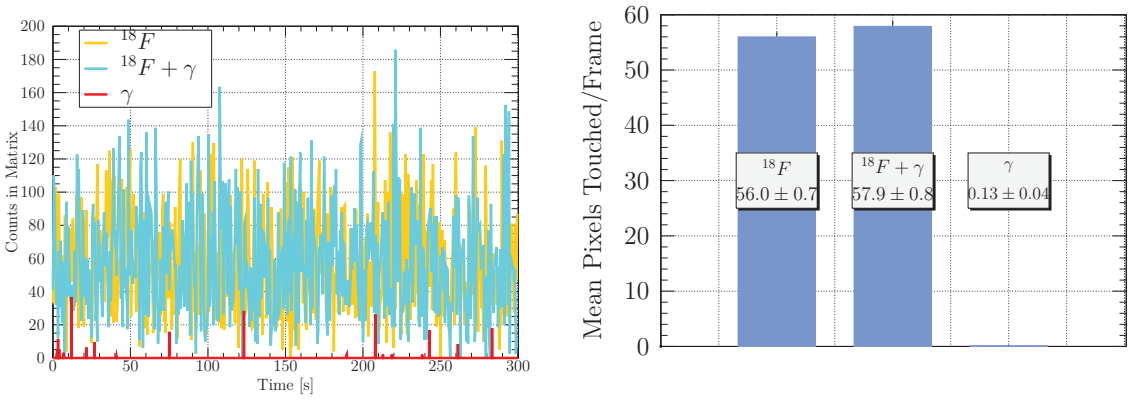

(a) (b)

Figure 8.9: Left: Evolution with time of the pixel count per 100 ms frame duration for the three source configurations described in the text. Right: Average pixel count per frame over five minutes data acquisition for the same configurations.

Data were taken with the IMIC sensor in three configurations, for 5 minutes each. The observed counts per time and average count rate are plotted in figure 8.9a, where the average count rates are corrected for the time decay of ^{18}F. Count distributions observed with both tanks present are labeled ^{18}F+γ, the distributions obtained with only the tank close to the sensor is tagged ^{18}F, and finally the label is γ when only the distant tank was used.

The counting rates for the three source configurations are displayed in figure 8.9b. Within uncertainties, the average counting rate with both sources (^{18}F+γ) or only with the closer tank (^{18}F) are equivalent, they amount respectively to 56.0 $\pm$ 0.7 and 57.9 $\pm$ 0.8 pixels/frame. This observation is coherent with the very small counting rate (0.13 $\pm$ 0.04 pixels/frame) measured when only the far-away source (γ) is used.
The experiment illustrates qualitatively the very small relative sensitivity of the thin IMIC sensor to γ-rays with respect to β+.

8.5 Conclusion

Following [172], we have designed a monolithic active pixel sensor to equip the next generation of intracerebral positron probes for deep brain imaging adapted to fully conscious and freely moving rodents. The IMIC chip features 2048 active pixels over a sensitive area of 480 $\times$ 6400 µm^2. The in-pixel amplification and 1-hit binary memory allows both a low detection threshold (400 eV for the energy deposited) and fully digital matrix readout. This front-end architecture benefits from an extremely low power, addressing the main challenge of heat dissipation within the implantation tissues. Finally, being fabricated on

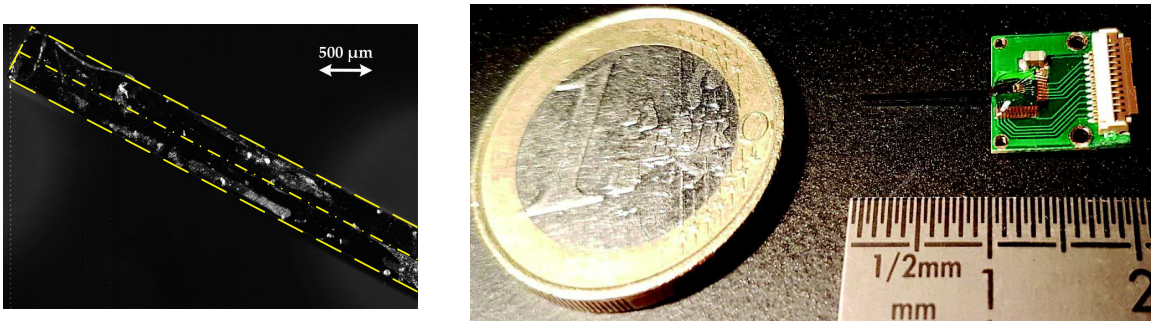

(a) (b)

Figure 8.10: Two IMIC sensors each thinned to 250 µm and glued back to back (8.10a). Picture by L. Ammour (IMNC). The double sided probe wirebonded on each side of its PCB and protected by globtop coating (8.10b). Picture by F. Gensolen (CPPM).

a 18 µm thick sensitive layer, the sensor is mostly transparent to γ-rays.

The first IMIC sample characterisations confirmed the successful operation of the sensor as a $\beta+$ activity locator. The measured power dissipation per sensor reached 160 µW. This performance sets the current state-of-the-art for a probe built in the CMOS pixel technology, and should allow the implantation of a few probes in a single animal with acceptable moderate overheating of the local brain tissues. Foreseen *in-vivo* experiments will be conducted to investigate the full compliance of the IMIC sensor with the application requirements.

A second generation sensor can benefit from a fully depleted thin sensitive layer, which would allow to increase the pixel size, hence decrease the total number of pixels and leading to a reduction of the total dissipated power.

To increase the 3D reconstruction of radiotracers clusters in the brain, pairs of IMIC sensors are assembled back-to-back to form the implantable part of the final MAPSSIC probe with a total volume of $560 \times 610 \times 12000$ µm^3.

Figure 8.10a is a microscope photograph of two IMIC sensors thinned to 250 µm and glued back-to-back. The double-sided probe is wirebonded on each side to its PCB which only acts as an iterface between the sensor and the connector which will be enclosed in cement above the head of the rodent. The wirebonds are protected with glob-top coating. The double sided probe connected to its PCB is shown on figure 8.10. A biocompatible parylene coating is being applied and the performances of the assembly will be evaluated.

Chapter 9

Conclusions

Extended studies based on a prototype of a depleted CMOS Pixel Sensor have been conducted. The PIPPER-2 sensor features a collecting diode AC-coupled to a source follower. The depletion voltage is applied from the frontside through a forward bias diode. The sensor prototype has been produced on two different sensitive substrates:

- an 18 µm thick epitaxial layer with a resistivity above 1 kΩ cm,
- a Czochralski bulk substrate with a resistivity above 600 Ω cm.

A few prototypes of the latter have been thinned to a total thickness of 50 µm which yields approximatively 40 µm sensitive to any ionizing particle.

Using a laboratory ^{55}Fe soft X-Ray source, and a X-Ray generator able to provide a wider range of energies, the performance reached by the prototype on both types of substrate have been assessed.
With an equivalent noise charge of 24 electrons on both types of substrate, and with up to 90 % of the generated charge collected by the seed pixel, the energy resolution at 5.9 keV is measured at 280 eV with the epitaxial layer version and at 288 eV in the thinned bulk substrate.
The performance of the sensor after NIEL irradiation (at fluences up to $5{\cdot}10^{14}$ $n_{eq}(1\ MeV)/cm^2$) have been characterized. Despite cooling at -20 °C, noise performance was degraded but, the signal to noise ratio remained acceptable for tracking application.

TCAD finite element simulations were conducted for each type of substrate with both a simplified and a realistic model of the pixel studied with applied depletion voltages from 0 to 45 V. Despite being easier to define while requiring less processing power to evaluate, the simplified model overestimates the depletion depth given by the realistic model.
The latter evaluates, with an applied depletion voltage of 45 V, a saturation of the extension of the depleted volume to 13 µm in the thin epitaxial layer because of the doping profile. With a low resistivity of 600 Ω cm, the simulated value for the bulk substrate configuration only reaches 17 µm. With a resistivity of 2 kΩ cm, the thickness of the depleted volume is estimated to reach 22 µm.

With a reference point from the simulations results, and with the data acquired for the characterization, the depth of the depleted volume was estimated within a few micrometers of uncertainty for each type of substrate using the relative attenuation of X-Rays in silicon.
The extension in the bulk substrate goes beyond what was estimated by simulations for the guaranteed resistivity of 600 Ω cm reaching approximatively 18±1 µm showing that the effective resistivity of the thinned bulk substrate is in reality much closer to 1 kΩ cm. The potential sensitive volume of 40 µm is then *not fully depleted*, but good collection properties is observed up to 35±2 µm, close to the full sensitive depth.

These estimations are on the maximum depth reached by the depleted volume and do not determine the shape of the depleted area. Measurements using a synchrotron pencil beam with photon energies in a given range, or with MIPs from a beam equiped with a telescope, could allow the mapping of the not-fully depleted volume within the sensitive substrate.
From the measurements and simulations results, to be fully depleted, the sensor must be produced on higher resistivity substrate (>10 kΩ cm) either using very low doped p-type Czochralski or Float-Zone wafers, or with thick epitaxial layer.

Constraints on the detection capabilites of high fluxes of photons imposed by the application of the depletion from the front side of the sensor lead to the design of a new sensor prototype, currently being fabricated. The structures aim to overcome limitations on the total amount of charge that can be integrated by the collecting diode within a given period of time using a standard PMOS as a reset transistor have been presented. Also, a low noise, low dispersion pixel structure able to reach a simulated energy resolution of 160 eV at 5.9 keV was proposed to enhance the energy resolution measured with the current design. The architectures embedded in the prototype have to be validated by measurements.

An undepleted needle-shaped pixelated sensor was designed for molecular neuroimaging. The characterizations results showed a low dissipated power of 160 µW in accordance with the requirements and the readout strategy is validated for the awaited low activity of the source. Thanks to the 18 µm thick thin epitaxial layer, the sensor is immune to the parasitic 511 keV annihiliation photons. Double-sided probes are being assembled by gluing two sensors back-to-back. These double sensors have to be validated *in-vivo* after being coated with a biocompatible polymer.

Bibliography

[1] I. Valin et al. “A reticle size CMOS pixel sensor dedicated to the STAR HFT”. In: *Journal of Instrumentation* **7**.*01* (2012), p. C01102.

[2] G. Contin. “The STAR PXL detector”. In: *Journal of Instrumentation* **11**.*12* (2016), p. C12068.

[3] A. Szczepankiewicz. “Readout of the upgraded ALICE-ITS”. In: *Nuclear Instruments and Methods in Physics Research Section A: Accelerators, Spectrometers, Detectors and Associated Equipment* **824** (2016). Frontier Detectors for Frontier Physics: Proceedings of the 13th Pisa Meeting on Advanced Detectors, pp. 465–469.

[4] M. Deveaux and J. M. Heuser. “The silicon detector systems of the Compressed Baryonic Matter experiment”. In: *PoS* **Vertex2013** (2013), p. 009.

[5] T. Flick. “The phase II ATLAS Pixel upgrade: the Inner Tracker (ITk)”. In: *Journal of Instrumentation* **12**.*01* (2017), p. C01098.

[6] A. Faruqi and G. McMullan. “Direct imaging detectors for electron microscopy”. In: *Nuclear Instruments and Methods in Physics Research Section A: Accelerators, Spectrometers, Detectors and Associated Equipment* **878** (2018). Radiation Imaging Techniques and Applications, pp. 180–190.

[7] J. Kirz, C. Jacobsen, and M. Howells. “Soft X-ray microscopes and their biological applications”. In: *Quarterly Reviews of Biophysics* **28**.*1* (1995), pp. 33–130.

[8] M. Veale et al. “Characterisation of the high dynamic range Large Pixel Detector (LPD) and its use at X-ray free electron laser sources”. In: *Journal of Instrumentation* **12**.*12* (2017), P12003.

[9] B. Marsh et al. “PERCIVAL: The design and characterisation of a CMOS image sensor for direct detection of low-energy X-rays”. In: *2014 IEEE Nuclear Science Symposium and Medical Imaging Conference (NSS/MIC)*. Nov. 2014, pp. 1–4.

[10] G. F. Knoll. *Radiation Detection and Measurement*. 4th Edition. John Wiley & Sons, Inc., 2012.

[11] L. Rossi, P. Fischer, T. Rohe, and N. Wermes. *Pixel Detectors, From Fundamentals to Applications*. Springer, Berlin, Heidelberg, 2006.

[12] S. Tavernier. *Experimental Techniques in Nuclear and Particle Physics*. Springer, Berlin, Heidelberg, 2010.

[13] K. A. Olive et al. “Review of Particle Physics”. In: *Chin. Phys.* **C38** (2014), p. 090001.

[14] G. Fraser et al. “The X-ray energy response of silicon Part A. Theory”. In: *Nuclear Instruments and Methods in Physics Research Section A: Accelerators, Spectrometers, Detectors and Associated Equipment* **350**.*1* (1994), pp. 368–378.

[15] W. R. Leo. *Techniques for Nuclear and Particle Physics Experiments*. 2nd Edition. Springer, Berlin, Heidelberg, 1994.

[16] R. C. Alig, S. Bloom, and C. W. Struck. “Scattering by ionization and phonon emission in semiconductors”. In: *Phys. Rev. B* **22** (12 Dec. 1980), pp. 5565–5582.

[17] R. Bock and A. Vasilescu. *The Particle Detector BriefBook*. Springer, Berlin, Heidelberg, 1998.

[18] K. Nagata et al. “Energy Loss and Straggling of High-Energy Electrons in Silicon Detectors”. In: *Japanese Journal of Applied Physics* **14**.*5* (1975), p. 697.

[19] C. Leroy and P. Rancoita. *Silicon Solid State Devices and Radiation Detection*. World Scientific Publishing Company Pte Limited, 2012.

[20] *Physical Reference Data*. NIST.

[21] S. M. Sze. *Semiconductor Devices. Physics and Technology*. John Wiley & Sons, Inc., 1985.

[22] S. M. Sze. *Physics of semiconductor devices, Third Edition*. John Wiley & Sons, Inc., 1985.

[23] B. Van Zeghbroeck. *Principles of Semiconductor Devices*. University of Colorado, 2011. URL: `http://ece-www.colorado.edu/~bart/book/`.

[24] E. Jaeschke, S. Khan, J. Schneider, and J. Hastings. *Synchrotron Light Sources and Free-Electron Lasers*. Springer International Publishing, 2016.

[25] S. Smith. *The Scientist and Engineer's Guide to Digital Signal Processing*. California Technical Publishing, 1997.

[26] S. Granato et al. “Characterization of eROSITA PNCCDs”. In: *IEEE Transactions on Nuclear Science* **60**.*4* (Aug. 2013), pp. 3150–3157.

[27] J. Janesick et al. *Fundamental performance differences between CMOS and CCD imagers: Part II*. 2007.

[28] J. Janesick et al. *Fundamental performance differences between CMOS and CCD imagers: Part III*. 2009.

[29] J. Janesick et al. *Fundamental performance differences between CMOS and CCD imagers: Part IV*. 2010.

[30] T. Hatsui and H. Graafsma. “X-ray imaging detectors for synchrotron and XFEL sources”. In: *IUCrJ* **2**.*3* (May 2015), pp. 371–383.

[31] R. Ballabriga et al. “Review of hybrid pixel detector readout ASICs for spectroscopic X-ray imaging”. In: *Journal of Instrumentation* **11**.*01* (2016), P01007.

[32] R. Ballabriga et al. “The Medipix3 Prototype, a Pixel Readout Chip Working in Single Photon Counting Mode With Improved Spectrometric Performance”. In: *IEEE Transactions on Nuclear Science* **54**.*5* (Oct. 2007), pp. 1824–1829.

[33] S. Cartier et al. “Micrometer-resolution imaging using MÖNCH: towards G_2-less grating interferometry”. In: *Journal of Synchrotron Radiation* **23**.*6* (Nov. 2016), pp. 1462–1473.

[34] J. Becker et al. “Architecture and design of the AGIPD detector for the European XFEL”. In: *2012 IEEE Nuclear Science Symposium and Medical Imaging Conference Record (NSS/MIC)*. Oct. 2012, pp. 585–590.

[35] E. R. Fossum. *Active pixel sensors: are CCDs dinosaurs?* 1993.

[36] H. Pernegger et al. “First tests of a novel radiation hard CMOS sensor process for Depleted Monolithic Active Pixel Sensors”. In: *Journal of Instrumentation* **12**.*06* (2017), P06008.

[37] B. Mikulec. “Single Photon Detection with Semiconductor Pixel Arrays for Medical Imaging Applications”. Presented on 20 Jun 2000. PhD thesis. Geneva: Vienna U., 2000.

[38] A. Fornaini, D. Calvet, and J. Visschers. “Soft X-ray sensitivity of a photon-counting hybrid pixel detector with a silicon sensor matrix”. In: *Nuclear Instruments and Methods in Physics Research Section A: Accelerators, Spectrometers, Detectors and Associated Equipment* **466**.*1* (2001). 2nd Int. Workshop on Radiation Imaging Detectors, pp. 142–145.

[39] C. Ponchut et al. “Evaluation of a photon-counting hybrid pixel detector array with a synchrotron X-ray source”. In: *Nuclear Instruments and Methods in Physics Research Section A: Accelerators, Spectrometers, Detectors and Associated Equipment* **484**.*13* (2002), pp. 396–406.

[40] E. Bertolucci et al. “BETAview: a digital β-imaging system for dynamic studies of biological phenomena”. In: *Nuclear Instruments and Methods in Physics Research Section A: Accelerators, Spectrometers, Detectors and Associated Equipment* **478**.*12* (2002), pp. 109–113.

[41] C. Ponchut and F. Zontone. “Evaluation of medipix-1 in X-ray scattering and X-ray diffraction applications ”. In: *Nuclear Instruments and Methods in Physics Research Section A: Accelerators, Spectrometers, Detectors and Associated Equipment* **510**.*12* (2003). Proceedings of the 2nd International Symposium on Applications of Particle Detectors in Medicine, Biology and Astrophysics, pp. 29–34.

[42] J. Uher et al. “Characterization of 3D thermal neutron semiconductor detectors ”. In: *Nuclear Instruments and Methods in Physics Research Section A: Accelerators, Spectrometers, Detectors and Associated Equipment* **576**.*1* (2007), pp. 32–37.

[43] R. de Vries et al. “Medipix 2 in X-ray diffraction”. In: *Nuclear Instruments and Methods in Physics Research Section A: Accelerators, Spectrometers, Detectors and Associated Equipment* **576**.*1* (2007), pp. 164–168.

[44] E. Manach and O. Gal. “Experimental and simulation results of gamma imaging with hybrid pixel detectors”. In: *Nuclear Instruments and Methods in Physics Research Section A: Accelerators, Spectrometers, Detectors and Associated Equipment* **531**.*12* (2004), pp. 38–51.

[45] M. Campbell. “10 years of the Medipix2 Collaboration ”. In: *Nuclear Instruments and Methods in Physics Research Section A: Accelerators, Spectrometers, Detectors and Associated Equipment* **633, Supplement 1** (2011). 11th International Workshop on Radiation Imaging Detectors (IWORID), S1–S10.

[46] C. Ponchut et al. “MAXIPIX, a fast readout photon-counting X-ray area detector for synchrotron applications”. In: *Journal of Instrumentation* **6**.*01* (2011), p. C01069.

[47] V. Pugatch et al. “Metal and hybrid TimePix detectors imaging beams of particles”. In: *Nuclear Instruments and Methods in Physics Research Section A: Accelerators, Spectrometers, Detectors and Associated Equipment* **650**.*1* (2011). International Workshop on Semiconductor Pixel Detectors for Particles and Imaging 2010, pp. 194–197.

[48] H. van der Graaf. “GridPix: An integrated readout system for gaseous detectors with a pixel chip as anode”. In: *Nuclear Instruments and Methods in Physics Research Section A: Accelerators, Spectrometers, Detectors and Associated Equipment* **580**.*2* (2007). Imaging 2006Proceedings of the 3rd International Conference on Imaging Techniques in Subatomic Physics, Astrophysics, Medicine, Biology and Industry, pp. 1023–1026.

[49] G. Mettivier, M. C. Montesi, and P. Russo. “Digital autoradiography with a Medipix2 hybrid silicon pixel detector”. In: *IEEE Transactions on Nuclear Science* **52**.*1* (Feb. 2005), pp. 46–50.

[50] R. Ballabriga et al. “Medipix3: A 64 k pixel detector readout chip working in single photon counting mode with improved spectrometric performance ”. In: *Nuclear Instruments and Methods in Physics Research Section A: Accelerators, Spectrometers, Detectors and Associated Equipment* **633, Supplement 1** (2011). 11th International Workshop on Radiation Imaging Detectors (IWORID), S15–S18. ISSN: 0168-9002.

[51] E. N. Gimenez et al. “Characterization of Medipix3 With Synchrotron Radiation”. In: *IEEE Transactions on Nuclear Science* **58**.*1* (Feb. 2011), pp. 323–332.

[52] E. N. Gimenez et al. “Medipix3RX: Characterizing the Medipix3 Redesign With Synchrotron Radiation”. In: *IEEE Transactions on Nuclear Science* **62**.*3* (June 2015), pp. 1413–1421.

[53] T. Poikela et al. “Timepix3: a 65K channel hybrid pixel readout chip with simultaneous ToA/ToT and sparse readout”. In: *Journal of Instrumentation* **9**.*05* (2014), p. C05013.

[54] H. Yousef et al. “Timepix3 as X-ray detector for time resolved synchrotron experiments”. In: *Nuclear Instruments and Methods in Physics Research Section A: Accelerators, Spectrometers, Detectors and Associated Equipment* (2016), pp. -.

[55] P. Kraft et al. “Performance of single-photon-counting PILATUS detector modules”. In: *Journal of Synchrotron Radiation* **16**.*3* (May 2009), pp. 368–375.

[56] T. Loeliger et al. “The new PILATUS3 ASIC with instant retrigger capability”. In: *2012 IEEE Nuclear Science Symposium and Medical Imaging Conference Record (NSS/MIC)*. Oct. 2012, pp. 610–615.

[57] *PILATUS 3R*. DECTRIS.

[58] *PILATUS 3 S and X series*. DECTRIS.

[59] R. Dinapoli et al. “EIGER: Next generation single photon counting detector for X-ray applications”. In: *Nuclear Instruments and Methods in Physics Research Section A: Accelerators, Spectrometers, Detectors and Associated Equipment* **650**.*1* (2011). International Workshop on Semiconductor Pixel Detectors for Particles and Imaging 2010, pp. 79–83.

[60] V. Radicci et al. “EIGER a new single photon counting detector for X-ray applications: performance of the chip”. In: *Journal of Instrumentation* **7**.*02* (2012), p. C02019.

[61] R. Dinapoli et al. “EIGER characterization results”. In: *Nuclear Instruments and Methods in Physics Research Section A: Accelerators, Spectrometers, Detectors and Associated Equipment* **731** (2013). PIXEL 2012, pp. 68–73.

[62] N. Boudet et al. “XPAD: a hybrid pixel detector for X-ray diffraction and diffusion”. In: *Nuclear Instruments and Methods in Physics Research Section A: Accelerators, Spectrometers, Detectors and Associated Equipment* **510**.*12* (2003). Proceedings of the 2nd International Symposium on Applications of Particle Detectors in Medicine, Biology and Astrophysics, pp. 41–44.

[63] S. Basolo et al. “XPAD: pixel detector for material sciences”. In: *IEEE Transactions on Nuclear Science* **52**.*5* (Oct. 2005), pp. 1994–1998.

[64] P. Delpierre et al. In: *IEEE Nuclear Science Symposium Conference Record, 2005.*

[65] P. Pangaud et al. “First results of XPAD3, a new photon counting chip for X-ray CT-scanner with energy discrimination”. In: *2007 IEEE Nuclear Science Symposium Conference Record*. Vol. 1. Oct. 2007, pp. 14–18.

[66] F. Cassol et al. “Characterization of the imaging performance of a micro-CT system based on the photon counting XPAD3/Si hybrid pixel detectors”. In: *Biomedical Physics & Engineering Express* **2**.*2* (2016), p. 025003. URL: `http://stacks.iop.org/2057-1976/2/i=2/a=025003`.

[67] K. Medjoubi et al. “Performance and Applications of the CdTe- and Si-XPAD3 photon counting 2D detector”. In: *Journal of Instrumentation* **6**.*01* (2011), p. C01080.

[68] P. Pangaud et al. “XPAD3: A new photon counting chip for X-ray CT-scanner”. In: *Nuclear Instruments and Methods in Physics Research Section A: Accelerators, Spectrometers, Detectors and Associated Equipment* **571**.*12* (2007), pp. 321–324.

[69] J.-F. Berar et al. “XPAD3 hybrid pixel detector applications”. In: *Nuclear Instruments and Methods in Physics Research Section A: Accelerators, Spectrometers, Detectors and Associated Equipment* **607**.*1* (2009). Radiation Imaging Detectors 2008Proceedings of the 10th International Workshop on RadiationImaging Detectors, pp. 233–235.

[70] R. Bellazzini et al. “PIXIE III: a very large area photon-counting CMOS pixel ASIC for sharp X-ray spectral imaging”. In: *Journal of Instrumentation* **10**.*01* (2015), p. C01032.

[71] M. C. Veale et al. “Investigating the small pixel effect in CdZnTe Hard X-ray detectors ; The PIXIE ASIC”. In: *Nuclear Science Symposium Conference Record (NSS/MIC), 2010 IEEE*. Oct. 2010, pp. 3789–3792.

[72] M. C. Veale et al. “An ASIC for the Study of Charge Sharing Effects in Small Pixel CdZnTe X-Ray Detectors”. In: *IEEE Transactions on Nuclear Science* **58**.*5* (Oct. 2011), pp. 2357–2362.

[73] R. Bellazzini et al. “Chromatic X-ray imaging with a fine pitch CdTe sensor coupled to a large area photon counting pixel ASIC”. In: *Journal of Instrumentation* **8**.*02* (2013), p. C02028.

[74] P. Hart et al. “The Cornell-SLAC pixel array detector at LCLS”. In: *2012 IEEE Nuclear Science Symposium and Medical Imaging Conference Record (NSS/MIC)*. Oct. 2012, pp. 538–541.

[75] H. T. Philipp et al. *Pixel array detector for the capture of femtosecond duration x-ray images*. 2007.

[76] L. J. Koerner et al. “X-ray tests of a Pixel Array Detector for coherent x-ray imaging at the Linac Coherent Light Source”. In: *Journal of Instrumentation* **4**.*03* (2009), P03001.

[77] L. J. Koerner. “X-Ray Analog Pixel Array Detector For Single Synchrotron Bunch Time-Resolved Imaging”. PhD thesis. Cornell University, 2010.

[78] P. Hart et al. *The CSPAD megapixel x-ray camera at LCLS*. 2012.

[79] A. Ercan, M. W. Tate, and S. M. Gruner. “Analog pixel array detectors”. In: *Journal of Synchrotron Radiation* **13**.*2* (Mar. 2006), pp. 110–119.

[80] L. J. Koerner, M. W. Tate, and S. M. Gruner. “An Accumulating Pixel Array Detector for Single-Bunch Synchrotron Experiments”. In: *IEEE Transactions on Nuclear Science* **56** (Oct. 2009), pp. 2835–2842.

[81] L. J. Koerner and S. M. Gruner. “X-ray analog pixel array detector for single synchrotron bunch time-resolved imaging”. In: *Journal of Synchrotron Radiation* **18**.*2* (Mar. 2011), pp. 157–164.

[82] H. T. Philipp et al. “High-speed x-ray imaging with the Keck pixel array detector (Keck PAD) for time-resolved experiments at synchrotron sources”. In: *AIP Conference Proceedings* **1741**.*1* (2016), p. 040036.

[83] H. T. Philipp et al. “High-speed X-ray imaging pixel array detector for synchrotron bunch isolation”. In: *Journal of Synchrotron Radiation* **23**.*2* (Mar. 2016), pp. 395–403.

[84] W. Vernon et al. *First results from the 128x128 pixel mixed-mode Si x-ray detector chip*. 2007.

[85] L. J. Koerner et al. “Small-angle solution scattering using the mixed-mode pixel array detector”. In: *Journal of Synchrotron Radiation* **18**.*2* (Mar. 2011), pp. 148–156.

[86] J. Weiss et al. “High Dynamic Range X-ray Detector Pixel Architectures Utilizing Charge Removal”. In: *IEEE Transactions on Nuclear Science* **PP**.*99* (2017), pp. 1–1.

[87] A. Dragone et al. “ePix: A class of front-end ASICs for second generation LCLS integrating hybrid pixel detectors”. In: *Nuclear Science Symposium and Medical Imaging Conference (NSS/MIC), 2013 IEEE*. Oct. 2013, pp. 1–5.

[88] S. Herrmann et al. “2nd generation cameras for LCLS and the new challenges of high repetition rates at LCLS-II”. In: *2014 IEEE Nuclear Science Symposium and Medical Imaging Conference (NSS/MIC)*. Nov. 2014, pp. 1–2.

[89] P. Caragiulo et al. “Design and characterization of the ePix10k prototype: A high dynamic range integrating pixel ASIC for LCLS detectors”. In: *2014 IEEE Nuclear Science Symposium and Medical Imaging Conference (NSS/MIC)*. Nov. 2014, pp. 1–3.

[90] B. Markovic et al. “Design and characterization of the ePix100a: A low noise integrating pixel ASIC for LCLS detectors”. In: *2014 IEEE Nuclear Science Symposium and Medical Imaging Conference (NSS/MIC)*. Nov. 2014, pp. 1–3.

[91] A. Dragone et al. “ePix: a class of architectures for second generation LCLS cameras”. In: *Journal of Physics: Conference Series* ().

[92] A. Mozzanica et al. “Prototype characterization of the JUNGFRAU pixel detector for SwissFEL”. In: *Journal of Instrumentation* **9**.*05* (2014), p. C05010.

[93] J. H. Jungmann-Smith et al. “JUNGFRAU 0.2: prototype characterization of a gain-switching, high dynamic range imaging system for photon science at SwissFEL and synchrotrons”. In: *Journal of Instrumentation* **9**.*12* (2014), P12013.

[94] J. H. Jungmann-Smith et al. “Radiation hardness assessment of the charge-integrating hybrid pixel detector JUNGFRAU 1.0 for photon science”. In: *Review of Scientific Instruments* **86**.*12* (2015), p. 123110.

[95] A. Mozzanica et al. “Characterization results of the JUNGFRAU full scale readout ASIC”. In: *Journal of Instrumentation* **11**.*02* (2016), p. C02047.

[96] S. Redford et al. “Calibration status and plans for the charge integrating JUNGFRAU pixel detector for SwissFEL”. In: *Journal of Instrumentation* **11**.*11* (2016), p. C11013.

[97] J. H. Jungmann-Smith et al. “Towards hybrid pixel detectors for energy-dispersive or soft X-ray photon science”. In: *Journal of Synchrotron Radiation* **23**.*2* (Mar. 2016), pp. 385–394.

[98] R. Dinapoli et al. “MÖNCH, a small pitch, integrating hybrid pixel detector for X-ray applications”. In: *Journal of Instrumentation* **9**.*05* (2014), p. C05015.

[99] S. Cartier et al. “Micron resolution of MÖNCH and GOTTHARD, small pitch charge integrating detectors with single photon sensitivity”. In: *Journal of Instrumentation* **9**.*05* (2014), p. C05027.

[100] S. Cartier et al. “Study of the signal response of the MÖNCH 25μm pitch hybrid pixel detector at different photon absorption depths”. In: *Journal of Instrumentation* **10**.*03* (2015), p. C03022.

[101] M. Ramilli et al. “Measurements with MÖNCH, a 25 µm pixel pitch hybrid pixel detector”. In: *Journal of Instrumentation* **12**.*01* (2017), p. C01071.

[102] A. Allahgholi et al. “AGIPD, a high dynamic range fast detector for the European XFEL”. In: *Journal of Instrumentation* **10**.*01* (2015), p. C01023.

[103] A. Allahgholi et al. “Front end ASIC for AGIPD, a high dynamic range fast detector for the European XFEL”. In: *Journal of Instrumentation* **11**.*01* (2016), p. C01057.

[104] D. Greiffenberg. “The AGIPD detector for the European XFEL”. In: *Journal of Instrumentation* **7**.*01* (2012), p. C01103.

[105] B. Henrich et al. “The adaptive gain integrating pixel detector AGIPD a detector for the European XFEL”. In: *Nuclear Instruments and Methods in Physics Research Section A: Accelerators, Spectrometers, Detectors and Associated Equipment* **633, Supplement 1** (2011). 11th International Workshop on Radiation Imaging Detectors (IWORID), S11–S14.

[106] A. Allahgholi et al. “The AGIPD 1.0 ASIC: Random access high frame rate, high dynamic range X-ray camera readout for the European XFEL”. In: *2015 IEEE Nuclear Science Symposium and Medical Imaging Conference (NSS/MIC)*. Oct. 2015, pp. 1–6.

[107] M. Hart et al. “Development of the LPD, a high dynamic range pixel detector for the European XFEL”. In: *2012 IEEE Nuclear Science Symposium and Medical Imaging Conference Record (NSS/MIC)*. Oct. 2012, pp. 534–537.

[108] A. Koch et al. “Performance of an LPD prototype detector at MHz frame rates under Synchrotron and FEL radiation”. In: *Journal of Instrumentation* **8**.*11* (2013), p. C11001.

[109] J. Coughlan et al. “The data acquisition card for the Large Pixel Detector at the European-XFEL”. In: *Journal of Instrumentation* **6**.*12* (2011), p. C12057.

[110] A. Blue, M. French, P. Seller, and V. OShea. “Edgeless sensor development for the LPD hybrid pixel detector at XFEL”. In: *Nuclear Instruments and Methods in Physics Research Section A: Accelerators, Spectrometers, Detectors and Associated Equipment* **607**.*1* (2009). Radiation Imaging Detectors 2008Proceedings of the 10th International Workshop on Radiation Imaging Detectors, pp. 55–56.

[111] G. D. Vita et al. “A 5MHz low-noise 130nm CMOS analog front-end electronics for the readout of non-linear DEPFET sensor with signal compression for the European XFEL”. In: *IEEE Nuclear Science Symposuim Medical Imaging Conference*. Oct. 2010, pp. 139–144.

[112] P. Lechner et al. “DEPFET active pixel sensor with non-linear amplification”. In: *2011 IEEE Nuclear Science Symposium Conference Record*. Oct. 2011, pp. 563–568.

[113] M. Porro. “Development of the DEPFET sensor with signal compression: A large format X-ray imager with mega-frame readout capability for the European XFEL”. In: *2011 IEEE Nuclear Science Symposium Conference Record*. Oct. 2011, pp. 1424–1434.

[114] G. Lutz et al. “The DEPFET detector-amplifier structure for spectroscopic imaging in astronomy and for experiments at free electron lasers”. In: *Nuclear Instruments and Methods in Physics Research Section A: Accelerators, Spectrometers, Detectors and Associated Equipment* (2016), pp. -.

[115] G. A. Carini et al. “Tests of small X-ray Active Matrix Pixel Sensor prototypes at the National Synchrotron Light Source”. In: *Journal of Instrumentation* **4**.*03* (2009), P03014.

[116] W. Chen et al. “Development of X-ray active matrix pixel sensors for detection of electrons in scanning transmission electron microscope”. In: *IEEE Nuclear Science Symposium Conference Record, 2005.* Vol. 3. Oct. 2005, pp. 1431–1435.

[117] A. Dragone et al. “XAMPS detector readout ASIC for LCLS”. In: *2008 IEEE Nuclear Science Symposium Conference Record*. Oct. 2008, pp. 2970–2975.

[118] G. A. Carini et al. “The XAMPS detector for the X-ray Pump-Probe instrument at LCLS”. In: *2009 IEEE Nuclear Science Symposium Conference Record (NSS/MIC)*. Oct. 2009, pp. 2151–2153.

[119] K. S. Green et al. “A prototype direct-detection CCD for protein crystallography”. In: *Journal of Applied Crystallography* **46**.*4* (Aug. 2013), pp. 1038–1048.

[120] D. Doering et al. “High speed, direct detection 1k Frame-Store CCD sensor for synchrotron radiation”. In: *2011 IEEE Nuclear Science Symposium Conference Record*. Oct. 2011, pp. 1840–1845.

[121] P. Denes et al. “A fast, direct x-ray detection charge-coupled device”. In: *Review of Scientific Instruments* **80**.*8* (2009), p. 083302.

[122] T. Kameshima et al. “Development of an X-ray pixel detector with multi-port charge-coupled device for X-ray free-electron laser experiments”. In: *Review of Scientific Instruments* **85**.*3* (2014), p. 033110.

[123] Riken. *Instructions of MPCCD detector specification and data format*. Riken. 2012.

[124] S. Ihle et al. "Direct measurement of the position accuracy for low energy X-ray photons with a pnCCD". In: *Journal of Instrumentation* **12**.*02* (2017), P02005.

[125] M. Porro et al. "VERITAS: A 128-Channel ASIC for the Readout of pnCCDs and DEPFET Arrays for X-Ray Imaging, Spectroscopy and XFEL Applications". In: *IEEE Transactions on Nuclear Science* **60**.*1* (Feb. 2013), pp. 446–455.

[126] "Characterization of a pnCCD for applications with synchrotron radiation". In: *Nuclear Instruments and Methods in Physics Research Section A: Accelerators, Spectrometers, Detectors and Associated Equipment* **711** (2013), pp. 132–142.

[127] M. Battaglia et al. "A rad-hard CMOS active pixel sensor for electron microscopy". In: *Nuclear Instruments and Methods in Physics Research Section A: Accelerators, Spectrometers, Detectors and Associated Equipment* **598**.*2* (2009), pp. 642–649.

[128] M. Battaglia et al. "Radiation hardness studies on CMOS monolithic pixel sensors". In: *Nuclear Instruments and Methods in Physics Research Section A: Accelerators, Spectrometers, Detectors and Associated Equipment* **624**.*2* (2010). New Developments in Radiation Detectors Proceedings of the 11th European Symposium on Semiconductor Detectors11th European Symposium on Semiconductor Detectors, pp. 425–427.

[129] M. Battaglia, D. Contarato, P. Denes, and P. Giubilato. "Cluster imaging with a direct detection CMOS pixel sensor in Transmission Electron Microscopy". In: *Nuclear Instruments and Methods in Physics Research Section A: Accelerators, Spectrometers, Detectors and Associated Equipment* **608**.*2* (2009), pp. 363–365.

[130] M. Battaglia et al. "Characterisation of a CMOS active pixel sensor for use in the TEAM microscope". In: *Nuclear Instruments and Methods in Physics Research Section A: Accelerators, Spectrometers, Detectors and Associated Equipment* **622**.*3* (2010), pp. 669–677.

[131] P. Giubilato et al. "LePixA high resistivity, fully depleted monolithic pixel detector". In: *Nuclear Instruments and Methods in Physics Research Section A: Accelerators, Spectrometers, Detectors and Associated Equipment* **732** (2013). Vienna Conference on Instrumentation 2013, pp. 91–94.

[132] P. Giubilato et al. "Monolithic pixels on moderate resistivity substrate and sparsifying readout architecture". In: *Nuclear Instruments and Methods in Physics Research Section A: Accelerators, Spectrometers, Detectors and Associated Equipment* **731** (2013). PIXEL 2012, pp. 146–153.

[133] S. Mattiazzo et al. “LePIX: First results from a novel monolithic pixel sensor”. In: *Nuclear Instruments and Methods in Physics Research Section A: Accelerators, Spectrometers, Detectors and Associated Equipment* **718** (2013). Proceedings of the 12th Pisa Meeting on Advanced DetectorsLa Biodola, Isola dElba, Italy, May 20 26, 2012, pp. 288–291.

[134] A. Potenza et al. “Radiation tolerance of a moderate resistivity substrate in a modern CMOS process”. In: *Nuclear Instruments and Methods in Physics Research Section A: Accelerators, Spectrometers, Detectors and Associated Equipment* **718** (2013). Proceedings of the 12th Pisa Meeting on Advanced DetectorsLa Biodola, Isola dElba, Italy, May 20 26, 2012, pp. 347–349.

[135] A. Rivetti et al. “CMOS sensors in 90 nm fabricated on high resistivity wafers: Design concept and irradiation results”. In: *Nuclear Instruments and Methods in Physics Research Section A: Accelerators, Spectrometers, Detectors and Associated Equipment* **730** (2013), pp. 119–123.

[136] A.Khromova et al. “Report on recent results of the PERCIVAL soft X-ray imager”. In: *Journal of Instrumentation* **11**.*11* (2016), p. C11020.

[137] C. Wunderer et al. “The PERCIVAL soft X-ray imager”. In: *Journal of Instrumentation* **10**.*02* (2015), p. C02008.

[138] P. Rymaszewski et al. *Development of depleted monolithic pixel sensors in 150 nm CMOS technology for the ATLAS Inner Tracker upgrade*. 2017. eprint: `arXiv:1711.01233`.

[139] T. Wang et al. *Depleted fully monolithic CMOS pixel detectors using a column based readout architecture for the ATLAS Inner Tracker upgrade*. 2017. eprint: `arXiv:1710.00074`.

[140] G. A. Rinella. “The ALPIDE pixel sensor chip for the upgrade of the ALICE Inner Tracking System”. In: *Nuclear Instruments and Methods in Physics Research Section A: Accelerators, Spectrometers, Detectors and Associated Equipment* **845** (2017). Proceedings of the Vienna Conference on Instrumentation 2016, pp. 583–587.

[141] G. Aglieri et al. “Monolithic active pixel sensor development for the upgrade of the ALICE inner tracking system”. In: *Journal of Instrumentation* **8**.*12* (2013), p. C12041.

[142] Y. Gornushkin et al. “Tracking performance and radiation tolerance of monolithic active pixel sensors”. In: *Nuclear Instruments and Methods in Physics Research Section A: Accelerators, Spectrometers, Detectors and Associated Equipment* **513**.*1* (2003). Proceedings of the 6th International Conference on Position-Sensitive Detectors, pp. 291–295.

[143] G. Deptuch et al. “Development of monolithic active pixel sensors for charged particle tracking”. In: *Nuclear Instruments and Methods in Physics Research Section A: Accelerators, Spectrometers, Detectors and Associated Equipment* **511**.*1* (2003). Proceedings of the 11th International Workshop on Vertex Detectors, pp. 240–249.

[144] W. Dulinski et al. “Beam telescope for medium energy particles based on thin, submicron precision MAPS”. In: *2007 IEEE Nuclear Science Symposium Conference Record*. Vol. 2. Oct. 2007, pp. 995–1002.

[145] M. Gelin et al. “Intermediate Digital Monolithic Pixel Sensor for the EUDET High Resolution Beam Telescope”. In: *IEEE Transactions on Nuclear Science* **56**.*3* (June 2009), pp. 1677–1684.

[146] J. Baudot et al. “First test results Of MIMOSA-26, a fast CMOS sensor with integrated zero suppression and digitized output”. In: *2009 IEEE Nuclear Science Symposium Conference Record (NSS/MIC)*. Oct. 2009, pp. 1169–1173.

[147] N. Chon-Sen et al. “Development of ultra-light pixelated ladders for an ILC vertex detector”. In: *ArXiv e-prints* (June 2010). arXiv: `1006.5424 [physics.ins-det]`.

[148] H. Jansen et al. “ Performance of the EUDET-type beam telescopes”. In: *ArXiv e-prints* (Mar. 2016). arXiv: `1603.09669v2`.

[149] C. Hu-Guo et al. “Development of the MISTRAL & ASTRAL sensors for the upgrade of the Inner Tracking System of the ALICE experiment at LHC”. In: *2013 IEEE Nuclear Science Symposium and Medical Imaging Conference (2013 NSS/MIC)*. Oct. 2013, pp. 1–7.

[150] F. Morel et al. “MISTRAL & ASTRAL: two CMOS Pixel Sensor architectures suited to the Inner Tracking System of the ALICE experiment”. In: *Journal of Instrumentation* **9**.*01* (2014), p. C01026.

[151] V. Vervisch et al. “Laser activation of Ultra Shallow Junctions (USJ) doped by Plasma Immersion Ion Implantation (PIII)”. In: *Applied Surface Science* **255**.*10* (2009). Laser and Plasma in Micro- and Nano-Scale Materials Processing and Diagnostics, pp. 5647–5650.

[152] J. Lincelles. “Étude dimageurs CMOS fortement dépeuplés pour lamélioration des performances des futurs instruments dobservation spatiaux”. PhD thesis. École Doctorale Génie Électrique, Électronique et Télécommunications (Toulouse), 2015.

[153] A. D. Polyanin and A. V. Manzhirov. *Handbook of Mathematics for Engineers and Scientists*. Chapman and Hall/CRC, 2006.

[154] *Sentaurus Device User Guide*. Synopsys.

[155] T. Skwarnicki. “A study of the radiative CASCADE transitions between the Upsilon-Prime and Upsilon resonances”. PhD thesis. Cracow, INP, 1986.

[156] A. Perez-Perez. “Enhancement of the Radiation Tolerance of High Resolution CMOS Pixel Sensors Using Strong Depletion in a High Resistivity Epitaxial Layer for Charged Particle Tracking”. In: *IEEE Nuclear Science Symposium NSS 2016*. Strasbourg, France, Oct. 2016. URL: http://www.iphc.cnrs.fr/IMG/pdf/aperez_ieee_nss_mic_3nov2016.pdf.

[157] Y.-R. Gao et al. “Time to wake up: Studying neurovascular coupling and brain-wide circuit function in the un-anesthetized animal”. In: *NeuroImage* **153**.*Supplement C* (2017), pp. 382–398.

[158] A. K. O. Alstrup and D. F. Smith. “Anaesthesia for positron emission tomography scanning of animal brains”. In: *Laboratory Animals* **47**.*1* (2013), pp. 12–18.

[159] S. Cherry. “Functional whole-brain imaging in behaving rodents”. In: *Nature Methods* **8**.*4* (Apr. 2011), pp. 301–303.

[160] C. Carter. *Brain Imaging in Behavioral Neuroscience*. Vol. 11. Springer-Verlag Berlin Heidelberg, 2012.

[161] V. D. Patel et al. “Imaging dopamine release with Positron Emission Tomography (PET) and 11C-raclopride in freely moving animals”. In: *NeuroImage* **41**.*3* (2008), pp. 1051–1066. ISSN: 1053-8119.

[162] A. Z. Kyme et al. “Optimised Motion Tracking for Positron Emission Tomography Studies of Brain Function in Awake Rats”. In: *PLOS ONE* **6**.*7* (July 2011), pp. 1–16.

[163] D. Schulz. “Integrating PET with behavioral neuroscience using RatCAP tomography”. In: *Reviews in the Neurosciences* **22**.*6* (2011), pp. 647–655.

[164] L. Zimmer et al. “SIC, an Intracerebral β+-RangeSensitive Probe for Radiopharmacology Investigations in Small Laboratory Animals: Binding Studies with 11C-Raclopride”. In: *Journal of Nuclear Medicine* **43**.*2* (2002), pp. 227–233.

[165] F. Pain et al. “SIC, an intracerebral radiosensitive probe for in vivo neuropharmacology investigations in small laboratory animals: theoretical considerations and practical characteristics”. In: *IEEE Transactions on Nuclear Science* **47**.*1* (Feb. 2000), pp. 25–32.

[166] B. Weber et al. “Quantitative Cerebral Blood Flow Measurements in the Rat Using a Beta-Probe and H215O”. In: *Journal of Cerebral Blood Flow & Metabolism* **23**.*12* (2003), pp. 1455–1460.

[167] C. L. Woody et al. “A study of scintillation beta microprobes”. In: *IEEE Transactions on Nuclear Science* **49**.*5* (Oct. 2002), pp. 2208–2212.

[168] J. Märk et al. “A wireless beta-microprobe based on pixelated silicon for in vivo brain studies in freely moving rats”. In: *Physics in Medicine & Biology* **58**.*13* (2013), p. 4483.

[169] J. Godart et al. “PIXSIC: A Pixellated Beta-Microprobe for Kinetic Measurements of Radiotracers on Awake and Freely Moving Small Animals”. In: *IEEE Transactions on Nuclear Science* **57**.*3* (June 2010), pp. 998–1007.

[170] L. Balasse et al. “PIXSIC, a Pixelated β+-Sensitive Probe for Radiopharmacological Investigations in Rat Brain: Binding Studies with [18F]MPPF”. In: *Molecular Imaging and Biology* **17**.*2* (Apr. 2015), pp. 163–167.

[171] L. Balasse et al. “PIXSIC: A Wireless Intracerebral Radiosensitive Probe in Freely Moving Rats”. In: *Molecular Imaging* **14**.*9* (2015), p. 7290.2015.00020.

[172] L. Ammour et al. “MAPSSIC, a Novel CMOS Intra-Cerebral β+ Probe for Deep Brain Imaging in Awake and Freely-Moving Rat: a Monte-Carlo Study”. In: *IEEE Transactions on Radiation and Plasma Medical Sciences (Manuscript ID TRPMS-2018-0027)* (2018).

[173] J. Baudot et al. “Optimisation of CMOS pixel sensors for high performance vertexing and tracking”. In: *Nuclear Instruments and Methods in Physics Research Section A: Accelerators, Spectrometers, Detectors and Associated Equipment* **732** (2013), pp. 480–483.

[174] M. Mager. “ALPIDE, the Monolithic Active Pixel Sensor for the ALICE ITS upgrade”. In: *Nuclear Instruments and Methods in Physics Research Section A: Accelerators, Spectrometers, Detectors and Associated Equipment* **824**.*Supplement C* (2016), pp. 434–438.

Appendix

List of Publications

Conference Proceeding

- J. Heymes et al. "IMIC – needle-shaped low-power monolithic active pixel sensor for molecular neuroimaging on awake and freely moving rats". In: *2016 IEEE Nuclear Science Symposium, Medical Imaging Conference and Room-Temperature Semiconductor Detector Workshop (NSS/MIC/RTSD)*. Oct. 2016, pp. 1–4. DOI: 10.1109/NSSMIC.2016.8069414

Journal

Submitted for review (14/06/2018):

- J. Heymes et al. "Implantable CMOS Pixel Sensor for Positron Imaging in Rat Brain". In: *Nuclear Instruments and Methods in Physics Research Section A: Accelerators, Spectrometers, Detectors and Associated Equipment* (2018)

Planned:

- Full length article on the evaluation of the depletion depth in CPS (simulations and measurements).

Journal as Co-author

Submitted for review (21/02/2018):

- L. Ammour et al. "MAPSSIC, a Novel CMOS Intra-Cerebral $\beta+$ Probe for Deep Brain Imaging in Awake and Freely-Moving Rat: a Monte-Carlo Study". In: *IEEE Transactions on Radiation and Plasma Medical Sciences (Manuscript ID TRPMS-2018-0027)* (2018)

To be submitted:

- M. Kachel et al. "A Fully Depleted CMOS Pixel Sensor for Soft X-ray Detection at Synchrotron Light Sources". In: *TBD* (2018)

- M. Kachel et al. "Monolithic Active Pixel Sensor for Low Energy X-ray Applications". In: *TBD* (2018)

Université de Strasbourg

Julian HEYMES

pcp

Désertion de Capteurs à Pixel CMOS : Etude, Caractérisations et Applications

Résumé

Une architecture de capteurs à pixels CMOS permettant la désertion du volume sensible par polarisation via la face avant du circuit est étudiée à travers la caractérisation en laboratoire d'un capteur prototype.

Les performances de collection de charge confirment la désertion d'une grande partie de l'épaisseur sensible. De plus, le bruit de lecture restant modeste, le capteur présente une excellente résolution en énergie pour les photons en dessous de 20 keV à des températures positives. Ces résultats soulignent l'intérêt de cette architecture pour la spectroscopie des rayons X mous et pour la trajectométrie des particules chargées en milieu très radiatif.

La profondeur sur laquelle le capteur est déserté est prédite par un modèle analytique simplifié et par des calculs par éléments finis. Une méthode d'évaluation de cette profondeur par mesure indirecte est proposée. Les mesures corroborent les prédictions concernant un substrat fin, très résistif, qui est intégralement déserté et un substrat moins résistif et mesurant 40 micromètres, qui est partiellement déserté sur 18 micromètres mais détecte correctement sur la totalité de l'épaisseur.

Deux développements de capteurs destinés à l'imagerie X et à la neuro-imagerie intracérébrale sur des rats éveillés et libres de leurs mouvements sont présentés.

Mots clés : Détecteurs Semi-conducteur, Capteur à pixels CMOS, Désertion, Développement de capteur, Radiotolérance, Spectroscopie

Résumé en anglais

An architecture of CMOS pixel sensor allowing the depletion of the sensitive volume through front-side biasing is studied through the characterization in laboratory of a prototype.

The charge collection performances confirm the depletion of a large part of the sensitive thickness. In addition, with a modest noise level, the sensor features an excellent energy resolution for photons below 20 keV at positive temperatures. These results demonstrate that such sensors are suited for soft X-ray spectroscopy and for charged particle tracking in highly radiative environment.

A simplified analytical model and finite elements calculus are used to predict the depletion depth reached. An indirect measurement method to evaluate this depth is proposed. Measurements confirm predictions for a thin highly resistive epitaxial layer, which is fully depleted, and a 40 micrometers thick bulk less resistive substrate, for which depletion reached 18 micrometers but which still offers correct detection over its full depth.

Two sensor designs dedicated to X-ray imaging and in-brain neuroimaging on awake and freely moving rats are presented.

Keywords: Semiconductor Detectors, CMOS Pixel Sensors, Depletion, Sensor Development, Radiation hardness, Spectroscopy